Large Eddy Simulations of Heat Transfer within Aircraft Engine Acoustic Treatments

Soizic Esnault

THÈSE

En vue de l'obtention du

DOCTORAT DE L'UNIVERSITÉ DE TOULOUSE

Délivré par :

Institut National Polytechnique de Toulouse (Toulouse INP)

Discipline ou spécialité :

Energétique et transferts

Présentée et soutenue par :

Mme SOIZIC ESNAULT

le mercredi 31 mars 2021

Titre :

Large Eddy Simulations of Heat Transfer within Aircraft Engine Acoustic Treatments

---

Ecole doctorale :

Mécanique, Energétique, Génie civil, Procédés (MEGeP)

Unité de recherche :

Centre Européen de Recherche et Formation Avancées en Calcul Scientifique (CERFACS)

Directeur(s) de Thèse :

M. FLORENT DUCHAINE

Rapporteurs :

M. FRANCK NICOUD, UNIVERSITE DE MONTPELLIER

M. MATTHIEU FENOT, ENSMA POITIERS

Membre(s) du jury :

M. ERIC LAMBALLAIS, UNIVERSITE DE POITIERS, Président

M. ARNULFO CARAZO MENDEZ, AIRBUS FRANCE, Invité(e)

M. FLORENT DUCHAINE, CERFACS, Membre

M. LAURENT GICQUEL, CERFACS, Invité(e)

MME ESTELLE PIOT, ONERA TOULOUSE, Membre

M. STÉPHANE MOREAU, UNIVERSITE DE SHERBROOKE, Membre

Contents

Remerciements

Il est à présent temps pour moi de rédiger les remerciements. Et c'est qu'il y en a des personnes à remercier ! Depuis les personnes qui m'ont donné l'envie de me lancer dans l'aventure de la thèse, à ceux ayant contribué à son bon déroulement, en passant par ceux qui m'ont soutenue de près ou de loin, j'ai eu la chance d'être bien entourée.

Je tiens à remercier en premier lieu l'ensemble des membres du jury pour leur lecture du manuscrit et les échanges particulièrement intéressants que nous avons eus durant la soutenance.

Effectuer ma thèse au Cerfacs a été une formidable opportunité, offrant un cadre très favorable et épanouissant. En particulier, je tiens à remercier mes encadrants de thèse. J'ai beaucoup apprécié travailler avec Florent, qui a été d'une grande aide sur de nombreux points, parmi lesquels la proposition de directions pour mener les travaux de recherche, les conseils pour la rédaction ou ceux pour les travaux de présentation, ainsi que la fameuse question "pourquoi" qui permet d'aller plus loin... ou encore pour me rassurer quant à mes travaux lorsque j'arrivais dans son bureau avec tout mon stress et mes questions. Merci également à Laurent pour le recul qu'il avait par rapport au sujet, qui m'a souvent permis de me poser les bonnes questions. Enfin, bien qu'il ne soit pas officiellement encadrant, Stéphane a largement contribué à la réussite de cette thèse notamment en apportant son appui sur les questions d'acoustique, vaste domaine que j'ai en grande partie découvert en entamant la thèse.

Cette thèse s'intègre dans le projet OPTIMA, financé par la DGAC et piloté par Airbus. Je remercie Maxime Zebian, Yannick Sommerer et Arnulfo Carazo Mendez pour les différents échanges que nous avons pu avoir dans ce cadre, qui m'ont permis de mieux appréhender les objectifs industriels. Dans ce cadre, j'ai également pu discuter avec différents chercheurs de l'institut Pprime ayant travaillé sur le banc expérimental. Je remercie donc particulièrement Bastien Giachetti et Matthieu Fénot. Plus généralement, cela a été un réel plaisir que d'échanger en tant que chercheuse avec des gens qui ont contribué à ma formation, puisque je suis passée par l'option Thermique de l'ENSMA et connaissais donc déjà plusieurs membres de l'équipe ("la thermique pour sauver l'Antarctique" restera toujours un grand classique, merci à nos enseignants de l'ENSMA pour cela).

D'autres chercheurs au Cerfacs ont également été de grands soutiens à différentes étapes de la thèse. Je tiens donc à remercier l'ensemble de l'équipe des chercheurs. Plus particulièrement, merci à Corentin, Franchine et Pierre pour les discussions que nous avons eues au début de la thèse sur la prise en main de certains outils numériques et à Gabriel pour avoir toujours pris le temps de répondre à mes questions sur les aspects numériques. Merci également à lui pour les conseils de cycliste, sans lesquels j'aurais probablement mis encore plus de temps à me mettre au vélotaf ce qui aurait été bien dommage. Un immense merci également à mon co-bureau Nico, surtout pour le temps accordé à répondre à mes questions sur AVBP, toujours avec patience et pédagogie, mais aussi pour le partage de chocolat et de gateaux (parce que apparemment "c'est bon pour ce que j'ai").

Si le Cerfacs est un lieu aussi propice à la bonne réussite de thèses, c'est aussi grâce aux différents services qui nous permettent de travailler dans les meilleurs conditions possibles. Merci donc à toute l'équipe administrative et en particulier Chantal, Michèle et Marie pour leur bonne humeur et leur travail efficace qui simplifie la vie au quotidien des doctorants. Merci également à toute l'équipe informatique, particulièrement Fred, Fabrice, Isabelle, Nicolas Gérard, pour le soutien qu'ils ont pu m'apporter face à tous les tracas d'origine informatique auxquels j'ai été confrontée, depuis mon arrivée au Cerfacs jusqu'au jour de la soutenance.

Et bien évidemment parmi les membres du Cerfacs que je tiens à remercier, il y a l'ensemble des doctorants et post-doctorants avec qui j'ai pu échangé lors de ces quatre dernières années, au travail, en pause ou en dehors du Cerfacs. J'ai donc une pensée pour tous ceux avec qui j'ai passé de longues pauses à discuter de science, de climat, de vélo, de café, de musique, de la vie après la thèse, ou à refaire le monde, pour les cruciverbistes de la pause de 10h et les joueurs de tarot du midi, pour les soirées jeux de société ou plus récemment among us. Parmi les plus proches, je souhaite citer Maël (bravo pour la quête de la Sainte Turbine), Fabien (jusqu'à l'écluse !), Simon (et les supers discussion autour de la musique, j'espère qu'un jour on arrivera à jouer ensemble), Fred, Quentin, Paul.

Enfin il me reste à remercier tous les gens hors du Cerfacs qui ont également pu me soutenir. En premier lieu, l'équipe de recherche rencontrée lors de mon stage à Strathclyde University, qui a fortement contribué à mon envie de faire une thèse. Il y a ensuite tous les amis que j'aurais voulu voir réunis lors d'un pot de thèse (peut-être en 2022 ?). Il y a les copines de prépa Camille Mélanie et Marie, même si on ne se voit pas souvent je suis ravie que l'on reste en contact. Les amis de l'ENSMA. Les copains du vélopicole 2020 (le meilleur concept possible de vacances !), Florian, Cyril et Maxime, avec qui l'on s'est aussi beaucoup retrouvés le soir en ligne en ces temps compliqués de confinement (j'ai hâte de voir fini le phare que vous construisez dans Valheim !). J'ai un remerciement tout particulier pour Florian, qui était sur Toulouse pendant une partie de ma thèse et qui a aussi participé aux soirées apéro / pizza / jeux de société / jeux vidéo / bar / restaurant (dans le monde d'avant) / et surtout Overcooked ! Et enfin les membres du bagad de Toulouse, que ce soit pour l'apprentissage de la cornemuse qui m'aidait à me sortir la tête de la thèse de

temps en temps, pour les apéros ou tout simplement pour la bonne humeur. En particulier, merci à Pierre (je n'aurais jamais cru tomber à Toulouse sur un Ensmatique jouant de la cornemuse, et encore moins qu'il m'apprendrait à en jouer), Ludo, Nico, Nolwenn, Judikaël, Clémence. En ce contexte particulier, je n'ai pas eu l'occasion de faire d'apéro d'au revoir mais ce n'est que partie remise, et j'espère bien que nous aurons d'autres occasions de sonner ensemble.

Parmi les gens qui m'ont soutenue tout au long de la thèse, je ne peux pas oublier ma famille, qui a toujours été là. Merci notamment à Marie pour m'avoir accueillie lors de mon arrivée à Toulouse. Merci à tous pour vos mots d'encouragements et de soutien. Bien évidemment je remercie en particulier mes parents, qui m'ont permis de suivre des études enrichissantes et m'ont encouragée tout du long. Merci à Gaëlle et Corentin aussi, pour votre présence malgré la distance.

A Arthur, merci pour tout.

Nomenclature

Latin letters

$\overline{P_t}$	Instantaneous, surface-averaged pressure	
$\overline{T_t}$	Instantaneous, surface-averaged vertical temperature	
$\overline{W_t}$	Instantaneous, surface-averaged vertical velocity	
$\overline{W}$	Jet velocity	$\mathrm{m.s^{-1}}$
$\vec{u}$	flow velocity	$\mathrm{m.s^{-1}}$
A	Neck section	$\mathrm{m^2}$
c_0	Speed of sound	$\mathrm{m.s^{-1}}$
D	Perforation diameter	m
d	Distance between two neighbour perforations	
f	Acoustic signal of piston motion frequency	Hz
f_H	Helmholtz resonance frequency	Hz
$F_{1/4}$	Quarter-wave resonance frequency	Hz
h	wall heat transfer coefficient	$\mathrm{W.m^{-2}.K^{-1}}$
K	Oscillation amplitude	m
L	Cavity length	m
l	Neck length	m
L_0	Stroke length	m
M	Velocity ratio	
m	Resonator equivalent mechanical system mass	
p	flow pressure	Pa

R	Acoustic resistance	
Re	Reynolds number	
rms	Root mean square	
S	Stokes number	
s	Resonator equivalent mechanical system stiffness	
s_{perfo}	Surface of all the perforations	m^2
S_{plate}	Plate surface	m2
St	Strouhal number	
T	Period	s
t	Instantaneous time	s
T_w	Wall temperature	K
T_{ref}	Reference temperature	K
u, v and w	Axial, spanwise and vertical velocities	$m.s^{-1}$
U_0	Grazing flow mean velocity	$m.s^{-1}$
V	Cavity volume	m^3
V_I	Vortex pair induced velocity	
V_S	Suction velocity	
X	Acoustic reactance	
x, y and z	Axial, spanwise and vertical coordinates	m
Y^+	Normalised wall distance	
Z	Specific impedance	$Pa.s.m^{-1}$
z	Reduced specific impedance	
Z^*	Dimensionless vertical distance	
Z_0	Ambient characteristic impedance	$Pa.s.m^{-1}$
z_{max}	Upper limit of the mesh moving part	
Z_{mean}	Medium course position of the pistons	m
z_{node}	Instantaneous position of a node	
$Z_{pistons}$	Vertical position of the pistons	m

Greek letters

α	Cell dilatation control parameter for the metric definition	
χ	Similitude ratio	
$\Delta\phi$	Phase difference between two inline synthetic jets	
λ	Acoustic wavelength	m
λ_{air}	Air thermal conductivity	$W.m^{-1}.K^{-1}$
ν	Fluid kinematic viscosity	$m^2.s^{-1}$
ω	Angular frequency	Rad
Ω_V	Vortex strength	
Φ	Nondimensionnal value to compute the metric	
ϕ	Convective wall heat flux	$W.m^{-2}$
ρ	flow density	$kg.m^{-3}$
σ	Porosity	
τ_w	Wall shear stress	Pa
ε_{max}	Metric maximum value	
ε_{min}	Metric minimum value	
ξ	Fluid displacement within the neck	

Subscripts and superscripts

$\bar{-}$	Time-averaged operation
$_0$	Hydrodynamic variables
$_H$	Helmholtz resonator value
$_{1/4}$	Quarter-wave resonator value
$_{engine}$	Value associated to the engine scale
$_{exp}$	Relative to the experimental values
$_{FP}$	Relative to the equivalent flat plate
$_{lab}$	Value associated to the lab scale
$_{M1}$	Relative to mesh M1
$_{rms}$	Root mean square value

$_{theo}$	Relative to the theoretical values
$'$	Acoustic variables

Abbreviations

ACARE	Advisory Council for Aviation Research and Innovation in Europe
ALE	Arbitrary Lagrangian-Eulerian
BPR	Bypass Ratio
CERFACS	Centre Européen de Rechercher et de Formation Avancée en Calcul Scientifique
CFD	Computational Fluid Dynamics
CORIA	COmplex de Recherche Interprofessionnel en Aérothermie
CRVP	Counter-Rotating Vortex Pair
DDOF	Double Degree of Freedom
DGAC	Direction Générale de l'Aviation Civile
DNS	Direct Numerical Simulation
IFPEN	Institut Français du Pétrole et des Energies Nouvelles
JICF	Jet In Cross-Flow
LES	Large Eddy Simulation
LODI	Local One Dimensional Inviscid formulation
LW	Lax-Wendroff
NSCBC	Navier-Stokes Characteristic Boundary Conditions
OPTIMA	OPtimisation Thermique de l'Intégration des Moteurs d'Avion
PIV	Particle Image Velocimetry
RANS	Reynolds Averaged Navier-Stokes
SDOF	Single Degree of Freedom
SJ	Synthetic Jet
SJA	Synthetic Jet Actuator
SPL	Sound Pressure Level dB
TTGC	Two-step Taylor-Galerkin C
URANS	Unsteady RANS

Context

Figure 1: Impact of noise at different Sound Pressure Levels orders of magnitude.

The aeronautic industry is currently facing two major challenges. The first one is the need for a cost reduction, that requires a decreasing fuel consumption. The second challenge is the reduction of its environmental impact, which is imposed by more and more restrictive international regulations in order to tackle both public health and global warming issues. In particular, requirements for noise and pollution reduction are increasing. Aircraft noise is a real nuisance for populations, especially at take-off and landing near airports. As can be seen in Fig. 1, which provides some orders of magnitude for sound levels, aircraft noise is high enough to be dangerous for human health. Although it is reduced with the distance, it can remain tedious for people living close to air lanes. In Europe, the ACARE (Advisory Council for Aviation Research and Innovation in Europe) objectives imply a halving of aircraft noise between 2000 and 2020 and a noise reduction of 65% between 2000 and 2050. The emissions due to aircraft engines also have a strong impact on public health, and even on the whole society, through their part on global warming. The targets fixed by the ACARE for aircraft emission reduction are a 1.5% annual fuel efficiency improvement until 2020 and a 75% reduction of emitted CO2 in 2050, compared to 2000. Modern and future engine architectures are thus designed to meet these two requirements: the reduction of fuel consumption and the reduction of noise and pollution.

Among the available architectures, the turbofan is widely used to power civil aircrafts. A turbofan cut is presented in Fig. 2. In these engines, the flow is divided

into a primary and a secondary flows. The primary flow is led through the compressor to the combustion chamber, or combustor, where the combustion releases the energy used to move the fan and the compressor through the turbine work. It is then expelled and contributes to the thrust. The secondary flow is propelled by the fan through bypass ducts and generates most of the thrust. The air mass flow going through the bypass ducts, divided by the air mass flow going through the core, is called the bypass ratio (BPR). Current and future turbofan architectures are based on an increasing bypass ratio, meaning that the part of the flow going through the bypass ducts is getting higher. This rising bypass ratio enables the engines to generate a higher thrust at iso-fuel consumption, therefore to reduce the fuel consumption and the pollutant emissions.

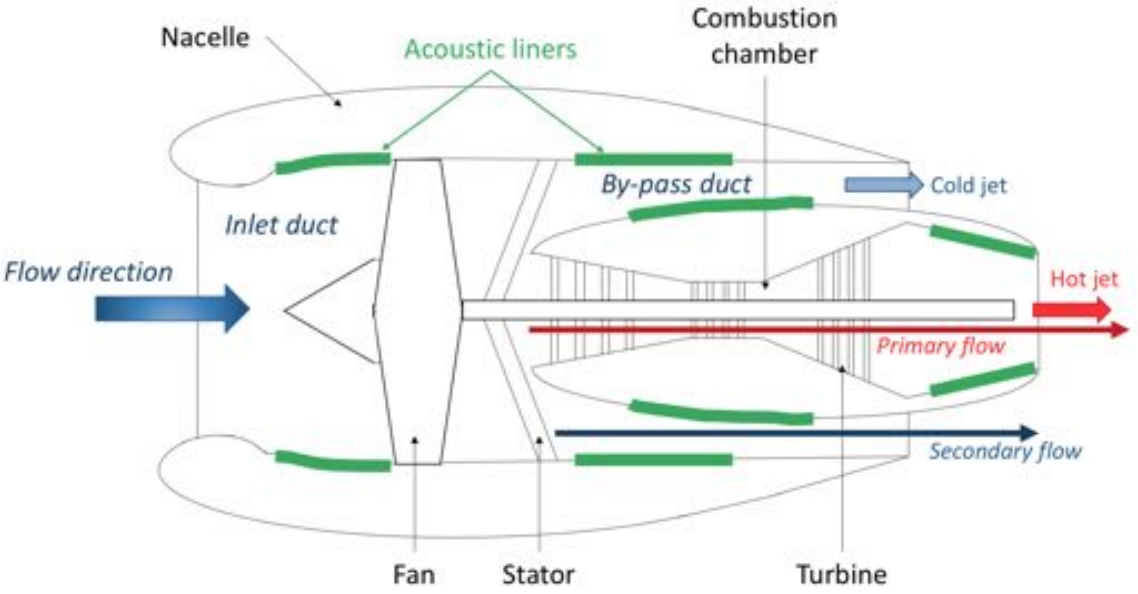

Figure 2: Turbofan scheme, partly adapted from the one proposed by Elnady [1]. The position of the acoustic liners can be seen in green on the intake and bypass duct walls.

In general, a turbofan engine is a complex, critically hot environment and different cooling issues have to be considered. These cooling requirements have become more drastic with time. A way to increase turbofan performance consists in increasing the combustion temperature. Indeed, the turbofan principle is based on that of a gas turbine [2], which relays on the Brayton thermodynamic cycle. Analysis of such systems [3] show that their efficiency is directly linked to the ratio of total temperature at the inlet of the turbine and the total temperature at the inlet of the compressor. This ratio is therefore a useful design parameter to increase the engine efficiency by to improving the cycle efficiency. However, the total temperature at the inlet of the compressor is fixed by the engine ambient conditions (altitude and Mach number), it is thus the total temperature at the inlet of the turbine which is increased, hence the higher combustion temperatures. With such high combustion temperatures, the combustion chamber walls need to be cooled down under their material melting temperature [4]. Similarly, the high turbine entry temperature has

to remain below this maximum allowable blade temperature. With the will to increase the efficiency, the inlet turbine temperature has increased with time, requiring more and more efficient cooling systems [5]. Another non-negligible issue raised by high temperatures within turbofans is linked to the electronic systems, which are increasingly used in aircraft engines in equipments around the engine core, but are very sensitive to high temperatures and once again require efficient cooling protections [6, 7].

The OPTIMA (OPtimisation Thermique de l'Intégration des Moteurs d'Avion) project, funded by the DGAC (Direction Générale de l'Aviation Civile) and led by Airbus, in France, aimed at considering heat transfer issues with engine embedding into nacelles in modern and future engine architectures. In this context, two major challenges are heat transfer enhancement and energy valorisation. The first one aims at developping new cooling systems, in order to protect the temperature sensitive systems in the engines, such as electronic systems or low melting temperature materials as mentionned above. The second point is based on the idea that energy is lost to the atmosphere through heat, and that it would be of interest to recover this energy and inject it back where needed in the engine.

One part of the OPTIMA project focuses on the heat transfer that takes place in the nacelle walls, more specifically within the bypass ducts. Indeed, the cold flow that goes through the fan ducts could be used as a cold source in order to enhance heat transfer within the nacelle. However, these walls are lined up with acoustic treatments, called "acoustic liners". These liners are used to damp the acoustic waves coming from the fan, and are in fact necessary to reduce enough the noise in order to meet the restrictive regulations concerning noise pollution near inhabited areas. Their position in the engine can be seen in Fig. 2. In the presence of acoustic liners, the flow presents a very specific, complex behaviour, with a consequent impact on the boundary layer. The acoustic resonance, which is at the root of liner design, leads to the formation of jets and vortices. Through this phenomenon, the acoustic energy is converted into kinetic energy, reducing the noise. Most of the research and design work on these devices concern noise reduction and there is very few knowledge about heat transfer within acoustic liners. Compared to a flat plate, it is expected that the complex flow developing on acoustic liners increases wall heat transfer. The OPTIMA project is thus considering the option of combining acoustic liners and heat exchangers, in order to maximise heat exchange. This has obviously to be done while minimising the impact on the acoustic treatment and aerodynamic performance.

This thesis, as a part of the OPTIMA project, aims at increasing the knowledge about heat transfer within acoustic liners: the flow behaviour within acoustic liners, although it has widely been studied in the context of acoustic damping, is not clearly understood when facing high temperatures, and its potential when dealing with heat transfer enhancement still has to be quantified. To do so, the study is mainly based on an experimental set-up that was designed at Institut Pprime, Poitiers, France in the context of the OPTIMA project. This rig, based on a similitude with an

increase in size, reproduces the behaviour of the flow within a liner while heating the system. LES (Large Eddy Simulations) are used to numerically reproduce the Pprime configuration. Confronting the numerical results with experimental data enables the validation of the simulations, before using them to further analyse the flow behaviour and heat transfer enhancement within liners.

The construction of the Pprime facility was justified by the observation that the process of importance in liner design is the so-called "synthetic jet" generation triggered by the acoustic resonance. This phenomenon of "synthetic jets" consists in a zero-net mass flow process that is characterised by the alternative succession of ejection and aspiration of the ambient flow through a perforated plate into cavities. The main limitation of the test rig is that here this specific flow behaviour is not triggered by acoustics but by pistons placed within the system. This difference in triggering mechanism can therefore lead to differences in flow dynamics and resulting wall heat transfer. Among other things, the pistons are all put into motion by the same engine and are thus in phase, while the synthetic jets along an acoustic liner are triggered by a propagating acoustic wave and a phase difference can be observed between perforation responses. Another point that can be noted is that due to the similitude ratios (increase in size), the flow velocities are much lower for the rig than for a liner. As a consequence, the flow can be considered incompressible for the Pprime rig case, while it is obviously compressible for a classic liner. A limitation of the test rig is that it was used with low grazing flow Mach numbers (under 0.3 when rescaled to the liner dimensions) while flight conditions can imply grazing flow Mach numbers up to 0.5. After validating the numerical set-up thanks to the available experimental data, a significant contribution of the present work has therefore consisted in validating the use of Pprime's rig as a proper representation of a classical liner and assess its potential limitations. This was done with additionnal numerical simulations, performed on a dedicated set-up with a similar geometry rescaled to the classical dimensions of an acoustic liner and acoustically triggered synthetic jets. This validation of the numerical set-up finally enabled to expand the investigation to more flight-representative operating points.

This manuscrit is divided into three parts. Part I provides a literature review about acoustic liners and synthetic jets. The objective is to understand how the synthetic jets generated through the acoustic liners can be used to enhance heat transfer, and to highlight the innovative character of the study. Chapter 1 focuses on acoustic liners with a description of their different geometries and acoustic features. The general context of synthetic jets, which have been widely studied in other contexts than acoustic damping, and their flow dynamics specificities are presented in Chapter 2. Chapter 3 recaps the most important points of the literature review and brings out the specificities of the present study, before detailing the thesis objectives in light of the literature. Then, Part II provides the validation of the numerical set-up and the liner-representativity of Pprime's rig. Chapter 4 presents the experimental configuration and the corresponding numerical set-up. Based on one specific operating point, the simulations are validated by comparing the numerical results to the experimental data in Chapter 5. The numerical results are

then used to deeply analyse the flow behaviour and the heat transfer. The liner-representativity of the rig is validated thanks to a similar configuration rescaled at the dimensions of a real acoustic liner, in Chapter 6, and for which the synthetic jets are triggered by the acoustic resonance, as for a classical acoustic liner. Chapter 7 is then dedicated to the study of upstream turbulence impact for both engine and lab scales. Finally, Part III exploits the whole database, composed of both the Pprime configuration (lab scale) and the realistic-scale set-up (engine scale), with different operating points to provide insights in heat transfer under different conditions. A specific operating point is used to provide a brief comparison with a jet in cross flow configuration in Chapter 8. In Chapter 9, the whole database, including both configurations, enables the confrontation of a large range of operating conditions and the quantification of heat transfer enhancement in different cases.

Part I

Introduction

1 Acoustic liners

Before considering heat transfer within acoustic liners, it is important to obtain a proper understanding of their acoustic behaviour only. After developping the aeronautical context of acoustic liners, this chapter provides some theoretical and practical background about liners, based on a literature review. A description of liners is first given, with a focus on their working principle, where the different acoustic damping mechanisms are described. The main geometrical parameters and their importance in the liner design are then provided, before detailing the flow behaviour in a quiescent environment as well as in presence of a grazing flow. Finally, the few available knowledge about heat transfer within acoustic liners is examined.

1.1 Aeronautical context

Noise can be a real nuisance for populations. Thus, in the aeronautical context, regulations are requiring from aircraft companies to built increasingly quieter planes. In Europe, the ACARE proposed an objective of noise reduction by 50% in 2020, and by 65% in 2050, compared to 2000 levels. Therefore, it is crucial in the aircraft industry to identify and handle noise sources. Many efforts have addressed these issues in recent years. They are outlined in an extensive literature review on aircraft noise sources and reduction technologies, proposed by Casalino *et al.* [8]. More recently, Leylekian *et al.* [9], in Europe, and Zante *et al.* [10], in the USA, provided overviews on research on aircraft noise reduction. As a matter of fact, recent work has already enabled aircraft manufacturers to design quieter planes: Fig. 1.1 shows the progress, in terms of noise level reduction, that has been made since the fifties, in correlation with the development of new engine architectures. The main noise sources in an aircraft are the airframe and the engine. Different engine noise sources can be identified: the fan, the jet, the compressor, the turbine and the combustion. In addition to a global noise decrease, the architecture evolutions led to a complete

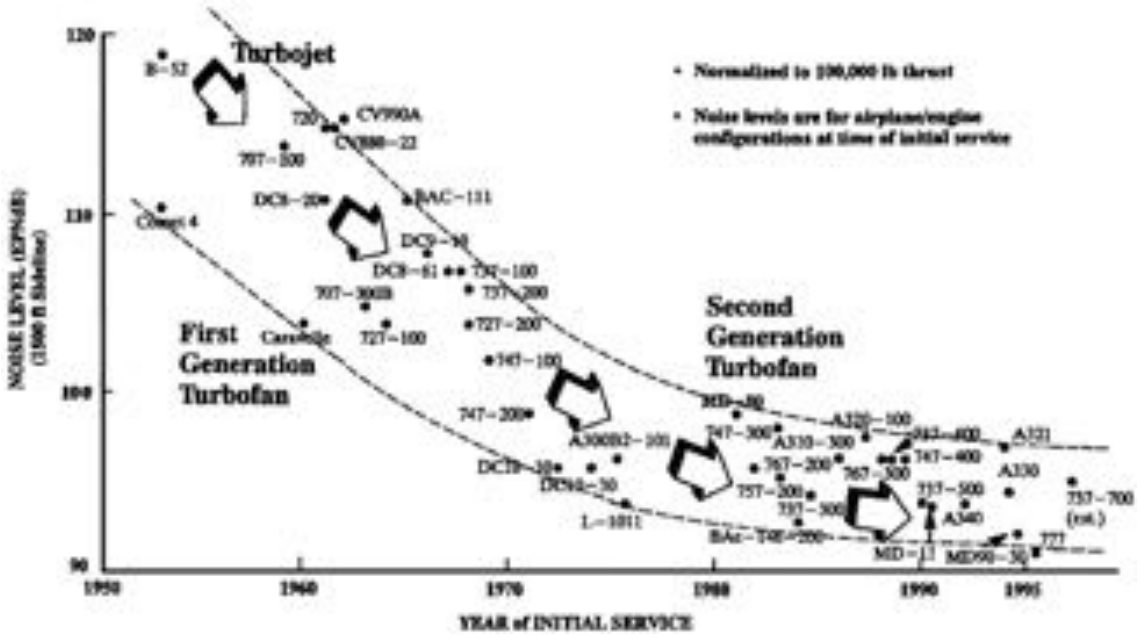

Figure 1.1: Progress in aircraft noise reduction [11].

modification of the importance of the different noise sources, relatively to each other. The jet noise in particular has drastically decreased (even though it remains a major noise source), while the fan has become predominant. It shall also be pointed out that the noise distribution depends on the flight phase. Typically, the airframe noise is much more important in the landing phase than in the take-off, while the jet noise is major during take-off and becomes minor at landing. These two flight phases are critical when studying noise since they correspond to the time when aircraft noise is generated near inhabited areas. During both of these phases, the engine represents a major source of noise.

Considering the forthcoming evolution from high-bypass-ratio to ultra-high-bypass ratio turbofans, the part of the fan in the engine noise production is expected to become even more significant. When considering engine noise issues, it is thus now essential to specifically tackle fan noise. Tonal noise, meaning that the sound corresponds to a specific, narrow range of frequencies, is due to the fan rotation and the rotor / stator interaction. It depends on the fan rotation speed and the number of blades. It is opposed to broadband noise (corresponding to a wide range of frequencies) and requires specific treatments to be reduced. Envia [12] gives an overview of research on fan noise reduction. He distinguishes two different ways of reducing fan noise: noise source control and noise propagation control. The present study is focusing on a specific noise propagation control system, that is widely used in modern turbofans: acoustic liners.

1.2 Acoustic liner working principle and associated geometry

This section is dedicated to the description of liners from the acoustic point of view. The working principle of a classic acoustic liner is first described: some acoustic notions are briefly defined, followed by a focus on acoustic resonance, a basic geometrical description of a classic liner and the different acoustic damping mechanisms. Different liner geometries are then presented, either already widely used or still subjects of research. Finally, the acoustic impedance, used to characterise and quantify the behaviour of a liner, is addressed.

1.2.1 Working principle of an acoustic liner

The working principle of acoustic liners is based on the conversion of acoustic energy into kinetic energy, through the formation of vortices. In order to properly understand this phenomenon, some notions of acoustics need to be described first. In particular, the resonance phenomena that can appear within a duct or a cavity have to be detailed, with a focus on quarter-wave and Helmholtz resonance. Finally, the strategy used to damp noise with an acoustic liner is described, leading to a description of the basic geometrical features of an acoustic liner.

1.2.1.1 Acoustic resonance: quarter-wave and Helmholtz resonator

This paragraph describes the basic notions of acoustics that are required to understand the working behaviour of an acoustic liner. It does not intend to give a complete, extensive description of acoustics theory. More details about the definitions that are provided here can be found in the chapter 8 of Poinsot and Veynantes's book [13] and in the book of Kinsler *et al.* [14]. The interested reader who would appreciate more information about the vast field of acoustics is advised to read the books of Kinsler *et al.* [14], Morse and Ingard [15] and Pierce [16].

A wave is a perturbation that is propagated through a domain, corresponding to changes of speed and thermodynamic variables within the domain. In particular, acoustic waves are waves that are moving at the speed of sound c_0. The variables of the considered domain can be defined as the sum of two values: a first part that describes the hydrodynamic part of the flow and a second one that represents the acoustic perturbations. This leads to the following definitions:

$$p(x,y,z,t) = \quad p_0(x,y,z,t) + p'(x,y,z,t); \tag{1.1}$$

$$\vec{u}(x,y,z,t) = \quad \vec{u_0}(x,y,z,t) + \vec{u'}(x,y,z,t); \tag{1.2}$$

$$\rho(x,y,z,t) = \quad \rho_0(x,y,z,t) + \rho'(x,y,z,t); \tag{1.3}$$

where p, $\vec{u}$ and ρ correspond to the flow pressure, velocity and density, while p_0, $\vec{u_0}$,

ρ_0 are the hydrodynamic variables and p', $\vec{u'}$, ρ' the acoustic variables.

Knowing the boundary conditions is crucial to study the acoustics of channels and ducts. Indeed, they impose conditions on p' and $\vec{u'}$, which imposes harmonic modes and modifies the acoustic behaviour of the fluid. In particular, some resonance effects, linked to the geometry, can be observed. The resonance is a phenomenon that appears in oscillating systems: at specific frequencies, called resonant frequencies, the amplitude of the oscillations is enhanced. In the case of acoustics, the resonant frequency mostly depends on the system geometry. From the application point of view, the resonance phenomenon can lead to damage or enhanced performance, and thus needs to be avoided or optimised. In the context of acoustic liners, the resonance is needed in order to improve the acoustic damping performance. Two particular resonator systems are further discussed in Section 1.2.1.1: the quarter-wave and the Helmholtz resonator.

To begin with, a quarter-wave resonator consists in a constant-section duct that is closed on one end and open on the other. The closed end being a rigid wall leads to $u' = 0$ at this boundary condition. On the other hand, the opend end of the duct is characterised by $p' = 0$. This resonator is well known and characterised by its resonant frequency $F_{1/4}$, given in Eq. (1.4):

$$\boxed{F_{1/4} = \frac{c_0}{4L}}, \tag{1.4}$$

where L is the duct length and c_0 the speed of sound, as defined in Eq. (1.5):

$$c_0^2 = (\frac{\partial p}{\partial \rho})_{s=s_0}. \tag{1.5}$$

The simplicity of this kind of resonator is very practical for many applications: since its resonant frequency only depends on the duct length, there is no constraint on the duct section surface and shape.

Another interesting resonator is the Helmholtz resonator. It is composed of a cavity and a neck, which links the flow within the cavity to the ambient flow. Historically, Helmholtz designed these devices in order to ease the identification of the different frequencies ("tones") [17] present in a complex sound when analysing music, including for "ears quite untrained in musical observation". The cavity could be spherical or cylindrical, and a second perforation was made in the cavity and "adapted for insertion into ear" (see Fig. 1.2). The second perforation is no longer needed for the applications considered here. These resonators can have different geometries such as a square section or a honeycomb cavity. In fact, the important parameters in the case of a Helmholtz resonator are:

- the cavity volume V;
- the neck section shape (round or slit) ;

Figure 1.2: Scheme of resonators designed by Helmholtz [17]; (a): funnel shaped opening, for insertion into the ear; (b): sharp edges opening, neck

- the neck section A, depending on its diameter D (round neck) or width and length (slit neck);
- the neck length l.

The Helmholtz resonator is usually compared to a mass-spring system, where the fluid present within the neck would be the mass, and the acoustic pressure within the cavity would be the stiffness. This model is valid under the condition that the acoustic signal wavelength λ is large enough when compared to the resonator dimensions. If $\lambda \gg l$, $\lambda \gg V^{\frac{1}{3}}$ and $\lambda \gg A^{\frac{1}{2}}$, it is considered that the small volume of fluid embodied within the neck will oscillate with the acoustic excitation. In order to calculate the "mass" m of the equivalent mechanical system, a correction on the neck length has to be made: $m = \rho_0 A l'$ with l' the corrected length, also called the "effective length" of the neck. This correction, which depends on the neck geometry, is due to the radiation-mass loading and $l' \geq l$. On the particular case of a circular neck with a diameter D and a small length l (for example, a hole in a thin wall) the effective length is given by Eq. (1.6):

$$l' = l + 1.7D. \tag{1.6}$$

With the dimensions V, A and l' (or l and D) it is now possible to use the analogy with a mechanical system that would be defined by the following parameters:

- the oscillating mass: $m = \rho_0 A l'$;
- the stiffness: $s = \rho_0 c_0^2 \frac{A^2}{V}$;
- the resistance: $R = \rho_0 c_0 \frac{k^2 S^2}{2\pi}$, with $k = \omega / c_0$ the wave number and $\omega = 2\pi f$ the angular frequency. This definition for R is valid under the assumption that l is small and the neck is round.

Such a system is well known for mechanical cases and is led by Eq. (1.7), where ξ corresponds to the displacement of the fluid embodied within the neck, and $f = AKe^{j\omega t}$ is the force driven by a sound wave of amplitude K that impacts the neck of the resonator.

$$m\frac{d^2\xi}{dt^2} + R\frac{d\xi}{dt} + s\xi = AKe^{j\omega t} \tag{1.7}$$

Finally, this well-known equation can be solved easily and leads to the definition of the system resonant frequency f_H:

$$\boxed{f_H = \frac{c_0}{2\pi}\sqrt{\frac{A}{l'V}}}. \tag{1.8}$$

The main geometric parameters and the corresponding resonant frequencies are summarised in Fig. 1.3 for both quarter-wave and Helmholtz resonators. Although both systems are not so different from each other, the calculation of their resonant frequencies depends on totally different parameters and thus can take different values. Indeed, the resonant frequency of the quarter-wave resonator depends only on the duct length, while the Helmholtz resonator resonant frequency depends on the cavity volume and neck dimensions, but not at all on the cavity length. Thus, for a targeted resonant frequency, it is possible to use both resonators but the constraints are much different in terms of volume and mass. Next section provides a discussion on the use of quarter-wave and Helmholtz resonators in the context of acoustic liners.

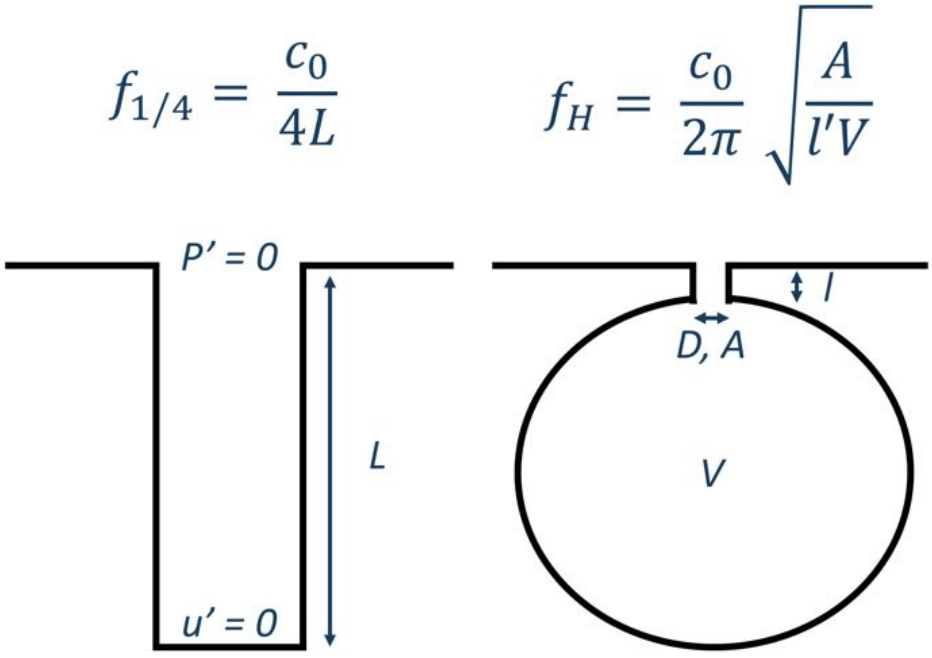

(a) Quarter-wave resonator (b) Helmholtz resonator

Figure 1.3: Schemes of resonators: main parameters and resonant frequencies.

1.2.1.2 Acoustic damping mechanisms of a liner

In aircraft engines, acoustic liners are used to damp the noise generated by the fan. The main mechanism it relies on consists in the conversion of acoustic energy into kinetic energy, through the formation of vortices. A classic acoustic liner is basically composed of two main parts: a perforated plate and a network of resonators. The formation of vortices mechanism is triggered by the perforations when they are impacted by the acoustic signal, and the resonator role consists in enhancing this mechanism. The present section focuses on the acoustic damping mechanisms, which requires the description of the flow dynamics. However, the purpose here is to discuss acoustics and not to provide an exhaustive literature review of acoustic liner flow dynamics. Therefore, the description provided here remains brief and the reader is advised to refer to Section 1.3 for a more detailed analysis of the flow dynamics.

In order to understand the liner working principle, it is important to comprehend the flow dynamics that is driven by an acoustic wave impacting a perforation within a wall. Indeed, as was shown several decades ago by Ingard and Labate [18], the flow behaviour around a perforation impacted by an acoustic signal presents an oscillatory pattern. When the local pressure rises due to the acoustic signal, the air tends to go through the perforation. This rise of pressure is followed by a relaxation, when the pressure decreases: the air flows back, still through the perforation but in the opposite direction. The flow around the perforation is thus characterised by the oscillation of the fluid, that goes through the perforation periodically in each direction. This behaviour is comparable to that of the fluid in the neck of a Helmholtz resonator and can be understood through the mass-spring analogy. An important distinction with classic Helmholtz resonators is that the liners are placed within the fan duct of the engine: in addition to the fan noise, the perforated wall of the liner is impacted by a grazing flow which can modify the flow dynamics. Nonetheless, the oscillating mechanism remains similar.

There are two types of dissipation mechanisms depending on the acoustic intensity, as numerically evidenced by Tam and Kurbatskii [19]: conversion of acoustic energy into heat by *friction in shear layer* and conversion of acoustic energy into kinetic energy, through the formation of vortices, identified as *vortex shedding*. At low Sound Pressure Level (SPL), that is to say at low acoustic intensities, the dissipation occurs through *friction in shear layer*. In these conditions, vortices are generated by the flow ejection however the acoustic excitation is not strong enough for the vortices to escape: they are sucked back into the neck. This behaviour is called linear regime. Friction is created in the perforation boundary layer, which is excited by the oscillatory behaviour of the flow near the aperture of the cavity. This absorption mode has been well known for a long time, since one of the first analytical models was proposed by Rayleigh in 1870 [20] and was followed by several finer models. However, they are valid only in linear acoustic conditions and fail to foresee the flow behaviour in case of a high acoustic intensity or a grazing flow. The *shedding of vortices*, which are then dissipated by the fluid viscosity, appears when the acoustic intensity is high enough. This phenomenon is a much more complex,

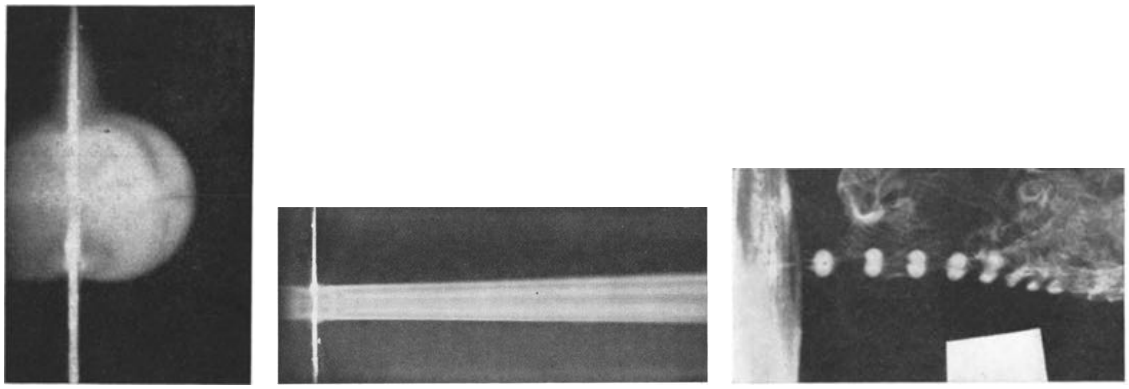

(a) Circulation in linear acoustics

(b) Jet in non linear acoustics

(c) Vortex shedding in non linear acoustics, higher SPL than for the jet

Figure 1.4: Different flow patterns identified by Ingard and Labate [18] around an orifice impacted by acoustic excitations at different SPL.

non-linear and efficient way of acoustic dissipation, and correspond to the liner non-linear regime. Although the friction in shear layer mechanism is still present, the vortex shedding is preponderant. Ingard and Labate [18] were among the firsts to observe it on their simplified configuration with a single hole and no cavity backing it. It enabled them to identify different flow patterns. Some of them are presented in Fig. 1.4: the circulation around the orifice in linear acoustics (Fig. 1.4a), the generation of a jet in non linear conditions (Fig 1.4b) and the vortex shedding that appear at even higher acoustic intensities (Fig.1.4c).

Adding a resonator to the perforation enables to increase the amplitude of the perforation flow oscillations at a given frequency and amplitude. Results of DNS performed by Roche [21], given in Fig. 1.5, illustrate the different flow patterns that can be observed when a perforation backed by a resonator is impacted by an acoustic signal. Roche considers a 2D simplified configuration inspired from Tam and Kurbatskii [19] for the sake of comparison. The flow velocity fields around the perforation are given for three different values of SPL: 75 dB, 135 dB and 155 dB. Similar flow behaviours than those observed by Ingard and Labate [18] can be identified, although the jet observed by Ingard and Labate is not retrieved in the numerical simulations of Roche (neither was it observed in Tam and Kurbatskii's simulations [19]). At a low acoustic intensity (75 dB), the velocities induced by the acoustic pulsations are weak and a viscous boundary layer develops along the hole walls. In this case, the acoustic absorption is achieved through the friction in the shear layers. Some vortices appear at 135 dB, but they remain attached to the perforation. Finally, the high acoustic intensity case (155 dB) shows much higher velocities (Roche mentions an instantaneous Mach number within the perforation up to 0.25, corresponding to a Reynolds number equal to 4500), with an apparent vortex shedding and a higher turbulence level. This corresponds to the non-linear behaviour of the liner, during which the acoustic energy is converted into kinetic energy mainly through the vortex shedding. The vortices are then dissipated by the

air viscosity. The friction in the shear layers within the perforation is still present but the vortex shedding is completely predominant in the acoustic absorption process.

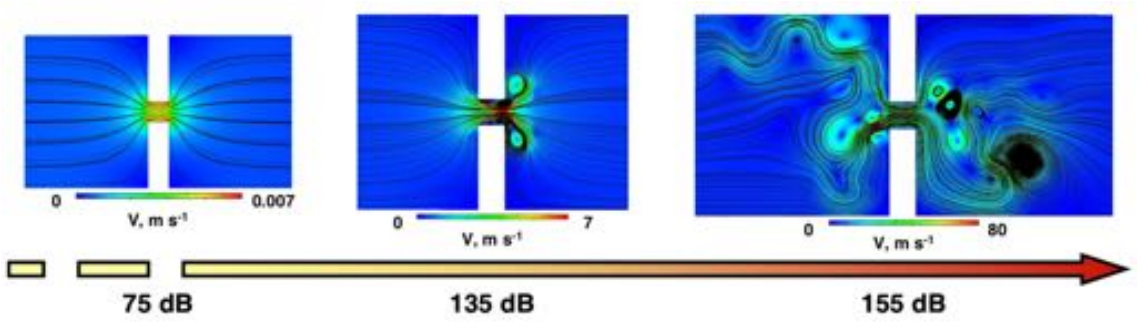

Figure 1.5: Evolution of the velocity field at the neck regarding the SPL. The formation of vortices is enhanced at higher SPL [21].

The resonators are used in addition to the perforated plate in order to enhance the vortex formation, leading to a higher acoustic damping. Indeed, if their resonant frequency corresponds to that of the noise generated by the fan, the amplitude of the flow oscillations at the neck is increased and so is the vortex formation. The resonators are a network of cavities placed between the wall and the perforated plate. The perforations act as necks, and the combination of the perforations and the cavities form Helmholtz resonators. Interestingly, both Helmholtz and quarter-wave resonance can be obtained with an acoustic liner. Since the resonant frequencies depend on different parameters, they are usually different. For example, Tam *et al.* [22] studied a liner geometry that corresponds to a Helmholtz resonant frequency equal to 450 Hz. In their configuration, the length (or depth) of the cavities is approximately equal to 56 mm, which leads to a quarter-wave frequency around 1500 Hz. The use of the Helmholtz resonance, compared to the quarter-wave resonance, enables to have less massive and cumbersome liners. Indeed, a quarter-wave resonator designed for a resonant frequency of 450 Hz would be 189 mm long, which is more than three times longer than the corresponding Helmholtz resonator. In the aeronautical context, light and aerodynamically-shaped systems are prefered. To target resonant frequencies as low as 500 Hz, Helmholtz resonators are thus privileged. However, since both of them can be triggered, it is of interest to understand which one is, and at which frequency. For example, Gomes *et al.* [23] compared the cavity resonance frequency they experimentally obtained for synthetic jet actuators (devices based on the Helmholtz resonator idea, used to generate jets at their necks, which can be triggered by acoustics as liners but also by moving parts placed within the cavity, see Chapter 2 for more details) to that predicted by the Helmholtz theory. They obtained important overpredictions with the Helmholtz theory, with an average of 18% and up to 35% error. Van Buren *et al.* [24] studied synthetic jet actuators with round cavities and showed that when the cavity is thin relatively to its diameter, that is to say pancake-shaped, the acoustics within the cavity is dominated by their quarter-wave resonance. This is even truer when the aperture is large, leading to a geometry that minimises the 3D impact on damping effect. On

the contrary, when the cavity is large, and even more when the aperture is small, the actuator geometry gets closer to an ideal Helmholtz resonator and the Helmholtz resonance dominates the cavity acoustics.

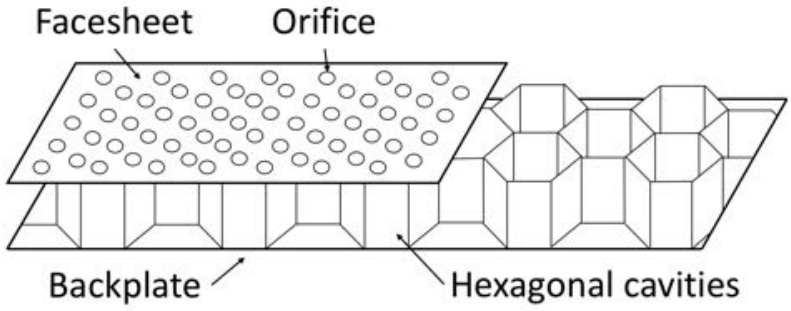

Figure 1.6: Classical acoustic liner scheme.

To conclude this section, a classical acoustic liner is composed of a perforated plate backed by a network of resonators. The perforated plate, when impacted by an acoustic excitation, triggers a complex flow oscillation that is amplified by the resonator if the acoustic frequency corresponds to its resonant frequency. A simplified scheme of a classical acoustic liner is presented in Fig. 1.6. For acoustic liners placed within the fan duct of an engine, the rigid backplate corresponds to the duct wall. For design and manufacturability reasons, the network of resonators are usually composed of honeycomb cavities. The next section discusses in more details the different geometries used for acoustic liners, and provides some orders of magnitude for the main geometrical parameters.

1.2.2 Evolutions of acoustic liner geometries

It has to be pointed out that different categories and geometries exist for acoustic liners. Some of them are presented in this section. A focus is first given on SDOF (Single Degree Of Freedom) and DDOF (Double Degree of Freedom) liners. An overview of future liner geometries is then provided.

1.2.2.1 Single-layer and two-layer liners

Different categories of acoustic liners can be distinguished: bulk absorbers are porous materials, while single- and two-layer liners are sandwich-structure composite materials [25]. Porous materials, efficient on broadband noise, are out of the scope of this study and thus will not be detailed here. On the contrary, the composite material category, efficient to treat tonal noise, is the one investigated here. Thus, in this manuscrit, the term "acoustic liners" is used only to refer to composite material liners. Among this kind of liners, two categories that are currently used in engines are presented. Their working principle is based on the mechanisms presented in the

previous section.

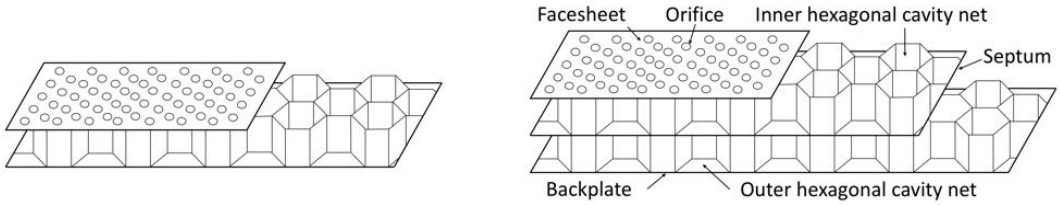

(a) Single-layer liner (b) Double-layer liner

Figure 1.7: Classic acoustic liner geometries

The simplest category of acoustic liners, called "single-layer liner" or sometimes "SDOF liner" (Single Degree of Freedom), is composed of a network of honeycomb cavities, backed by a rigid wall that is lined up, and covered by a perforated plate. It is the simplest category of liners based on the combination of a perforated plate and resonators. Due to their simplicity, these liners are the most widely studied.

Also called "DDOF liners" (Double Degree of Freedom), two-layer liners are built on the same principle than single-layer one, but two networks of honeycomb cavities are present, separated by an intermediary layer, or septum, as can be seen on Fig. 1.7b. The objective of combining two sets of cavities is to extend the range of frequencies over wich the resonance is efficient [21].

As mentioned above, SDOF and DDOF liners are efficient on tonal noise, meaning that they damp acoustic noise on a selective, narrow range of frequencies. Their geometry is therefore essential to obtain the required frequency range. The liner geometry is also determinant for the acoustic damping efficiency. For example, Jones *et al.* [26] proposed a parametric study on different geometrical parameters among which the sheet thickness, the sheet thickness-to-hole diameter ratio or the cavity depth and showed their impact on the acoustic absorption. The different design parameters playing a role in the frequency range selection are basically the same as for a Helmholtz resonator:

- The *cavity dimensions* are predominant to select the accurate frequency range. Indeed, as detailed in the previous section, acoustic liners are enhanced by acoustic resonance. According to their working principle, the cavity volume (for the Helmholtz resonance) and depth (for the quarter-wave resonance) will determine the frequencies for which the liner is efficient. The use of the Helmholtz resonance enables to limit the cavity heigth to around 50 mm when targeting resonant frequencies around 500 Hz, which also limits the bulkiness of the liner when compared to the equivalent quarter-wave resonance.

- A *porosity* σ is associated with the perforated plate, based on the number and area of the perforations in regard to the whole plate surface S_{plate}. It is

defined as $\sigma = \frac{s_{perfo}}{S_{plaque}}$, where s_{perfo} is the surface of all the perforations. The *position of the perforations*, relatively to each other, is directly linked to the porosity and plays a part in the liner working. Indeed, the jets and vortices generated at each hole impact the near flow. In case of a high enough porosity, that is to say when the different holes are close to each other, the jets can reach the closest perforations and thus modify the behaviour of the flow around them, leading to a modified acoustic absorption [27]. This is especially the case in the presence of a grazing flow, where the vortices generated at each hole are convected downstream and thus impact the following perforations [21]. Note finally that the porosity of a classical liner is around 10 % [22].

- The *shape and dimensions of the perforations* are also crucial, since they impact the formation of jets and vortices in the presence of an acoustic signal, which leads to a direct impact on the acoustic damping efficiency. For example, Tam *et al.* [28] found out that 45°-beveled apertures are more efficient than classic 90°-cornered apertures to create vortices. Moreover, under a certain value of SPL, no more vortex shedding can be observed for the right-angle aperture, while it is still the case for beveled aperture for lower values of SPL. The vortex shedding being the most important noise absorption mechanism (*cf.* section 1.2.1.2), this information is of importance for the liner geometry optimisation. Jing *et al.* [29] also evidenced the influence of the *plate thickness*, that is to say the perforation depth, on the liner performance in the presence of a grazing flow (*cf.* section 1.3.2). Finally, the *perforation section and diameter* are among the most important parameters, since they drive the Helmhotz resonance frequency, alongside the plate thickness. Typical liners rely on a perforation diameter around 0.8 to 1 mm and a section that is usually round.

1.2.2.2 A note on future liner designs

Acoustic liners have been shown to be an efficient fan noise damper, enabling the aircraft builders to meet strict noise regulations. A lot of modern engines are thus equiped with these acoustic treatments. Although future engine architectures might require an evolution on the use of acoustic liners, they shall still be present in turbofans. Future turbofans are expected to present a geometry different from current engines. In particular, the BPR will be higher and the engine will be shortened to reduce the nacelle drag [30]. With a potentially higher fan noise but less space to put the acoustic liners, solutions are required to avoid a global engine noise increase. Among the main studied ideas, we can quote the use of an extended and smarter liner distribution and the improvement of liner performance thanks to new geometries. Since the place for liners will be reduced, it can be of interest to use every possible location within the engine fan duct to put the acoustic liners. One of the possibilities is the inlet lip, although problems of compatibility with the de-icing systems need to be solved [31]. The distribution of the liners along the walls can also be optimised in order to improve the acoustic damping [32]. Finally, the design of the

liners can also be optimised, and adapted to the evolution of fan noise. For example, Jones [33] describes five concepts of liners targeting broadband noise. Among the different new liner designs, multi-layer and variable-depth liners are currently studied. Other new concepts are also under investigation. The acoustic metamaterial proposed by Beck *et al.* [34] combines a classic SDOF liner design with an array of round Helmholtz resonators. This enables the liner to damp noise at low frequencies (under 1000 Hz) while keeping the classic SDOF liner behaviour at higher frequencies with little impact on its performance. Another interesting concept is that of a bio-inspired liner with a structure reproducing a reed bundle, efficient on broadband noise and very interesting to damp frequencies under 1000 Hz [35].

In the current study, the aim is to use a well-known and widely used technology, the acoustic liner, to tackle two of the main issues that engine manufacturers are currently facing: noise reduction, which is the liner first purpose, as well as the increasing problem of heat transfer. The idea consists in taking advantage of the liner working principle by coupling them with heat exchangers, in order to enhance heat transfer. In a similar way than the other technologies under investigation, presented in the previous paragraph, the liner geometry might evolve. However, the main working principle and flow physics, based upon the formation of jets and vortices, shall be unchanged.

1.2.3 Liner performance: the impedance

The previous sections provided information about the working principle of an acoustic liner and the main flow dynamics features that can be found around it. This description would not be complete without the definition of the parameter that is used to characterise the liner performance: its specific impedance Z. This parameter is used to quantify the response of a system to an acoustic excitation. As Kinsler *et al.* [14] indicate, an analogy can be built between the acoustic system and an equivalent electrical circuit in which the flow behaviour would be represented by the current behaviour. Then, the voltage corresponds to the pressure difference and the current to the acoustic velocity. The acoustic specific impedance is then close to the electrical impedance, leading to:

$$Z = \frac{p'}{u'}. \tag{1.9}$$

The ambient characteristic impedance Z_0, defined by:

$$Z_0 = \rho_0 c_0, \tag{1.10}$$

is usually used to normalise the liner specific impedance Z into the reduced specific impedance z:

$$z = \frac{Z}{Z_0} = \frac{1}{\rho_0 c_0} \frac{p'}{u'}. \tag{1.11}$$

The impedance is a complex variable that can be decomposed into its real part R, also called resistance, and its imaginary part X, the reactance. It should be pointed out that the resonant frequency, described by Eq. (1.8), corresponds to the value of ω for which the reactance $X = \Im(Z) = 0$. In addition to being complex, the specific impedance of a liner depends on several parameters: not only the geometrical parameters such as the perforation and resonator dimensions, but also the acoustic parameters such as the frequency f or the SPL and finally the flow parameters such as the grazing flow velocity. The impedance can then be complicated to be accurately measured or calculated.

A first way to determine a liner impedance is to experimentally measure it. Different methods have been developped through time. This paragraph does not intend to be exhaustive and briefly presents a few of them. The standing wave tube, also refered to as impedance tube or Kundt's tube [36], was firstly used in 1868 and initially designed to measure the speed of sound within different materials. It was then developped for other acoustic measurement purposes, including that of the impedance [37]. A review of different historical approaches developped since then was proposed by Dean [37], before exposing his one-microphone and two-microphone methods. The first one is limited to simple cases (for example: no shear flow) and requires to know *a priori* the relation between different parameters. On the contrary, the two-microphone method has been shown to be simple to set up, both experimentally and numerically, and to provides accurate results. Moreover, it also works in the presence of a grazing flow which is particularly appreciated to study acoustic liners. It has therefore been widely used. The idea is to precisely place one microphone on the cavity backplate and another one near the aperture. The pressure signals are then measured and, knowing their relative phases and the relation between the cavity acoustic pressure and the flow velocity fluctuations, the impedance can be calculated.

Different analytical and empirical models enable to determine a liner impedance, given different parameters. For a classic Helmholtz resonator, the specific impedance Z_H is calculated directly from the equation discribing the equivalent mass spring system (Eq. (1.7): $m\frac{d^2\xi}{dt^2} + R\frac{d\xi}{dt} + s\xi = SAe^{j\omega t}$), leading to Eq. (1.12):

$$Z_H = R + j(\omega m - \frac{s}{\omega}). \tag{1.12}$$

For the quarter-wave resonator case, the impedance of the complete liner can be decomposed as the sum of the resonator impedance and that of the perforated plate [38]:

$$Z = Z_{1/4} + Z_{plate}. \tag{1.13}$$

The impedance of a quarter-wave resonator $Z_{1/4}$ is also well-known and is given by Eq. (1.14):

$$Z_{1/4} = -jcot(kl). \tag{1.14}$$

As for the perforated plate, it is much more complex to evaluate. There are two reasons for that. First, if the porosity σ is low enough it is possible to assume that the plate specific impedance Z_{plate} is linked to a single perforation specific impedance Z_{perfo} through Eq. (1.15) [38]:

$$Z_{plate} = \frac{Z_{perfo}}{\sigma}. \tag{1.15}$$

However, if the porosity is too high, the perforations are close enough to each other to trigger an acoustic interaction between neighbour perforations [27, 38]. Thus, Eq. (1.15) is no longer valid and a correction needs to be integrated to the model in order to take into account this interaction. Secondly, the main issue when modelling a liner impedance is the impedance of a perforation, which is much more complicated to assess and depends on more parameters (geometrical but also acoustic). A great number of models have been developped to model the impedance of a single perforation, either empirical or analytical, as can be seen through the extended literature review proposed by Malmary [38]. The linear and non-linear behaviours of the liner being totally different, specific models have to be thought for each of them. The influence of different parameters, such as the acoustic frequency or grazing flow velocity, has also to be taken into account which can be made through observations. A study worth noticing is that of Melling [27], who experimentally determined the impedance of perforated plates and used this data to propose an impedance prediction model, with a focus on the non-linear regime. In particular, he compared two different kinds of cavities to be placed under the perforated plate: a plain cavity and a honeycomb cavity network. Among his main observations, he noticed that the honeycomb cavities provided a higher resistance than the plain cavity. The resistance difference was found for all the tested SPL values, and was even more important at high frequency and porosity.

Finally, the impedance of a liner can also be numerically predicted. As mentionned above, the two-microphone method proposed by Dean is not only used in experiments, but also in numerical simulations, where the microphones are replaced by numerical probes. The other way around, impedance models can be used in numerical simulations in order to replace the liner geometry (necks and cavities) by a complex boundary condition, in order to assess the impact of liners on the flow with a reduced numerical cost. The use of numerical simulations to study acoustic liners (among other synthetic jet actuators) is more discussed in Section 2.3.

To conclude, the impedance is a useful design parameter used to characterise the acoustic liner performance. In particular, the frequency value that corresponds to a null imaginary part of the impedance corresponds to the resonant frequency. However, it is not so easy to determine and several studies have focused on how to determine it, either experimentally [37, 38] or numerically [39].

This section was dedicated to the description of liners from an acoustical point of view. The acoustic damping mechanisms were detailed, before describing different liner geometries and geometrical design parameters. Finally the acoustic impedance,

which is a design parameter used to quantify the liner acoustic performance, was provided. When discussing the damping mechanisms, the flow dynamics was briefly described. The following section focuses on extending this description within and around an acoustic liner.

1.3 Acoustic liner flow dynamics

The mechanisms of acoustic damping were detailed in Section 1.2.1. The flow dynamics generated by the impact of an acoustic excitation on an acoustic liner were thus briefly described. The present section is entitled to provide a more complete literature review about the flow behaviour around and within an acoustic liner. Section 1.3.1 focuses on cases where the ambient fluid is quiescent. This is not representative of the flight conditions for an acoustic liner placed within an aircraft engine, however it represents an interesting simplification of the problem that has been much used to enable the study of liner fluid dynamics in experiments and numerical simulations. Then, the impact of the grazing flow on the acoustic liner is described in Section 1.3.2.

1.3.1 Acoustic liner flow dynamics within a quiescent ambient flow

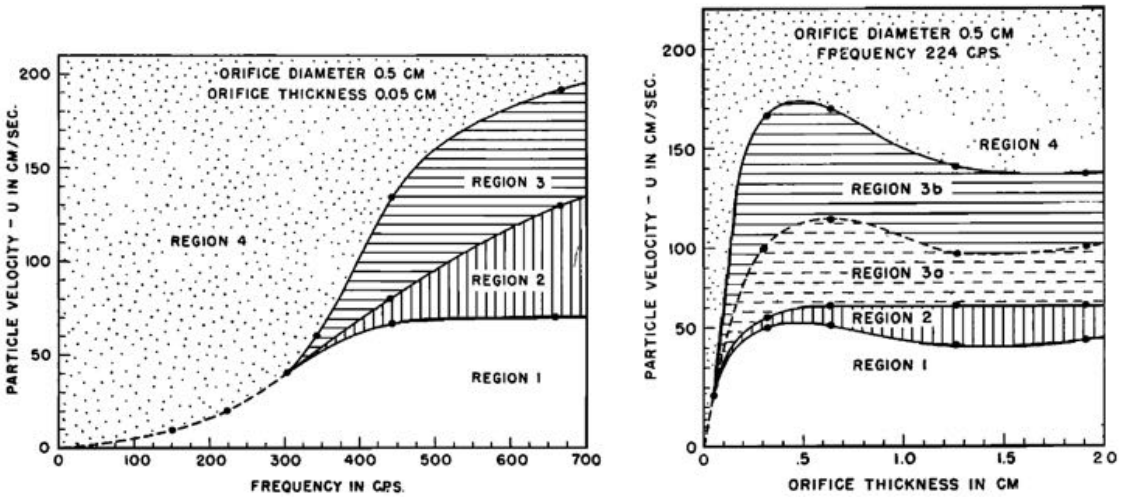

(a) Dependency on frequency.

(b) Dependency on orifice thickness.

Figure 1.8: Phase diagrams for 0.5 cm orifices [18].

As mentioned in Section 1.2.1.2, Ingard and Labate [18] were among the first to observe the flow dynamics around a perforated plate impacted by an acoustic excitation and they identified different flow patterns (see Fig. 1.4). They identified four different regimes, and represented them as "regions" on phase diagrams. An example of these phase diagrams is provided in Fig. 1.8, corresponding to an aperture

diameter equal to 5 mm. The first region, or regime, corresponds to the absence of jet, and is characterised by a stationary circulation zone around the aperture, as can be seen in Fig. 1.4a. A second regime, at higher sound intensity, is identified with another stationary circulation zone in which the direction of flow along the axis is opposite to the first regime. Some turbulent effect can appear at the aperture edges at the highest sound intensities for this zone, leading to the next regime. With the third regime, jets really appear while a stationnary recirculation zone is still present. Finally, with a still rising sound intensity, a jet is fully formed. This corresponds to the fourth and final regime. Interestingly, vortex shedding appear at even higher sound intensities but Ingard and Labate [18] still classify them with the jet. Examples of jet and vortex shedding can be seen in Figs. 1.4b and 1.4c. It can be seen in Fig. 1.8 that it is possible for the fluid to go directly from the first regime to the fourth: the second and third regimes might be seen as close to the transition between no jet formation and jet formation.

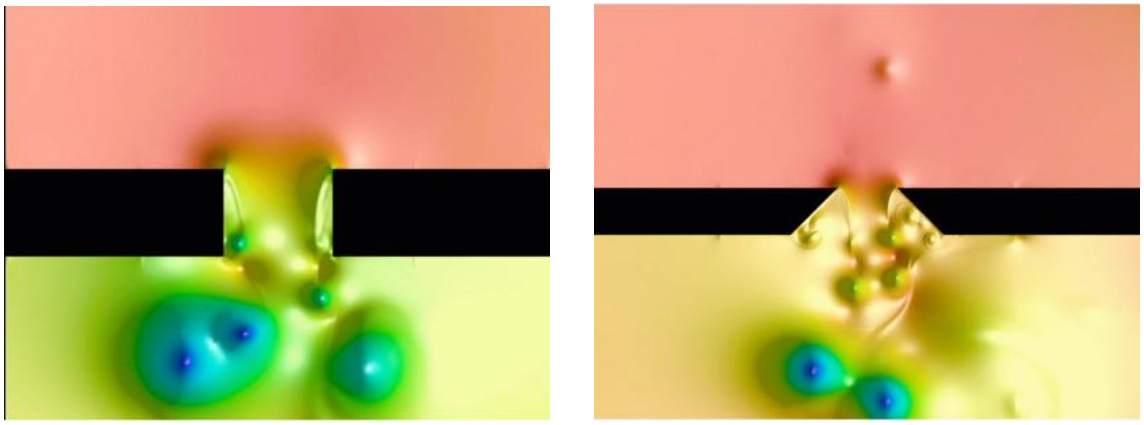

(a) 90° (b) 45°

Figure 1.9: Comparison of vortex shedding for 90° and 45° slit necks [28].

Melling [27] further investigated the non-linear behaviour of liners at high acoustic intensities with an experimental configuration closer to the reality. Indeed, he considered a whole plate, insisting on the interactions between holes that can occur in case of a high porosity (although in his configuration, the hole diameters were slightly larger than modern liners installed in turbofans: he used 1 to 3 mm diameter holes, while they are usually less than 1 mm). Although several experiments were conducted on the subject, the small dimensions of the perforations prevented studies to reach detailed observations of the flow around this specific zone, and considered holes were usually larger than those of a classic liner. Since the operating conditions (frequency and acoustic amplitude) were usually chosen based on the resonator (in order to trigger - or not - the resonance), and not on the perforation dimensions, the Reynolds number of the flow around the perforation was not scaled to that of a realistic aircraft liner [19]. Tam and Kurbatskii [19] were among the first to simulate the acoustic damping within a liner, by the means of a 2D DNS. Unlike in experimental results, such as those of Ingard and Labate [18], they observed no turbulent jet for high SPL values. Instead of that they evidenced the vortex shedding only. They

consider this vortex shedding as "chaotic and aperiodic, a state somewhere between laminar and turbulent". They attributed the difference between their results and those of the experiments to the difference in the Reynolds number, due to the augmented perforation dimensions that are used for experimental visualisations. Later on, Tam *et al.* [28] showed that the vortex shedding can be enhanced by the neck geometry, for example by using 45° bevel slits instead of a 90° slit (*cf.* Fig. 1.9). Since the vortex shedding is the most efficient way to damp acoustic, it could be assumed that the 45° configuration should be privileged. Roche [21] used different analytical and numerical tools to study liners, in 2D or 3D simplified configurations. Considering the vortex shedding, his simulations showed that the phenomenon is axisymmetric in a quiescent ambient flow. In case of a grazing flow, this axisymetry is broken, as explained in Section 1.3.2. He also noticed a threshold phenomenon implying that the liner acoustic performance is not systematically enhanced by the vortex shedding [21, 40]. For low values of SPL, a rising SPL corresponds to a more important vortex shedding and an increasing acoustic damping. However, at some SPL threshold value, the acoustic damping decreases while there is still an important number of vortices. He concluded that an important, energetic vortex shedding does not ensure a maximum acoustic damping. This implies that modifying the perforation geometry to enhance the vortex shedding would not necessarily increase the acoustic absorption, contrarily to what Tam *et al.* suggested. He also showed that, at high acoustic intensities, the friction in shear layer becomes dependent on the SPL, implying that this phenomenon is not always linear [41].

1.3.2 Acoustic liner flow dynamics within a grazing flow

Until recently, research about acoustic liners usually considered configurations with a quiescent fluid. However, when placed within a turbofan walls in flight conditions, a liner is confronted to a grazing air flow the Mach number of which is greater than 0.5. It is thus of interest to understand the impact of the grazing flow on the liner performance and recent studies have been working in that direction. Conversely, the generation of a turbulent jet and the vortex shedding due to the liner modify the flow and its boundary layer. In the context of the study of heat transfer within acoustic liners, understanding the flow and boundary layer behaviours is crucial. Roche [21] numerically evidenced the impact of this grazing flow on acoustic liner flow dynamics. At low SPL, the flow still oscillates around the neck however the vortices generated into the grazing flow are convected and are thus not sucked back into the neck. The flow dynamics within the neck, which is symmetrical in the absence of grazing flow, becomes strongly assymetrical with the grazing flow. At high SPL (see Fig. 1.10), the strong vortices generated into the main flow are also convected away from the resonator, before being dissipated by viscosity.

Theoretical analysis predicted the presence of an instability in case of a grazing flow impacting an acoustic liner [42]. This instability was experimentally evidenced by Brandes and Ronneberger [43] and later on by Aurégan and Leroux [44]. Although this instability is not always present, the grazing flow implies at least non

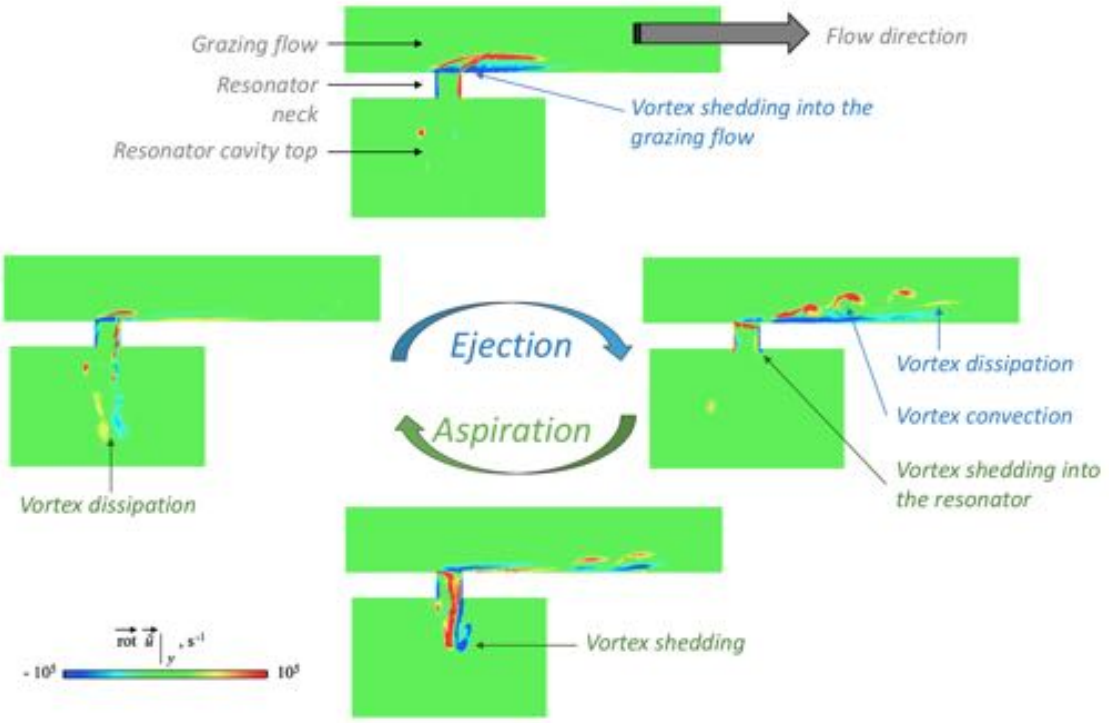

Figure 1.10: Vorticity field over an acoustic period, adapted from Roche 3D DNS results [21]. $f = 1592$ Hz (near resonance), $SPL = 140.5$ dB, Mach 0.1 grazing flow.

linearities within the liner behaviour. Different models have been developped and enhanced for several years to understand this phenomenon, as can be perceived through Brambley's literature review on acoustic liner models with flow [45], which includes the description of boundary conditions used to model the presence of an acoustic liner. Jing *et al.* [29] experimentally examined the impact of grazing flow on acoustic liners, in order to propose a representative boundary condition model. However, the grazing flow was low-speed (up to Mach 0.1) and the SPL was chosen low enough to remain in the linear domain. They also evidenced the influence of the perforated plate thickness on the liner acoustic performance. Several experiments were conducted in order to investigate the acoustic performance of the liner when facing a grazing flow. An extensive literature review of those studies, with a deep interest on the different measurement methods, is provided by Malmary [38], who developped a rig to study liner acoustic performance and compared different acoustic measurement methods. A more recent literature review, including the ONERA B2A aeroacoustic test bench [46, 47] and the indirect methods (for example the one developped by the NASA [48]) is given by Roche [21].

Recent numerical simulations enabled a better understanding of the acoustic-hydrodynamic interaction between liners and grazing flow. Among the first to provide a visualisation of the flow within the liner, Tam *et al.* [49] considered a 2D Helmholtz resonator with a normal incident acoustic signal. The grazing flow Mach number was equal to 0.15. Roche [21, 41] provided 3D DNS of Helmholtz resonators in the presence of a 0.1 Mach number grazing flow, at low and high acoustic inten-

sities. Tam's and Roche's results are similar. On the simulations with the grazing flow only, two main vortices appear: a clockwise-rotating vortex in the hole and a counter-clockwise-rotating recirculation flow inside the cavity. At low acoustic intensity, there is a strong vorticity within the resonator hole, that impacts the flow at the resonance frequency, and a strong recirculation flow along the wall donwstream the cavity. When considering a high SPL, a higher vorticity can be observed. The vortex shedding in the presence of a grazing flow is no longer axisymmetric and the vortices present different behaviours regarding the sense of rotation. Some of them merge into a larger vortex. All of the vortices are convected by the flow. Outside of the cavity, they are convected downstream by the main flow while whithin the cavity, due to the counter-clockwise-rotating recirculation, they are convected upstream, before being dissipated by the air viscosity. The vortex convection and their dissipation can be visualised on Fig. 1.10, which shows the evolution of the vorticity field around the resonator neck, over an acoustic period, for low and high SPL and with a grazing flow.

In flight conditions, the grazing flow is characterised by a high velocity, usually of the order of Mach 0.5. However, few studies have included the visualisation of high-velocity grazing flows: experiments scarcely considered a flow with a Mach higher than 0.25. Early experiments, such as that of Worraker and Halliwell [50], considered realistic flow and acoustics conditions. In their study, Worraker and Halliwell used a Mach 0.5 grazing flow and the acoustic signal presented a SPL higher than 130 dB. Nevertheless, here again the geometry was not representative of a realistic liner (a single cavity with a 3.5 mm slot as aperture). Among their main conclusion is noted that the acoustic performance is not well predicted by contemporary models, and that it is crucial to better understand the impact of the grazing flow on the liner. Malmary [38] conducted experiments with a grazing flow up to Mach 0.6 but her study was focused on the acoustic performance and she provided no direct observation of the flow dynamics. However, she compared her results to the empirical model of Kirby and Cummings [51] and showed that their model, designed for flows with a Mach number under 0.2, could be extended for grazing flows with a Mach number up to 0.5. Even recent numerical studies remained in low-velocity conditions. For example, Tam *et al.* [49] used a Mach 0.15 flow and Roche's simulations [21, 41] implied a Mach 0.1 flow. Zhang and Bodony [39] performed 2D simulations of a Helmholtz resonator similar to Tam *et al.*'s configuration [49], targeting high-speed grazing flows. Considering that future turbofan architectures might involve to use unconventional positions for the liners, including exterior surfaces, they studied the impact on the liner of a grazing flow up to a 0.85 Mach number. They found out that the vortex shedding gets stronger with an increasing Mach number, while still depending on the frequency. Moreover, the vortices produced at low Mach number penetrate higher into the boundary layer, while those generated at high Mach number are lowered by the grazing flow and stay nearer to the wall. In their study, they considered only one perforation over one cavity however it is suggested that for conventional liners, that is to say with several perforations, these lower vortices might have a different impact on the downstream perforations. Such a configuration has been simulated by Duchaine [52] through 3D LES (Large Eddy Simulations),

confirming their hypothesis. Focusing on the perforation, Zhang and Bodony also examined the time dependance of the mass flux, the boundary layer thickness and the wall shear stress. They evidenced a significant asymmetry between the upstream and downstream perforation walls, rising with the Mach number.

The grazing flow characteristics also influence the liner performance. Kompenhans and Ronneberger [53] experimentally investigated the acoustic performance of orifices in wall, in presence of laminar and turbulent grazing flows. They found out that the boundary layer thickness impacted the acoustic performance. They also concluded that the impact of the grazing flow would be the same, whether the flow were turbulent or laminar. However, their study remained in the linear acoustics conditions and, as well as in other experiments, the hole dimensions were not representative at all of a classic liner: their diameter were bigger (mainly 4 mm), and their depth (in other words: the plate thickness) was way higher (up to 11 cm). Later on, Zhang and Bodony [54] ran DNS of a 3D Helmholtz resonator and compared the impact of a laminar and a turbulent grazing flow. In order to make possible the use of DNS, they had to lower the Reynolds number from approximately 23 000 to 2300; however, they kept constant the ratio of the momentum thickness to the perforation diameter. Their results show a strong influence of the laminar or turbulent character of the grazing flow. Indeed, at low SPL, the turbulence enables the vorticity to go deeper within the cavity during the aspiration, and to get a higher magnitude during the ejection, than for the laminar simulation. These differences are even more visible at high SPL: the vortices are way more intense and less organised in the turbulent case than in the laminar simulation. Moreover, their laminar simulations evidenced the possibility of the vortex shedding to trigger a transition to turbulence for the laminar boundary layer, in case of a high enough acoustic intensity. Similar conclusions were made by Duchaine [52], who performed a 3D LES of a SDOF liner configuration, composed of 20 staggered rows of two cavity and 11 perforations per cavity, with a Mach 0.5 grazing flow and different inlet conditions: laminar, with and without acoustic signal, and turbulent without acoustic signal. When comparing laminar and turbulent grazing flows with no acoustic signal, he observed more energetic aspiration and ejection around the perforations for the turbulent case. The main differences between the various cases take place around the first rows of perforations. Moreover, both laminar cases (with and without acoustics) transitioned to turbulence due to the presence of the liner. Thus, in the presence of a Mach 0.5 grazing flow, the combination of 20 staggered rows of two cavities appears to be enough to trigger a transition to turbulence. Such an effect shows that, compared to a classic flat plate, the wall shear stress is much higher in the presence of a liner, which can lead to an enhanced wall heat transfer.

1.4 Liners and heat transfer

The flow behaviour triggered by acoustic liners present specific features that imply complex heat transfer. As detailed in the previous sections, the boundary layer of the grazing flow is strongly impacted by the vortex shedding. Moreover, a conse-

quent wall shear stress takes place within the perforations. Even the geometry of the liners is determinant: the honeycomb network provides a significant surface, much more important than that of a flat plate. Some of this extended surface could be used as a heat transfer surface. Finally, the grazing flow coming through the fan and the bypass ducts consists in cold air which represents a cold source while the engine walls can reach high temperatures due to electronic equipments and combustion chamber heat sources. For all these reasons, acoustic liners could be used to help enhancing heat transfer in future increasingly hotter turbofan architectures. However, this participation in heat transfer need to be quantified. There is currently not so much knowledge about heat transfer within acoustic liners when they are designed specifically to treat fan noise. Usually, when liners are studied from a thermal point of view, they are designed for another purpose. For example, Nordin *et al.* [55] developped a liner specifically for hot stream areas of the engine. Here, their main concern was not heat transfer enhancement but the production of a liner that could handle high temperatures.

There exists a specific category of liners that have been widely studied in a context of hot temperatures: combustion chamber liners. Indeed, perforated plates are found within the combustor. Their key role is to play a part in cooling the walls, the combustion temperature usually being higher than the melting temperature of the combustion chamber wall materials. Therefore, a cold flow is injected through the liner perforations, in order to generate a film that protects the walls by keeping them under their melting temperatures [56]. The flow dynamics generated by this continuous, bias flow is thus different from that found in the case of fan duct liners. These liners also play a role in acoustic damping, which is even more crucial in this context than with fan noise since thermoacoustic instabilities can occur within the combustion chamber: when the flame heat release interacts with acoustics, it generates a positive feedback loop. These instabilities, whose existence has been known for a long time [57] can damage the engine when uncontrolled. With combustor liners, the ambient flow is hot compared to the walls. However, the acoustic damping mechanisms, if present, remain similar and parallels can be drawn between both kinds of liners. In particular, Cosic *et al.* [58, 59] showed that the hot air and the density gradients have a significant impact on the resonant frequency and the acoustic absorption performance.

The interest on heat transfer within fan duct liners is very recent. Wood *et al.* [60] developped an acoustic absorber combined to a heat exchanger specifically for the Outlet Guide Vane that is impacted by the secondary cold flow. The idea, very similar to that of the OPTIMA project, is to have a single element to handle either heat transfer enhancement and noise damping, in order to take advantage of the greater surface possible. Very recently, Méry *et al.* [47] proposed an experiment to understand the impact of a temperature gradient across an acoustic liner. To do so, they used two different configurations: an impedance tube and an aeroacoustic test bench, called B2A, that enabled them to integrate a grazing flow in the experiment. Focusing more specifically on the acoustic performance, their study is one of the few to consider a configuration where the liner walls are heated while

the grazing air is cold. In their experiment, the heat flux is imposed on the cavity bottoms. The liner geometry, the materials and the cold air temperature imply the generation of temperature gradient all along the liner, from the bottom to the perforated plate. Regarding the acoustic performance, the results show a shift of the maximum acoustic absorption frequency. With a 150 K thermal gradient, this shift is up to 3 kHz. An interesting part of their study is the effect of acoustics on the thermal gradient. Indeed, when a high SPL acoustic excitation is switched on, a 7 K to 10 K decrease occurs at the liner surface. This phenomenon does not appear at low SPL. They suspect the vortex shedding mechanism to be responsible of this temperature shift: the wall convection heat transfer coefficient would thus be increased, impacting the wall temperature. This phenomenon, that appears only close to the perforated plate, is also present in a grazing flow configuration.

Duchaine [52] numerically considered the sensitivity of heat transfer within a SDOF liner to the grazing flow conditions. To the author's knowledge, it is the first study considering the heat transfer issues within these kind of liners. In his configuration inspired from Jones [48], 20 staggered rows of two cells are perforated with 11 holes each, leading to a 10.85% porosity. The liner perforated wall temperature is fixed at 400 K, while a 300 K, Mach 0.5 grazing flow is injected at the inlet. Different inflow conditions are tested: laminar with and without acoustic forcing, turbulent without acoustic forcing. Two cases are considered for the acoustic signal: the liner resonance frequency, and a non resonant frequency (2600 Hz and 3800 Hz, respectively), both of them at low SPL (109 dB). The results show that the injection of turbulence or the resonant acoustic forcing generate intense phenomena, with a pulsating flow penetrating deeply within the cavities and the grazing flow boundary layer. On the contrary, the non resonant acoustic forcing is very similar to the laminar case, with less intense phenomena. In all four cases, the complex flow dynamics leads to a mixing between the cold grazing flow and the air heated by the plate, leading to heat transfer higher than the case of a flat plate with a laminar grazing flow. These phenomena are more or less stronger, regarding the inlet conditions: the mixing is more enhanced with the resonant acoustic forcing and in the turbulent case. The main differences appear on the first rows of perforations, where the grazing flow is not destabilised the same way by the pulsating flow generated at the perforations. With the transition to turbulence that is triggered by the liner, the heat transfer evolution tends to that of a turbulent boundary layer over a flat plate at the end of the domain. The establishment distance of this behaviour is not the same for all the cases, however in the end the difference between the several cases is small.

The recent studies of Méry *et al.* [47] and Duchaine [52] suggest a strong multiphysics coupling between the flow dynamics, the acoustics and the heat transfer within acoustic liners. In particular, the wall heat transfer is complex and still not completely understood. The rise of heat transfer coefficient in the presence of vortex shedding, suspected by Méry *et al.*, as well as the rising heat transfer driven by the turbulence, evidenced by Duchaine [52], imply that the wall heat transfer is enhanced when compared to a flat plate. In order to better understand heat transfer along turbofan walls, the phenomena present in acoustic liners need to be

better understood, motivating the present study. To do so, some help can be found when looking upon another recent, widely studied field: synthetic jets. These particular jets are characterised by the periodic succession of an aspiration and ejection from and into a cavity, triggered by different kinds of actuators. As a matter of fact, the complex flow dynamics that occurs within acoustic liners makes them a specific category of synthetic jets. However, other kinds of devices can be used to create synthetic jets, in particular moving actuators, such as pistons or piezoelectric membranes. These different categories of synthetic jets, although their applications are usually different, are based on the same flow physics and some of them have already been used to deal with heat transfer enhancement issues. A literature review focusing on synthetic jets is provided in Chapter 2.

2
Synthetic jets

As discussed in introduction of this manuscript, the test rig on which the present study is based on relies on the use of pistons to reproduce the fluid dynamics generated by acoustic liners. In spite of their differences, both pistons and acoustic liners belong to the category of synthetic jet actuators and are use to trigger the same phenomenon: synthetic jets. As a reminder, one of the objectives of the study is to assess whether this use of pistons to reproduce liner flow dynamics and resulting wall heat transfer is valid. This chapter provides a literature review on the subject of synthetic jets, more general than the specific context of acoustic liners given in Chapter 1. The objective is to describe the phenomenon more thoroughly than in the previous chapter, including especially the definitions of the different parameters that play a role in synthetic jets, whether geometric or related to the flow operating conditions. Aspects of synthetic jets which impact the specific case of acoustic liners are highlighted.

Synthetic jets are a very specific category of jets, with a zero net mass flux. They are naturally present in the presence of an acoustic liner and can be triggered by different kinds of actuators, such as pistons or piezoelectric membranes. These actuators can be refered to as SJA (Synthetic Jet Actuators) in the literature. One of the first actuators, other than an acoustic liner, was presented by James *et al.* [61], who also introduced the designation of "synthetic jet". They used a piezoceramic membrane to generate a synthetic jet in water. Shortly after, Smith and Glezer [62] proposed a more complete geometry by embedding the membrane within a cavity, leaving only a small aperture through which the jet is formed. In this case, the fluid put in motion was air, as it is most often the case. Since then, synthetic jets have been widely studied and different kinds of actuators have been developped, although Smith and Glezer's configuration remained a reference in this domain. Holman *et al.* [63] provided a complete definition of synthetic jets: this specific **"jet formation is defined as the appearance of a time-averaged outward velocity along**

the jet axis and corresponds to the generation and subsequent convection or escape of a vortex ring". Thus, the vortex shedding that is triggered by high intensity acoustic excitations within liners do correspond to the definition of a synthetic jet.

Thanks to the fact that the jet is composed of the ambient flow, no inflow is required and thus there is no need of complex and heavy pipes. This has made synthetic jets a privileged choice when compared to classic jets in different situations, and synthetic jets have been proven useful in different domains. Apart from the acoustic liners, which are specifically targeted here, two domains where synthetic jets can be found are of interest for the present study: flow control and heat transfer enhancement. Indeed, on the one hand heat transfer configuration implying synthetic jets are usually designed in quiescent flow conditions. On the other hand, flow control strategies, although they do not consider heat transfer issues, usually have to deal with grazing flows. They cover a large number of applications, with for example boundary layer separation control or mixing enhancement. Both of these aspects, heat transfer and grazing flow, are present in our study.

This chapter provides a literature review on the subject of synthetic jets. The first section focuses on the flow and geometrical parameters. In particular, the definition of a jet formation is given. Then, the following section describes more thoroughly the jet flow dynamics in different conditions: the main regimes and flow structures are detailed, a comparison with continuous jets is provided and the specific case of cross-flow configurations is tackled. Heat transfer enhancement applications can then be described. Finally, the third section provides a literature review of the analytical models and numerical simulation methods used to study synthetic jets. The aim is to compare these different methods and justify the choices made through the present study.

2.1 General description

This section focuses on the description of synthetic jet main features. To begin with, the dimensionless flow parameters that characterise synthetic jets are defined, along with an explanation of the conventions chosen for the present manuscript. Thanks to these parameters, a criterion is proposed to identify the formation of a synthetic jet. Finally, the main geometrical parameters of an actuator are described, along with their importance on the flow dynamics.

2.1.1 Main flow parameters

The definition of a reference velocity is not direct since a synthetic jet is characterised by the succession of an ejection and an aspiration through the aperture, leading to a null time average velocity at the aperture exit. Therefore, it needs to be described with specific, dedicated parameters. Different conventions exist to do so.

In this work, those proposed by Holman *et al.* [63] are used. Considering a cartesian coordinate system, with axial direction x and velocity u, spanwise direction y and velocity v as well as vertical direction z and velocity w, it will be considered here that the synthetic jet axis corresponds to the vertical axis. In order to define a non null time averaged velocity, the time averaging is performed over the ejection mid-period only; the surface average is made over the neck section. The resulting jet velocity $\overline{W}$ is defined as:

$$\overline{W} = 2f\frac{1}{A}\int_A\int_0^{1/2f} w(t,x,y)\mathrm{d}t\mathrm{d}A, \tag{2.1}$$

where f is the oscillation frequency (either it is triggered by a piston, a piezoelectric membrane, or an acoustic excitation), A is the neck area and $w(t,x,y)$ is the instantaneous vertical velocity along the neck surface. This definition of the jet velocity, along with the kinematic viscosity of the fluid ν (most usually air) and the neck diameter D can be used to define two major dimensionless flow parameters that are used to characterise the synthetic jets: the **Reynolds number** Re and the stroke length L_0, usually normalised as the **dimensionless stroke length** $\frac{L_0}{D}$. These respectively read:

$$Re = \frac{\overline{W}D}{\nu},\ L_0 = \frac{\overline{W}}{2f}. \tag{2.2}$$

In the presence of a grazing flow, a third parameter is required to characterise the synthetic jet in cross-flow dynamics: the **velocity ratio** M, defined as the ratio of the jet mean velocity on the grazing flow mean velocity. In this study, the grazing flow corresponds to the axial direction x and its mean velocity is U_0, so that:

$$M = \frac{\overline{W}}{U_0}. \tag{2.3}$$

It should be underlined that synthetic jets are completely characterised by these three parameters (with the need of only the Reynolds number and dimensionless stroke length in case of a quiescent environment). In particular, synthetic jets generated at different scales but characterised by exactly the same Reynolds number, dimensionless stroke length and velocity ratio, will present similar flow features. The Reynolds number Re is a classic dimensionless number in the study of fluid dynamics. It corresponds to the ratio of inertial forces and viscous forces and is used to characterise the turbulence of a flow. Similitudes can be considered for flow features appearing at different scales but corresponding to a similar Reynolds number. The Reynolds number based on the velocity $\overline{W}$ also enables the comparison of synthetic jets with classic continuous jets. The dimensionless stroke length L_0/D corresponds to the distance the fluid can travel during the ejection mid-period, normalised by the aperture diameter. If this parameter is too low, the fluid is not ejected far enough from the actuator and is completely sucked back through the neck during the aspiration phase. In this case, no jet is formed. A synthetic jet formation parameter can thus be defined based on the dimensionless stroke length (see Section 2.1.2).

Finally, the velocity ratio M characterises which part of the flow is dominant in case of a cross-flow: if it is high, the synthetic jet is predominant and is not much influenced by the grazing flow. On the contrary, a low velocity ratio implies that the grazing flow drives the flow dynamics. In this case, synthetic jets are weakened and penetrate lower within the grazing flow boundary layer.

Other interesting parameters can be defined to compare and characterise the synthetic jets. It is possible to find in the literature jets characterised by three different parameters than those proposed here. However, this is not a contradiction. Indeed, any other parameter can be expressed as a combination of these fundamental jet parameters. The **Strouhal number** St is a classic parameter that is used to characterise oscillating phenomena. It represents the ratio of the advection and oscillation characteristic times and is defined by $St = (2\pi f D)/\overline{W}$. The Strouhal number and the dimensionless stroke length are directly related: $\frac{1}{Sr} = \frac{1}{\pi}\frac{L_0}{D}$. The **Stokes number** S, defined by $S = \sqrt{\omega D^2/\nu}$, where $\omega = 2\pi f$, is linked to the Strouhal and Reynolds numbers by $S = \sqrt{Re\ Sr}$ and is commonly used for the definition of synthetic jet formation criterion.

Different flow regimes can appear for specific ranges of all above discussed parameters. In particular, there are cases where no jet formation can be observed. In order to ensure the formation of synthetic jets, and enhance their performance, it is of great interest to know in which regime the flow is. Thus, synthetic jet formation criteria based on dimensionless parameters have been developped. They are detailed in the following section.

2.1.2 Jet formation criterion

The jet formation definition, as proposed by Holman *et al.* [63], was given at the beginning of this chapter. The main idea is that, in order to get a proper synthetic jet, the ejection velocity needs to be strong enough for air to be convected far enough, in order not to be sucked back through the aperture during the following aspiration. The idea of finding a jet formation criterion was early considered by Ingard [64], whose study focused on axisymmetric perforation configurations. Later on, Smith *et al.* [65] proposed a similar criterion. Their common conclusion indicates that, for axisymmetric aperture geometries, the condition $L_0/D > 1$ leads to synthetic jet formation. The experimental work of Shuster and Smith [66] was in agreement with a threshold value for L_0/D around 1 for axisymmetric actuators. Moreover, they showed that the neck geometry greatly impacts the value of the threshold. Smith and Swift [67] focused on 2D aperture configurations. They also found out the existence of a threshold for the dimensionless stroke length L_0/D below which no jet is formed, although they did not provide its value. Rampunggoon [68] used an order of magnitude analysis to consider jet formation, which led him to assume that the jet formation is directly linked to the parameter Re/S^2. However, the importance of the Stokes number S on the jet formation was out of the scope of his study, which prevented him to provide a more detailed criterion. Later on, Utturkar *et al.* [69] and finally Holman *et al.* [63] developped his analysis and validated it both numerically

and experimentally. They pointed out that the threshold value $L_0/D > 1$ proposed in previous work had been found for high Stokes number conditions ($S > 35$), while it would be preferable to consider low Stokes number flows to treat specific applications, as encountered with acoustic liners for instance. To do so, they validated their criterion with an experiment designed for low Stokes conditions ($6 < S < 36$). In the end, the synthetic jet formation criterion is quite simple, mainly based on the jet Stokes number and geometric parameters. It is described hereafter, and the flow and geometrical parameters leading to the criterion definition are illustrated in Fig. 2.1.

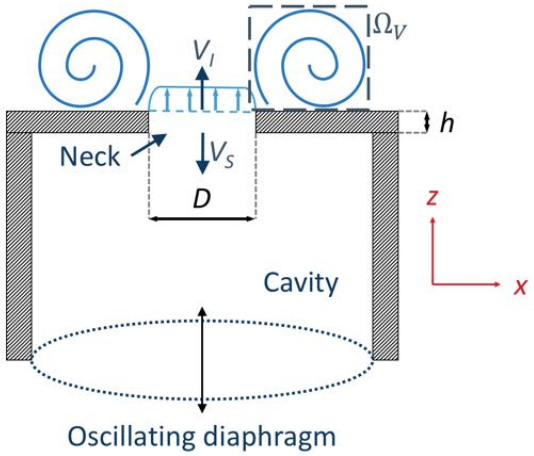

Figure 2.1: Scheme of a synthetic jet actuator, adapted from [63].

The main assumption behind the development of the jet formation criterion is that, in order not to be sucked back into the cavity, the vortex pair induced velocity V_I has to be higher than the average suction velocity V_S. This self-induced velocity of the vortex ring is proportional to the vortex strength Ω_V divided by the aperture diameter D. An order of magnitude analysis of Ω_V shows that $\Omega_V \sim \overline{W}^2/\omega$ [63], with $\omega = 2\pi f$. The suction velocity V_S can be directly linked to the jet velocity $\overline{W}$: $V_S \sim \overline{W}$. It finally turns out that the ratio of the vortex pair velocity V_I and the suction velocity V_S is of the same order of magnitude as $1/Sr$, as shown in Eq. (2.4):

$$\frac{V_I}{V_S} \sim \frac{\Omega_V/D}{\overline{W}} \sim \frac{\overline{W}}{\omega D} = \frac{1}{Sr} = \frac{\overline{W}D/\nu}{\omega D^2/\nu} = \frac{Re}{S^2} \tag{2.4}$$

Finally, since the fundamental assumption of this analysis requires to have $V_I > V_S$, the jet formation criterion is given by Eq. (2.5):

$$\boxed{\frac{1}{\pi}\frac{L_0}{D} = \frac{1}{Sr} = \frac{Re}{S^2} > C,} \tag{2.5}$$

where C is a constant. Considering thick orifices, with thickness-to-width ratios greater than approximately 2, Utturkar *et al.* [69] evaluated the values of C: around 0.16 for the axisymmetric configurations, and near 2 for 2D geometries. However,

this criterion is valid only for thick apertures: they consider that the thickness-to-width ratio l/D should not be smaller than 2. Holman *et al.* extended the criterion to more cases. They validated the first value but corrected the 2D geometry case by stating that C is nearer to 1. However, they pointed out the dependency on C to different geometric parameters, such as the aperture shape, the radius of curvature and the aspect ratio, and these values for C are approximations. In order to improve the accuracy of their results, they enhanced their database by using literature results from Ingard and Labate [18] and Smith *et al.* [65] in complement to their own results. This criterion is very useful to estimate if given conditions can lead to synthetic jet formation or not. Indeed, it is directly related to the aperture diameter, jet velocity and oscillation frequency which are usually known parameters. Very recently, Jankee and Ganapathisubramani [70] confronted their results with the criterion provided by Holman *et al.*. On their axisymmetric configuration including the presence of a second, inner lip within the cavity, they found the same value: $C = 0.16$. This supports the validity of Holman *et al.*'s criterion even for unusual geometries, as long as they are axisymmetric.

It should be noted that the jet formation criterion was defined and tested for quiescent conditions. The presence of a grazing flow, as it is the case for acoustic liners modifies the flow features: the fluid that would be sucked back within the cavity in quiescent conditions can be convected dowstream by the grazing flow. In this case, the vortex convection is a consequence of the grazing flow and not the evidence of a jet formation.

Acoustic liner context

The reader might have noticed that in Chapter 1 no mention was made of "synthetic jet formation". As a reminder, in the context of acoustic liners, it is more common to refer to "vortex shedding", which only appears when the acoustic excitation intensity is high enough (non-linear regime / jet formation), while at low SPL (linear regime / no jet formation) no jet is formed. Acoustic liners are more efficient to damp noise in non-linear regime, which makes it useful to be able to predict the conditions required to generate a synthetic jet.

As mentionned above, the neck geometry impacts the value of the threshold in the jet formation criterion. In fact, different geometrical aspects of synthetic jet actuators influence the flow features. The following section describes the importance of these parameters.

2.1.3 Actuator geometry

Different categories of actuators exist: synthetic jets can be generated through resonant phenomena as observed in the specific context of acoustic liners, thanks to the motion of pistons or piezoelectric membranes. These different categories of actuators

present different but also similar geometrical parameters. Note that an actuator can be divided into three main parts: the cavity, the neck and the "triggering" part (the moving part in the cases of pistons and piezoelectric membranes, and the acoustic resonance in the case of liners, which is directly linked to the geometry). All of these geometrical features have a direct impact on the synthetic jet formation and flow features.

Cavity geometry. Rizzetta *et al.* [71] showed that the flow within the cavity does not present the same dynamics whether the cavity is long or short. With the same forcing amplitude, but a different cavity length, the vortex strength is different: it strengthens in the shortest case when compared to the long case. Moreover, the vortex pair that is formed inside the cavity stays closer to the neck, along the cavity centreline, in the short case than in the long case. However, Utturkar *et al.* [72] showed that, for classic geometries, even particularly significant changes of the cavity aspect ratio have a limited impact on the jet exit flow, as long as the cavity volume remains unchanged. Considering five different geometries with equal cavity volume and diaphragm cumulative volume displacement, they studied the impact of the cavity aspect ratio and the piezoelectric membrane positions to observe little impact of both of these parameters on the outside flow. Their conclusion is valid either in a quiescent fluid and in the presence of a grazing, laminar flow. Only one important effect, linked to the position of the oscillating membrane more than to the cavity geometry itself was raised. This particular case is more detailed hereafter. It is worth noting at this point that their study remained in incompressible conditions, while the flow is often compressible within a synthetic jet actuator (it is particularly true for acoustic liners but it is also valid with piezoelectric membranes), which represents a major limitation of their study. Jain *et al.* [73] numerically compared a conical and a parabolic cavity to a classic cylindrical one. Comparing the jet velocities at the exit of the neck, they found very few differences for the different cavity shapes. This result corroborates the results of Utturkar *et al.* about the cavity geometry that would not affect the jet flow dynamics. However, another interesting point about the cavity dimensions is its thinness. Indeed, Van Buren *et al.* [24] studied actuators with round cavities and showed that when the cavity is thin relatively to its diameter, that is to say pancake-shaped, the acoustics is not dominated by the same phenomena than when the cavity is spherical. In addition to Van Buren *et al.*, Feero *et al.* [74] disagree with Utturkar *et al.* when they consider that the cavity shape has no effect on the actuator performance. Indeed, Feero *et al.* experimentally studied three different axisymmetric shapes for the actuator cavity: a cylindrical one, which corresponds to classic actuators, but also a conical and a contraction. Their results indicate non negligible differences in velocity radial profiles at the exit of the neck for the different cavity shapes, with different magnitudes. Moreover, the jet time-averaged momentum fluxes, compared at the neck exit and dowstream of the neck, also are different from one shape to the other: it is more important for the cylindrical cavity, and the weakest is obtained for the contraction cavity. They conclude their study by advising to choose a cavity shape in accordance with the main objective. A cylindrical shape leads to a maximised momentum flux, while more complex geometries can lead to a lower Helmholtz reso-

nant frequency, implying a power consumption reduction and an improved efficiency.

Neck dimensions. The neck diameter D has a significant impact on the flow. Indeed, as was detailed in Section 1.2.2.2, Tam and Kurbatskii [19] observed different flow features between their numerical simulations and contemporary experiments, attributed to the neck diameter. Moreover, the neck diameter D is usually used to get non-dimensional values, either for geometrical or flow parameters. Concerning the neck height h, Mittal *et al.* [75] compared results of simulations of synthetic jets whith different geometries. They found out that for h/D ratios equal to 1 and 3, the flow dynamics is significantly similar, although some differences can be spotted, with a trend for the velocity shape to become more parabolic at higher h/D values. On the contrary, Jankee and Ganapathisubramani [70] describe a blockage effect that appears at high h/D ratios and reduces the actuator performance, due to an oscillating separation bubble that gets trapped within the neck (see Fig. 2.2). Therefore, with an increased aspect ratio h/D, there is more flow resistance within the neck and the jet gets slower.

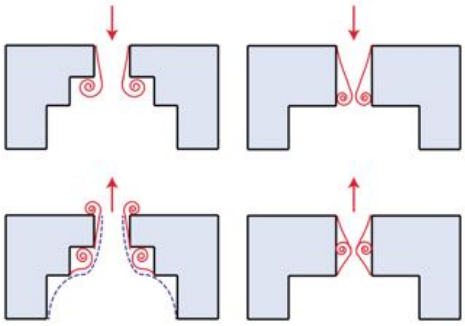

Figure 2.2: Sketch of the hypothesized flow dynamics within the neck for Jankee and Ganapathisubramani [70] (left) and a classic, high aspect ratio neck (right).

Neck shape. What was true about neck shapes in the specific context of acoustic liners remains valid in the general context of synthetic jets: the aperture shape has a significant impact on the vortex shedding. Moreover, two main shapes exist for the actuator neck: round and slot. Leschziner and Lardeau [76] gave an extensive literature review on the subject, focusing on numerical simulations in the context of flow control. While the slot geometry is considered more efficient to deal with flow control issues, the round configurations present weaker, more subtle and more complex flow features and interaction with the cross flow. Numerical simulations of this latter geometry are also more complex, partly due to a need of higher local mesh resolution around the neck, higher complexity of the flow within the neck but also within the cavity, and, contrarily to slot necks, no statistically homogeneous directions. In the context of acoustic liners, the aperture is usually a round perforation (in fact, several perforations per cavity, as discussed in chapter 1), which also increases the simulation complexity. Nonetheless, looking upon slot jets is still relevant since liners are regularly simplified as 2D configurations in numerical simulations, which is also representative of a slot neck configuration. In addition to the round *versus* slot shape, another classification can be made regarding the neck walls. Indeed, the edges can be sharp (or straight), rounded or beveled. Shuster and Smith [66] observed for example that the jet formation criterion is not the same for straight and beveled necks. Jain *et al.* [73] considered several kinds of neck geometries. In particular, they compared necks with round or sharp edges (both inner and outer)

and concluded that one shall privilege the choice of round edges on the outer side and sharp edges on the inner side. This leads to a higher mass flow rate while not affecting the peak velocity. Moreover, they considered angle-varying beveled-shape necks. They found out that when the angle was increased above 15°, the velocity gets higher but the mass flow rates is badly impacted and falls down. Nani and Smith [77] considered round inner edges, while the outer edges were left sharp, and studied the impact of the lip radius. Focusing on the efficiency issues, they noticed that the power necessary for the actuator to properly work was highly dependent of the inner orifice edge radius. Since aperture geometry appeared to be promising for synthetic jet actuators performance, Jankee and Ganapathisubramani [70] proposed an enhanced neck geometry: the idea is to modify the internal orifice by adding a second perforated plate under the top one, with an increased perforation diameter. Thanks to this change, the actuator performance is improved, and the presence of the inner lip leads to a homogeneisation of the results between low and high aspect ratio necks. There was no flow visualisation, however their results enabled them to assume the flow dynamics within the neck, which is presented in Fig. 2.2. The secondary, inner lip is assumed to avoid the presence of the oscillating separation bubble that appear in case of a long neck. The ratio of the two aperture diameters impact on the actuator performance was studied and results showed that there is an ideal inner lip size, a threshold beyond which there is no further enhancement. Moreover, with all other conditions being similar, they observed at least one case where changing the lip size led to a change of regime. To be clearer, for a similar Stokes number, a weak inner lip diameter prevent the jet formation while the vortex shedding clearly appeared when the inner lip diameter was increased.

Moving part features. Mittal *et al.* [75] point out that the flow features triggered by an oscillating membrane or a piston are not the same. Indeed, the motion of a piston consists in the movement of the boundary whole at once and presents no deformation of the piston. On the contrary, for a piezoelectric membrane, the boundary is bent; the membrane centre presents the highest deformation amplitude and the ends of the membrane, on the contrary, are fixed. These different actuator moving parts trigger different flow features. Mittal *et al.* also consider that Rizzetta *et al.* [71] obtained significant differences between their results and the reference regarding the flow within the cavity because of their model of the piezoelectric diaphragm using a piston-like motion. The work of Jain *et al.* [73] supports this hypothesis: among other things, their numerical simulations compared the flow dynamics triggered by a piston and an oscillating diaphragm for the same actuator. Their results showed important differences between the two boundary conditions. They suggest that compressibility effects explain the observed differences. Another interesting point of the moving parts is their position. Utturkar *et al.* [72] tested different configurations: a single diaphragm in the bottom of the cavity, a single diaphragm on one lateral wall, two diaphragms with one on each of the lateral walls, and finally the two lateral walls in addition of the bottom of the cavity. In every case, whatever the number and position of the diaphragms, their cumulative volume displacement is identical. The conclusion is more or less the same as for the aspect ratio: the impact is quite insignificant. However, there is one case that

shows an important impact of the diaphragm configuration: the single diaphragm on one of the lateral cavity walls. Indeed, this case presents an asymmetric configuration which modifies the vortices formation. A small horizontal velocity is added to the vertical jet velocity, which leads the vortices to drift. On the contrary, the other quiescent fluid configurations, which are symmetric, present a vertical jet only.

Acoustic liner context

Apart from the triggering part (moving element *versus* acoustic resonance), the different conclusions obtained in the general context of synthetic jets are valid in the specific case of acoustic liners. However, three specific aspects of liners have to be taken into account. The multi-perforated aspect should not be forgotten: although liners are usually modelled as a cavity and a single neck, there are usually several perforations corresponding to a single cavity. The other important aspect is the manufacturability, which can be impacted by the great number of cavities and perforations. Finally, in the aeronautical context, weight considerations are especially influential in the system design. These different aspects can restrain the use of complex liner geometries.

To sum up, the main geometric parameters that impact the flow features nearby an actuator are the cavity dimensions, the neck diameter D and length h, the neck shape (round or slot) and the moving part characteristics. Next section describes the main flow parameters that characterise the synthetic jets.

2.2 Synthetic jet flow dynamics

The flow dynamics in the presence of a synthetic jet has already been briefly described in the previous section, and more thouroughly in the specific case of acoustic liners in Chapter 1. It has to be reminded that synthetic jets are nowadays used for a wide range of applications, which leads to a great number of different configurations and specific flow features. This sections gives more details about specific flow features that can be found in different configurations and are of interest for our study. To begin with, the main flow regimes are described. Then a comparison with classic, continuous jets is provided. Finally, the cases of cross-flow configurations and heat transfer enhancement applications are discussed.

2.2.1 Main regimes and flow structures

As already stated in Chapter 1 for the case of acoustic liners, different flow regimes can be observed in the presence of a synthetic jet. In particular, the absence of jets corresponds to the first "regime" that can be observed when studying synthetic jets. The jet formation criterion, detailed in section 2.1.2, is very useful to discriminate cases with and without jet formation. When a jet is formed, different flow

features appear which makes possible to distinguish more regimes. For example, Gharib *et al.* [78] studied synthetic jets generated by a piston and found a threshold function of the dimensionless stroke length that discriminates between two different flow behaviours. Indeed, for $L_0/D < 4$, they observed a single vortex ring while for $L_0/D > 4$ the vortex ring is followed by a "trailing jet". Milanovic and Zaman [79] found a similar threshold phenomenon around $L_0/D = 5$, with the normalised centreline velocity profiles of different cases being all similar above this threshold. The threshold value of $L_0/D = 4$ was retrieved by Jabbal and Zhong [80] for a round synthetic jet. They attribute the appearance of secondary vortices to a maximum value for the circulation contained in the primary vortex that is reached at $L_0/D \simeq 4$. Later on, they studied the flow dynamics of a round synthetic jet in the presence of a grazing flow [81] and found out the same threshold phenomenon: for a case where L_0/D is equal to 5.1, which is greater than the threshold value identified in quiescent configurations, the appearance of secondary vortices is observed.

In their early study of the impact of acoustic signal on an orifice, Ingard and Labate [18] had already identified four different flow regimes (see Section 1.3.1). More recently, Travnicek *et al.* [82] experimentally studied a more classic synthetic jet actuator. The geometry included a round perforation, which makes it similar to the case of Ingard and Labate although the diameters were smaller and the actuator was based on a piezoelectric membrane, instead of the acoustic excitation used by Ingard and Labate. They identified four different flow regimes, and provided *Re-S* parameters maps to distinguish them. An example of these four regimes, for a case with $S = 21.8$, is given in Fig. 2.3. As for Ingard and Labate [18], the first regime corresponds to the absence of jet formation (a). It is characterised as a "creeping flow": the flow oscillations are not strong enough for vortices to escape before being aspirated back. Then, the three other regimes define different flow features that appear in case of jet formation: no vortex rollup (b), vortex rollup (c) and finally vortex structure breakdown, associated to instabilities and transition to turbulence (d). A *Re-S* parameter map obtained with their results is complemented by different results from literature, including one of their own previous studies. In general, their classification is in good agreement with the literature.

2.2.2 Comparison with Jets in cross-flow

Compared to continuous jets, synthetic jets represent a recent field of research. One of their main advantage is the production of jets from the ambient fluid, which implies that no complex plumbing is required to generate them. However, their particular production mode leads to strong differences with conventional jets. Quite obviously, the unsteady character of a synthetic jet is a substantial difference with the steady behaviour of a classic continuous jet. In particular, the suction phase triggers a flow dynamics that is not observed with continuous jets. Thus, it is important to understand these differences as well as the similarities that could be observed, especially in a context where continuous jets in cross-flow (JICF) are to be replaced with synthetic ones. Moreover, jets in cross-flow represent a well-known

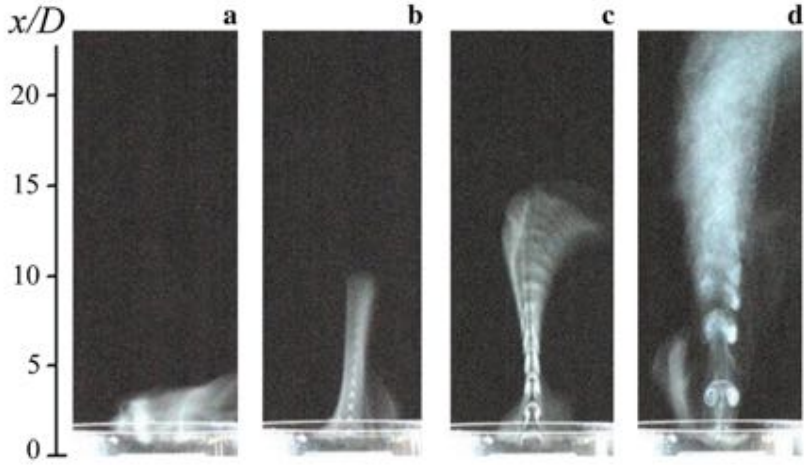

Figure 2.3: Visualisation of flow features from [82] for S=21.8, with a: $Re = 94$, b: $Re = 124$, c: $Re = 201$ and d: $Re = 464$.

reference basis.

Béra *et al.* [83] proposed one of the first experimental flow analysis where synthetic jets were properly compared with continuous ones, based on the same actuators and with equivalent velocities. Indeed, low velocity and high velocity continuous jets were injected at 10 m.s^{-1} and 20 m.s^{-1}, which respectively corresponds to the mean and maximum velocities of the synthetic jet case. They also considered a mixed case, where a continuous jet was added to the synthetic jet, in order to avoid the aspiration phenomenon. In this case, the velocity of the continuous jet is equal to 20 m.s^{-1}, which corresponds to the second purely continuous jet. In their study, both pulsed cases (synthetic and mixed jets) presented a flow dominated by the presence of the contra-rotating vortex pairs. The neck was a 100 mm long slit of width $D = 1$mm (for dimensionless parameters, the slit width plays the role of the diameter in case of a round neck). In particular, they focused on the jet half-width b which they defined as the "lateral distance at which the mean jet profile is reduced to half of its maximum velocity w_{max} at the same axial section". Figure 2.4 compares the dimensionless jet half-width b/D and maximum velocity w_{max} for the different cases as functions of the distance from injection nozzle Z/D. The synthetic jet presents a higher spreading than the other cases (Fig. 2.4a). Moreover, a sharp increase of the half-width occurs near $Z/D = 15$ while the continuous cases follow a linear increase. Concerning the maximum velocity (Fig. 2.4b), the continuous jets roughly respect the theoretical power law, while the synthetic jet present a velocity that rises from 0 m.s^{-1} to a maximal value around $Z/D = 12$, before slowly decreasing. After $Z/D = 15$, the synthetic jet maximum velocity is close to one of the continuous jet case at 10 m.s^{-1} (corresponding to the mean velocity of the synthetic jet case). The main conclusion of their study is that when compared to classic, steady jets, a larger jet lateral expansion and a more important external fluid entrainment rate were found for both pulsed cases. This is attributed to the self-induced velocity of the vortex pairs.

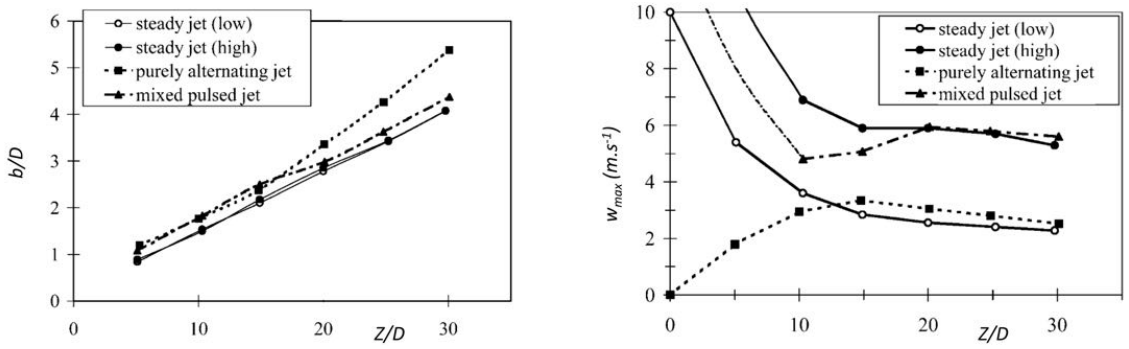

(a) Half-width of the jet.

(b) Maximum jet velocity.

Figure 2.4: Different jet parameters as fonctions of distance from injection nozzle adapted from [83]. The "purely alternating jet" case corresponds to a synthetic jet.

Another interesting study comparing continuous and synthetic jets is that of Smith and Swift [84]. Their experiment differs from that of Béra *et al.* by the aperture width h. Indeed, Smith and Swift consider an actuator with an aperture width equal to 5.1 mm while that of Béra *et al.* is equal to 1 mm. As mentioned above, this parameter is particularly important when studying synthetic jets and can lead to differences in the flow dynamics. In this study, two continuous and two synthetic jet cases with a Reynolds number around 2200, with different stroke lengths, are considered. Two additional cases are also tested: synthetic jets with a maximum jet velocity equal to the velocity of the continuous jet cases. It should be noted that Smith and Swift use a different convention for the jet velocity and thus the Reynolds number than the one used in this thesis. In their cases, the jet velocity is the centreline aperture velocity, averaged over the ejection half-period. Similarly to Béra *et al.*, they observe that the expansion rate is more important for the synthetic jets than for the continuous ones. Moreover, they notice that this point is even more important for synthetic jets with a large stroke length. When focusing on the near field, the synthetic jets are shown to be wider and slower than the corresponding continuous jets. Finally, they studied self-similar velocity profiles. They mainly showed that, far from the actuator, those profiles are similar while the near-field is characterised by important differences between synthetic and continuous jet cases. As for the study of Béra *et al.*, these differences are attributed to the presence of the vortex pairs that entrain more fluid in the case of synthetic jets than the continuous jets.

Finally, Milanovic and Zaman [79] compared synthetic jets with continuous jets in the presence of a cross flow. They found similar flow features such as the distribution of mean velocity, the streamwise velocity, and the turbulence intensity. Moreover, for different neck geometries, they obtained good results when comparing the trajectory of synthetic jets with a correlation established for continuous jets. To perform good comparisons, they used the momentum-flux ratio $J = (W_{max}/U_0)^2$, where W_{max} is the maximum jet velocity obtained during the ejection mid-period. Nonetheless, some differences occured regarding the jet penetration, which is lower for a synthetic jet.

2.2.3 Cross-flow configurations

Different applications of synthetic jets, such as impinging jets for heat transfer enhancement, imply a quiescent environment. However, in the context of acoustic liners, a grazing flow is present and impacts the jet formation. This interaction has already been described in section 1.3.2. There is another domain where synthetic jets are particularly helpful in a cross-flow configuration: flow control. Indeed, synthetic jets have been proven useful to control flow separation. In this context, the flow dynamics have thus been extensively studied. This is of a major interest for our study since understanding the evolution of the boundary layer in the presence of a synthetic jet is crucial in the context of heat transfer. In particular, the main flow structures have been identified, and the impact of turbulence on the jets has been studied, as well as the impact of the jets on the boundary layer.

A note on the definition of boundary layers: before detailing the impact of synthetic jets on the boundary layer, this concept needs to be properly defined. The boundary layer is the zone within which viscosity effects are important. There, significant velocity gradients can be observed from the wall (where the velocity is null) to the freestream zone. A classic definition of the boundary layer thickness is the distance between the wall and the point where the velocity reaches 99% of the freestream velocity. In the case of synthetic jets, this thickness can be more complex to be defined for two reasons: (i) the presence of the perforations implies the existence of zones where there is no wall and (ii) in some cases, the jets contribute to increase the boundary layer thickness and can even be strong enough to outreach by far the boundary layer of an equivalent flat plate configuration. Through the present study, the boundary layer thickness definition is similar to the classical one by considering that, along the perforations, there is a hypothetical wall in the prolongation of the plate. For most of the cases that are analysed here, the jets contribute to thicken the boundary layer but remain within it. The issue remains subject to debate for cases where synthetic jets outreach the boundary layer.

Synthetic jets were considered useful for flow control applications and were studied with this purpose after Smith and Glezer [62] proposed a modern version of synthetic jet actuators. Indeed, studies as those of Amitay *et al.* [85,86], Nae [87,88] or McCormick [89] showed promising results. Amitay *et al.* [85, 86] experimentally studied a bluff body (2D cylinder model) within a wind tunnel, with embedded synthetic jet actuators. Among their main observations, they showed that the jets generate a recirculation bubble, which is described as a "virtual surface" that moves the streamline positions. The lift and drag can be increased or decreased, regarding the position of the actuators. Finally, the jets modify the flow strongly enough to significantly impact the wake. Nae [87] numerically investigated the interest of using synthetic jets on a NACA 0012 airfoil and observed a lift improvement at low angles of attack, and at higher angles a delayed stalling that can be controlled through synthetic jets. McCormick [89] proposed a slightly different configuration,

which he called a "Directed Synthetic Jet". It is based on a classic synthetic jet, however the actuator neck is curved in the downstream tangential direction. It was experimentally tested on a diffuser and an airfoil, and was shown to efficiently control the boundary layer separation. Since these studies, the subject of flow control through synthetic jets has been widely considered. An extensive literature review was delivered by Glezer [90].

Thanks to the studies focusing on flow control, the flow dynamics generated by synthetic jets and the main structures that appear in presence of a cross-flow have been thoroughly studied, both experimentally and numerically. An early study of Crook and Wood [91], using oil to visualise the flow patterns around synthetic jets interacting with a turbulent boundary layer, evidenced the presence of two longitudinal structures developping after each jet, that can be identified as the footprint of streamwise vortex pairs. These structures interact with the separating shear layer in a complex, three-dimensional way. Zhong *et al.* [92] provided dye flow visualisations of a circular synthetic jet in a laminar boundary layer and determined the importance of different flow parameters. In particular, they concluded that the Reynolds number Re is useful to quantify the vortical structures vorticity strength; the velocity ratio $\overline{W}/U_0$ is crucial when considering the structure trajectories; a variation of the Strouhal number St impacts the spacing between following structures. It should be pointed out that in their study, the Reynolds number is based on the stroke length rather than on the aperture diameter. Concerning the vortical structures, several of them can be identified: hairpin vortices (at low Reynolds number and velocity ratio), stretched, tilted vortex rings (at intermediate Reynolds number and velocity ratio) and finally tilted vortex rings (at high Reynolds number and velocity ratio). The vortex tilting and stretching are considered to be the dominant structures in their studies, however the hairpin vortices are strongly suspected to generate streamwise vortex pairs that are the source of the flow separation delay.

Following Zhong *et al.* [92], different experimental and numerical studies dug deeper to understand the formation of the vortical structures generated by synthetic jets in cross flow. Jabbal and Zhong [81, 93], in addition to dye flow visualisations, used a temperature sensitive coating that enabled them to observe the impact of the flow structures on the wall, through their footprint on the heat transfer coefficient. It can be pointed out that they found out a similar threshold phenomenon as described in section 2.2.1 and discovered by Gharib *et al.* [78] in a quescient flow configuration: below a threshold value of L_0/D, a single vortex ring is generated by the synthetic jet while above this threshold the vortex is followed by a trailing jet. In their grazing flow configuration, Jabbal and Zhong noticed the same phenomenon however the threshold value of L_0/D was above that of a quiescent flow case. As well as Zhong *et al.*, they observed three main kinds of vortex structures: hairpins, stretched vortices and tilted (or distorted) vortices. Figure 2.5 shows the formation of the different structures, how they develop within the boundary layer, and their impact on the wall. The tilted vortices are evacuated very early out of the boundary layer, while the two other kinds of vortices remain longer in it. Thus, their impact on the boundary layer is more important and it is assumed that both of them are

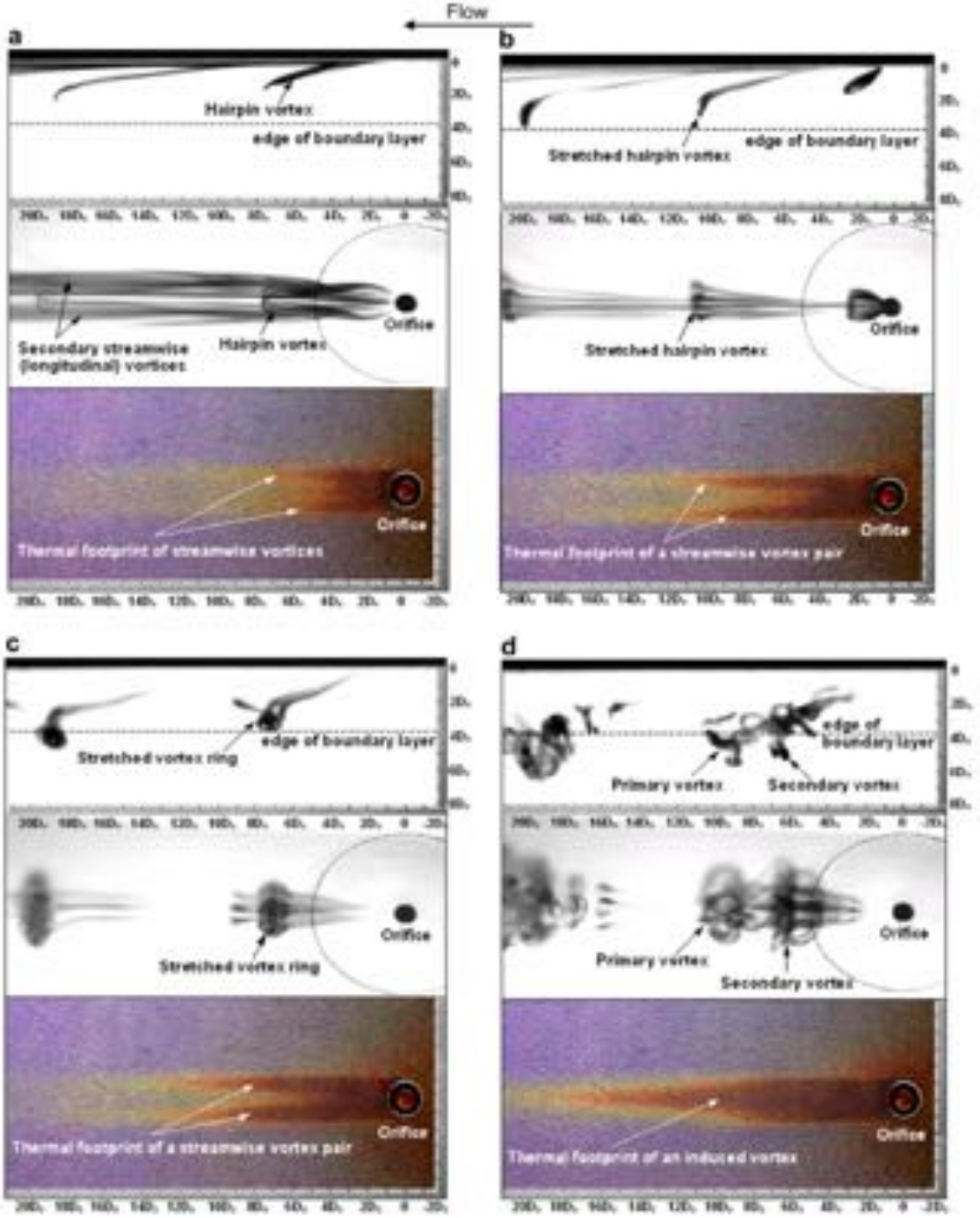

Figure 2.5: Stereoscopic dye flow and surface liquid crystal visualisation of (a) hairpin vortices, (b) stretched haiprins, (c) stretched vortex rings, (d) distorted vortex rings [81].

responsible of the flow separation delay (contrarily to Zhong *et al.*, who considered that the delay is due to hairpins only). Another interesting part of their study is the parameter maps they proposed, shown in Fig. 2.6.

Zhou and Zhong [94] numerically studied the flow dynamics of synthetic jets in cross flow. Their results were validated by comparison with the experiments of

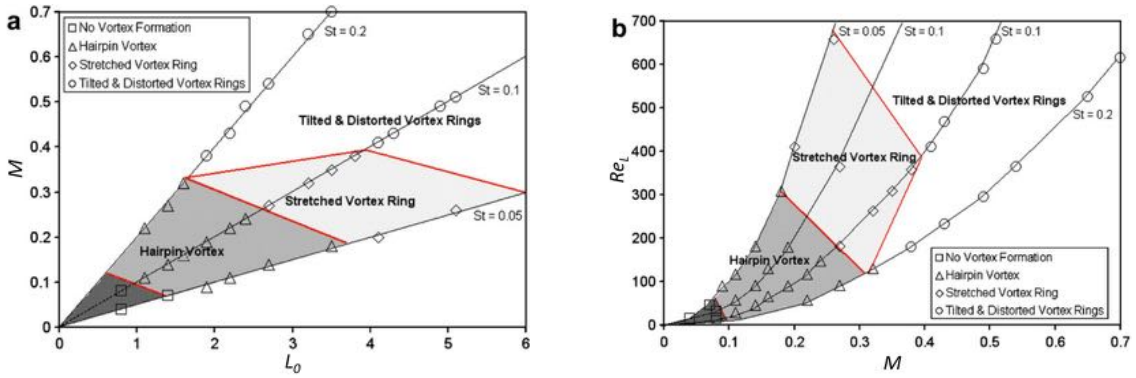

(a) Velocity ratio - stroke length.

(b) Reynolds number - velocity ratio

Figure 2.6: Parameter maps for the different vortical structures generated by a synthetic jet in presence of a laminar boundary layer, adapted from [81].

Jabbal and Zhong [81]. Focusing on two main operating points, the observed the formation of hairpins and tilted vortex rings. For the two cases, they observed the same flow structures than those observed in the experiment, as well as patterns in the wall shear stress similar to those of the heat transfer observed through the temperature sensitive coating. Moreover, they brought more information about the interaction of the jets with the boundary layer: some secondary and tertiary structures, that could not appear through the dye flow visualisation, were observed in the numerical simulations and are coherent with the corresponding footprint on the wall shear stress. In the hairpin case, two streamwise streaks of high heat transfer are present, as can be seen in Fig. 2.5b. They are attributed to the hairpin counter-rotating legs and the secondary structures generated by the hairpins, visualised only on the simulation results. For the tilted vortex case, a single high heat transfer streak is observed (Fig. 2.5d). However, the tilted vortices are evacuated out of the boundary layer very rapidly and they are thus not assumed to be directly responsible for the high wall heat transfer. In fact, they trigger tertiary vortices that remain closer to the wall and are supposed to be responsible for the observed streak. Following this study, Zhou and Zhong [95] extended the number of operating points, in order to identify more flow structures depending on the Reynolds and Strouhal numbers, and proposed new parameter maps corresponding to their observations. One of them is visible in Fig. 2.7. In particular, they distinguish two categories of structures, depending on their footprint on the wall shear stress that can present one or two streamwise streaks. The boundary between these two categories is also established as follows: for a Strouhal number below 1, it corresponds to a velocity ratio M equal to 0.4 while for higher than 1 Strouhal numbers it corresponds to a dimensionless Stroke L_0 length equal to 1.6. It should be noticed that they also observe structures similar to the stretched vortices described by Jabbal and Zhong [81]. However, they observe that these vortices evolve rapidly into hairpins and thus prefer to use this term to identify them. For them, it is thus another kind of hairpins that is formed downstream the actuator aperture.

Sau and Mahesh [96] performed DNS of a round synthetic jet in cross flow. Sim-

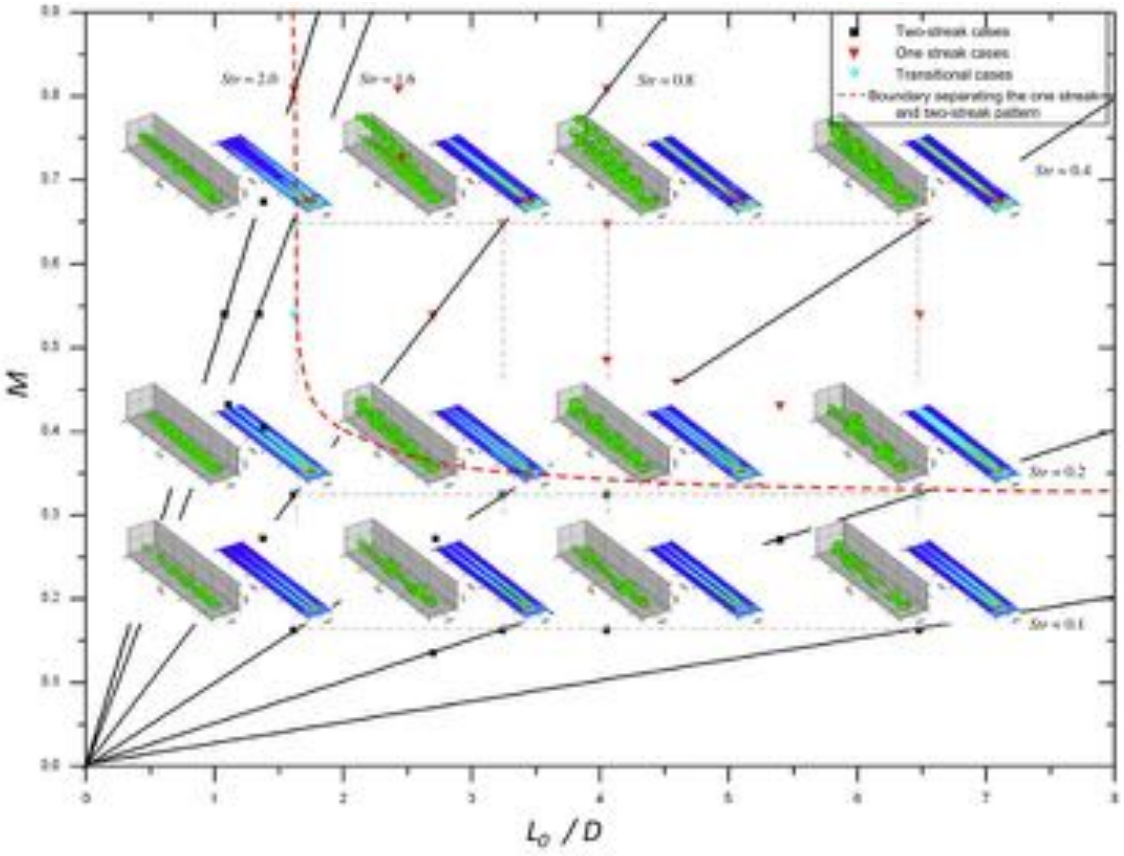

Figure 2.7: Velocity ratio - dimensionless stroke length parameter map of vortical structures and corresponding time-averaged wall shear stress due to the interaction of a round synthetic jet and a laminar boundary layer, adapted from [95].

ilarly to Zhou and Zhong [95], they identified three different kinds of structures. However, they considered velocity ratios from 1 to 6, wich is way higher than the values considered for Zhou and Zhong's study (velocity ratio up to 0.64). As Zhou and Zhong, they distinguish hairpins and vortex rings. In their study, no vortex ring can be observed for a velocity ratio equal to 2, which is a higher transition value than for Zhou and Zhong's study. Regarding the vortex rings, they discriminate single vortex rings and vortex rings accompanied by a trailing jet. The transition between these two kinds of structures appear below a threshold number of $L_0/D = 3.6$, which is close to the threshold number observed for the cases of quiescent flow observed by Gharib *et al.* [78] and Jabbal and Zhong [80] ($L_0/D = 4$). It should be noticed that for the study of Sau and Mahesh [96] the threshold for L_0/D is a bit below 4 for the cross flow case. It is also shown in their study that the discrete vortex rings are characterised by an upstream tilting, while the vortex rings with trailing jet present a dowstream tilting.

The turbulent levels of the grazing flow boundary layer also impacts the flow features that can be observed. Zhong *et al.* [92] consider only a laminar boundary layer in their study. Indeed, they state that in preliminary experiments the vortical structures are "essentially similar" with either a laminar or a turbulent boundary

layer. However, Jabbal and Zhong [81] expect the wall friction coefficient to have an impact on the streamwise dissipation of the vortical structures, a rising wall friction coefficient leading to a higher vortex dissipation rate. This implies differences between laminar and turbulent boundary layers: regarding the targeted application, this point is crucial. Indeed, the increase of the friction coefficient due to turbulence is of great interest in the context of wall heat transfer. On the contrary, for flow control applications, the flow structures have been identified as the main mechanism enabling the control of flow separation. Thus, a higher dissipation rate is bothering and higher Reynolds number, dimensionless stroke length and velocity ratio would be needed for the turbulent case, compared to the laminar case, in order to generate similar structures. However, some results seem to indicate that, as well as in the study of Zhong *et al.* [92], the synthetic jet presents a similar interaction with laminar and turbulent boundary layers. The more recent study of Wen and Tang [97] focused on determining the impact of turbulence on the formation of the hairpin vortices. To do so, they ran numerical simulations with a laminar and a turbulent boundary layers, other things being equal, and compared the structures generated in both simulations. At first sight, similar hairpin vortices appear in both configuration, as already stated by Zhong *et al.* and Jabbal and Zhong. In particular, the same formation of secondary structures is observed in both cases. Nonetheless, further investigation reveals that the differences of velocities in the boundary layer, as well as background turbulent structures that exist in the turbulent boundary layer but not in the laminar boundary layer, do have an impact on hairpin formation. In particular, the hairpin velocity is higher in the turbulent case than in the laminar one, and it is also more bent shaped, assymetric, and presents a higher dissipation rate. This leads to a wider but weaker influence on the turbulent boundary layer, as well as on the wall shear stress. Moreover, it should be pointed out that in the presence of a turbulent boundary layer some hairpins can be auto-generated. Finally, the secondary vortices also present a more complex formation in the turbulent case. It is indeed shown that, in addition to secondary vortices generated by the hairpins, some of them can be triggered by the actuator directly, this phenomenon prevailing in the turbulent case. It is also more complex than for the laminar operating point, with the downstream horseshoe vortex that seems to partly merge with secondary vortices, producing more complex structures.

2.2.4 Heat transfer enhancement

As seen through the previous sections, the flow dynamics generated by a synthetic jet implies the creation of vortices that impinge on the wall, modify the boundary layer, increase the wall shear stress and enhance the flow mixing. All these features make synthetic jets an attractive system to work on heat transfer enhancement.

Most of the aplications targeting heat transfer and implying synthetic jets are based on impinging configurations [98–101]. In particular, early results such as that of Trávníček and Tesař [98] showed that impinging synthetic jets were promising for electronic applications. Indeed, this domain implies very important heat fluxes

that have to be evacuated from relatively small surfaces, while there is little place for the cooling set-up. The absence of complex plumbing, the small size of synthetic jet actuators and their good results on heat transfer enhancement have made them a good tool for these cases. Kercher *et al.* [99] showed that the performance of synthetic jets in cooling a heated device is comparable to that of commercially available cooling fans. Moreover, they found out that the thermal behaviour of synthetic jets could be modelled by correlations based on conventional impinging jets, if introducing proper correction. Since these early studies, impinging synthetic jets have been widely studied for heat transfer applications as can be seen through the extensive literature review of Krishan *et al.* [101].

Contrarily to impinging synthetic jets, only few research works consider the heat transfer of the wall that is crossed by the jets. The specific case of acoustic liners have already been developped in section 1.4, in particular with the studies of Duchaine [52] and Méry *et al.* [47]. One study that should be mentionned in the present context is the experimental work of Jabbal and Zhong [81], followed by the numerical simulations of Zhou and Zhong [94,95], already discribed in section 2.2.3. These studies are particularly adapted to our concerns about heat transfer in acoustic liners since they implied the presence of a cross flow. Although they were focused on flow control applications instead of heat transfer enhancement, they paid a special attention to the wall shear stress and developed knowledge about the synthetic jet impact on walls. The recent work of Manning *et al.* [102] considered the heat transfer of a heated plate crossed by synthetic jets in quiescent flow. They compared different Reynolds number and dimensionless stroke length values, and two configurations were used: a single jet and a four jet configurations. They found out that, similarly to impinging configurations, a higher stroke length leads to an enhanced heat transfer. Moreover, the multi-perforated configuration is also more efficient in increasing the heat transfer. They also identified the flow structures in the multi-perforated case, concluding that the flow entrainment due to the vortex roll-up and the suction phase contribute to reducing the thermal boundary layer thickness. Another interesting structure is the secondary vortex that is generated between two jets. It entrains the fluid in the opposite direction of the jet, that is to say towards the wall. The impingement of this structure on the wall also contributes to the heat transfer enhancement.

2.3 Analytical models and numerical simulations for the prediction of synthetic jets

As overviewed through the previous literature review, there are many ways to study synthetic jets, from experimental visualisations to complex numerical simulations. Since the present study is based on numerical simulations, this section focuses on describing the different models and methods that can be used to simulate synthetic jets, including analytical models, boundary conditions and CFD methods used to simulate the whole domain. The objectives are to provide a more complete view of

the available numerical methods and to justify the choices made during this study.

2.3.1 Analytical models

As seen through this thesis, acoustic liners are designed on the Helmholtz resonator principle. More generally, any synthetic jet configuration can also be considered as a Helmholtz resonator. Simple analytical models exist to design liners or actuators allowing to predict, among other things, the Helmholtz resonance frequency, as seen in Chapter 1. However, the Helmholtz resonator theory is not enough to account for parameter effects on the jet velocity and dynamics, for example. Knowing this jet velocity is particularly important when studying a synthetic jet, since it is required to know the Reynolds and Strouhal numbers that define the operating point. Since complete numerical simulations can be expensive, several analytical models have been developped over the years to help understand and design synthetic jet actuators.

A usual way to model synthetic jet actuators is to consider an equivalent electric circuit model. Several models were developped to link the jet velocity to the actuator excitation voltage, like in McCormick [89] or Gallas *et al.* [103, 104], based on this kind of equivalent circuits. However, these models present some significant limitations. In particular, actuators are subject to degradation with time that leads models to lose their accuracy. Another limiting point is that the model is no longer representative when two adjacent actuators are driven at a different phase. Indeed, Smith and Glezer [105] observed that the velocity of a synthetic jet is impacted by the adjacent jet, and even more strongly when the jets are not in phase. For these two reasons, several authors prefer to avoid velocity-voltage models.

Another kind of model consists in linking the jet velocity to the pressure, which can be easily measured. These models are resilient to the limitations observed for velocity-voltage models. One of such first actuator model was proposed by Rathnasingham and Brauer [106]. This model is based on the coupling of a stuctural model that takes into account the actuator itself and a fluidic model that considers the flow features at the neck. It also takes into account the unsteady Bernoulli equation. This coupling leads to a set of five coupled non-linear state equations and is hepful to evidence the non-linear effects due to compressible and unsteady effects. Later on, Persoons *et al.* proposed [107] and then experimentally [107] and numerically [108] validated a similar model. This semi-empirical model also couples the electromechanical and fluid dynamics equations. Two empirical coefficients need to be determined. Although the eletromechanical part of the model was specifically designed for piezoelectric membranes, the fluidic model is valid for any kind of actuators. Indeed, this model, which had previously been presented in another paper [109], is based only on pressure which can be measured independently of the actuator type. Based on a "simplified" gas dynamics, this model distinguishes linear and non-linear cases. Their complete model (coupling of fluidic and electromechanical parts) helped evidencing the impact of the neck on the overall system response. The two empirical parameters were also discussed as "easily estimated or calibrated".

The presence of a grazing flow, as it is the case in flow control applications or with acoustic liners, can require to adapt the model. McCormick's model [89] was developped in a context of boundary layer separation control. Persoons [107] expects his model to be valid in crossflow, at least for "moderate" velocity ratios.

Finally, a recent literature review on the subject of Lumped Element Models was proposed by Chiatto *et al.* [110]. The reader who wants more information on that subject is invited to consider this paper. Analytical models are not the only way to study synthetic jets: numerical simulations offer different useful tools to do so. The two following sections focus on these methods.

2.3.2 Boundary conditions

Numerical simulations are a privileged tool to study the flow behaviour induced by a synthetic jet actuator or an acoustic liner. However, the different orders of magnitude (from the small aperture diameter to the main domain dimensions) as well as the complex geometries and moving features (in particular, for a piezoelectric membrane, the movement is particularly complex) can increase drastically the simulation cost. Thus, it is common to simplify the numerical configuration by not representing the actuator or liner, representing the neck end only: the actuator is therefore replaced by a boundary condition, which has to be adequately defined. To do so, different methods exist; two of them are presented hereafter: the imposition of the velocity field directly at the neck and the use of an impedance model. Moreover, even when the whole cavity is simulated, the moving part of the actuator can lead to a challenging boundary condition definition. This specific issue is also described in this section.

Imposed velocity at the neck. A simple way to numerically simulate the flow dynamics generated by a synthetic jet actuator is to model its presence through a simplified boundary condition. This avoids to consider the actuator geometry. The simplest boundary condition that can be used to represent a synthetic jet is to impose the fluid velocity at wall [68, 112]. For conventional actuators (with piezoelectric membranes or pistons), the velocity can be imposed as a signal function of space and time, usually based on a sinus. For example, Rampungoon [68] considers the signal $w(x,t) = T(x)sin(2\pi F^+ t)$, where F^+ is a dimensionless forcing frequency and $T(x)$ represents a family of jet profiles that depends on the considered phase (aspiration or ejection). However, as seen in section 2.1.3, the geometry of the neck and the cavity of the actuator can have a considerable influence on the velocity shape at the aperture, which makes the use of a sinusoidal-shaped velocity signal much too simplified. Although the sinusoidal signal ensures a symmetric velocity shape, this is untrue in case of a cross-flow. Raju *et al.* [111] proposed a reduced-order model to impose a boundary condition that represents the presence of the cavity; however in their case the neck is simulated and the boundary is imposed at its bottom. The results show a much improved accuracy in representing the flow physics, compared to a boundary condition that also models the neck and is applied directly at the wall.

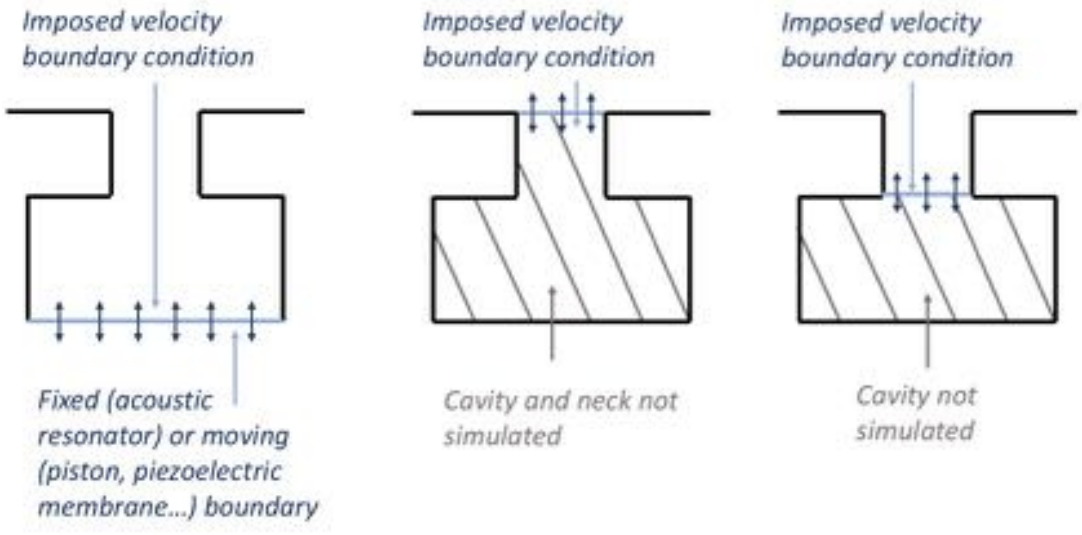

(a) Full cavity configuration (b) Imposed velocity boundary condition (c) Slot-only model proposed by Raju *et al.* [111]

Figure 2.8: Schematic of different numerical approaches, adapted from [111].

Figure 2.8 illustrates the imposed velocity method by comparing a fully simulated configuration, a case where the actuator is replaced by a boundary condition and finally the simulation of the slit as proposed by Raju *et al.* [111].

Impedance models. For the case of acoustic liners, a specific kind of boundary condition has been developped over the years, making use of the notion of impedance. The impedance is a key notion of acoustics, which was decribed in Section 1.2.3. As a reminder, it is defined as $z = p'/u'$ with p' and u' the acoustic pressure and velocity, respectively: it connects the acoustic pressure and velocity fluctuations. In a way, it is close to the imposed velocity method developped previously, since imposing the impedance is equivalent to imposing a velocity. However, it should be pointed out that in the case of an acoustic liner, the impedance boundary condition is not restricted to the perforations. On the contrary, it corresponds to the whole surface of the liner.

The Ingard-Myers boundary condition is one of the models that can be found for the impedance. A description of that model is proposed by Brambley [45]. The fluid and boundary normal displacement are matched, rather than the normal velocity. This is completed by a model for the impedance calculation, which can be done with the Helmholtz resonator formalism. The Ingard-Myers boundary condition is still a reference in the domain, in spite of its recently highlighted weaknesses. Indeed, it was found that the boundary condition implies an extremely thin boundary layer, which does not always make sense from a physical point of view. Indeed, the boundary condition simplifies the acoustic and hydrodynamic fields, whereas Aurégan and Leroux [44] experimentally showed that in some cases these two fields are coupled, leading to instabilities. Brambley [113] showed mathematically the limitations of

this model, in terms of illposedness, and studied different stability criterions. Brambley [114], considering a laminar boundary layer (based on Blasius equations) within a cylindrical duct, studied the importance of viscosity on liners. His work showed that the Ingard-Myers is applicable only for high frequencies.

The impedance models are usually developped in the frequency domain. However, several quantities of interest in the study of liners are dependent on time instead of frequency. It is especially the case for the flow hydrodynamic properties: the pressure and mass flow rate within the neck are time dependent, among other variables. Different studies of time-domain models for liners have thus been developped. Rienstra [115] proposes a definition based on an extended version of the Helmholtz resonator. Converting a frequency domain boundary condition to the time domain is however difficult: it implies a Fourier transform that requires to define an impedance for all complex frequencies. The problem is that this definition is physically impossible in some cases. Zhang and Bodony [39, 54, 116] used numerical simulations to investigate how different flow parameters (velocity profile, boundary layer thickness, aperture wall shear stress...) are connected and how to use this information to develop a time-domain impedance model.

Actuator moving part. When the cost of simulating the whole system can be afforded, a boundary condition difficulty remain: the definition of the boundary corresponding to the actuator moving part. Regarding the actuator kind, different choices can be made: the moving part can be represented through a piston-like movement or a membrane-like movement. The second one is much more expensive, however it is not advised to replace it by the piston-like movement to face cost issues: it has been shown that the flow generated by pistons and piezoelectric membranes are different [73]. Reducing the cost of a simulation by using a piston-like movement instead of a proper membrane can thus lead to degraded results. For example, Mittal *et al.* [75] assume that the results of Rizzetta *et al.* [71] diverge from their reference because of a bad choice for the boundary condition.

Acoustic liner context

Quite obviously in the acoustic liner context, when the cavities are not represented and the liner is replaced by a boundary condition, the impedance model is privileged since it has been developped specifically for this context.

2.3.3 CFD methods

Different strategies can be chosen when performing CFD (Computational Fluid Dynamics) to simulate turbulent flows and LES (Large Eddy Simulations) are the most adequate to study synthetic jets. After providing some theoretical details on turbulent flows, the main characteristics of the methods used here are briefly described.

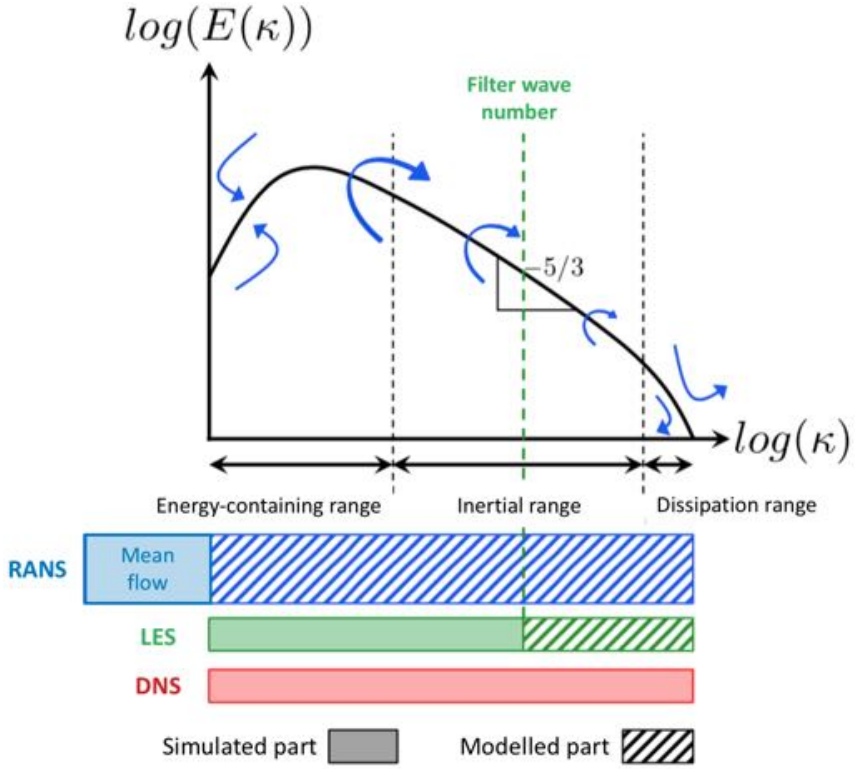

Figure 2.9: Kinetic energy spectrum of a turbulent flow and associated modelisation strategies (translated from [2]).

Figure 2.9 displays a kinetic energy spectrum which is characteristic of a turbulent flow. This kind of spectrum is adapted from the model of Pope [117], who based his work on the cascade energy model proposed by Richardson [118] and the hypotheses of Kolmogorov [119]. The idea of the cascade energy model is that the turbulence is present at different sizes, called *eddies*. The largest eddies, characterised by the flow scale and velocity, are unstable and transfer their energy to the smaller eddies, until the kinetic energy of the smallest, more universal eddies which are dissipated by molecular viscosity. This phenomenon is described by Richardson as follows:

Big whorls have little whorls,
Which feed in their velocity;
And little whorls have lesser whorls,
An so on to viscosity
(in the molecular sense).

The Reynolds number is defined as the ratio of inertial forces to viscous forces. The Reynolds number of large eddies is high and comparable to that of the flow, while smaller eddies are characterised by smaller Reynolds numbers, until the smallest eddies whose Reynolds number is small enough: the eddies are stabilised and then dissipated by the viscous forces, which are then strong enough compared to inertial forces. The size of the smallest eddies can be found out with a theory developped by Kolmogorov [119], based on three main hypotheses. The first hypothesis

states that if the Reynolds number is high enough, the small-scale eddies are statistically isotropic, which makes them "universal" in high Reynolds number flows. The second and third hypotheses state that, for high Reynolds number flows, the small-scale and medium-scale eddies, from a statistical point of view, have a universal form which depends on ϵ and ν, and ϵ only, respectively. The parameters ϵ and ν correspond to the rate of dissipation and the viscosity, respectively.

On the spectrum presented in Fig. 2.9, the different scales are represented with the energy transfer from biggest to smallest scales, alongside a shematic description of different CFD strategies. The DNS (Direct Numerical Simulation) consists in simulating all of the turbulent spectrum, including the smallest turbulent eddies. It provides particularly accurate results but its cost rises with Re^3 which becomes unaffordable at high Reynolds numbers. This method is thus usually dedicated to simple, academic configurations and is avoided in complex geometries with high velocity flows. On the contrary, the RANS (Reynolds Averaged Navier-Stokes) method is characterised by a "low" cost, but at the expense of some accuracy loss. It is based on the averaging of the Navier-Stokes equations, and completed by models in order to close the equations. Thanks to its low cost, it is now a privileged tool in the industry to study complex geometries. As represented in Fig. 2.9, the turbulent part of the flow is not simulated at all. Usually categorised inbetween DNS and RANS from the simulation accuracy and cost points of view, LES (Large Eddy Simulation) is the third main strategy among CFD methods. The idea is to use a spatial filter (usually linked to the mesh size): the biggest eddies are simulated while the smallest eddies are modelled. This way, the simulation is much more accurate than RANS, since it simulates at least part of the turbulence, while the cost remains reasonable compared to DNS, with the modelling of the smallest eddies. With the enhancement of computing power, this method is now affordable for industrial, complex configurations [2, 120–122] with an interesting trade-off between cost and accuracy.

An early workshop was performed in order to compare a great number of codes on three academic, experimental set-ups [123]. At this time, none of the methods seemed to provide particularly enhanced results, however it was already stated that the LES and DNS codes were very promising and would give much better results when an improved machine performance would be available. It should be noticed that because of the unsteady behaviour of synthetic jets, RANS methods are particularly inadapted to correctly reproduce the flow features, and at least URANS (Unsteady RANS) methods should be used. Following research, like the one by Dandois *et al.* [124], showed the limitations of RANS and even URANS when compared to LES. In fact, the highly unsteady character of flow dynamics in the presence of a synthetic jet makes it very hard for RANS to efficiently simulate this phenomenon. A more recent litterature review by Leschziner and Lardeau [76] also pointed out the limitations of RANS, while emphasizing the good results obtained with LES and DNS. With accurate results and a simulation cost inferior to that of DNS, LES thus seems a privileged method to study synthetic jets. It is the method that was chosen for this study; more details about the numerical methods are provided in Section 4.2.

Acoustic liner context

Due to the different orders of magnitude (neck width and diameter, cavity length and surrounding flow), the simulation cost of a whole liner is substantial. Therefore, numerical simulations usually reduce the whole liner to a single cavity with a single perforation, which corresponds to a classic Helmholtz resonator. This neglects the effects of the interaction between the different perforations as well as the effect of the multiple cavities, however it offers the benefit of an affordable simulation.

After the presentation of acoustic liners in Chapter 1, the present chapter, with a detailed literature review on the suject of synthetic jets, provided information about the main parameters and flow features of synthetic jets that are useful to better understand the behaviour of acoustic liners. Numerical tools were also reviewed in order to justify the choices made throughout the present study. In the light of these elements, Chapter 3 develops the objectives of the thesis and the means implemented to perform the study.

3
Thesis objectives

As seen in Chapter 1, acoustic liners are treatments usually applied on engine nacelle walls in order to reduce the fan noise. Although their hydrodynamic behaviour and acoustic performance have been widely studied, there is still little knowledge about the impact of liners on wall heat transfer. Recent studies suggest a strong coupling between aerodynamics, acoustics and heat transfer which would lead to an increased wall heat transfer when compared to a classic flat plate. A better understanding of these phenomena seems crucial for the design of future aircraft engine nacelles to tackle heat transfer enhancement and energy valorisation challenges.

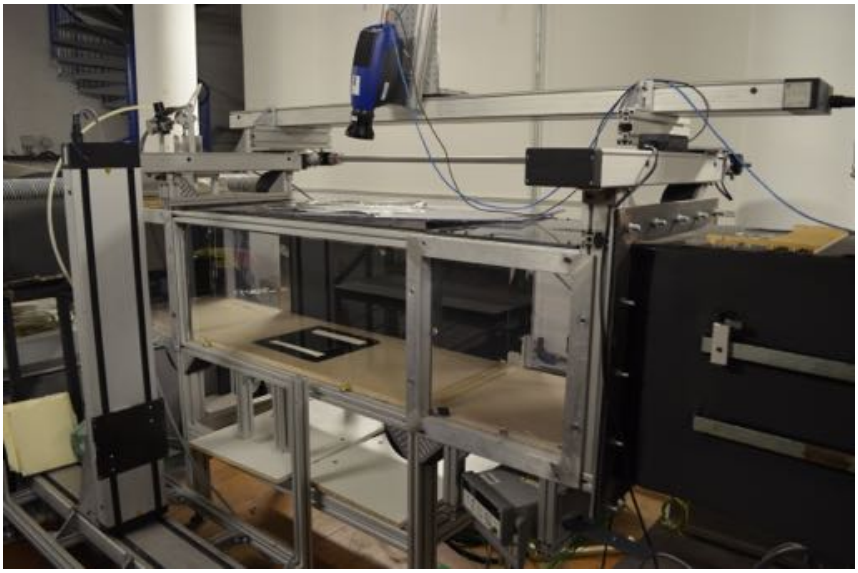

Figure 3.1: Pprime experimental test bench. Courtesy of B. Giachetti.

Acoustic liners are a specific kind of synthetic jet actuator, a device used to trigger a zero net mass flow jet directly from the ambient fluid. Other kinds of actu-

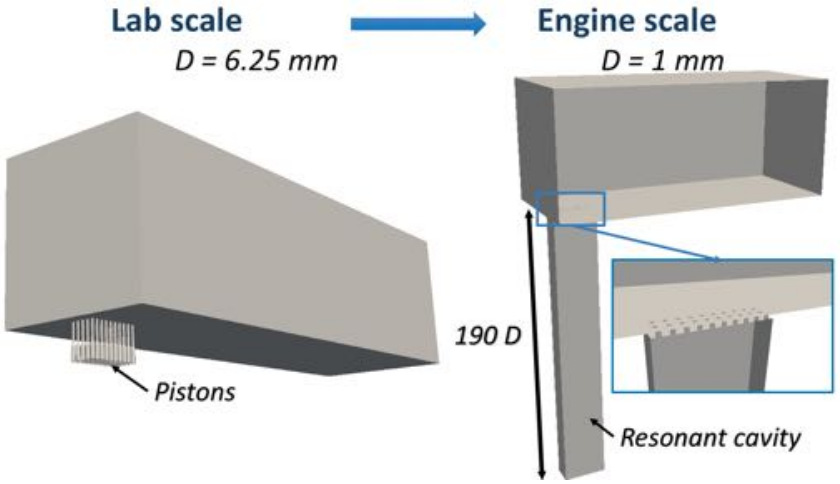

Figure 3.2: Comparison of the two numerical configurations used to validate the liner-representativity of the Pprime rig.

ators are based on the same architecture, with a cavity and a neck, but the jets are triggered by a moving piece such as pistons or piezoelectric membranes. A literature review on synthetic jets, proposed in Chapter 2, provided a better understanding of hydrodynamics near actuators. In particular, the impact of several design parameters on the flow dynamics was considered, along with the behaviour of synthetic jets in the presence of a grazing flow. The specific flow structures generated by the jets were observed, and their thermal footprints on the plate, experimentally observed through the wall shear stress, is a good indicator of the increased wall heat transfer due to the jets. Impinging synthetic jets, more usually triggered by piezoelectric or electromagnetic membranes, are now a well known tool used to enhance heat transfer, notably for electronics applications. However, such as for the liners, very scarce studies consider the heat transfer occuring in the plate crossed by the jets. The point of the present numerical study is therefore to investigate heat transfer within acoustic liners. As seen in the literature review, several simulation methods can be used to simulate a synthetic jet, among which the use of a boundary layer to replace the actuator, or simulation of the complete system. It is chosen here to completely reproduce the system, in order to better simulate the flow physics near the plate. Large Eddy Simulations are used: as pointed out in previous studies, they reproduce the synthetic jet physics in a much more accurate way than RANS methods, while keeping an acceptable numerical cost when compared to DNS.

This numerical study is based on the experimental rig used by Giachetti *et al.* at Institut Pprime, Poitiers, France, to investigate the influence of synthetic jets on heat transfer enhancement in a cross-flow muti-perforated configuration [125, 126]. A photo of the test rig is provided in Fig. 3.1. The perforated plate and chosen operating points are based on a similitude with a classical acoustic liner. To the author's knowledge, it is the first study focusing on wall heat transfer in such a configuration. It offers an interesting database, useful to validate a numerical simulation. From there, the numerical results can be used to enhance the understanding of flow physics. Contrarily to classic liners, the jets are triggered by pistons placed

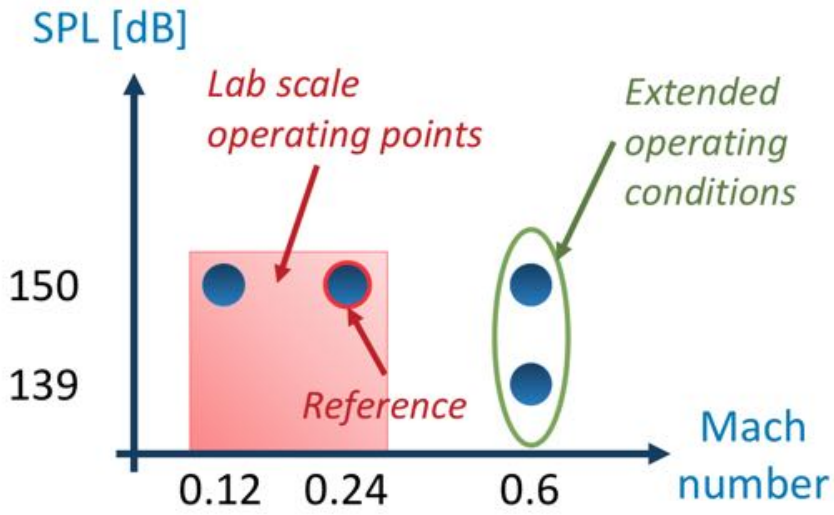

Figure 3.3: Overview of different operating conditions used throughout the study in the engine scale. The experimental conditions, converted to engine-scale values through the similitude ratios, are provided in the red field. Blue circles represent some of the LES performed during this work.

underneath the perforated plate and not by acoustic resonance. As seen through the previous literature review, synthetic jets are characterised by three defining parameters, meaning that the triggering mechanism should not lead to important differences if these parameters are correctly reproduced. However, it was also shown that the cavity and neck geometries do have an impact on the formation of flow structures, and therefore it might modify their impact on the plate, leading to a different wall heat transfer. Moreover, although the similitude ensures the correct reproduction of the flow dynamics around the perforated plate, for which the geometry is correctly maintained, the triggering mechanism is completely different for the synthetic jets than for a classical acoustic liner (acoustics for the liner, and piston for the rig). It is thus necessary to validate the use of this test rig and its reprentativity of a classic acoustic liner. To do so, two different configurations are simulated: one reproducing the rig (refered to as "lab scale") and one with liner dimensions (called "engine scale") where the pistons are replaced by a resonant cavity. An overview of these two configurations is provided in Fig. 3.2. Finally, the experimental operating points are limited to a maximal grazing flow Mach number equal to 0.24 at the engine scale while classical liners can face much higher Mach number grazing flows. Numerical simulations are used to extend these operating points up to Mach 0.6, as shown in Fig. 3.3. This is more representative of the real conditions at which a classical liner is confronted in flight. The three main objectives of this thesis are thus as follows:

- propose a numerical set-up that reproduces the Pprime rig (lab scale configuration), and use the available experimental data to validate the simulations (reference on Fig. 3.3);

- once the numerical set-up is validated, use the simulations to assess whether

the Pprime rig is representative of a classical acoustic liner, in spite of the different jet triggering mechanism, by comparing simulations on both lab scale and engine scale configurations (reference on Fig. 3.3);

- finally, use all of the available data (both experimental data, lab scale simulations and engine scale simulations) to analyse the flow dynamics generated by acoustic liners and the resulting wall heat transfer. In particular, the simulations are used to extend results to more flight-representative operating conditions (extended operating conditions on Fig. 3.3), the experimental conditions being restricted to low Mach number upstream conditions.

Part II

Numerical validation
Similitude validation
Flow and heat transfer analysis

4

Experimental scale model

The present chapter objective is to provide a complete description of the main configuration used throughout this study. To begin with, the experimental rig developped at Institut Pprime is detailed. In particular, the similitude choices and chosen approaches are explained. Subsequently, the numerical set-up is provided, with a focus on the adopted boundary conditions and meshing strategy.

4.1 Experimental set-up

The numerical study is based on the experimental work of Giachetti *et al.* [125,126]. Their test rig, shown in Fig. 3.1, is dedicated to the understanding of the impact of synthetic jets on wall heat transfer in the presence of a crossflow. To do so, synthetic jets are generated within the test section of a closed wind tunnel loop, while the wall they cross is heated. The Pprime test bench geometry and the considered operating points are scaled on those of a classical acoustic liner through a similitude. As detailed in Part I, only few studies considered using synthetic jets to enhance the heat transfer alongside the wall from which they are ejected. This study uses a multi-perforation configuration while observing the role of the grazing flow. The 5-perforation rows were specifically designed to avoid these edge effects in the Pprime configuration [125]. Finally, the different operating points present a wide range of Reynolds number, dimensionless stroke length and velocity ratio. The velocity fields are obtained by Particle Image Velocimetry (PIV) and an infrared camera is used to measure the wall temperature. Different aspects (grazing flow, multi-perforated configuration, extensive number of operating points) are crucial to study heat transfer within acoustic liners. This section provides details about the similitude methodology, set-up geometry, measurement methods and limitations of the test rig.

4.1.1 Similitude

The concept of similitude, as defined by Chassaing [127], is based on a simple idea: in spite of scale difference, if the fluid dynamics in two different scale configurations is characterised by identical dimensionless parameters, then it is governed by the same dimensionless equations. Thus, provided that the initial and boundary conditions are also scaled, the flow dynamics is supposed to be similar in both configurations. As for Pprime test bench, the dimensionless parameters that characterise the synthetic jets can be kept equal while modifying the flow parameters (grazing flow velocity, jet frequency and velocity). As a reminder, the Reynolds number, dimensionless stroke length and velocity ratio are defined as $Re = \frac{\overline{W}D}{\nu}$, $\frac{L_0}{D} = \frac{\overline{W}}{2fD}$ and $M = \frac{\overline{W}}{U_0}$. In particular, having an identical velocity ratio M in two different configurations implies the relation given in Eq. (4.1):

$$M = \frac{\overline{W}_{engine}}{U_{0_{engine}}} = \frac{\overline{W}_{lab}}{U_{0_{lab}}} \Longrightarrow \frac{\overline{W}_{lab}}{\overline{W}_{engine}} = \frac{U_{0_{lab}}}{U_{0_{engine}}} = \chi. \tag{4.1}$$

The ratio χ enables to link the velocities between the liner (engine scale) and the rig (lab scale) configurations, with $\overline{W}_{lab} = \chi \overline{W}_{engine}$ and $U_{0_{lab}} = \chi U_{0_{engine}}$. It also correlates the dimensions of both configurations. Indeed, in addition to the velocity ratio M, the Reynolds number needs to be kept similar. Assuming that the temperature is also unchanged (and thus that the air kinematic viscosity is also unchanged), this leads to Eq. (4.2):

$$Re = \frac{\overline{W}_{engine} D_{engine}}{\nu} = \frac{\overline{W}_{lab} D_{lab}}{\nu} \Longrightarrow \frac{D_{lab}}{D_{engine}} = \frac{\overline{W}_{engine}}{\overline{W}_{lab}} = \frac{1}{\chi}. \tag{4.2}$$

Finally, the frequency of piston motion can still be linked by the similitude parameter χ between the two configurations. The dimensionless stroke length L_0/D is also kept constant, which leads to Eq. (4.3):

$$\frac{L_0}{D} = \frac{\overline{W}_{engine}}{2 f_{engine} D_{engine}} = \frac{\overline{W}_{lab}}{2 f_{lab} D_{lab}} \Longrightarrow \frac{f_{lab}}{f_{engine}} = \frac{D_{engine}}{D_{lab}} \frac{\overline{W}_{lab}}{\overline{W}_{engine}} = \chi^2. \tag{4.3}$$

Since the perforation diameter is equal to 6.25 mm in the rig, while a classical acoustic liner perforation diameter is around 1 mm, the relation $D_{lab} = \frac{1}{\chi} D_{engine}$ extracted from Eq. (4.2) provides $\chi = 1/6.25$. Thus, the geometry and flow parameters at the lab scaled are easily calculated. They are summarised in Tab. 4.1, along with the engine scale parameters and the similitude ratios. The flow values provided in Tab. 4.1 correspond to the "reference" operating point, that is presented later on in this manuscript. The 12.8 Hz frequency of the piston corresponds, through the similitude, to 500 Hz, which is a value that is commonly found for liner applications. Finally, the cross flow velocity is equal to 80 m.s^{-1} at the engine scale, which corresponds to a Mach number around 0.24.

There is still one category of parameters that needs to be considered through the similitude methodology: heat transfer parameters. Indeed, this study is targeting a better understanding of wall heat transfer. It is thus crucial to correctly analyse the fluxes and heat transfer coefficients that correspond to the test bench, with an adequate matching with a liner configuration. In this context, the interesting parameter that needs to be transformed through the similitude is the convective heat transfer coefficient h. Downstream of the jets, the configuration corresponds to a flat plate with a grazing flow and the heat transfer coefficient is defined by $h = \frac{\lambda_{air} Nu}{L}$, where Nu is the Nusselt number, which as well as the Reynolds number is unchanged through the similitude, and L is a characteristic length (for example the plate length). Similarly to the perforation diameters, geometric parameters such as the characteristic length L are linked through the similitude by the similitude ratio χ: $L_{lab}/L_{engine} = 1/\chi$. Since the temperature is assumed identical for both scales, so is λ_{air}. Thus:

$$Nu = \frac{h_{engine} L_{engine}}{\lambda_{air}} = \frac{h_{lab} L_{lab}}{\lambda_{air}} \Longrightarrow \frac{h_{lab}}{h_{engine}} = \frac{L_{engine}}{L_{lab}} = \chi. \tag{4.4}$$

The conversion of h from the rig scale to a classical liner scale is also summarised in Tab. 4.1. However, contrarily to the other parameters, no additionnal example is provided for this parameter since, while geometrical and aerodynamics parameters correspond to the chosen operating conditions, heat transfer parameters are under investigation in the study and thus not known *a priori*. Moreover, the heat transfer coefficient can be calculated in different ways (for example, either localised or surface-averaged).

Similitude ratios		Parameters	
Parameter X	X_{lab}/X_{engine}	X_{lab}	X_{engine}
Geometrical parameters			
D (mm)	$1/\chi$	6.25	1
L (mm)	$1/\chi$	300	48
Flow parameters (reference operating point)			
U_0 (m.s^{-1})	χ	12.8	80
$\overline{W}$ (m.s^{-1})	χ	2.07	12.94
f (Hz)	χ^2	12.8	500
Heat transfer parameters			
h (W.m^{-2}.s^{-1})	χ	-	-

Table 4.1: Summary of the similitude ratios between the rig and a classical liner configuration (left) and example from one of the experimental operating points (right).

4.1.2 Experimental configuration

Now that the similitude approach has been detailed, the experimental set-up can be described more thoroughly. A perforated plate is placed within the test section of a closed wind tunnel loop. Each perforation leads to a cavity, at the bottom of which a piston is used to generate a synthetic jet. It has to be noted that all the pistons

are moved by the same engine: all of the synthetic jets are therefore in phase. Two main configurations were studied: a single row of 5 jets [125] and a multi-perforated configuration implying 10 rows of 5 jets [126]. The set-up, presented in Figs. 3.1 and 4.1, enables the generation of 5 or 50 synthetic jets that interact with the cross flow created thanks to the wind tunnel. Finally, the perforated plate is heated and its temperature is observed with an infrared camera, which enables to analyse the impact of the synthetic jets on wall heat transfer.

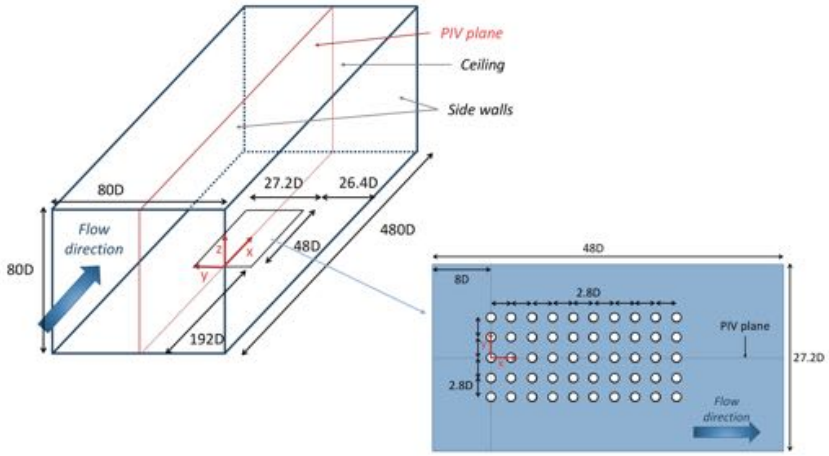

Figure 4.1: Scheme of the experimental set-up.

The useful investigation domain dimensions are $80D$ x $80D$ x $400D$, where D is the common diameter of the perforations. The perforated plate is $48D$ long in the flow direction and $27.2D$ long in the spanwise direction. The perforations all share the same diameter, $D = 6.25$ mm, and are distributed in 1 [125] or 10 [126] rows of 5 perforations. The lateral and spanwise hole distances equal $2.8D$. The main investigations are focused on the central line synthetic jets, which are affected by the nearby jets. The use of 5-perforation rows is meant to limit edge effects: if a single perforation line were investigated, the jet flow dynamics would be impacted only by the grazing flow while here it is symmetrically impacted by its neighbouring jets. The system used to generate the jets, placed underneath the perforated plate, is presented in Fig. 4.2. Each of the plate perforations is extended by a cavity, a pipe that is ended by a piston. The 50 pipes can be seen in Fig 4.2a, without the perforated plate. All of the pistons are moved by the same engine, shown in Fig. 4.2b.

Different operating points are considered, that can be defined by three parameters: the peak-to-peak amplitude $2K$, the frequency f of piston motion and the velocity U_0 of the grazing flow. Fixing these three parameters is equivalent to fixing the jet Reynolds number Re, dimensionless stroke length L_0/D and the velocity ratio $M = \overline{W}/U_0$. As seen in section 2.1.1, these three parameters completely charaterise a synthetic jet in crossflow. The different cases are presented in Tab. 4.2 which includes the values of $2K$, f and U_0 as well as the corresponding dimensionless parameters. In the context of this study, only the 50-perforation configuration is numerically simulated. Thus, Tab. 4.2 references only the corresponding cases, and not that of the 5-perforation configuration.

(a) Overview of the 50 pipes used as cavities to extend the plate perforations, with pistons underneath.

(b) Overview of the engine used to move the pistons.

Figure 4.2: Overview of the system placed underneath the perforated plate in order to generate the synthetic jets. Courtesy of B. Giachetti.

U_0 (m.s^{-1})	f (Hz)	$2K$ (mm)	Re	L_0/D	M ($\times 10^{-2}$)
1,9	0	0	0	0	0
	9.6	22	625	13.00	82.11
	6.4	22	416.7	13.00	54.74
	3.2	22	208.3	13.00	27.37
	12.8	22	829.3	12.94	108.95
	12.8	11.2	424.7	6.63	55.79
	12.8	4.7	176.3	2.75	23.16
	12.8	1.4	52.1	0.81	6.84
6.6	0	0	0	0	0
	9.6	22	625.1	13.00	23.64
	6.4	22	416.7	13.00	15.76
	3.2	22	208.4	13.00	7.88
	12.8	22	829.2	12.94	31.36
	12.8	11.2	424.7	6.62	16.06
	12.8	4.7	176.4	2.75	6.67
	12.8	1.4	52.1	0.91	1.97
12.8	0	0	0	0	0
	9.6	22	625.1	13.00	12.19
	6.4	22	416.9	13.00	8.13
	3.2	22	208.2	13.00	4.06
	12.8	22	829.2	12.94	16.17
	12.8	11.2	424.6	6.62	8.28
	12.8	4.7	176.4	2.75	3.44
	12.8	1.4	52.3	0.82	1.02

Table 4.2: Overview table of the experimental operating points for the 50-perforation configuration, as reported by Giachetti *et al.* [126]. Main flow parameters (left) and corresponding dimensionless parameters (right).

Three cross flow velocities are considered: 1.9 m.s^{-1}, 6.6 m.s^{-1} and 12.8 m.s^{-1}.

For each of these velocities, the impacts of the piston frequency and amplitude are studied. A case with motionless pistons is also studied, in order to clearly identify the importance of the grazing flow on the wall heat transfer. The large ranges of flow velocity, piston amplitude and frequency enable the study to cover a large range of jet Reynolds number, dimensionless stroke length and velocity ratio. Moreover, according to Holman criterion (*cf.* section 2.1.2), the piston motion is supposed to be strong enough to generate synthetic jets in all cases. Indeed, the criterion states that a synthetic jet is formed if the condition $\frac{1}{Sr} = \frac{1}{\pi} \times \frac{L_0}{D} > C$ is fulfilled. For axisymmetric cases, C is around 0.16. Appart from the motionless cases, the smallest dimensionless stroke length for the presented operating points is equal to 0.81, which implies that $\frac{1}{Sr} \simeq 0.26 > C \simeq 0.16$. This implies that a synthetic jet formation should be observed in all cases. Note however that the lowest amplitude cases ($2K = 1.4$) are very close to the threshold value. Thus, these cases might be in a transitionnal state rather than with a complete formation of a synthetic jet.

4.1.3 Measurement methods

The measurement techniques used by Giachetti *et al.* are detailed in [125,126]. More details for the heat transfer measurement methodology can also be found in previous papers, including that of Fénot *et al.* [128]. This section however provides a brief description of these methods, in order to highlight the available experimental data used to validate the numerical results. Measurements essentially target the velocity fields along the symmetry plane of the system and the wall heat transfer coefficient along the multiperforated plate. Note that specific attention is given here to the heat transfer measurement method, which is then reproduced numerically.

A PIV system was used to obtained the velocity fields along the plate symmetry plane, which corresponds to the XZ plane passing through the central perforation line centres. This plane can be seen in Fig. 4.1. This is the only plane where velocity experimental data is available, and the aerodynamic validation (see Chapter 5) of the numerical set-up is based on this data. For measurements, the flow was seeded with an oil generator: 1 μm particles were injected in the wind tunnel, usptream the test section. Since the synthetic jets are created with the ambient air, no other specific seeding was necessary. Measurement uncertainties were estimated at 4% for mean velocities and at 8% for *rms* values.

The heat transfer measurement methodology requires a more detailed description. For this specific diagnostic, the perforated plate is covered with an engraved copper foil which enables to heat the plate thanks to the Joule effect. Since this effect is controlled, the imposed wall heat flux is precisely quantified. The heat losses due to radiation and conduction have been estimated, which enables to calculate the convective heat flux ϕ. For every operating point, different heat fluxes are imposed on the perforated plate and the temperature is measured with an infrared camera. The local heat transfer coefficient h can then be calculated with Newton's cooling

law, presented in Eq. (4.5):

$$\phi = h(T_w - T_{ref}), \tag{4.5}$$

where T_w is the wall temperature, T_{ref} is a reference temperature and ϕ is the convective heat flux. As well as the convective heat transfer, the reference temperature is a local variable and is calculated with Newton's cooling law. In the experiment, several fluxes are used and a linear regression has to be performed to find out T_{ref} and h. The convective heat transfer coefficient can then be normalised as the Nusselt number $Nu = hD/\lambda_{air}$. In [128], Fénot *et al.* argue that the reference temperature corresponds to the adiabatic temperature and that the air thermal conductivity λ_{air} should be taken at this temperature when normalising the wall heat transfer coefficient h into the Nusselt number Nu. Experimental uncertainties are evaluated to be lower than 10% for the Nusselt number. Although the numerical set-up directly computes the wall temperature from imposed heat fluxes, the linear regression method is also used in that case. However, only two fluxes are imposed for each of the operating points, which is the minimum value to obtain such a result for a linear regression (see Section 4.2.3 for more details).

4.1.4 Differences of triggering mechanisms between the Pprime test bench and acoustic liners and limitations of the Pprime test bench

Although the similitude principle ensures that the perforated plate and operating points lead to similar fluid dynamics, several differences between the rig and classical liners and limitations of the rig need to be kept in mind. The main difference that has to be pointed out is the choice of piston-driven synthetic jets. In the rig, the jets are generated by hydrodynamics while in a liner they are due to the acoustics. This induces different issues, such as the incompressibility of the rig configuration while fluid dynamics in a liner is compressible. Moreover, the 10 piston rows are driven at the same phase, whatever their position along the flow while for an acoustic liner, the jets are generated with a delay corresponding to the propagation of the acoustic wave. Assuming that this phase difference does not impact the global heat transfer enhancement performance is a strong hypothesis used in the framework of the similitude. Wen *et al.* [129] showed on an in-line twin synthetic jet configuration that hairpins have a completely different behaviour regarding the phase difference between the two jets. However, regarding the orders of magnitude at stake, the distance between two successive perforations should be small when compared to the acoustic wavelentgh, leading to a phase difference close to 0°.

Another issue due to this difference in triggering mechanisms, discussed in more details in Chapter 6, is about the jet velocity $\overline{W}$. In the rig case, the jet velocity is entirely defined by the piston motion amplitude and frequency, whatever the upstream conditions. This is not the case for a liner, for which the acoustic response is determined by the acoustic amplitude and frequency but also by the grazing flow velocity. If not taken into account, this point can lead to discrepancies when comparing

operating points on the rig with cases simulated on the engine scale configuration. Indeed, with the rig, modifying the axial velocity between to different operating conditions only modifies the velocity ratio M of the synthetic jets. With the liner, modifying the axial velocity modifies the velocity ratio, but also the velocity of the jets and therefore their Reynolds number and stroke length. Characterised by different jet parameters than for the rig operating point, the jets would therefore not be equivalent through the similitude.

Due to the use of pistons instead of resonant cavities, different geometries are used for the cavities underneath the perforated plate: a classic SDOF liner is composed of a perforated plate and a Helmholtz resonator network, where each resonator covers several perforations. In the rig case, the Helmholtz resonator network is replaced by isolated, cylindrical cavities that correspond to a single perforation. As discussed in Section 2.1.3, it was shown that the neck of an actuator is crucial in the synthetic jet formation, while the cavity geometry plays a lesser part. These different geometries could lead to some differences in the jet structure between the rig and a liner configuration. Nonetheless, the main parameters that characterise the jets can be chosen to be similar which is supposed to minimise these differences.

The final limitation of the rig is not due to the triggering mechanisms, but to the position of the plate perforations relatively to each other. Indeed, they are perfectly aligned in both axial and spanwise directions. However, the perforations are usually staggered for classical acoustic liners. Since the perforations are close enough to interact with their neighbours, it is assumed that the boundary layer perturbation due to the synthetic jets is different between aligned and staggered configurations. Thus, the results obtained with the Pprime configuration will be valid for aligned perforation configurations only. The results should nevertheless be of great interest, being the first to consider wall heat transfer along a multi-perforated, synthetic jet in cross-flow configuration. Moreover, a parallel could be drawn with the case of continuous jets that are used in film cooling or effusion cooling. These jets have indeed been extensively studied, including for aeronautic applications: for blade cooling, see Bunker [130] and for combustion chamber cooling, see for example Bizzari *et al.* [4]. In particular, the combustion chamber effusion cooling is also based on multiperforated configurations, with jets distributed all over the wall. In that context, the position of the perforations relatively to each other have been analysed and optimised. It has been shown that a staggered configuration provides a much more efficient cooling than aligned configurations (among many others, see the works of Metzger *et al.* [131] and LeBrocq *et al.* [132]). Although the flow dynamics of synthetic jets is quite different from that of continuous jet in the near field, it might be possible to assume that the distribution of the perforations along the wall could have the same impact on the heat transfer for both cases. Thus, studying wall heat transfer in an aligned configuration is still of interest since it could be assumed that a staggered configuration would be even more efficient. In other words, finding out a valuable heat transfer enhancement in the Pprime aligned configuration would imply that the enhancement would be even better in a classical staggered configuration. Finally, the flow dynamics and its impact on the wall heat transfer can be deeply

analysed in the present aligned configuration, before hypothesising its behaviour in a staggered configuration.

To conclude this section, the experimental configuration has been extensively described. The advantages and drawbacks of using Pprime set-up to analyse wall heat transfer within acoustic liners have been discussed, and a special care has been brought to the similitude methodology development and the description of the rig limitations. The numerical set-up that was built upon the test bench can now be described, which is the purpose of the following section. Numerical simulations run to discuss the rig liner-representativity are presented in Chapter 6, where the descriptions of the engine scale configuration and the validation process are provided.

4.2 Numerical set-up

As explained in the previous section, the numerical set-up is based on Pprime experiment. A first overview, alongside an analysis of preliminary results on a specific operating point, was provided in a recent paper [133]. In addition to present the LES code used for our simulations, the objective of this section is to extensively describe the numerical set-up, including the different boundary condition formalisms and the meshing strategy. The list of operating points, which is shorter than for the experiment, is also discussed.

4.2.1 The AVBP code

An insight into the literature showed that different methods can be considered to simulate synthetic jets (*cf.* Section 2.3.3). It was in particular pointed out that the RANS methods are inappropriate to reproduce the complex, unsteady flow features that appear in the presence of such jets. On the contrary, LES as well as DNS provide interesting results. Thus, with its lower cost and its relevant accuracy, the LES method is the one that was selected to perform the simulations in this work.

All the simulations run for this study rely on the use of the AVBP code. This solver, co-developped by CERFACS and IFPEN, solves the three-dimensional compressible Navier-Stokes equations. AVBP is highy scalable and the code can be run on parallel architecture based supercomputers with a high performance. Moreover, it is specifically designed to be used on unstructured and hybrid grids, which makes it an ideal tool to simulate complex geometries. For example, the numerical schemes are based on finite volume methods. The reader who wants a detailed description of the schemes and numerical methods implemented in AVBP is invited to read Lamarque's PhD thesis [134]. The parallel aspect of AVBP in addition to the use of unstructured meshes enable the accurate investigation of complex configurations.

In this study context, the Lax-Wendroff (LW) numerical scheme [135], 2^{nd} order in time and space, is used. The TTGC (Two-step Taylor-Galerkin C) scheme [136],

3^{rd} order in time and space, was considered to enhance the simulation however the numerical cost was considered too expensive, while the LW scheme led to satisfying results that were in agreement with the experimental data. Two different sub-grid-scale models are used for the simulations: the classic Smagorinsky model [137] and the σ model [138]. Contrarily to the Smagorinsky model, the σ model reproduces the behaviour of turbulent viscosity close to walls correctly, which is necessary for wall-resolved simulations as targeted in this study. However, the Smagorinsky model is more dissipative and is thus preferably used to smooth the high gradients that appear during the transitory phase at the initialisation. The Smagorinsky model is therefore used to initialise the different simulations before switching to the σ model.

It should be highlighted that the AVBP code, being compressible and explicit, can lead to significant costs when simulating low Mach number configurations, which is the case for the Pprime rig and its characteristic axial and jet velocities which are in the ordre of 1 $\mathrm{m.s^{-1}}$ to 10 $\mathrm{m.s^{-1}}$. Besides, the physical time which is required for a complete simulation gets higher when the frequency gets lower. On the contrary, the time step is low since we are using a compressible code. Note that the YALES2 code, developped by CORIA (COmplex de Recherche Interprofessionnel en Aérothermie) , was tested in order to decrease these costs: it is uncompressible, which is cheaper and more adequate for low Mach cases. However, this code is particularly sensitive to mesh skewness and the mobile mesh required several refinement and coarsening steps through a single period T of the motion of the pistons, leading to an increase of the computational cost. At the end no significative cost reduction was achieved in comparison with AVBP simulations. For the AVBP simulations, the time step is also impacted by the ALE (Arbitrary Lagrangian-Eulerian) methodology, which is used to reproduce the movement of the piston (see Section 4.2.2.3): it is directly linked to the smallest cell volume, which is evolving with the piston motion. When the pistons are at the top dead centre, the cells are compressed and the smallest cell volume is minimal. Eventually, the physical time that needs to be simulated is large when compared to the time step.

4.2.2 Numerical domain and boundary conditions

The retained numerical domain is fully described in this section alongside a comparison with the experimental set-up. In addition, the boundary conditions are detailed and a focus is given for two of them: the NSCBC(Navier-Stokes Characteristic Boundary Conditions) formalism that is used for the inlet and outlet of the domain, and the ALE formalism that enables to numerically reproduce the piston motion.

4.2.2.1 Numerical Domain

The numerical domain, shown in Fig. 4.3a, represents a part of the wind tunnel test section. In the experiment, the velocity fields are measured starting from the upstream limit of the plate. The upstream part of the test section is therefore not

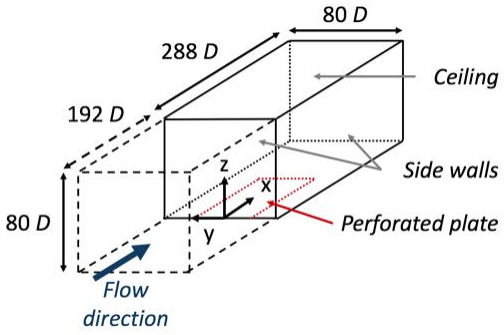

(a) Test section (solid and dashed lines) and numerical domain (solid lines only). D is the perforation diameter.

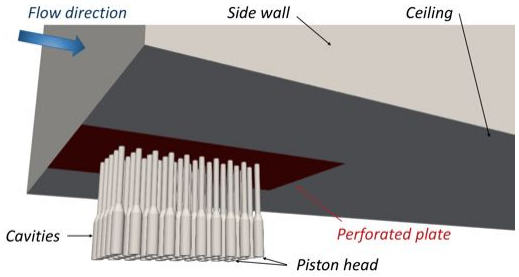

(b) Underview of the numerical domain, focus on the perforated plate and cavities.

Figure 4.3: Numerical domain [133].

simulated: the numerical domain inlet corresponds to the upstream limit of the perforated plate, where the velocity field is known and thus can be imposed as a boundary condition. The coordinate system origin, as shown in Fig. 4.3a, is located at the inlet for the axial direction, on the symmetry plane for the transverse direction and at the lower wall for the vertical direction. This way, the plane $x = 0$ m corresponds to the numerical inlet. The plane $y = 0$ m corresponds to the symmetry plane, which is the plane where the experimental velocity fields are measured. Finally, the plane $z = 0$ m corresponds to the perforated plate.

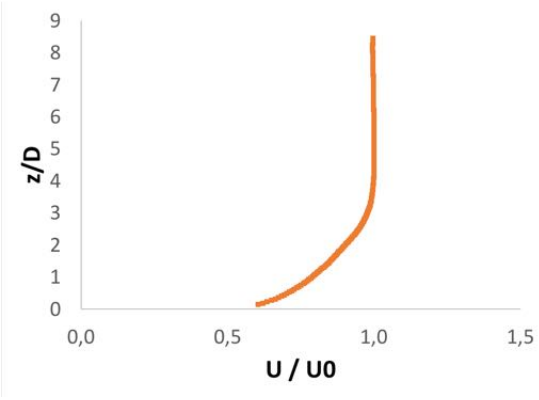

(a) $U_0 = 12.8$ m.s^{-1}

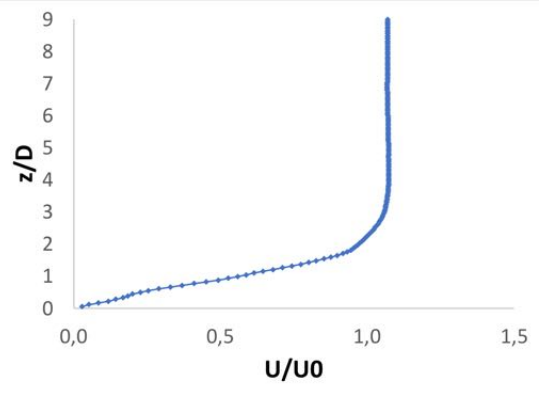

(b) $U_0 = 1.9$ m.s^{-1}

Figure 4.4: Velocity profiles provided by the experimental results for two of the considered U_0 values.

Velocity profiles extracted from the experimental data, shown in Fig. 4.4, are used to impose the velocity at the inlet. This enables to have a similar boundary layer on both the experimental and numerical configurations at the beginning of the perforated plate. It can be noted that the low velcity profile is laminar while the other two profiles correspond to turbulent cases. Only the axial velocity u was imposed as matching the experimental profile, while the spanwise and vertical velocity (respectively v and w) where imposed to 0 m.s^{-1}. Also, the profiles have to

be extended close to the wall. Indeed, the measurement system is limited when too close to walls and the experimental velocity is thus not known in this area (for $Z^* = z/D \lesssim 0.1$) . To bypass this lack of data, the profiles were extended with a polynomial extrapolation while imposing $u = 0$ m.s^{-1} at the wall. The null velocity at the wall is known through theory, but is also a condition that is imposed by the numerics with the use of a non slip wall. Besides, since the flow is not known above the PIV window, the profile is also extended at higher z values as equal to the maximum velocity U_0. Moreover, the experimental velocity inlet profile is known only within the symmetry plane, around the perforated plate. Thus, the shapes of the boundary layers that develop along the ceiling and the side walls are not known. The velocity profile obtained for the symmetry plane is thus used along the whole inlet, even along the side walls. Finally, turbulence can be injected at the inlet. In the experiment, the $U_0 = 1.9$ m.s^{-1} case is laminar, with *rms* levels lower than 4%. The other two cases are turbulent, with *rms* maxima equal to 8.3% and 10.5% at $U_0 = 6.6$ m.s^{-1} and $U_0 = 12.8$ m.s^{-1}, respectively [126]. In order to isolate the turbulence effect on heat transfer, it was chosen to dedicate a specific operating point to study it. Thus, for most of the operating points (see Section 4.2.3), no turbulence is injected at the inlet. The turbulence injection issue is more discussed in Chapter 7 which explains the impact of the main flow turbulence on the synthetic jet dynamics and the associated wall heat transfer. In addition, the inlet flow temperature is imposed at 300 K. The formalism used to handle the inlet is called NSCBC (Navier-Stokes Characteristic Boundary Conditions) [139]. The outlet is also treated with the NSCBC formalism. For this boundary condition, the pressure is imposed at 101 325 Pa. The three-dimensional extension of the traditional LODI (Local One Dimensional Inviscid formulation) method [139] developped by Granet *et al.* [140], using space-averaged values, is used.

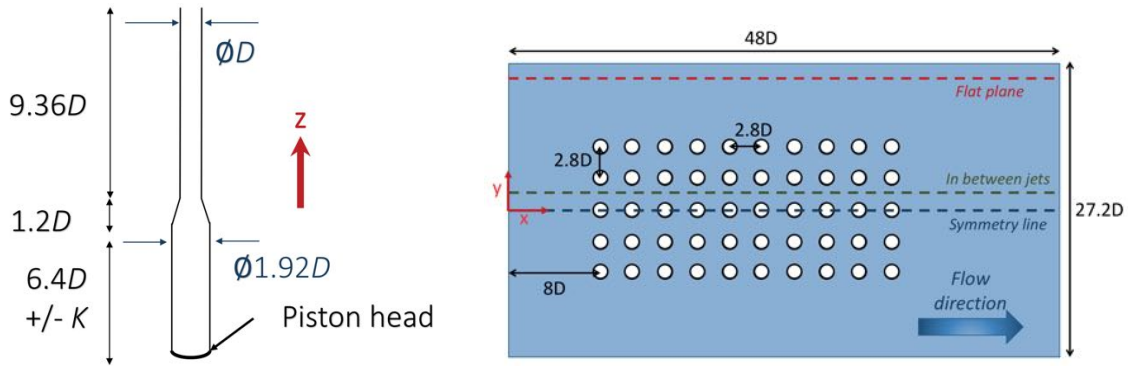

(a) Cavity and piston [133].

(b) Perforated plate.

Figure 4.5: Focus on the plate and pistons. D is the perforation diameter and K the piston motion amplitude. x: positions for the velocity profiles provided in the following chapters.

The other boundaries of the numerical domain (that is to say transverse and longitudinal) correspond to the real test section dimensions. Under the perforated plate, each of the cavity is also represented, as can be seen in Fig. 4.3b. The geometry of a single cavity is more detailed in Fig. 4.5a. The cavity lower wall corresponds

to the piston head. The side walls and the ceiling of the test section are considered to be far enough of the zone of interest (that is to say the perforated plate) to not interact with the flow in the investigated area. Thus, they are treated as slip walls. This also simplifies the velocity injection at inlet: using slip walls makes possible the use of non zero velocity at the considered walls. Moreover, the piston motion has to be reproduced, which is made through the ALE (Arbitrary Lagrangian-Eulerian) formalism, detailed in Section 4.2.2.3. Finally, as discussed in Section 4.5, the perforated plate is heated. Thus, a condition of constant heat flux is applied on the plate. The flux values are further discussed alongside the considered operating points in Section 4.2.3.

4.2.2.2 Meshing strategy

The aim of the present section is to present the mesh adaptation strategy. Three different meshes were used for the study. All of them are composed of tetrahedral cells. The first mesh M1 is user-defined: a refining effort was made by hand, in particular around the plate and cavities. However, it contains only 13 million elements and is quite coarse. On the contrary, M2 (66 million elements) and M3 (58 million elements) were generated with an automatic adaptation method, in order to take into account the flow physics in a more accurate way.

The mesh adaptation strategy is inspired from that used by Odier *et al.* [121], which is based on a double criterion to define the refinement. The idea is to perform a first simulation on a coarse mesh in order to get average fields that contain physical quantities of interest. These quantities are then used to define a metric: a field that can take any positive values. The adaptation process implies that the mesh is coarsened wherever the metric is greater than 1, and refined wherevere it is lower than 1. The refinement is unchanged for a metric equal to 1 and the farther the value is from 1, the more important is the coarsening of refinement.

In the present case, a simulation run with the coarse mesh M1 provided velocity fields averaged over six periods of the piston motion, that enabled the definition of a two-criterion based metric. Since the study aims at understanding synthetic jet flow physics, the metric is mainly based on velocity gradients: the higher the velocity gradient is, the more grid refinement is imposed. This enables to capture as accurately as possible the boundary layer and its deformation due to the presence of the synthetic jets. This part of the metric is close to the criterion proposed by Daviller *et al.* [141], which is based on kinetic energy dissipation. The other criterion is the normalised wall distance Y^+: in order to properly simulate the flow impact on wall heat transfer, the simulation needs to be as resolved as possible along the wall. Thus, the metric is defined so as to target a Y^+ value as close as possible to 1. The adaptation process is also geometry dependent. Indeed, the zone of interest is the area around the perforated plate and the cavities. It is not necessary for the rest of the domain to be as refined as this part. Thus, a zone of interest is applied around the perforated plate, where the metric is defined based on the proposed double criterion (Y^+ and velocity gradients). Outside of this zone, the metric is put at

its maximum value, in order to limit the refinement.

Since the mesh M1 is rather coarse, refinement only is targeted and the metric values are thus below 1. It is chosen to fix the maximum value of the metric to $\varepsilon_{max} = 0.9$. Moreover, a too strong refinement would lead to way too small cells, which should be avoided for numerical reasons, among which the will to maintain a reasonable simulation cost. Thus, a minimal threshold $\varepsilon_{min} = 0.3$ is defined. To conclude, the metric is firstly defined as equal to ε_{max} everywhere in the domain. Then, within a zone of interest embracing the perforated plate, the metric is based on the double criterion: at walls, the condition $Y^+ = 1$ is targeted and, within the flow, the metric is based on velocity gradients. This leads to the definition of the non-dimensional Φ number (Eqs. 4.6 and 4.7), which is then used to define the metric (Eq. (4.9)).

- At walls, if $Y^+ > Y^+_{target}$:

$$\Phi = Y^+_{target}/Y^+_{M1} \tag{4.6}$$

- Within the flow:

$$\Phi = \left[1 - \frac{|\overrightarrow{\nabla}(\|\overrightarrow{U_{M1}}\|)| - |\overrightarrow{\nabla}(\|\overrightarrow{U_{M1}}\|)|_{min}}{|\overrightarrow{\nabla}(\|\overrightarrow{U_{M1}}\|)|_{max} - |\overrightarrow{\nabla}(\|\overrightarrow{U_{M1}}\|)|_{min}}\right]^{\alpha} \tag{4.7}$$

In the first condition, $Y^+_{target} = 1$ since wall-resolved simulations are targeted. In the second condition, the normalized velocity gradient, $|\overrightarrow{\nabla}(\|\overrightarrow{U_{M1}}\|)|$, is defined as:

$$|\overrightarrow{\nabla}(\|\overrightarrow{U_{M1}}\|)| = \|\overrightarrow{grad}(\sqrt{\overline{u^2_{M1}} + \overline{v^2_{M1}} + \overline{w^2_{M1}}})\|, \tag{4.8}$$

where $\bar{}$ stands for a time-averaged operation, $|\overrightarrow{\nabla}(\|\overrightarrow{U_{M1}}\|)|_{min}$ and $|\overrightarrow{\nabla}(\|\overrightarrow{U_{M1}}\|)|_{max}$ are the minimal and maximal values of the $|\overrightarrow{\nabla}(\|\overrightarrow{U_{M1}}\|)|$ field obtained from the simulation on Mesh M1 , respectively; α is used to control the cell dilatation within the mesh [141], a low value will generate less cells while a too high value will increase too much their number within the domain. Here it is equal to 50. Finally, with the two thresholds previously described, $\varepsilon_{min} = 0.3$ and $\varepsilon_{max} = 0.9$, the metric used for grid adaptation is given by:

$$metric = \Phi(\varepsilon_{max} - \varepsilon_{min}) + \varepsilon_{min}. \tag{4.9}$$

Meshes M2 and M3 are generated with the automatic adaptation methodology that was just described. The difference between these two meshes is the operating point on which their refinement metric is based. Indeed, as described in the following Section 4.2.3, different operating points are simulated which imply a wide range

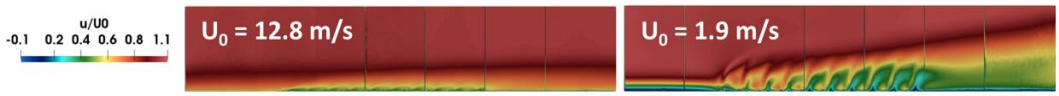

Figure 4.6: Experimental axial velocity fields [126] for the operating points used for automatic mesh adaptation. Up: $U_0 = 12.8$ m.s^{-1} and M=0.16, used for mesh M2; down: $U_0 = 1.9$ m.s^{-1} and M=1.09, used for mesh M3.

of velocity ratio M. The mesh M2 was adapted from the mesh M1 with velocity fields obtained for the reference operating point, which implies a velocity ratio M equal to 0.16. This mesh is therefore fine enough to capture the boundary layer modification that occurs in this specific case. As detailed in the following section, most of the other operating points correspond to a velocity ratio equal to or lower than 0.16. This leads to jets that penetrate lower in the main flow and a less important boundary layer deformation. It is assumed that the mesh M2 mesh is also fine enough for cases which imply a lower boudary layer displacement than that of the reference operating point. However, for one of the operating points, the velocity ratio is equal to 1.09, which is around seven times higher than that of the reference case. This leads to a higher jet penetration into the main flow, and the boundary layer displacement is more important, as can be seen in Fig. 4.6. The mesh M2 corresponds to the $U_0 = 12.8$ m.s^{-1} case in Fig. 4.6, while the high M case corresponds to the $U_0 = 1.9$ m.s^{-1} case. Obviously, a mesh adapted for a low M value will not be fine enough to correctly reproduce the boundary layer displacement for the highest $Z^* = z/D$ values (top of the boundary layer). Thus, a third mesh, M3, is generated specifically for this case. Similarly to the mesh M2, a simulation is firstly run with mesh M1 on the appropriate operating point, and the average velocity and Y^+ fields are used to automatically generate an adapted mesh.

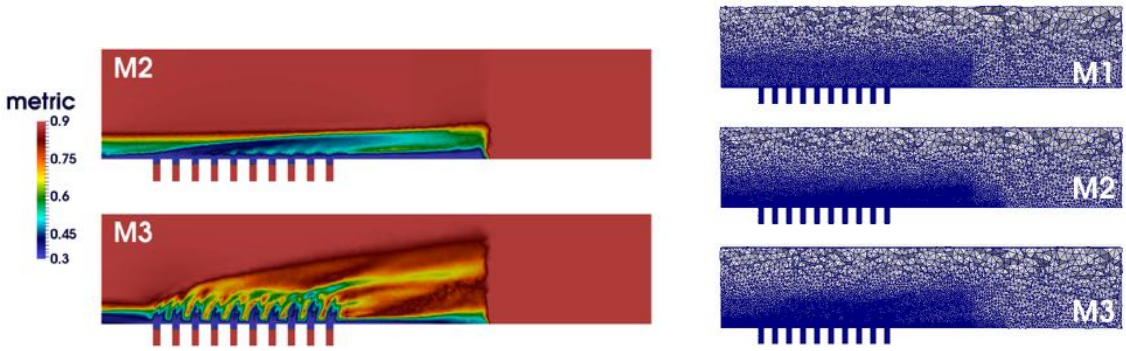

(a) Metrics obtained on M1 to generate M2 and M3. (b) Meshes M1, M2 and M3.

Figure 4.7: Comparison of the three meshes on a cut along the symmetry plane of the domain; focus on the perforated plate zone.

Figure 4.7 provides a comparison of the meshes, with a focus on the two metrics (Fig. 4.7a) and a focus on the symmetry plane around the perforated plate (Fig. 4.7b). The mesh M1, which is user defined, is fine near the plate. However, the two other meshes are way finer and the refinement corresponds to the bound-

ary layer displacement, as can be seen through the axial velocity U_0 (Fig. 4.6) and metric fields (Fig. 4.7a). Thus, the automatic adaptation methodology leads to the generation of meshes that are adequately refined and in accordance with the flow physics, with a refinement that matches the boundary layer evolution. This is also confirmed by the Y^+ fields (shown in Figs. 4.8 and 4.9), which show that the refinement at the wall is adequate. The spatial mean time-averaged Y^+ is equal to 3.7 for M2. The instantaneous spatial mean Y^+ is equal to 3.7 and 3.6 at $t = T/4$ (corresponding to the end of the ejection mid-period) and $t = 3T/4$ (end of the aspiration mid-period), respectively. The spatial mean time-averaged Y^+ in the upper 5 mm of the neck is equal to 3.4. For mesh M3, the wall Y^+ is lower than 5 all over the plate.

In Fig. 4.7, the limits of the geometric zone used in the metric definition is also quite visible, in particular in the axial direction and within the cavities. As a reminder, the adaptation was performed in the specific zone while the metric was fixed to 0.9 in the remaining part of the domain. Above and downstream this zone, the flow does not impact the boundary layer and the wall heat transfer, thus it is not necessary to use a costly mesh. Within the cavities, a user-defined refinement effort had already been performed and it was estimated that no major refinement was necessary in this area. For both meshes M2 and M3, there are approximately 40 cells in the diameter of a hole which is considered to be adequate in such a configuration.

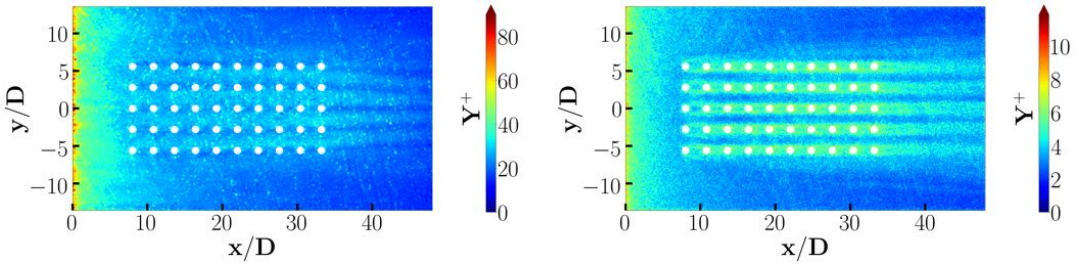

Figure 4.8: Comparison of time-averaged wall Y^+ fields on the perforated plate, for meshes M1 and M2; fields averaged over five periods

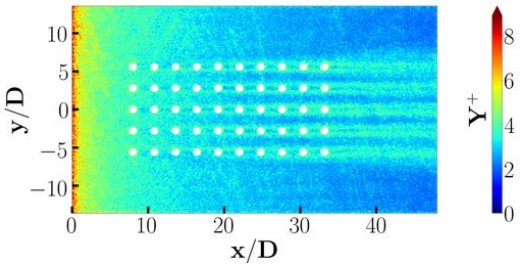

Figure 4.9: Time-averaged (over five periods) wall Y^+ field on the perforated plate, mesh M3.

4.2.2.3 Mouvement of the pistons

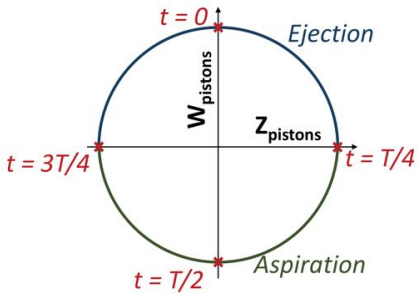

Figure 4.10: Piston motion along a period T [133].

In the context of our numerical study, the piston motion is assumed to be perfectly sinusoidal, following the law presented in Eq. (4.10):

$$Z_{pistons}(t) = Z_{mean} + Ksin(2\pi ft), \qquad (4.10)$$

where $Z_{pistons}(t)$ is the instantaneous piston position, Z_{mean} is the medium course piston position and K is the piston motion amplitude. The cycle of the piston motion is illustrated in Fig. 4.10. Note that the amplitude K as defined here corresponds to half of the peak-to-peak amplitude $2K$ given in the experimental operating points. The values were presented so as to remain consistent with the data provided by Giachetti *et al.* [126] when describing their configuration. However, for the remaining part of this manuscript, all reference to the amplitude corresponds to K as defined in Eq. (4.10).

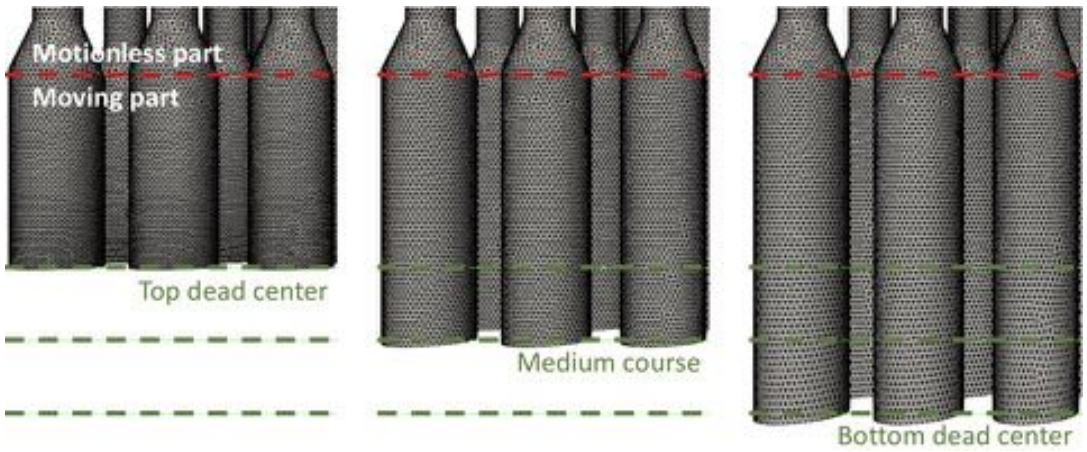

Figure 4.11: Different piston positions and associated mesh deformation. The red line separates the moving and the motionless parts of the mesh.

The movement of the pistons is numerically reproduced thanks to the ALE (Arbitrary Lagrangian-Eulerian) formalism. This method was proposed by Hirt *et al.* [142]; a more recent description, with equations proposed for finite volumes as well as for finite element schemes, was given by Moureau *et al.* [143]. The idea is to attribute a displacement velocity to each mesh node. The mesh is divided into two parts: a static part and a moving part. The static part corresponds to the wind tunnel test section and the upper part of the cavities, where no wall movement needs to be represented. On the contrary, the cavity lower part and the pistons are moved. A grid velocity is imposed to the mesh nodes, which are set in motion. Since the cavity walls are treated as non slip walls, this velocity is also imposed to the flow at the walls. The initial position of the mesh corresponds to the medium course position for the pistons. During a cycle, the mesh cells are successively compressed and

stretched: the position of a node only evolves along the vertical direction, the axial and transverse components of its coordinates remaining unchanged. This evolution along a cycle can be seen in Fig. 4.11, which shows the cavity mesh deformation at different piston positions. The top dead centre is the highest piston position and corresponds to the highest compression. On the contrary, the bottom dead centre is the lowest piston position and the cell expansion is maximum. Finally, the medium course is also the initial position of the pistons ($t = 0$ in Fig. 4.10). In order to avoid an abrupt transition between the static and moving parts of the mesh, a quadratic law was defined so as to have a null node velocity on the transition zone (seen as the red line in Fig. 4.11) and a maximal movement on the piston walls. Thus, the maximal stretching is obtained for the lowest cells, near the pistons, while the highest cells near the fixed part of the mesh are hardly modified. The position z_{node} of a node at the instant t_1 is defined from its position at the previous instant t_0 as follows:

$$z_{node}(t_1) = z_{node}(t_0) + (t_1 - t_0) * 2\pi f K cos(2\pi f t - 1) \frac{(z_{max} - z_{node}(t_0))^2}{(z_{max} - z_{pistons}(t_0))^2}, \quad (4.11)$$

where $z_{max} = -0.066$ m corresponds to the upper limit of the mesh moving part.

4.2.3 Operating points

The experiment provided data for a large amount of operating cases, exploring the impact of different parameters over a wide range (*cf.* Tab. 4.2). However, the simulation of all of the experimental operating points is not necessary since the objective is not to find out the correlations already provided by Giachetti *et al* [126] but to provide a complementary analysis of the flow, mainly by simulating the parts of the flow that could not be experimentally observed. In particular, the main flow structures and their impact on the heated plate is numerically investigated, which was not possible with the experimental set-up since the velocity fields were visible in the symmetry plane only. Besides, simulating all of these operating points would be way too costly. Indeed, the frequencies used in the experimental context are really low. For the sake of a proper averaging, the fields need to be acquired on several periods of the piston motion, which increases the cost of the simulations. Thus, only a small number of operating points are selected to be simulated.

A first operating point was chosen as a "reference case". It was used for the preliminary validations and analysis of the numerical set-up, as presented in a recent paper [133]. It corresponds to the highest grazing flow velocity ($U_0 = 12.8$ m.s^{-1}), piston amplitude ($K = 11$ mm) and frequency ($f = 12.8$ Hz). Then, other operating points were selected by changing a single flow parameter, other things being equal. In particular, a case with a lower piston amplitude ($K = 2.35$ mm) and another one with a lower grazing flow velocity ($U_0 = 1.9$ m.s^{-1}) were considered. Contrarily to the experimental set-up, no operating point with a different frequency was considered. Indeed, jet velocity $\overline{W}$ is an important parameter impacting the wall heat transfer, which depends on both f and K. However, Giachetti *et al.* [126]

showed that there is no difference on the impact on wall heat transfer if it is the piston frequency f or amplitude K that is used to modify the jet velocity $\overline{W}$. Since the simulation cost is rising with the frequency decrease, it was chosen to modify the jet velocity only through the amplitude, which does not bring any additional computational cost.

In addition to the reference, low K and low U_0 cases, three other specific operating points were simulated. The first one is dedicated to study the impact of the grazing flow turbulence on the wall heat transfer. Indeed, for the reference case, the grazing flow is turbulent with rms values up to 10.5%. However, as discussed in Section 4.2.2.1, it was chosen as a first step not to simulate the turbulence and to secondly dedicate a specific operating point to the investigation of the turbulence impact of wall heat transfer. For fhe fifth operating point, the grazing flow velocity is equal to that of the reference case while the pistons are at rest. Thus, there is no jet in this case. Finally, for the sixth operating point, the synthetic jets are replaced by continuous jets. The ALE formalism is not used, and the walls remain still. The lower walls within the cavities, corresponding to the piston heads, are replaced by inlets. A constant velocity is imposed, calculated to obtain a jet Reynolds number at the perforations equal to the reference case synthetic jet Reynolds number (Re =829.2).

Case name	U_0 (m.s^{-1})	f (Hz)	K (mm)	Re	L_0/D	M ($\times 10^{-2}$)
Reference	12.8	12.8	11	829.2	12.94	16.17
Low M (Low K)	12.8	12.8	2.35	176.4	2.75	3.44
High M (Low U_0)	1.9	12.8	11	829.3	12.94	108.95
Turbulent	12.8	12.8	11	829.2	12.94	16.17
No jet	12.8	0	0	0	0	0
Continuous jet	12.8	-	-	829.2	-	16.17

Table 4.3: Overview table of the numerical operating points. Main flow parameters (left) and corresponding dimensionless parameters (right).

Finally, the methodology used to calculate the heat transfer coefficient (described in Section 4.1.3) requires to run, for each of those operating points, at least two distinct simulations with different wall heat fluxes. As a reminder, the perforated plate is heated in order to study wall heat transfer, and Newton's cooling law is used to estimate the heat transfer coefficient h. To do so, each of the six operating points are run with heat fluxes equal to 500 W.m^{-2} and 1500 W.m^{-2}, which leads to a total of 12 simulations to be run.

The different cases are synthesised in Tab. 4.3. Similarly to Tab. 4.2, which summarises the experimental cases, this table presents the flow parameters (U_0, f, K) alongside the dimensionless parameters characterising the synthetic jets (Re, L_0/D, M). In order to compare the results to those of the literature, the operating points were confronted with the parameter maps that were presented in Section 2.2.3. However, most of the studied cases are out of range when compared to the parameter maps. For example, the maps proposed by Jabbal and Zhong [81] cannot really be

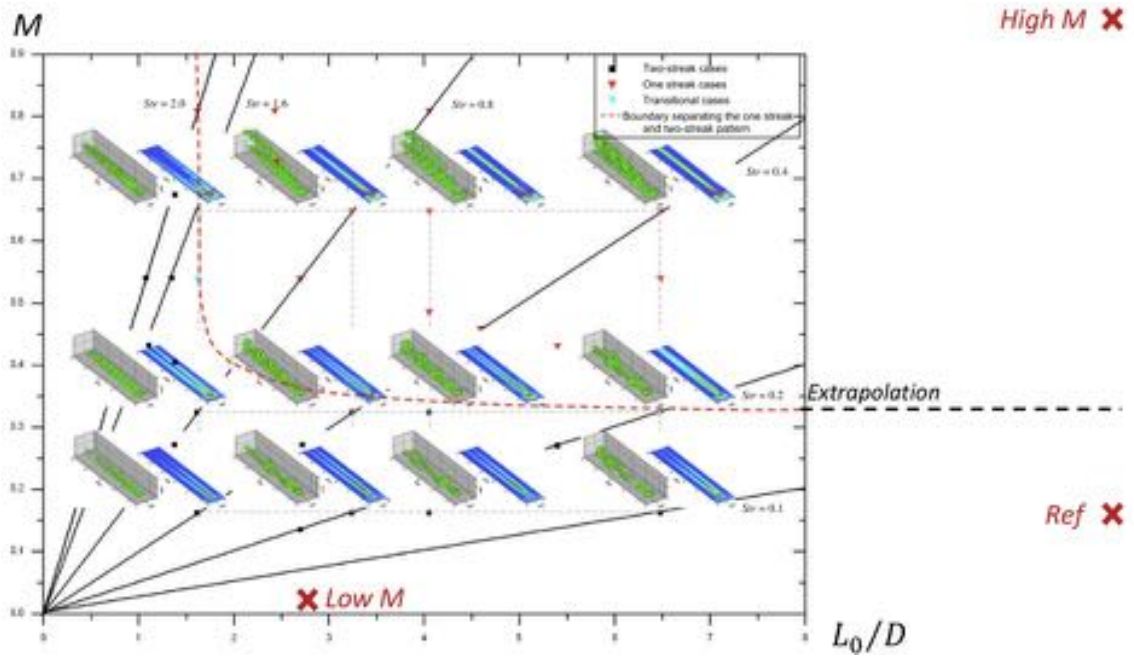

Figure 4.12: Operating points confronted to the parameter map of Zhou and Zhong, adapted from [95].

exploited in the current study. On the contrary, the parameter map proposed by Sau and Mahesh [96] enables to predict the flow main structures and their impact on the heated plate, at least for the "low amplitude" case. For the other cases, it is possible to extrapolate what could be observed, the operating conditions being not that far of the considered dimensionless stroke lentgh and velocity ratio ranges. According to the parameter map, and with some extrapolation for the outside points, it should be expected for all cases to observe the formation of hairpin structures. Indeed, in all cases the velocity ratio M is lower than 2 and Sau and Mahesh showed that, in this condition, the formation of such structures is observed instead of that of complete vortex rings. Relying on the parameter map poposed by Zhou and Zhong [95] and presented in Fig. 4.12, the same conclusion can be made for the "reference" and the "low amplitude" cases: instead of complete vortex rings, the flow conditions should lead to the formation of hairpin structures. However, for the "low velocity" case, extrapolation based on this map suggests that complete vortex rings should be observed. Finally, the data of Zhou and Zhong also provide information on the flow impact along the plate: the two-streak pattern is expected to be observed on the "reference" and "low amplitude" cases while the one-streak pattern should be seen for the "low velocity" case. It should nonetheless be noted that these patterns are observed for a one-jet configuration: in the current study, the structures generated by the jets are impacted by the downstream jets and thus the wall heat transfer patterns observed in Zhou and Zhong cases may not be found here.

Machine	M1 - still	M1 - mobile	M2 - still	M2 - mobile
Turing	11 000	18 000	-	605 000
Occigen	-	-	53 000	94 000
Jean Zay	-	-	-	57 000

Table 4.4: Estimation of the simulation costs (hCPU) for the simulation of a period of the piston motion for the reference operation point (f=12.8 Hz), on meshes M1 and M2, with and without motion of the pistons, for three different machines.

The different frequencies of the pistons and grazing flow velocities, the use of a moving mesh and the mesh refinement imply different simulation costs for a piston motion period or the flow convection through the numerical domain. Estimations of these costs are provided in Tabs. 4.4 and 4.5.

Case name	Machine	mesh	piston period
Reference	Occigen	M2	94,000
Low M	Jean Zay	M2	58,000
High M	Jean Zay	M3	50,000
No jet	Occigen	M2	35,000
JICF	Occigen	M2	49,000

Table 4.5: Estimations of the simulation costs (hCPU) for the different operating points on adapted meshes M2 and M3. The piston period is the same for all of the operating points, including the no jet and JICF cases.

Chapter conclusions

This chapter was dedicated to the description of the studied configuration and the numerical strategies. The Pprime test rig, which is used for this numerical study, has many interests in the present context. Indeed, although some limitations can be pointed out, the simulation on which it is based makes it representative of an acoustic liner. Moreover, it is to the author's knowledge the first configuration to consider synthetic-jet-induced wall heat transfer in a context including both multi-perforation and cross-flow.

It was chosen to perform LES, which have been shown to be a privileged CFD tool to consider synthetic jets. Indeed, RANS was shown to provide inaccurate results while DNS remains much too expensive. The presence of moving pistons in the configuration imposed the choice of a moving strategy: the ALE method. Finally, in order to enhance numerical results, a mesh adaptation methodology was used and led to meshes adequately refined to better reproduce the flow behaviour. The combination of simulation choices (LES, refined moving mesh) and of the experience-based operating points (very low frequency) leads to high simulation costs.

The reference case was chosen to run the preliminary simulations that were used to validate the numerical set-up and provide an initial insight on the

flow and wall heat transfer behaviour. These initial analyses are presented in Chapter 5. The following part (Parts III) focuses on the database analysis, with further analysis of the flow behaviour and its impact on wall heat transfer, and a comparison of the different operating cases which provides the importance of the different flow parameters in heat transfer enhancement.

5

Reference case simulation: validation of the numerical set-up and flow analysis

This chapter details results and analysis on the reference case. It is also used for a proper comparison between numerical results and experimental data in order to validate the numerical set-up.

5.1 General description of the flow

Before providing a detailed analysis of the flow, it is of interest to describe its main features. Figure 5.1 provides instantaneous views of the axial velocity in the symmetry plane and the wall shear stress along the perforated plate for the simulation using mesh M2. Four instants are provided, corresponding to the four specific points evidenced in Fig. 4.10. For all moments, the wall shear stress decreases from the inlet to the first row of holes due to an increase of the boundary layer thickness. Then, the piston motion induces two different phases: the ejection (for instant $t \in [-T/4; T/4]$, $-T/4$ being equivalent to $3T/4$) and the aspiration mid-periods (for $t \in [T/4; 3T/4]$). The flow behaviour in the perforation region is significantly different between these two mid-periods. During the ejection phase, the jets interact with the incoming boundary layer leading to the creation of unstable shear layers. The boundary layer is thus destabilised with the formation of different coherent structures and turbulence increases. These structures are then convected by the flow, as seen in Fig. 5.1 on the symmetry plane at $t = 0$ and $t = T/4$. Their impact on the plate can be noticed through their footprint on the wall shear stress. In particular, horseshoe vortices are clearly identifiable around the first row of holes, at $t = 0$. On the contrary, during the suction mid-period, the boundary layer is sucked by the jets which stabilises it. Between the holes, one can observe the development of an undisturbed boundary layer until the end of the plate. Within the hole wakes, the boundary layer is clearly seen to be sucked by each perforation. A

new boundary layer then starts to develop after each hole, leading to a local increase of the shear stress. These phenomena are visible at $t = T/2$ and even more clearly at $t = 3T/4$ in Fig. 5.1.

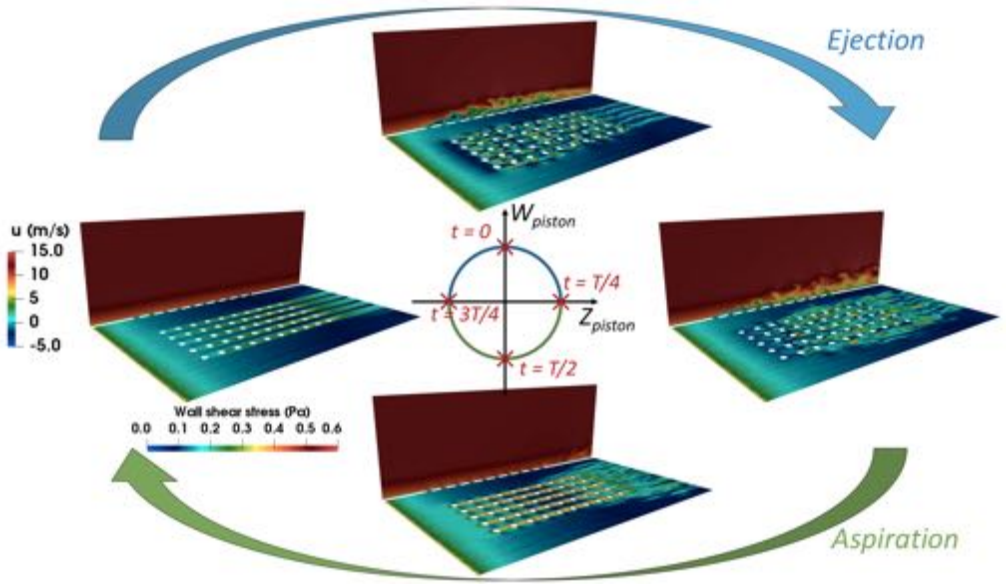

Figure 5.1: Instantaneous axial velocity field in the symmetry plane with wall shear stress along the perforated plate at different times distributed along a period T, mesh M2.

Looking at coherent structures thanks to the Q criterion (Fig. 5.2), horseshoe vortices can be seen along the first row of cavities at $t = 0$. Their presence is due to a blockage effect, linked to the presence of the jets: the incoming grazing flow gets blocked by the jets, and thus circumvents them, creating structures that seem to be counter-rotating vortex pairs (CRVP in Fig. 5.2a). These structures are charateristic of jets in cross-flow [144, 145]. Downstream the jets, several rows of bigger structures can be spotted on top of the others, corresponding to vortices generated around the first rows of jets before $t = 0$ and then convected. These structures, called hairpins, are mainly created by the unstable shear layer at the jet interface with the main grazing flow. They are similar to the hairpin vortices showed by Wen and Tang [97], Zhong *et al.* [92] or Sau and Mahesh [96] on different operating points. In section 4.2.3, the considered operating points were confronted to different parameter maps provided in the literature. The map proposed by Jabbal and Zhong [81] is exceedingly hard to exploit since the operating points of the present study are way too far from theirs. On the contrary, the parameter map given by Sau and Mahesh [96] implies that it is not completely unexpected to observe hairpins in the present context, although some extrapolation of their data has to be assumed. Downstream, the flow seems more turbulent and with a mixing of different smaller structures. This turbulent zone is the result of the destabilisation and interaction between the upstream structures and the jets. The first row of jets is the first to be impacted by the incoming boundary layer: the following jets are impacted by a flow that is already more turbulent. All these different structures are convected by the main stream, as can be seen through the comparison of the Q criterion at $t = 0$

(Fig. 5.2a) and $t = T/4$ (Fig. 5.2b). It can also be noticed that the structures are at first concentrated within the hole wakes, the space between the perforations being free of any structures, at least until the third row of holes (Fig. 5.2a). Then, at the end of the ejection period (Fig. 5.2b), the mixing of the flow has been enhanced by all the structures that are not any more aligned in the axial direction and spread laterally on the whole plate.

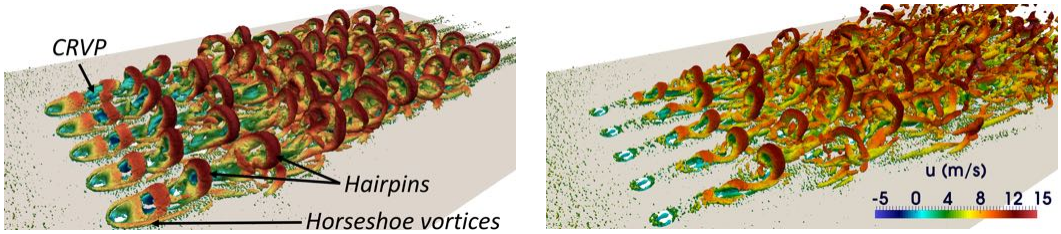

(a) $t = 0$ (b) $t = \frac{T}{4}$

Figure 5.2: Q criterion colored by the axial velocity ($m.s^{-1}$), during the ejection mid-period. Simulation run on mesh M2 [133].

As seen in Fig. 5.3, the flow behaviour is not as resolved with mesh M1 than with mesh M2. Indeed, M2 is more refined within the boundary layer, targeting a wall-resolved simulation. Moreover, the σ model is used for the simulation with M2, in place of the Smagorinsky model with M1, leading to better flow predictions. Velocity gradients are sharper with M2 and the axial velocity field contains more flow structures with M2 than with M1. During the ejection mid-period, some of these structures impact the plate temperature T_w fields that show significant differences from one mesh to the other.

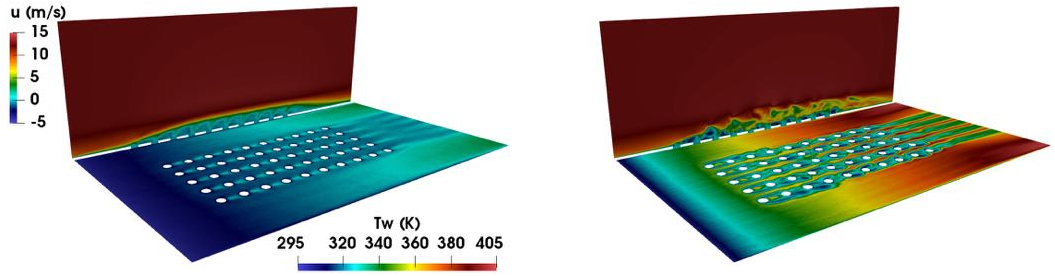

(a) Mesh M1 (b) Mesh M2

Figure 5.3: Meshes M1 and M2, axial velocity on the symmetry plane and plate temperature instantaneous fields, $t = 0$ [133].

5.2 Comparison between numerical results and experimental data

The numerical results are compared to the experimental data. A good agreement is found for the velocity fields. The heat transfer coefficient field is also close to the experimental data, with some discrepancies that can be explained. The aim of this section is to validate the numerical set-up and not to analyse the flow: the following section is dedicated to this analysis.

5.2.1 Flow velocities

Velocity fields are compared to the available experimental data on the symmetry plane of the domain in Fig. 5.4. To do so, only time-averaged fields are considered, the numerical results being averaged over five periods of the pistons motion. Convergence has been checked by comparing 3-, 4- and 5-period averaging. As shown in Fig. 5.5, an excellent convergence is reached. The experimental uncertainty is estimated at 4% for the mean velocities, and at 8% for the root mean square (rms) values [126]. Figures 5.4a to 5.4d present the mean axial, mean vertical, rms axial and rms vertical fields, respectively. The corresponding dimensionless velocity profiles are shown in Figs. 5.4e to 5.4h. The six profiles are taken at the following positions presented in Fig. 4.5b: the beginning of the plate ($x/D = 0$), the centre of the first row of holes ($x/D = 8$), the centre of the fourth row of holes ($x/D = 16.4$), the centre of the seventh row of holes ($x/D = 28.4$), the centre of the tenth (and last) row of holes ($x/D = 33.2$) and finally dowstream the perforated plate ($x/D = 40$).

The time-averaged velocity fields show that the boundary layer thickens faster than a boundary layer on a flat plate. The first jet modifies the flow behaviour within the boundary layer, leading to a progressive thickening of the boundary layer which is maintained and reinforced by the successive jets. This behaviour of the boundary layer is also visible with the velocity profiles. These velocity fields also show that the simulation with M1 reproduces the good orders of magnitude, especially far from the plate, but tends to overestimate the boundary layer displacement, as well as the jet penetration heights within the main flow. The simulation with M2 produces much better results if compared to the experimental data. This is confirmed by the velocity profiles: M1 overestimates velocities within the boundary layer, while M2 reproduces the flow behaviour quite well. Vertical velocity profiles are not as well predicted as the axial velocity profiles. A second level of refinement or a higher order numerical scheme would probably help to better capture the profiles. Nonetheless this is out of the scope of this study for which the results are satisfactory. Moreover, further investigation presented in Chapter 7 showed that the upstream turbulence influences the jet development: by simulating velocity fluctuations which are more representative of the experimental conditions the numerical jet velocities are closer to that of the experimental data.

Looking at rms fields and profiles, some differences are observed between the ex-

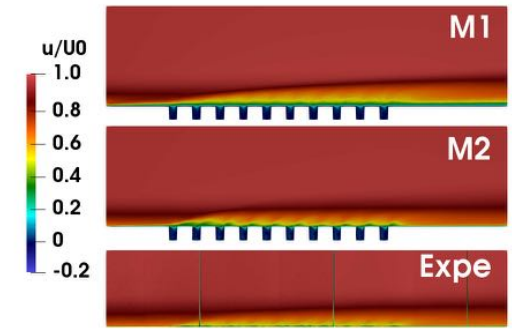

(a) Mean axial velocity

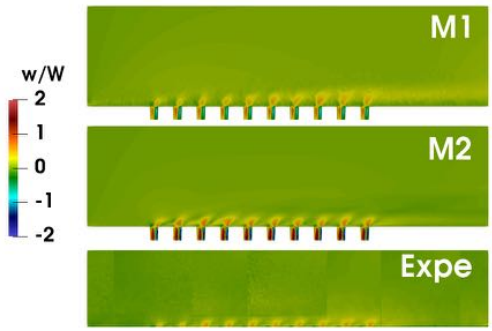

(b) Mean vertical velocity

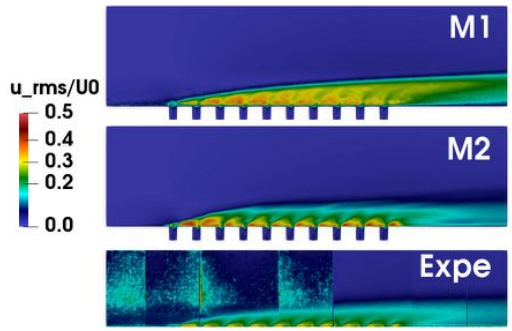

(c) *rms* of axial velocity

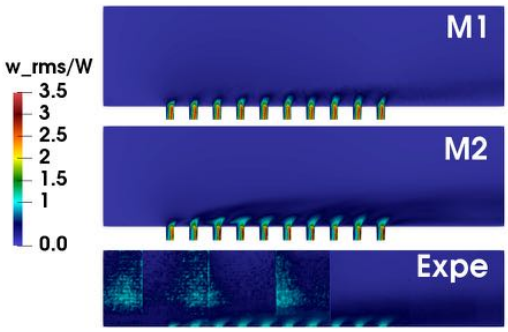

(d) *rms* of vertical velocity

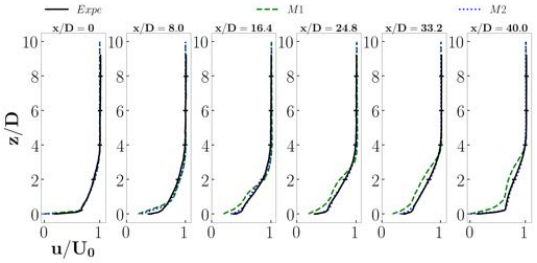

(e) Mean axial velocity profiles

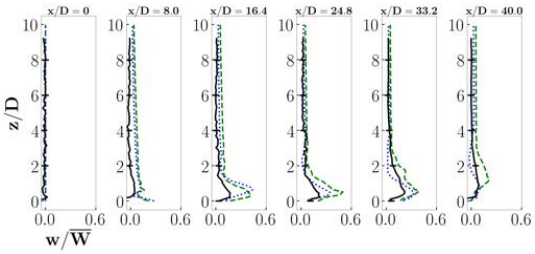

(f) Mean vertical velocity profiles

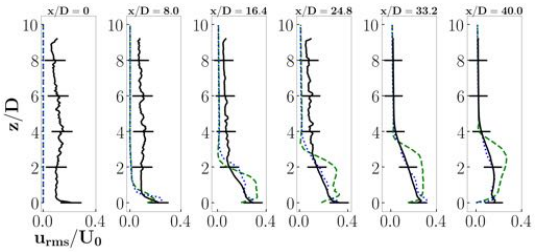

(g) *rms* of axial velocity profiles

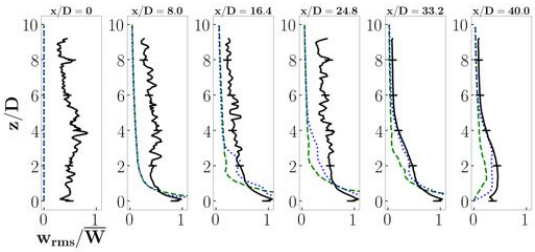

(h) *rms* of vertical velocity profiles

Figure 5.4: Comparison of numerical results on M1, M2 and experimental data for the velocity fields along the symmetry plane. Fields averaged over several periods of the piston motion [133].

perimental data and the numerical results. It should be reminded that no turbulence is injected at the inlet of the simulations, which is different from the experimental case. The measurement techniques can also explain some of the observed differences. Indeed, fluctuations are observed for the upstream part of the experimental data that come to a certain extent from the lack of seeding particles far from the

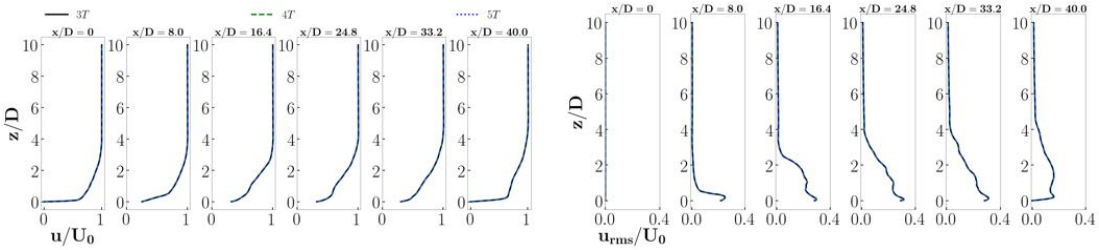

(a) Mean axial velocity (m.s^{-1}) along symmetry plane

(b) *rms* axial velocity (m.s^{-1}) along symmetry plane

Figure 5.5: Comparison of velocity profiles for results averaged over 3, 4 and 5 periods of the piston motion.

plate. Differences between the experimental data and the numerical results very close to the plate can also partly be explained by the measurement technique, that is also restricted when too close to walls.

5.2.2 Heat transfer coefficient

A comparison between experimental data and numerical results is provided in Fig. 5.6. More precisely, Fig. 5.6a compares the heat transfer coefficient h field over the whole perforated plate while Figs 5.6b and 5.6c illustrate the h profile along the jet axis and inbetween the jets, respectively. On these two latter figures, the position of the perforation is indicated with the grey, dotted, vertical lines. At first sight the conclusion is that the good orders of magnitude are retrieved by simulations with mesh M2, although differences are also observed.

Three main zones can be defined: the perforated zone, the upstream part and the downstream part of the plate. Concerning the upstream part, the numerical results obtained with mesh M1 clearly do not correspond to that of the experimental data. Mesh M2 enables to get much closer to the experimental reference. However, the thermal boundary layer obtained with the simulation on mesh M2 remains a little different from that of the experimental data. This could be due to the mesh, since the Y^+ values, although very low, remain higher than 1, but also to the numerical scheme. Then, for the perforated and downstream zones, two axis need to be distinguished: the jet axis, which corresponds to the plate symmetry axis, and the in-between-jet axis. For both of them, mesh M2 enables to have enhanced results when compared to that obtained with mesh M1. However, significant differences can be observed.

Along the jet axis, as shown in Fig. 5.6b, M2 numerical results are very close to the experimental data. A small gap is observed between numerical results and experimental data for the two first perforations, but this gap is then reduced and results coincide pretty well for the remaining perforations and the downstream zone.

On the contrary, the results for the in-between-jet axis illustrate significant dif-

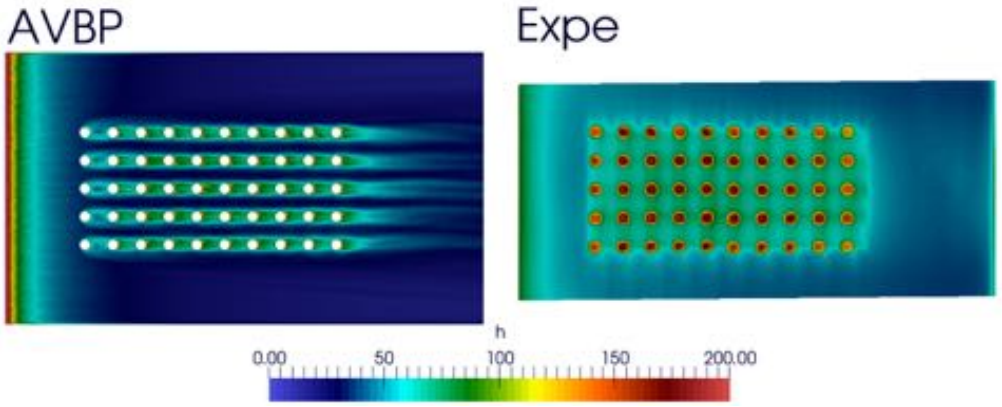

(a) Mean wall convective heat transfer coefficient h ($\mathrm{W.m^{-2}.K^{-1}}$) field along the perforated plate.

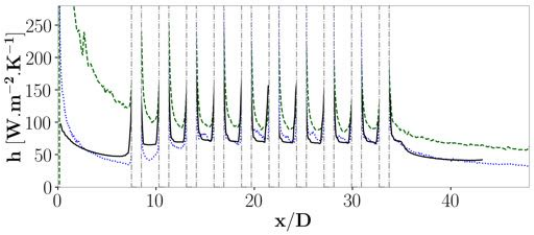

(b) Mean wall convective heat transfer coefficient h ($\mathrm{W.m^{-2}.K^{-1}}$) profile along the jet axis (symmetry line) [133].

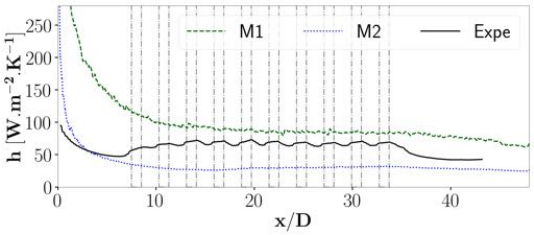

(c) Mean wall convective heat transfer coefficient h ($\mathrm{W.m^{-2}.K^{-1}}$) profile inbetween the jets.

Figure 5.6: Comparison of numerical results on M1, M2 and experimental data for the heat transfer fields. Fields averaged over several periods of the pistons motion.

ferences. These differences are of two kinds. The first one is the "wavy" aspect of the h profile over the perforated plate which is observed on experimental results only, while the numerical profiles are "flat". The wavy aspect of the experimental data can also be observed in Fig. 5.6a. It is attributed to the experimental set-up: the heating of the plate, used to determine h, was not completely homogeneous. On the contrary, the numerical set-up is based on a perfectly homogeneous heat flux at wall. Thus, the numerical results cannot reproduce the wavy aspect, which in itself does not impact the study conclusion. However, appart from the wavy aspect which is not numerically reproduced, the numerical results are far from the numerical data mean value along the perforated area and this gap remains of importance dowstream the perforations. Although the wavy aspect difference is understood, it is expected that the mean values should be closer, especially downstream the perforations. This specific point was more deeply investigated and underlined the importance of correctly taking into account the upstream turbulence, as detailed in Chapter 7.

Despite known limitations from the experiment and the simulations, the comparisons of numerical simulation results and experimental data provides some quite good confidence in the results given by the simulation on M2. In particular, the flow behaviour within the boundary layer is well reproduced. Using this simulation, the

next section investigates the flow development in the presence of the synthetic jets as well as its impact on wall heat transfer.

5.3 Analysis of the flow development

This section is dedicated to the flow analysis, based on the reference case that was used for the numerical set-up validation in the previous section. The section is organised as follows. The flow within the ducts beneath the cavities, which drives the synthetic jet formation, is first investigated. Comparison with results of the literature are proposed. Then, the main flow structures that are produced by the synthetic jets are observed. Different view angles are used. The impact of the jets on the boundary layer development is analysed. A comparison with an equivalent flat plane enables to comprehend how the jets drive the flow behaviour. Finally, the resulting wall temperatures and heat transfer are presented.

5.3.1 Flow within the ducts

As mentionned above, the lab scale geometry differs from a classic liner. Indeed, long ducts connect the perforations to the pistons. These ducts have the same diameter as the perforations along a long height, before a small increase. This is far from the small neck above a resonant cavity that is usually found on liners and can therefore modify the formation and evolution of flow structures (see Section 2.1.3). In this section, the flow evolution is analysed within the cavities and compared to literature results. To do so, three cuts at different heigths (z/D = -0.16, -1.6 and -8) along the ducts, illustrated in Fig. 5.7, are considered. Along these cuts, different flow parameters are averaged: the vertical velocity $\overline{W_t}$, the pressure $\overline{P_t}$ and the temperature $\overline{T_t}$. Their time evolution over five periods of the piston motion is provided in Fig. 5.8.

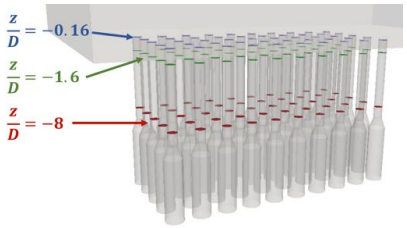

Figure 5.7: Positions of the cuts used for Figs. 5.8 and 5.9.

First of all, the velocity is found similar in each of the cuts and the variations of pressure between each of the cuts is particularly small. It has to be kept in mind that the velocities in the lab scale configuration are rather low. The jet average velocity $\overline{W}$ corresponds to a Mach number around 6.10^{-3}, thus the flow can be considered quasi incompressible. On the contrary, a temperature gradient is observed along the ducts. Near the plate, two peaks of high temperature can be observed over one period of the piston motion. This is directly due to the flow dynamics.

During the aspiration, the hot boundary layer is sucked within the cavities. This leads to the thinning of the boundary layer, and cold flow is brought close to the wall. During the second part of the aspiration mid-period, the hot flow has been sucked by the upstream cavity which leaves only cold flow to get sucked in. This corresponds to the first temperature peak. The second temperature peak is due to the beginning of the ejection mid-period, during which the hot air that had been previously sucked is now ejected from the cavities. Since there is not enough hot flow to fill the cavities, once it has been expelled there is only cold flow left in the cavities and the temperature decreases. This behaviour is different for the first cavity, for which there is no upstream cavity to suck the hot air. The hot boundary layer is thus sucked during the whole aspiration phase, which leads to more hot air within the cavity and during the ejection the temperature remains higher than for the other cavities. The thermal behaviour around the second cavity is partly similar with that of downstream cavities, with the double temperature peak, and also with that of the first cavity. Finally, although the velocity and pressure are steady, the temperature seems to drift towards higher temperatures. This is especially true for the deepest cut ($z/D = -8$), which is the further from the heated plate. It seems likely that over a longer time the temperatures reach a steady mean value, as suggested by the almost-steady temperature at $z/D = -0.16$. However it is unclear whether it would keep drifting. Note nonetheless that a longer simulation cost would not be affordable on this configuration. Still, results close to the plate are relevant for the present study since it focuses on wall heat transfer.

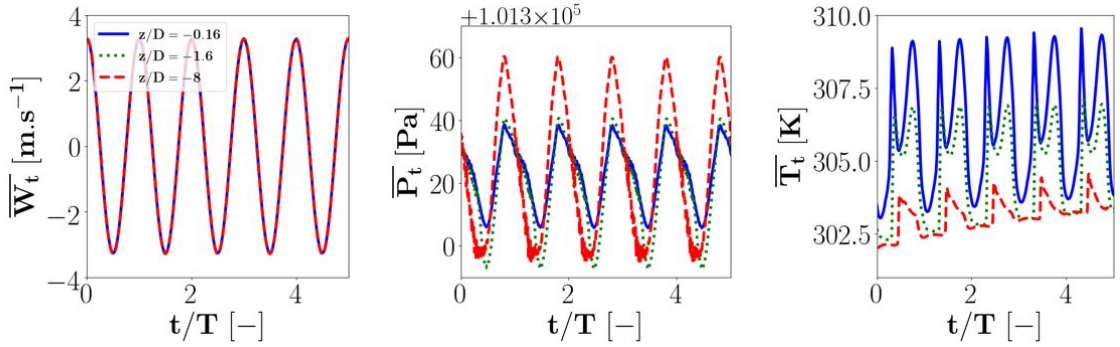

(a) Jet (vertical) velocity (b) Pressure (c) Temperature

Figure 5.8: Time evolution of flow parameters within the cavities, averaged on vertical sections over the 50 ducts.

The phase difference observed between the signals of velocity (Fig. 5.8a) and pressure (Fig. 5.8b) in the necks is linked to the jet formation physics. When the pistons move up, they modify the pressure within the cavities and thus the flow velocity. A phase diagram providing the pressure evolution as a function of the jet velocity is provided in Fig. 5.9. Here again, results are compared for the three different z/D cuts. The time evolution is also indicated for the $z/D = -1.6$ profile, with the specifications of the four piston motion specific instants detailed previously: the top dead centre ($t = T/4$), bottom dead centre ($t = 3T/4$), rising medium course ($t = 0$) and descending medium point ($t = T/2$). As seen in Fig. 5.8, the velocity

time evolution is similar for the three cuts and the pressure time evolution is almost identical. This leads to three similar phase diagrams, with a pressure amplitude a bit more important for the $z/D = -8$ cut. If the flow were totally incompressible, the diagram phase would look like a single line since no change in pressure would be seen. However it is not completely the case which explains the ovoid shape of the diagram. The wavy aspect of the diagrams, from $t = 0$ to $t = T/2$, is not seen with the coarse mesh M1 and it is not sure whether it is due to the mesh, a numerical artefact or a physical phenomenon.

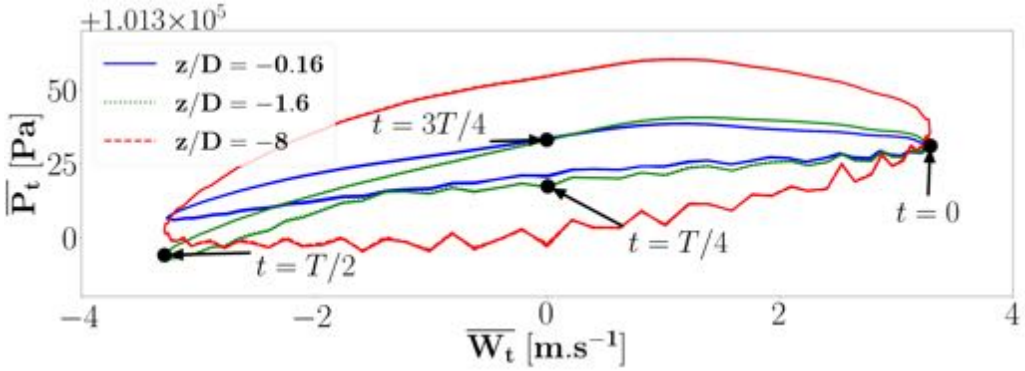

Figure 5.9: Phase diagram of the surface-averaged pressure as a function of the surface-averaged jet vertical velocity at different positions within the cavities. Lab scale.

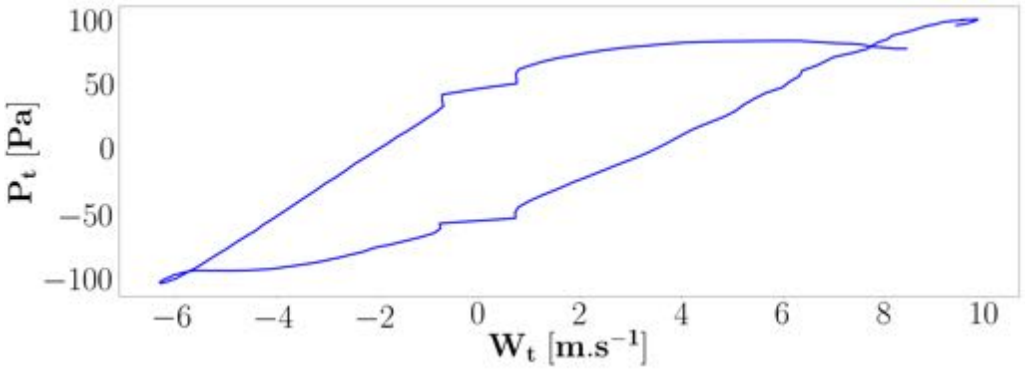

Figure 5.10: Phase diagrams of the cavity pressure (relative to the ambient pressure) as a function of the neck velocity for one operating point based on the experimental results of Persoons *et al.* [108].

Persoons *et al.* proposed [107, 109] to then validate experimentally and numerically [108] a model describing the neck velocity as a function of the cavity pressure. Although the considered operating points are not exactly identical, it is of interest to compare the results of the present study to this model. Note that in their cases, the pressure considered is that of the cavity while in the present study the pressure is considered at the neck. Moreover, they consider the varying pressure (relatively to the ambient pressure), also refered to as acoustic pressure in the present study. A phase diagram was established based on the experimental results obtained on one

of the cases (refered to as case A in their study) they studied in their experimental validation [108]. The phase diagram adapted from these results is presented in Fig. 5.10. Although the pressure and velocity amplitudes are different, due to the different operating conditions, a similar pattern is retrieved, with a rising pressure that globally leads to a rising velocity, and a decreasing velocity that globally leads to a decreasing velocity. In their case, the actuator is a membrane that oscillates, so its boundaries are fixed and the membrane centre has the maximum movement amplitude. For this set-up, they indicate that the relations obtained between the cavity pressure and the neck velocity is unaffected by the type of driver, whether it is a piston, an electromagnetic loudspeaker or a piezoelectric bending element, which is in accordance with the similar trends observed for their results with an oscillating membranes and the present study based on piston-driven jets. Similar phase diagrams are drawn for the engine scale configuration in Section 6.2.1 in order to find out whether the same trends can be observed for an acoustic liner.

5.3.2 Main flow structures

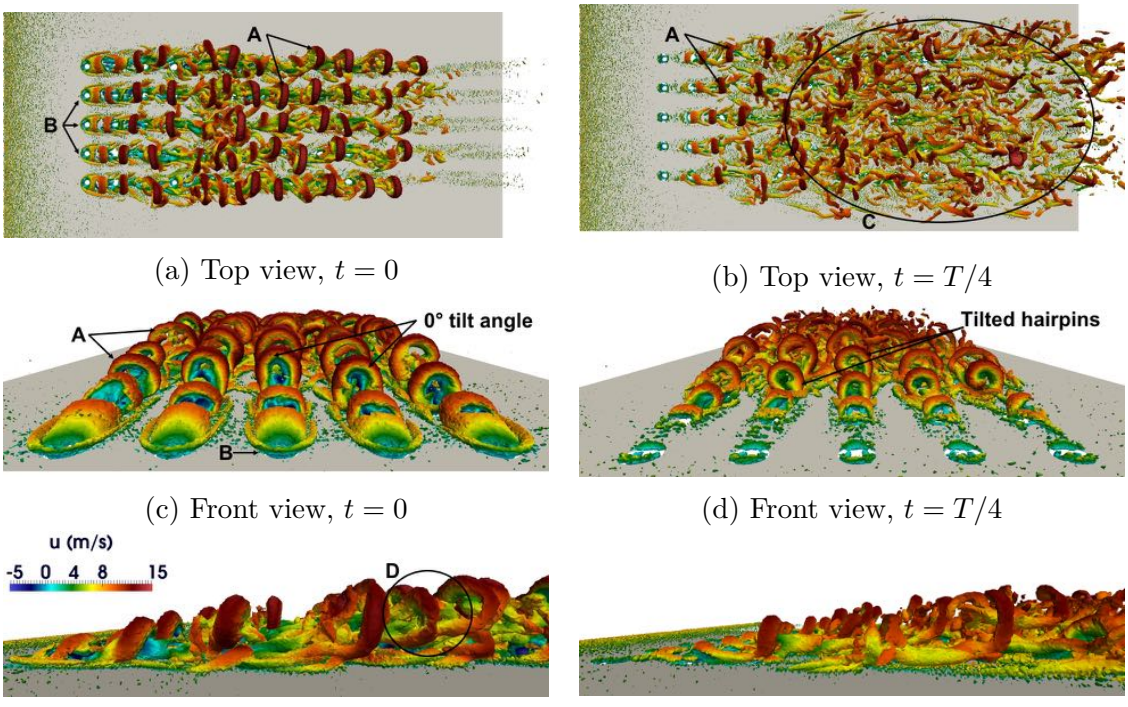

(a) Top view, $t = 0$

(b) Top view, $t = T/4$

(c) Front view, $t = 0$

(d) Front view, $t = T/4$

(e) Side view, $t = 0$

(f) Side view, $t = T/4$

Figure 5.11: Instantaneous Q criterion isosurfaces (10^6 s^{-2}) along the plate.

A first overview of the main flow structures (horseshoe vortices, counter-rotating vortex pairs and hairpins) colored by the axial velocity u was presented in Fig. 5.2. In order to analyse more deeply the flow development, different views of the Q criterion isosurface are presented in Fig. 5.11: top, front and side views, at $t = 0$ and $t = T/4$ (respectively: middle and end of the ejection mid-period). As a comparative element, dye images obtained by Wen *et al.* [129] on a twin inline synthetic

jet are considered. In their experiment, they observed the impact of the phase difference $\Delta\phi$ between the jets on vortex formation. Figure 5.12 shows the results obtained for $\Delta\phi = 0°$, which corresponds to this study. In their configuration, jets are separated by a distance d/D equal to 2, the jet Reynolds number is $Re = 5.3$, the dimensionless stroke length is $L_0/D = 1.7$ and the velocity ratio is $M = 0.15$ while in our simulation these values are $d/D = 2.8$, $Re = 829$, $L_0/D = 12.94$ and $M = 0.16$. Although hairpins are expected to be observed in both configurations, their formation should logically be different. There, the hairpins remain coherent even far from the actuator however they do not encounter donwstream jets that contribute to break them. The hairpins are also seen to partially interact, the legs of the dowstream vortex rolling around the head of the upstream hairpin.

In the simulation, the hairpins are clearly visible on the top views (A in Figs. 5.11a and 5.11b), their head appearing in red as well as the blockage effect and the resulting horseshoes upstream of the first perforations (B in Fig. 5.11a). The hairpins lose coherence during their convection, as seen at $t = T/4$ in Fig. 5.11b (zone C) when they interact with the downstream jets. The structures also expand on the transverse axis as shown at $T/4$, when nearly all of the plate is impacted by the vortices while at $t = 0$ the vortices remain aligned in the jet axis.

The front view at $t = 0$ (Fig. 5.11c) shows the blockage effect and the resulting horseshoe vortices (B). As in the corresponding top view, the hairpins appear aligned in the jet axis. Their tilt angle is close to 0°. At $t = T/4$ (Fig. 5.11d), it is still close to 0° for the middle line jets at least alongside the first rows of perforations. On the contrary a small tilt angle is visible for the side line jets. There is no clear pattern whether the hairpins are more bent on one side or the other.

Finally, on the side views (Figs. 5.11e and 5.11f), the partial interaction of the downstream hairpin legs with the upstream hairpin head can be observed (D in Fig. 5.11e). It is however not so obvious and the hairpins seem to remain separated.

A more detailed comparison with the flow topology observed by Wen *et al.* [129] (Fig. 5.12) is provided in Fig. 5.13, where the Q criterion isosurfaces at $t = 0$ colored by the streamwise vorticity. Only the Q criterion of the jet symmetry line is shown here to simplify the visualisation, and the figure is focused on the first two perforations, for which coherent flow structures are easier to identify. The hairpins can clearly be visualised, especially in the general view in Fig. 5.13a, as well as the horseshoe vortex upstream the first perforation in the top view in Fig. 5.13b. The top view enables the identification of more structures. First of all, secondary and tertiary vortices are generated on both sides of the perforation line. The first tertiary vortices that are observed are expelled from the horseshoe vortex. It is not clear whether there are other horseshoe vortices for the following jets, which would be the source of the downstream tertiary vortices. Then, the structure that was previously identified as a CRVP in Fig. 5.2 in Section 5.1 appears to be "hairpin-like" shaped. It might be a combination of both structures. Since it appears above the second perforation, it could be a CRVP generated by the first jet, that would

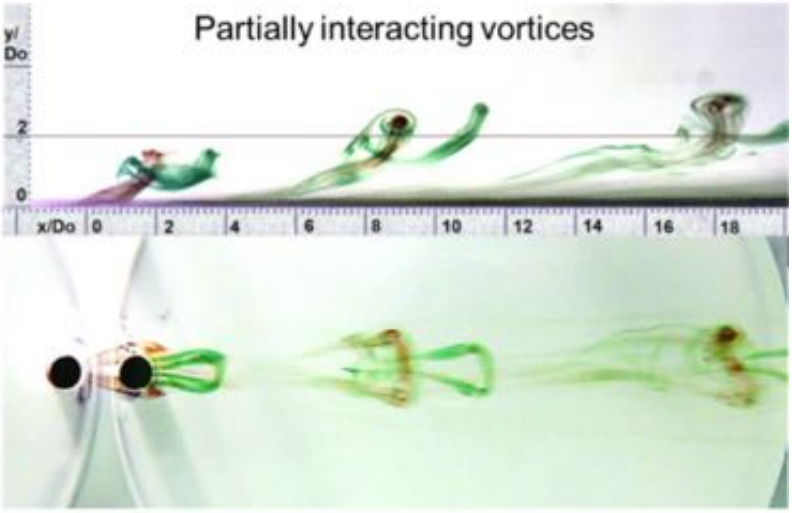

Figure 5.12: Stereoscopic dye images of in-line twin synthetic jets, observed by Wen *et al.* [129]. $\Delta\phi = 0°$

evolve into a hairpin as it meets the downstream jet or is entrained by the legs of the downstream hairpin. Finally, above the first perforation, there is a big CRVP-like structure which convection and deformation through time leads to hairpin shedding.

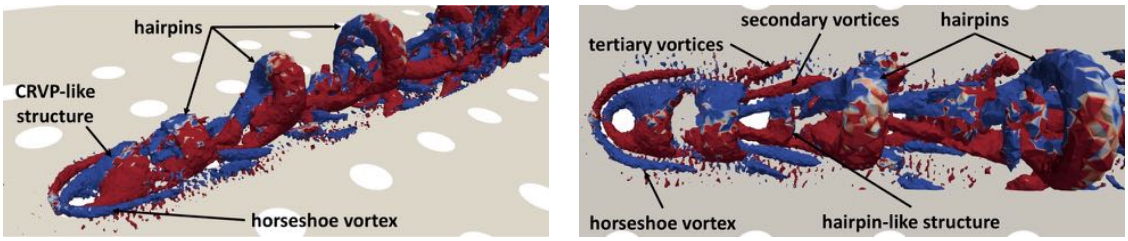

(a) General view (b) Top view

Figure 5.13: Instantaneous Q criterion isosurfaces (10^6 s^{-2}) along the plate, colored by the streamwise vorticity (colors volontary saturated, blue=negative and red = positive), focused around the first, symetry line perforations.

5.3.3 Boundary layer development along the perforated plate

As pointed out previously, an undisturbed boundary layer develops from the inlet to the first row of holes, while the flow around the perforations presents two distinct behaviours that depend on the considered mid-period. Figure 5.14 compares these evolutions, at $t = T/4$ and $t = 3T/4$, by looking at the axial velocity profiles at different positions along the plate. The profiles are taken at the same axial positions x/D as for the comparisons of averaged fields in Fig. 5.4. Moreover, the flow evolution being different in the jet axis and inbetween them, the profiles are also taken for an "in-between jet" axis, corresponding to $y/D = 2.8$. Figure 5.14 also compares the wall shear stress over two different lines (the symmetry line and inbetween the

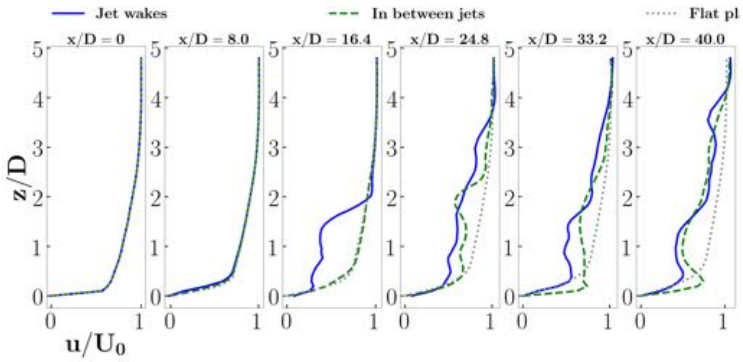

(a) Mean axial velocity profiles, $t = \frac{T}{4}$

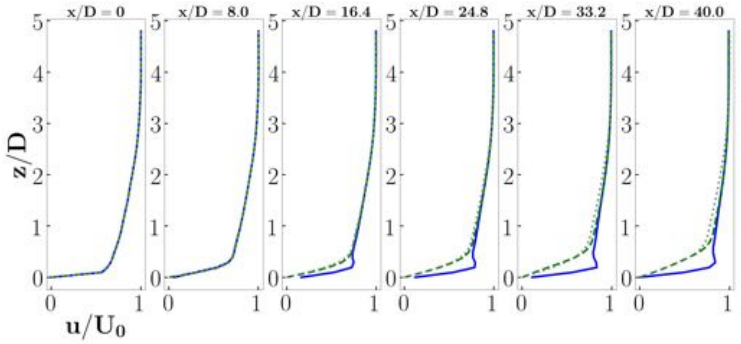

(b) Mean axial velocity profiles, $t = \frac{3T}{4}$

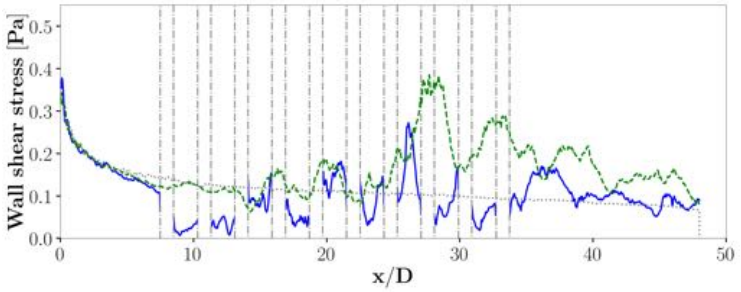

(c) Wall shear stress, $t = \frac{T}{4}$

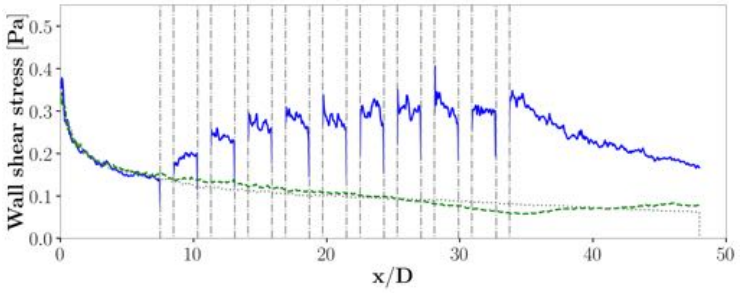

(d) Wall shear stress, $t = \frac{3T}{4}$

Figure 5.14: Instantaneous axial velocity profiles and wall shear stress along the perforated plate, at different times distributed along a period T. Simulation run on mesh M2.

holes) on the plate and corresponds to the same instants. Note that the grey dashed vertical lines correspond to the limits of the perforations where the wall shear stress

cannot be computed. In Fig. 5.14, the profiles corresponding to $y/D = 12.8$ are also added as a reference: they are taken far enough of the perforations to assume that the synthetic jets barely impact the flow. Thus, they are used to illustrate the evolution of the velocity profile imposed at inlet over a classical flat plane.

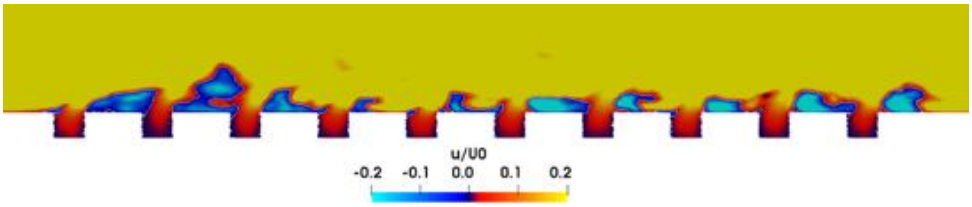

Figure 5.15: Recirculation zones near the perforations, in the symmetry plane at $t = 0$. The white line corresponds to the isoline $u/U_0 = 0$ m.s^{-1}. Colours are volontarily saturated, in order to better identify the recirculation zones.

During the ejection mid-period, the jets induce the presence of unstable shear layers that lead to the creation of vortices such as the structures previously described and turbulence generation. The velocity profiles at $t = T/4$ (Fig. 5.14a) show some perturbations illustrating the trace of the jets, close to the walls, and the chaotic behaviour of the flow, with perturbations that reach a higher point in the boundary layer along the plate. Meanwhile, the wall shear stress presents important fluctuations all along the plate (Fig. 5.14c), due to the flow structures. Looking back at the wall shear stress field along the plate in Fig. 5.1, it can be seen that the whole perforated area of the plate is impacted by the flow structures. The wall shear stress appears to be quite higher inbetween the holes than in the hole wakes. This difference can be explained by two aspects. First, the impact of hairpins on the plate is characterised by two stripes of high wall shear stress, on both sides of the jet wake (see discussion on Section 2.2.3, more specifically Fig. 2.5 and the results of Jabbal and Zhong [81]). Secondly, the very low values of wall shear stress downstream the first and second perforations suggest the presence of a boundary layer separation that would lead to low velocity recirculation zones in the jet wakes. The presence of such recirculation zones is confirmed by the u/U_0 field at $t = 0$ (middle of the ejection mid-period, piston top dead centre) in Fig. 5.15. There, colours are volontarily saturated to better see the boundary layer separation and the isoline $u/U_0 = 0$ m.s^{-1} identifies the recirculation zones. It appears that boundary layer separation happens not only dowsntream of the first and second perforations, but also downstream all of the perforations. Another recirculation zone is also visible right upstream the first jet, due to the blockage effect. Additionnal observations on the recirculation zones due to boundary layer separation downstream the perforations can be pointed out when considering the u/U_0 field evolution over the whole ejection mid-period (not shown here): although they are similar at the beginning of their formation, the evolution of the first and second recirculation zones are different than that of the downstream zones. The recirculation zones downstream the first and second perforations expand higher than the following ones, and present velocities close to zero. On the contrary, the other recirculation zones are folded close to the wall and

the absolute velocities are higher. The presence of these recirculation zones explains why the wall shear stress is lower in the jet axis than inbetween the jets at $t = T/4$, especially downstream the first and second perforations.

The boundary layer remains undisturbed on the entire plate during an important part of the suction phase, as can be seen on the axial velocity profiles at $t = 3T/4$ in Fig. 5.14b. Indeed, the profiles inbetween the hole lines are characteristic of the development of a boundary layer on a flat plate: its thickening leads to a decrease of the wall shear stress from the inlet to the outlet. Within the hole wakes, the profiles are different: the flow is sucked within the cavities and the boundary layer restarts at the end of each perforation. The wall shear stress globally increases but, despite the important fluctuations, a small decreasing tendency can be spotted between two following holes, in accordance with the idea that the boundary layer restarts after a hole. Finally, after the tenth row of perforations, the wall shear stress within the hole wakes starts decreasing again, corresponding to a freely developping boundary layer.

5.3.4 Resulting plate wall temperatures and heat transfer

In the previous section, different flow parameters were studied to better understand the development of the boundary layer and the impact of the synthetic jets on the perforated plate. The wall heat transfer can now be considered, in regard to the previous results on flow dynamics. Figure 5.16 gives the wall temperature along the plate at the different instants previously described, for a 1500 W.m^{-2} wall heat flux. For a better understanding, a focus around three perforations of the first line, at $t = 0$, is provided in Fig. 5.17. Two elements, coherent with the previous results, can first be pointed out:

- the temperature field from the inlet to the first row of holes corresponds to a developping thermal boundary layer;
- the ejection and suction phases present distinct behaviours.

In order to better apprehend the development of the thermal boundary layer along the perforated plate, instantaneous temperature profiles along the plate are provided in Fig. 5.18 at $t = T/4$ (end of ejection mid-period), $t = 3T/4$ (end of aspiration mid-period), along with the equivalent time-averaged profiles. As for the flow dynamics boundary layer, these profiles are provided for the jet axis and between the jets, and compared to profiles obtained far from the perforations, standing for the equivalent flat plate. The main observations are similar to that obtained with the flow dynamics analysis:

- during both mid-periods, the temperature profiles in the jet axis are different to those of the flat plate. In particular, the thermal boundary layer in the jet axis is much thinner than that of the equivalent flat plate. This leads, for the time-averaged profiles, to a thinner boundary layer.
- On the contrary, the behaviour of the thermal boundary layer between the jets depends on the considered mid-period. During the ejection mid-period, it is

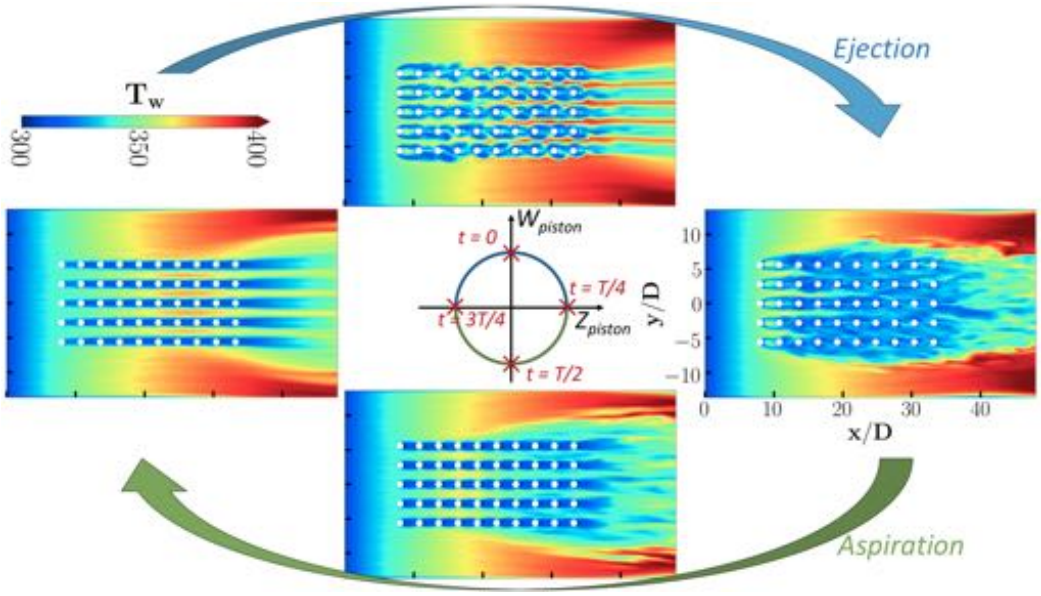

Figure 5.16: Instantaneous plate temperature field along the perforated plate at different times distributed along a period T. Simulation run on mesh M2.

thinner than the equivalent flat plate. Although it is in general thicker than in the jet axis, its behaviour is closer to that oberved in the jet axis than that of the equivalent flat plate. In particular, downstream of the perforated zone ($x/D = 0.25$), the behaviours in the jet axis and between the jet are almost equivalent. During the aspiration mid-period, the thermal boundary layer between the jets thickens almost until it corresponds to that of the equivalent flat plate. In the time-averaged profiles, the thermal boundary layer between the jets is thus thicker than in the jet axis, but thinner than that of the equivalent flat plate.

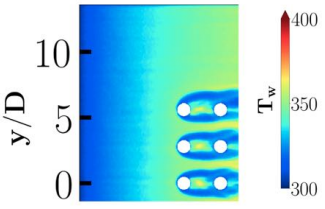

Figure 5.17: Plate temperature field at $t = 0$. Focus around the first perforation lines.

During the ejection mid-period, the impact of the different structures that have been identified can be observed on the temperature field. The blockage effect is particularly visible at $t = 0$ in Fig. 5.17: the horse-shoe vortices can be detected around the first line of holes and the circumvention of the jets appears clearly in the temperature field. Through the ejection mid-period, apart from the cold stripes that are the footprints of the horseshoe vortices and hairpin legs, the temperature right downstream of the first row of perforations rises. This local rise is attributed to the boundary layer separations and the resulting low-velocity recirculation zones that were observed in section 5.3.3. Along the plate, the vortices bring the cold incoming flow nearer to the hot plate, leading to a higher thermal gradient and a thinner thermal boundary layer. The alignment of the structures with the flow direction and the perforation arrangement, followed by their mixing along the plate during the ejection mid-phase and the increase of turbulence, that have been noticed with the study of the Q cri-

terion (Fig. 5.2) is also retrieved here, when comparing the temperature fields at $t = 0$ and $t = T/4$. Comparing the wall temperature field within the perforated area of the plate with unperforated regions on the lateral sides, it can be stated that the vortices generated during the ejection mid-period contribute to efficiently cool down the plate. The temperature within the perforated area is indeed lower at the end of the mid-period compared to the side regions.

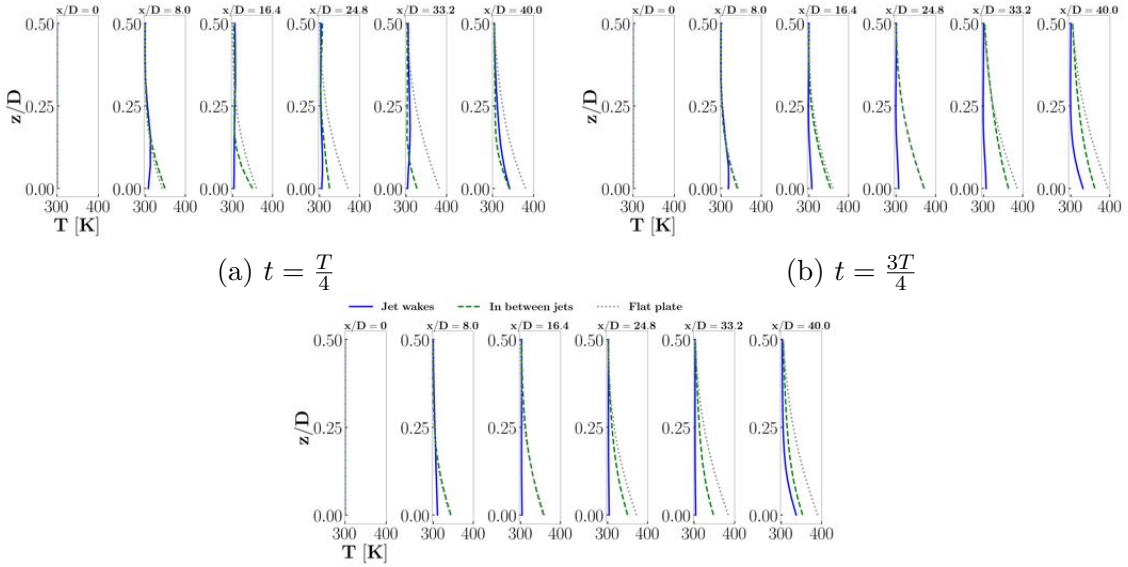

(a) $t = \frac{T}{4}$ (b) $t = \frac{3T}{4}$

(c) time-averaged

Figure 5.18: Instantaneous and time-averaged temperature profiles along the perforated plate in the jet axis, between the jets, and far from the plate.

In a similar way, the temperature evolution during the suction period can be understood through the previous observations of the boundary layer development. The hole wakes present a significantly lower wall temperature than the rest of the plate; the axis between the holes present a rising temperature once the impact of the vortices has been convected by the main flow. Coming back to the axial velocity profiles at $t = 3T/4$ (Fig. 5.14b) and corresponding wall shear stress (Fig. 5.14d), the boundary layer development explains the phenomenon. Within the hole wakes, the flow gets sucked by the jets within the holes and the boundary layer becomes thinner, starting again at the end of each hole. The wall shear stress increases. This contributes to a thin thermal boundary layer within the hole wakes, and thus colder temperatures. In addition, the heated boundary layer, which is sucked into the cavities, is replaced by cold air after each perforation. On the contrary, between the hole lines, the flow is not disturbed by the aspiration, leading to a developing boundary layer from the inlet to the outlet. The thermal boundary layer develops in a similar way, thickening along the plate and leading to higher wall temperatures.

To further analyse these different evolutions, Fig. 5.19 shows the different values that can be taken by the temperature through several periods of the piston motion, for the reference case on the lab scale configuration, along these three axes: the jet

axis (Fig. 5.19a), between the jets (Fig. 5.19b) and far from the jets (Fig. 5.19c). In addition, the time-averaged values are provided for the whole period ("global mean"), the ejection mid-period ("ejection mean") and the aspiration mid-period ("suction mean"). PDF values are obtained by recording, for each position x/D, all of the temperature values that can be reached over time. The sampling chosen here is 40 savings per period T. The enveloppes are finally colored by the PDF for the symmetry plane (Fig. 5.19a and between the jets (Fig. 5.19b): the darker the color, the higher the probability to reach this temperature value.

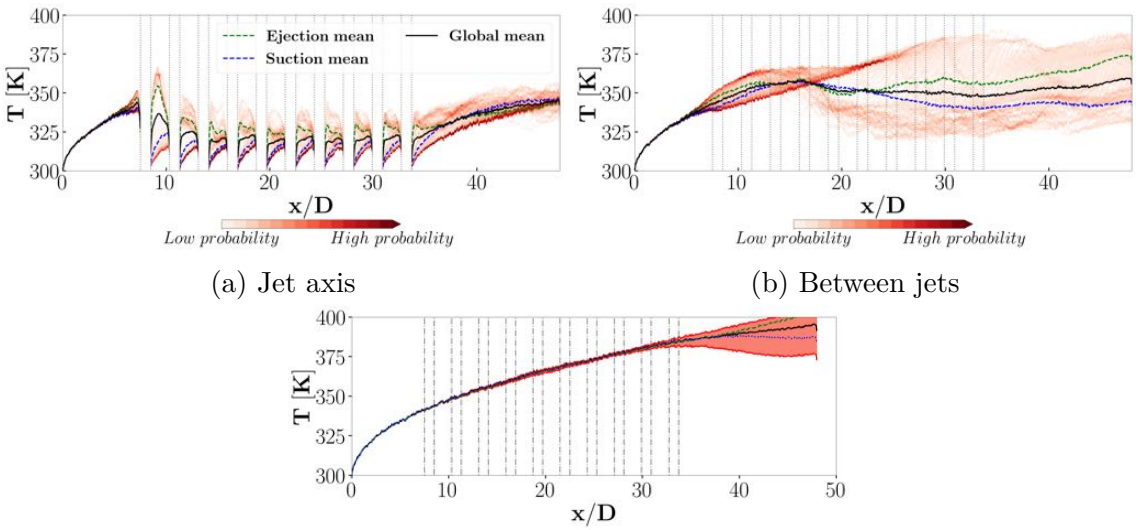

(a) Jet axis

(b) Between jets

(c) Flat plate

Figure 5.19: Temperature possible values over time. Lab scale, reference case, no upstream turbulence, $\Phi = 1500$ W.m^{-2}.

The flat plate case (Fig. 5.19c) is characterised by a very narrow range of possible temperature values upstream and along the perforated zone. This is coherent with the steady development of a thermal boundary layer along a flat plate. Downstream the perforations, this range starts to broaden, showing that the synthetic jets can impact this part of the plate due to their spanwise expansion. There, the hypothesis that this axis is far enough of the perforations to be considered as a classical flat plate is less justified. Nevertheless, the results are acceptable in the perforated zone which is the zone of interest, and can thus be taken as a reference to be compared with the synthetic jet impacts on the wall temperature.

Along the jet axis (Fig. 5.19a), the range of temperature values is much wider. Moreover, along the perforated zone, the temperature is lower than that of the flat plate. After a peak around 370 K around the first perforation, the maximum temperature decreases and tends to a plateau around 340 K, while that of the flat plate keeps increasing and reaches around 380 K at $x/D = 34$ (last perforation). After the third perforation, a pattern appears between each of the perforations. Another information provided by this figure is the difference between aspiration and ejection mid-periods. Indeed, the lower part of the temperature enveloppe, under the global

mean value, can be greatly attributed to the suction phase while the upper part is supposed to be due to the ejection. It appears that the difference between the upper part of the temperature enveloppe and the ejection mean value is larger than the difference between the lower part of the temperature enveloppe and the suction mean value. This can be confronted to the previous analysis: in the aspiration, the flow is completely driven by the suction while the boundary layer is stabilised. The flow is cooled down efficiently and the temperature values remain close to the mean value, a narrow range of values can be observed. This explains why the suction mean value is so close to the minimal value. On the contrary during the ejection mid-period the jets generate turbulence and several flow structures that impact the plate. It is expected to get a large range of temperatures. Regarding the PDF, two main "paths" can be observed. Each of them matches one of the mid-period means, supporting the hypothesis that these two paths can be attributed to each of the mid-periods. The one at the bottom of the enveloppe, which corresponds to the suction mid-period, is narrow. If the ejection phase were excluded, this would correspond to a PDF with a small standard deviation. On the contrary, the ejection PDF is broader, corresponding to a larger standard deviation. This again supports the previous analysis. The flow is stabilised during the aspiration, the thin, new boundary layer after each of the perforation contributes to efficiently cool down the wall. The heat transfer, as well as the flow dynamics, is totally driven by the suction. On the contrary during the ejection phase the jets increase the turbulence levels and the different flow structures impact the plate in a more chaotic way. Finally, it can be noticed that a temperature decrease is observed just upstream of the first perforation. This phenomeon, which is observed for this axis only, is attributed to the blockage effect and the generation of a horseshoe vortex.

Finally, between the jets (Fig. 5.19a), the temperature range is the wider of what can be observed in these three figures. This, again, is consistent with the previous analysis. It should be noticed that the two mid-period mean temperature profiles seem to be in contradiction with the previous analysis: the aspiration profile reveals higher temperature values than those obtained for the ejection. It was shown that during the aspiration, the boundary layer between the perforations evolves as along a flat plate, leading to an increasing temperature, while during the ejection the plate is impacted by the flow structures, which bring cold flow near the wall, leading to lower temperatures. Therefore, the opposite trend should be expected, with a lower ejection mean temperature than the aspiration one. This is due to the latency between the jet formation and their impact on this zone. As can be seen in Fig. 5.16 with the temperature field evolution along the whole plate through a period, it takes the whole ejection mid-period for the jets to impact the zone between the perforations. At the middle of the ejection phase ($t = 0$), the vortices are still not spread enough to reach the axis between the jets and the temperatures are therefore still high. In the same way, it takes the whole suction phase to evacuate all of the flow structures: at the middle of the aspiration ($t = T/2$), their impact can still be observed from the fifth perforation row to the end of the plate. That being said, observations are coherent with the previous analysis. The ejection mid-period is efficient to decrease the plate temperature, with wall temperatures equal to that

observed in the jet axis, but during the aspiration the thermal boundary layer thickens in a way similar to that of a flat plate, leading to high temperatures at the end of the perforated area. The maximum temperatures observed for this axis are close to that of the flat plate case. Around the first perforations, it is even higher. With the PDF, two similar "paths" can be observed along the first part of the plate, from $x/D = 7$ to $x/D = 20$. For $x/D \geq 20$, no specific path is seen and the standard deviations of both ejection and aspiration are much larger.

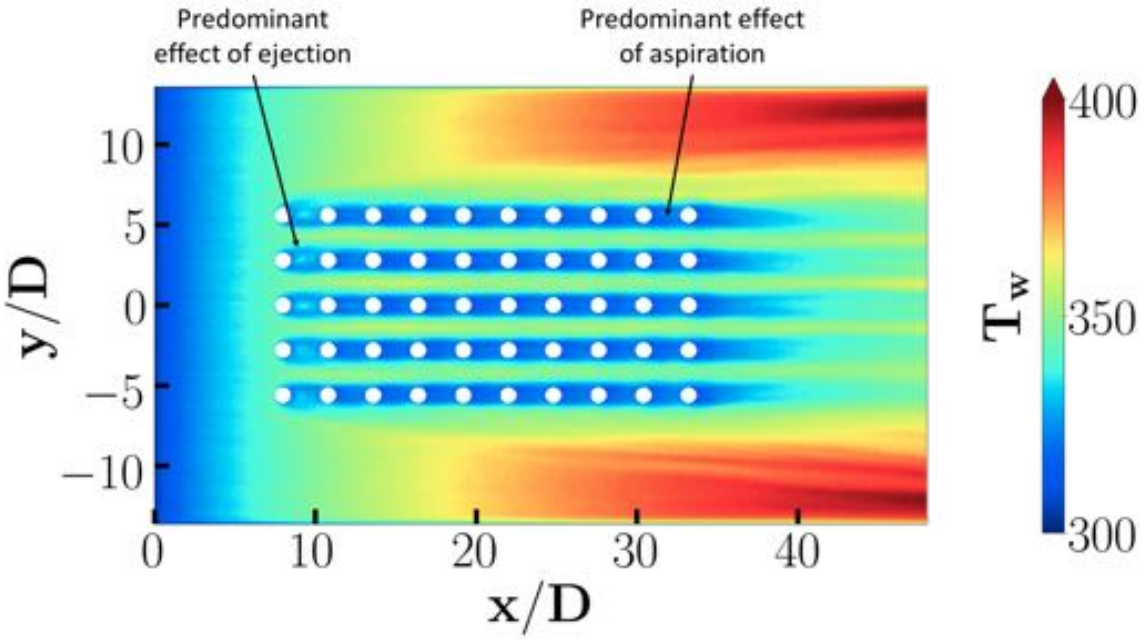

Figure 5.20: Plate temperature field averaged over five periods. Simulation run on mesh M2.

The plate temperature field averaged over five periods of the piston motion is given in Fig. 5.20. The developping boundary layer at the inlet is retrieved. The effects of both mid-periods can be noticed, in a smoother way than for instantaneous fields. The blockage of the jets appears on the first row of holes. The temperature is cooler within the hole wakes, which is due to the strong temperature gradients observed during the suction phase.

Before looking upon the wall heat transfer, the reference temperature T_{ref} fields can be observed. As a reminder, the calculation of the heat transfer coefficient relies on Newton's cooling law:

$$\Phi = h(T_w - T_{ref}), \tag{5.1}$$

where T_w is the wall temperature and T_{ref} is a reference temperature. Since neither the reference temperature nor the heat transfer coefficient are known, at least two different operating points have to be considered to obtain h. Figure 5.21 shows the T_{ref} values for the reference operating point. It appears that T_{ref} is globally

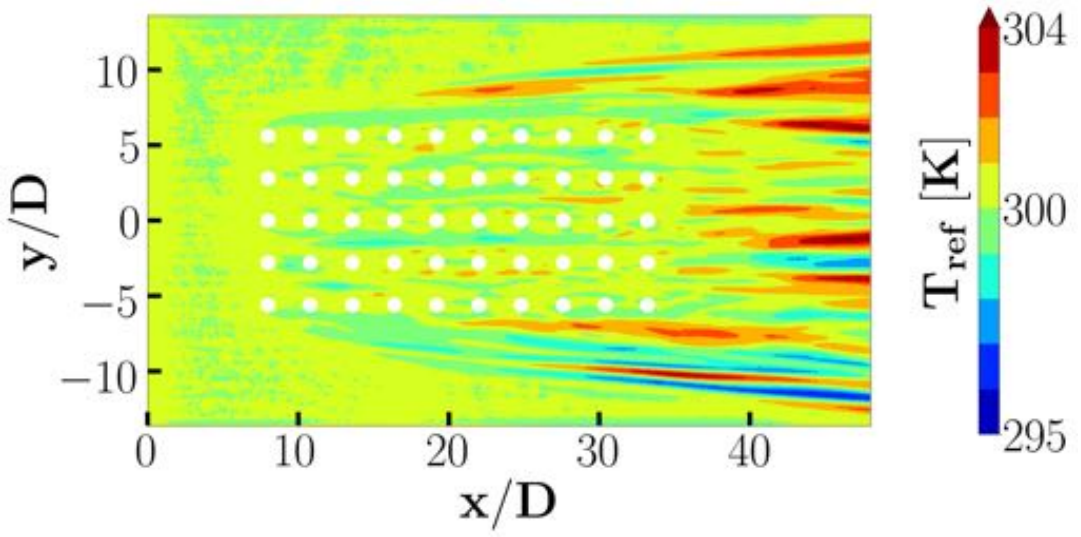

Figure 5.21: Reference temperature T_{ref} for the lab scale, reference operating point.

close to 300 K, especially near the perforations which is the zone of interest. It is mostly between 295 K and 305 K. It seems therefore acceptable to approximate $T_{ref} = 300$ K for the whole plate. With this hypothesis, h could be estimated with a single wall flux operating point. In order to reduce the number of simulations, and therefore the global simulation costs, some of the engine scale operating points that are analysed in Chapter 9 were thus simulated only once, with a single wall flux operating point.

As mentionned in Chapter 4, the wall heat transfer coefficient can be normalised into the Nusselt number with:

$$Nu = \frac{hD}{\lambda_{air}}, \tag{5.2}$$

with D the perforation diameter and λ_{air} the air thermal conductivity. As detailed in Chapter 4, this thermal conductivity is obtained for the reference temperature T_{ref}. With the approximation $T_{ref} = 300$ K to calculate the thermal conductivity λ_{air} is equal to 26.38 mW.m^{-1}.K^{-1}. The Nusselt field over the plate for the reference operating point, normalised from the heat transfer coefficient h field shown in Fig. 5.6, is provided in Fig. 5.22.

Results are consistent with the other elements previously described throughout the present chapter: the boundary layer is developping between the inlet and the first row of holes, leading to a decreasing heat transfer coefficient; in the hole area, the heat transfer increases, due to the enhanced turbulence creating vortices. Finally, downstream the holes, the heat transfer coefficient starts to decrease.

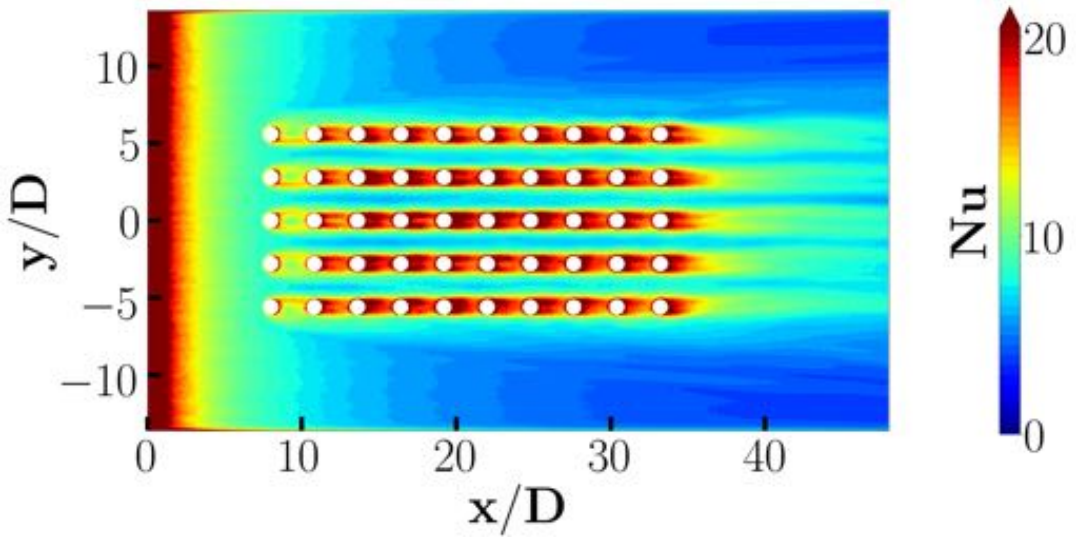

Figure 5.22: Reference operating point Nusselt number Nu field over the perforated plate.

Chapter conclusions

The reference operating point was used to provide a general description of the flow, validate the numerical strategy, and analyse more deeply the flow development and resulting wall heat transfer. The comparison of the numerical results with the experimental data showed that the simulations reproduce the aerodynamic flow behaviour very well. The mesh adaptation methodology is shown to greatly improve the results, both for the aerodynamic and thermal fields. Some differences appear for the wall heat transfer. However, the proper orders of magnitude and trends are retrieved, and some of these differences can easily be explained by differences between experimental and numerical set-ups. The importance of the upstream conditions, including the turbulence levels, on these differences is investigated later in this manuscript, including the Chapter 7 dedicated to the upstream turbulence.

The flow analysis showed the different mechanisms that impact the wall heat transfer in presence of synthetic jets. In particular, the ejection and aspiration mid-periods trigger completely different flow behaviours. During the ejection, the jets trigger the formation of vortices that contribute to bring cold flow close to the plate and to increase the wall shear stress. They also lead to the formation of blockage effects and recirculation zones, which can locally increase the plate temperature. The expansion of the flow structures along the plate contributes to obtain a quite homogeneous cooling of the plate, and the wall heat transfer is efficiently enhanced when compared with a flat plate under the same upstream conditions. On the contrary, the aspiration phase leads to strong spanwise heterogeneities along the plate. In the jet axis, the aspiration sucks the boundary layer within the perforations and contributes to reducing its thickness; moreover a new boundary layer restarts after each perforation, leading to a strong wall shear stress and therefore a strong wall

heat transfer enhancement. It is the most efficient mechanism of wall heat transfer enhancement due to synthetic jets observed in this study. However, inbetween the jet axis, there is a zone not impacted by the aspiration. There, during the aspiration phase, no heat transfer enhancement (when compared to a flat plate), but a classical flat plate boundary layer development is observed.

Now that the numerical set-up has been validated, the simulations are used to validate the test rig liner-representativity in Chapter 6. This step is necessary to apply Giachetti *et al.* results to classic acoustic liners and will enable the use of liner scale simulations based on the Pprime set-up.

6

Engine scale configuration: validation of the rig liner-representativity

In the present chapter, the goal is to assess the liner-representativity of the piston-driven rig, using the reference operating point. To do so, the engine scale geometry and specific aspects of the numerical set-up are detailed and the rig limitations are reminded and discussed. Then, results obtained with this new configuration are confronted to that of the lab scale set-up alongside the experimental results. The flow is investigated within the cavities, before looking at the main flow structures that are formed by the synthetic jets. Their impact on the boundary layer development is then discussed before observing the resulting wall heat transfer.

6.1 Configuration description

The test section and perforated plate of the engine scale configuration are similar to that of the lab scale, except for their dimensions, which are $1/\chi = 6.25$ times smaller than that of the lab scale configuration. The ducts and pistons below each of the perforations are replaced by a single cavity, as can be seen in Fig. 6.1. The cavity dimensions are chosen to get a quarter-wave resonator, corresponding to a resonance frequency $f_{1/4} = 500$ Hz. The choice of a quarter-wave resonator leads to a cavity length around 190 mm, which is too long for an acoustic liner. In real applications, a Helmholtz resonator would be privileged to target such a resonant frequency while maintaining the minimum clutter required in an aeronautical context. However, the quarter-wave resonator is much simpler to design: the cavity length is the only impacting parameter, while for the Helmholtz resonator the neck shape and dimensions as well as the cavity volume (which depends on its shape, section, length, surface...) play an important role. Since the choice of resonator does not impact the synthetic jet generation (*cf.* Section 1.2.1.2), a quarter-wave

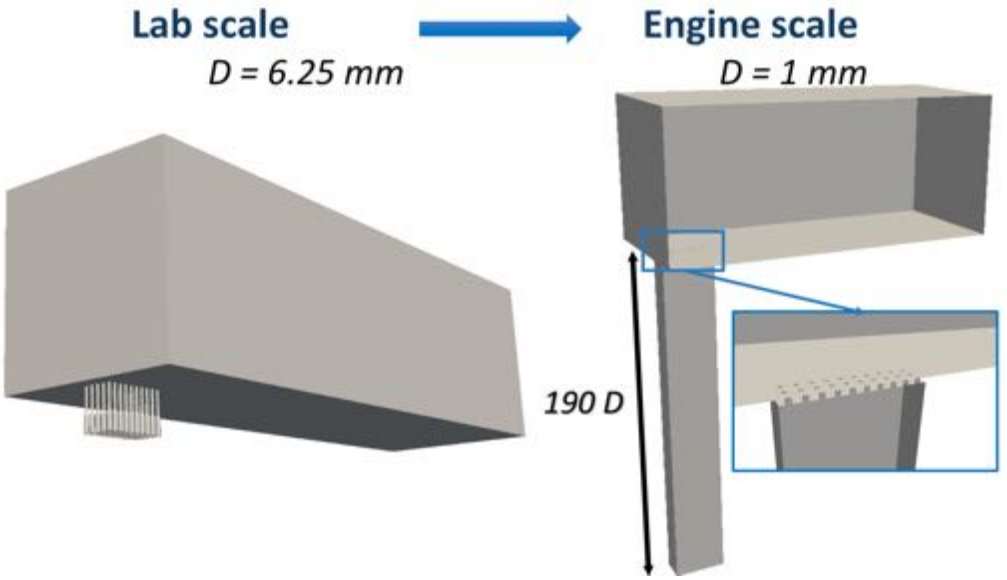

Figure 6.1: Comparison of the two configurations.

resonator is preferred. Figure 6.1 shows the geometrical differences between both configurations. An acoustic signal is superimposed on the grazing flow at the inlet of the domain, characterised by its frequency $f = 500$ Hz and Sound Pressure Level (SPL) $SPL = 150$ dB. This signal reproduces the fan noise that impacts an acoustic liner in flight conditions, triggering the liner acoustic resonance and synthetic jet formation. The quarter-wave that is generated within the cavity by this incoming signal can be seen in Fig. 6.2a, where the p_{rms} field is shown in the symmetry plane within the cavity and necks. This signal also leads to a rms pressure at the inlet that is around 650 Pa, as can be seen in Fig. 6.2b, while the mean pressure is imposed at 101325 Pa. This SPL value enables to retrieve a proper jet amplitude K, which enables to reproduce a jet velocity $\overline{W}$ equivalent to that of the lab scale case, through the similitude ratio. It should be noticed that the ratio $\overline{W}_{rig}/\overline{W}_{liner}$ does not exactly corresponds to the chosen similitude ratio, due to the fact that the link between the SPL and the jet velocity is not direct, making it difficult to parametrise. This point is discussed in more details hereafter.

The geometry is closer to that of a real liner, with the perforated plate over the resonating cavity, and the acoustic triggering of the synthetic jets is correctly recovered. Here, the set-up is in accordance with the statement that the acoustic wavelength is large when compared to the distance between two successive perforations and the phase difference between two successive jets is around 1.5° which is very close to the null phase difference of the lab scale. A particular attention should be brought to the jet velocity $\overline{W}$ of the liner. That of the rig is equal to 2.07 m.s^{-1}. With a perfect respect of the similitude ratios, the equivalent liner jet velocity should be 12.94 m.s^{-1}. However, the value obtained for the liner is 14.2 m.s^{-1}. While the jet velocity of the rig is directly and only led by the motion of the pistons, and thus can be imposed by fixing their amplitude and frequency, it is more complex in the case of a liner. Indeed, there, the jet velocity is directly impacted by the acoustic

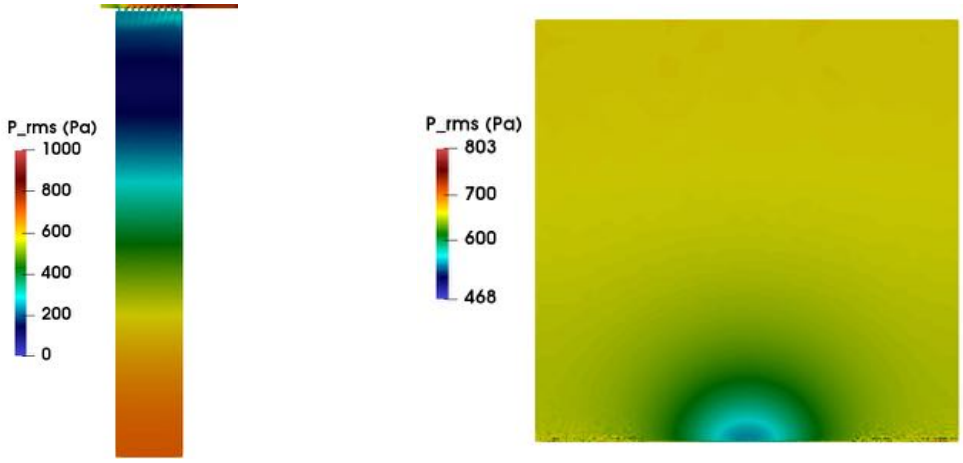

(a) Cavity and perforations, symmetry plane

(b) Inlet

Figure 6.2: P_{rms} fields for the engine plane configuration.

signal amplitude and frequency, but also by the grazing flow velocity. Finding a closer value would have required to spend more simulation time on this task. The results obtained with this jet velocity on the engine scale numerical simulations, when confronted to experimental data and lab scale numerical results, where considered good enough to accept this 10% difference.

The mesh was generated with the same method as for the lab scale, based on the two-criterion adaptation. In the end, the mesh is composed of around 55 million tetrahedrons. The adaptation was more efficient for the lab scale mesh: the averaged normalised wall distance Y^+ along the plate is equal to 9.7, while it is equal to 3.7 in the lab scale case. Figure 6.3 shows the time-averaged Y^+ fields over the plate for both configurations on the adapted meshes. The numerical set-up and boundary conditions are similar to that of the lab scale configuration, except for the absence of the ALE formalism (since the cavity walls are fixed) and the inlet velocity file, on which the acoustic signal is superimposed. Due to the higher frequency of the synthetic jets, the engine scale configuration significantly reduces the CPU costs. A simulation along a period T with the IDRIS Jean Zay computer (Intel Cascade Lake 6248 processors, with 20 cores at 2.5 GHz) costs approximately 57 000 hCPU for the lab scale configuration while this cost is equal to 9 000 hCPU for the engine scale.

With its lower simulation cost, the engine scale configuration is a privileged numerical set-up to explore conditions that have not been experimentally considered. In particular, high velocity grazing conditions can be simulated. The operating points for this configuration are defined by the grazing flow Mach number and the SPL of the acoustic signal that is injected at the inlet. Because the geometry was designed to resonate at 500 Hz, the frequency is unchanged and equal to that resonant frequency for every simulation. This is to ensure the synthetic jet formation. The operating point used throughout the present chapter is built, with the choice

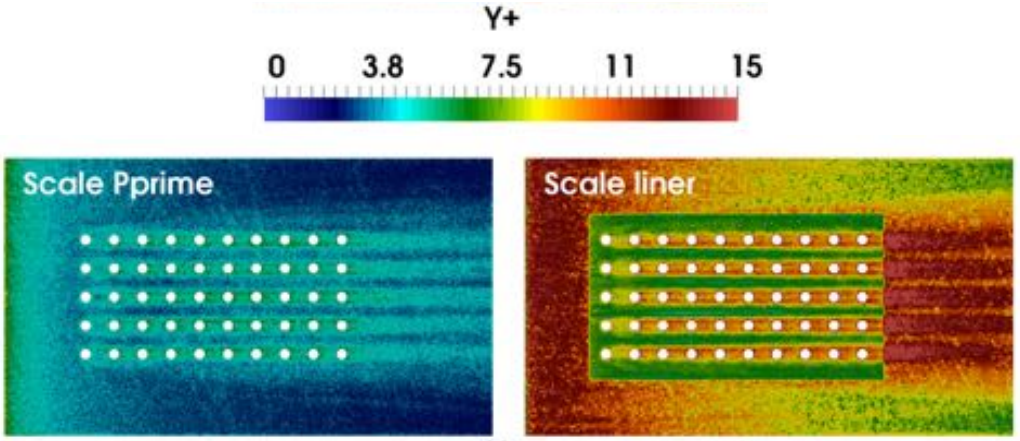

(a) Y^+ field along the perforated plate

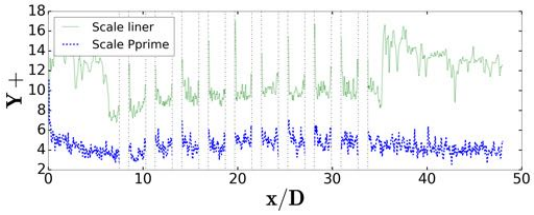

(b) Y^+ profile along the symmetry line

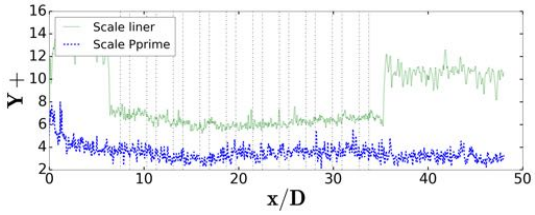

(c) Y^+ profile along the in-between jet axis

Figure 6.3: Comparison of Y^+ between the lab scale and engine scale configurations.

of the upstream conditions and acoustic parameters, to correspond to the reference operating point of the lab scale configuration though the similitude ratios. More operating points were simulated on this configuration and are analysed in the following chapters.

6.2 Liner-representativity of the rig

Now that the engine scale set-up has been introduced, results obtained for simulations on this configuration are used to validate the test rig liner-representativity. As for the lab scale configuration, in section 5.3, the flow is analysed with the following steps: first of all, the flow within the necks is observed. Then, the main flow structures are considered, before analysing the boundary layer evolution. Finally, the resulting wall temperatures and wall heat transfer are compared for both configurations.

6.2.1 Flow within the necks

The time evolution of the vertical velocity, pressure and temperature averaged over the surfaces of all necks is provided in Fig. 6.4. It is compared to the results obtained for the lab scale. The velocity signals are normalised by the jet mean velocities ($\overline{W}_{lab} = 2.07$ m.s^{-1} and $\overline{W}_{engine} = 14.2$ m.s^{-1}), in accordance with the similitude

ratios. It should be noticed that, for the velocity signals in the engine scale configuration, there is an asymetry between the ejection and the aspiration that is not present in the lab scale results. In both cases, the velocity profiles are almost sinusoidal however in the engine scale configuration the maxima are not equivalent (the ejection maximum velocity is higher than the maximum aspiration velocity). Moreover, the ejection and aspiration phases do not exactly correspond to the mid-periods. For the sake of comparison and consistency, the instant $t = 0$ was fixed for both configurations at the instant when the ejection velocity is maximal. In the lab scale velocity profile, the instants where the jet velocity is null are exactly $t = T/4$ and $t = 3T/4$, which is not the case for the engine scale configuration. Similarly, the minimum jet velocity is not exactly obtained at $t = T/2$ while it is the case for the lab scale configuration. An asymmetry in the velocity signal was also observed by Persoons *et al.* who attributed this to the different ambient conditions within and without the cavity. Since the pressures are characterised by completely different amplitudes, the pressure signals are normalised in order to get a signal between 0 and 1. The important information from this figure are the general shape of the signals and their phase difference. Finally, raw temperature values are provided. The temperatures are close, which was one of the similitude hypotheses (see Section 4.1.1: the temperature is assumed to be the same in both rig and liner scales.). Therefore, no normalisation is required and the signals can be directly compared.

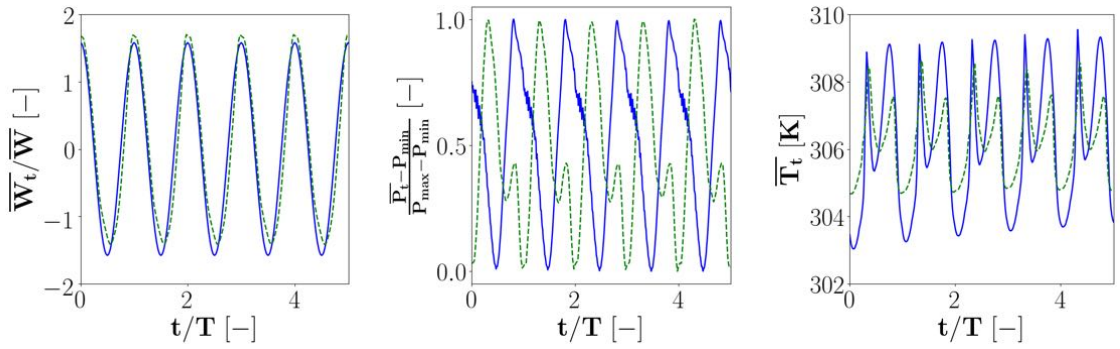

(a) Jet normalised velocity (b) Normalised pressure (c) Temperature

Figure 6.4: Time evolution of flow parameters within the cavities, averaged on a vertical section over the 50 ducts. Comparison of the lab scale and engine scale results. ——: lab scale ($z/D = -0.16$); - - -: engine scale ($z/D = -0.5$).

Looking at the engine scale vertical velocity (Fig. 6.4a), the synthetic jet mechanism is well retrieved with the succession of an ejection and a suction mid-periods. The signal is almost sinusoidal, similarly to the lab scale case, however there is a small asymmetry that leads to a higher minimal as well as a higher maximal jet velocity than for the lab scale. Regarding the temperature evolution (Fig. 6.4c), the profiles are quite similar for both scales. They are characterised over a period by the succession of two main peaks, as already described in Section 5.3.1. The first peak is due to the aspiration of hot air, followed by the aspiration of cold air when the whole hot boundary layer has been sucked within the cavities. Then, the second peak occurs at the beginning of the ejection mid-period when the hot flow

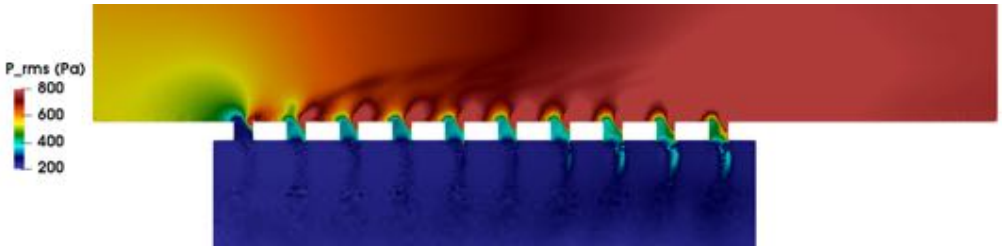

Figure 6.5: P_{rms} field within and around the perforations for the engine scale (colours volontarily saturated).

that was previously sucked within the cavities is expelled. Since the hot flow does not fill the entire cavity, the ejection leads to lower temperatures. The signals are in phase and their magnitudes are almost identical in both cases. However, the shape of the signals is not completely identical: for the engine scale, the second peak is much smaller than for the lab case. This is due to the different geometries. In the lab scale configuration, each perforation leads to its associated cavity, characterised by a diameter that is identical to that of the cavity and a long duct (high aspect ratio). There, the hot flow is trapped within the ducts and, although it starts to get mixed with the cold flow, this mixing is not efficient to significantly decrease the temperature. On the contrary, with the engine scale geometry, the perforations lead directly to a single cavity the dimensions of which are big when compared to their diameter. There, the mixing is much more efficient. Thus, when the hot air is expelled from the cavity through the perforations, its temperature has already decreased due to this mixing. The drift that appears for the lab scale is not seen anymore in the engine scale. It has to be kept in mind that the two configurations do not have the same simulation cost. Therefore, the engine scale configuration, which was way cheaper than the lab scale one, was used to run simulations on a higher number of synthetic jet periods. A steady regime, even for the temperature fields, can thus be reached more easily.

Contrarily to the velocity and temperature, the pressure evolution (Fig. 6.4b) is different in the two configurations. First of all, the magnitude of the signal is much more important for the engine scale (this does not appear in Fig. 6.4b, where the signals were normalised). The peak-to-peak pressure amplitude is a bit higher than 1000 Pa for the engine scale configuration, and close to only 40 Pa for the lab scale one near the perforations (it is higher closer to the pistons, as can be seen in Fig. 5.8 in Section 5.3.1, but remains of the same magnitude order). This is expected: as stated in section 5.3.1, the lab scale configuration is quasi incompressible. On the contrary, the engine scale synthetic jets are triggered by an acoustic signal, the flow is then compressible. The corresponding rms pressure field, around the perforations, is provided in Fig. 6.5. Colours are volontarily saturated for a better focus on what happens within the necks (the levels can be compared to those of the cavity and inlet in Fig. 6.2 to get the orders of magnitude along the whole cavity). The second difference is the shape of the signal over a period: while the pressure signal in the lab scale configuration tends to be sinusoidal, the pressure evolution for the engine scale displays a second peak during the descending mid-period. As for the

temperature, this difference is suspected to be a consequence of the neck geometries. The third and final difference is the phase difference between the two signals: they are in phase opposition. Another way to visualise this phase difference consists in the phase diagram $P_t = f(W_t)$ and is shown in Fig. 6.6. The phase diagram of the lab scale (Fig. 6.6b) is compared with that of the engine scale (Fig. 6.6a). The phase difference leads to a difference in the main trends that were observed when comparing results to Persoons *et al.* data in Section 5.3.1. The physical origin of the jets explains this phase difference: for the lab scale configuration, it is due to the pistons, placed *below* the cavities, and for the engine scale configuration it is due to the acoustic signal, which is coming from the upstream conditions, outside of the actuator and thus *above* the perforations. For the lab scale, the pressure rises when the pistons are going up, which corresponds to the ejection phase. It decreases when the pistons go down, leading to the suction mid-period. On the contrary, for the engine scale, the increase of pressure induced by the acoustic wave pushes the air within the cavity through the neck, which triggers the aspiration. When it decreases, the pressure becomes higher within the cavity, which leads to the ejection mid-period. This phase difference appears to be the first main observation of discrepancy between the piston-driven rig and a classical acoustic liner.

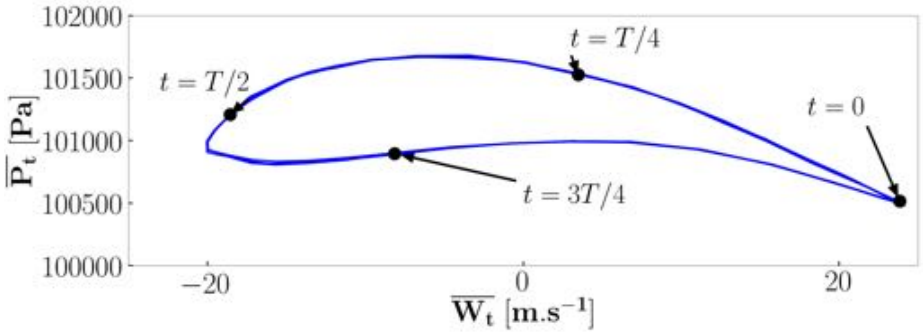

(a) Engine scale. $z/D = -0.5$

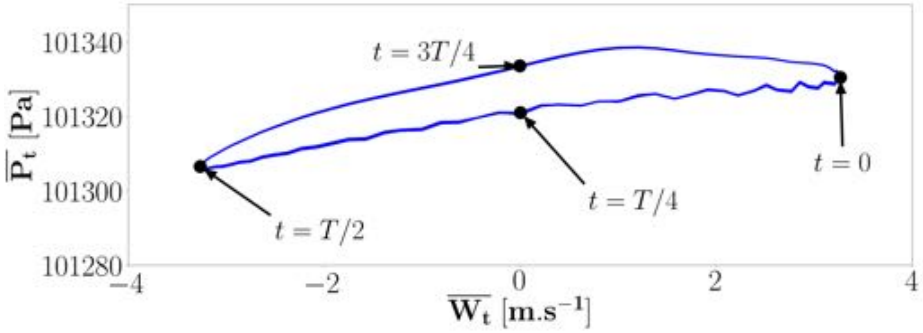

(b) Lab scale. $z/D = -0.16$

Figure 6.6: Phase diagram of the pressure as a function of the jet vertical velocity.

6.2.2 Main flow structures

As for the lab scale configuration, different views of the flow structures, shown in Fig. 6.7, are investigated. Similar conclusions can be drawn, with some specificities that are discussed hereafter. In general, the same flow structures are observed. The Q criterion is colored by the axial velocity. The hairpins penetrate high into the boundary layer and are easily identified with the high velocity of their heads. The horseshoe, due to the blockage effect provoked by the first row or perforations, is also retrieved. However, although the structures are globally similar, some differences that are discussed hereafter can be pointed out. As discussed in Section 6.2.1, the neck geometry is different in both scale geometries which is assumed to lead to these differences.

The top views at $t = 0$ (Fig. 6.7a) and $t = T/4$ (Fig. 6.7b) show the impact of the vortices along the whole plate. At $t = 0$, they are still aligned while at the end of the ejection they expand in the spanwise direction. Three differences with the lab scale results can be pointed out. Firstly, as discussed before, there is a phase difference between successive jets, which is not present in the lab scale. At $t = 0$ for the lab scale, the structures and more specifically the hairpins are generated at the same time: they are characterised by a similar size and shape (*cf.* Fig. 5.11a), at least after the third or fourth perforation row (the first rows are directly impacted by grazing flow and the blockage effect, which is not the case for the downstream jets). On the contrary, differences in shape and size can be observed along the axial direction. For example, the biggest hairpins at $t = 0$ are seen above the fourth row of perforations. The second difference, particularly visible at $t = T/4$ lies in the density of the structures: they are more numerous and the flow appears more turbulent, which would imply a higher flow Reynolds number and would be in contradiction with the similitude principle and further results (see Fig. 6.8 below). It should however be noticed that the Q criterion iso-surfaces were not scaled through the similitude ratios in order to fit those observed with the lab scale simulations. Therefore, several of the differences observed here might be, at least partly, due to this fact. The third difference is the surface covered by the structures, especially along the downstream part of the plate at $t = T/4$. Indeed, the distance from the symmetry axis over which the flow structures expand along the spanwise direction is not the same in both scales.

Similar remarks can be made with the front views at $t = 0$ (Fig. 6.7c) and $t = T/4$ (Fig. 6.7d). The structures are aligned at $t = 0$ before the spanwise expansion at the end of the ejection mid-period. The blockage effect and the horseshoe vortices are also clearly identified at $t = 0$. The tilt angles of the hairpins, at $t = 0$ and at $t = T/4$, appear to be similar to that of the lab scale case.

Finally, the side views at $t = 0$ (Fig. 6.7e) and $t = T/4$ (Fig. 6.7f) are analysed in a similar way. At $t = 0$, due to the phase differences between successive jets, the structures do not have the same shape and size. The highest and biggest hairpins can be observed on the third or fourth jet row. The roll-up of the hairpin legs around the head of upstream hairpins appear more clearly than for the lab scale

configuration. Finally, the vortices seem to penetrate less high within the grazing flow than for the lab scale.

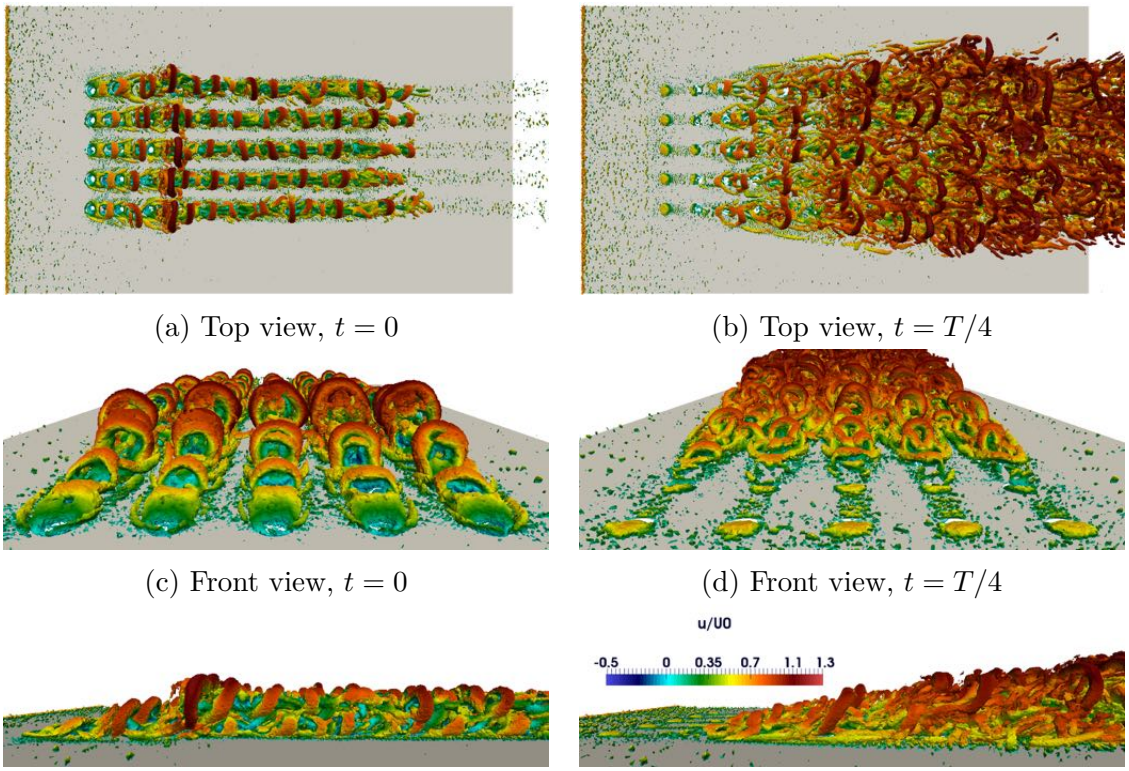

(a) Top view, $t = 0$

(b) Top view, $t = T/4$

(c) Front view, $t = 0$

(d) Front view, $t = T/4$

(e) Side view, $t = 0$

(f) Side view, $t = T/4$

Figure 6.7: Instantaneous Q criterion isosurfaces (10^9 s^{-2}) along the plate. Engine scale.

6.2.3 Boundary layer development

Numerical velocity fields (Figs. 6.8a to 6.8h) and profiles (Figs. 6.8e to 6.8h) corresponding to both lab and engine scales are compared to the experimental data (Fig. 6.8). These cases correspond to the simulations without turbulence injection at the inlet. The experimental uncertainty, shown by the error bars in the velocity profiles, is equal to 4% for mean velocities and 8% for *rms* velocities [126]. As for the lab scale results provided in Chapter 5, the profiles correspond to the following coordinates: $x/D = 0$, $x/D = 8$, $x/D = 16.4$, $x/D = 28.4$, $x/D = 33.2$ and $x/D = 40$, which are shown in Fig. 4.5b.

The first observation is the destabilisation and thickening of the boundary layer due to the synthetic jets. The numerical results are similar for the two scales, the boundary layer thickness is particularly well retrieved, as seen with the u/U_0 profiles in Fig. 6.8e. Both configurations overpredict the jet maximal velocity, as seen in the $w/\overline{W}$ (Fig. 6.8f) profiles. On the first part of the plate (inlet and first perforation, $x/D = 8$), the vertical velocity is similar, except very close to the wall were they are of different signs, which might be explained by the different mesh

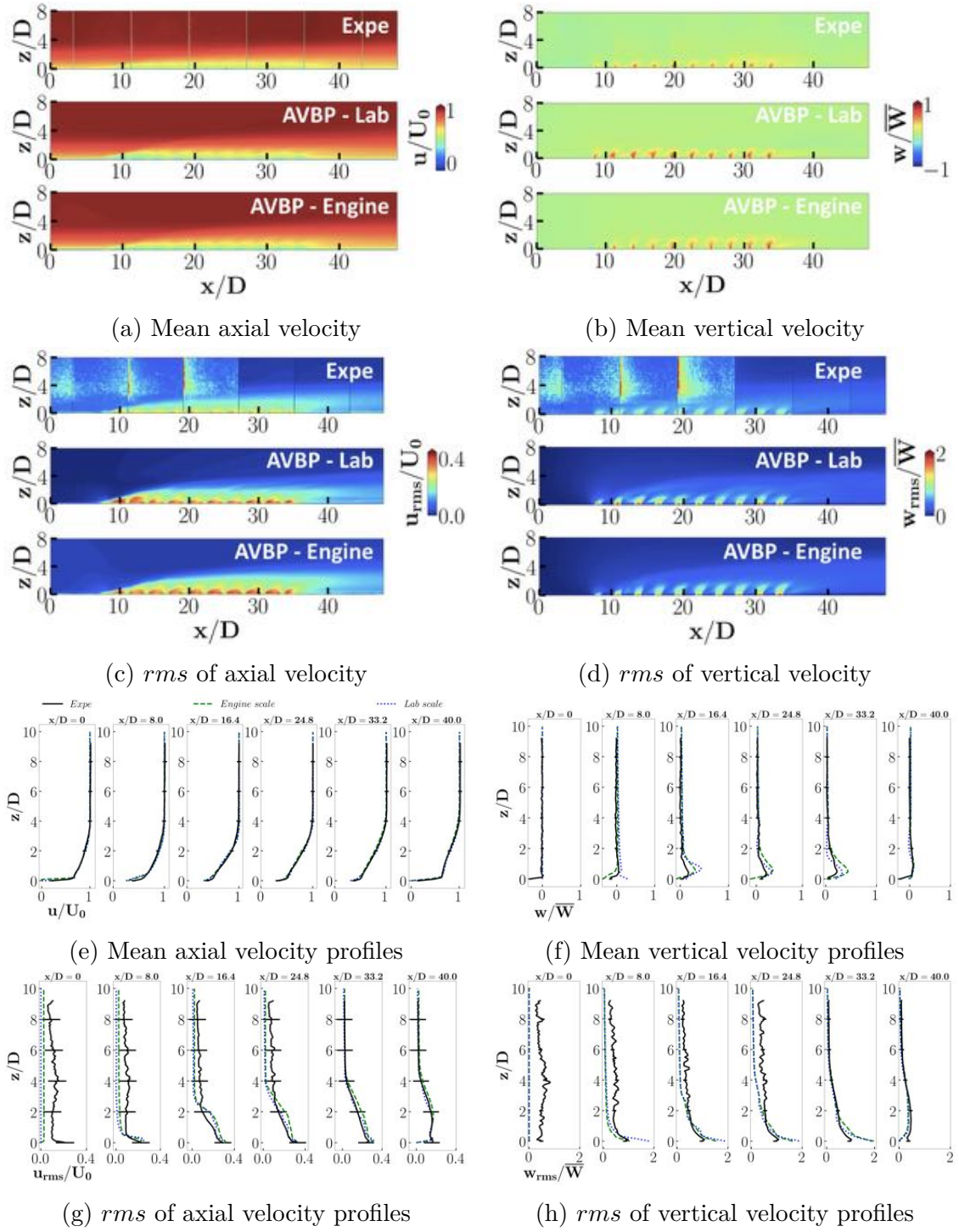

(a) Mean axial velocity

(b) Mean vertical velocity

(c) *rms* of axial velocity

(d) *rms* of vertical velocity

(e) Mean axial velocity profiles

(f) Mean vertical velocity profiles

(g) *rms* of axial velocity profiles

(h) *rms* of vertical velocity profiles

Figure 6.8: Comparison of numerical velocity results along symmetry plane for lab and engine scales with experimental data, without turbulence injection. Fields averaged over several periods of the piston motion.

refinements. Then ($x/D = 16.4$), it is higher for the lab scale configuration. It is the opposite for the downstream perforations ($x/D = 28.4$ and $x/D = 33.2$) where the maximal jet velocity is higher for the engine scale case. For both configurations, the jet velocities are overestimated when compared to the experimental data. Finally,

similar vertical velocities are retrieved downstream the perforations ($x/D = 40$). The jet velocity overestimation leads to some overprediction of u_{rms} values, as can be observed for u_{rms}/U_0 (Fig. 6.8g), however the boundary layer displacement close to the wall does not seem affected too much since the mean axial velocities u (Fig. 6.8e) match that of the experimental data particularly well. As the flow evolves along the plate, the experimental axial and vertical velocity profiles are better reproduced by both lab and engine scale simulations. The first profiles present some differences while downstream of the 7^{th} row of jets numerical results reproduce very well the experimental measurements for both scales.

6.2.4 Resulting plate wall temperatures and heat transfer

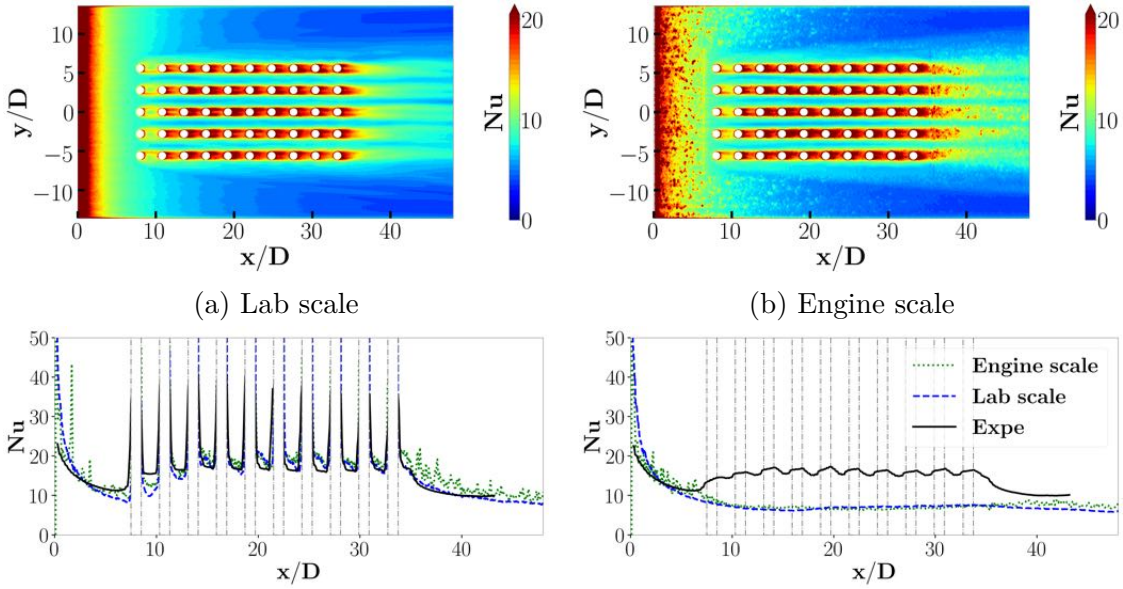

(a) Lab scale

(b) Engine scale

(c) Nusselt profiles in the jet axis

(d) Nusselt profiles between the jets

Figure 6.9: Comparison of Nusselt number numerical results for lab scale and engine scale (no turbulence injection) and experimental data. Fields averaged over several periods of the piston motion.

The Nusselt number Nu obtained by LES is compared to the experimental results in Fig. 6.9. The considered axis correspond to those shown in Fig. 4.5b: symmetry line going through the centre of the middle perforation row, axis between the jet, and axis far from the jets that is used as a "flat plate" reference. First, both simulations retrieve the good order of magnitude compared to experimental data. Moreover, the lab scale and engine scale present similar results, which supports the validation of the use of the Pprime rig as representative of an acoustic liner. Since these results are similar, the analysis developped for the lab scale in Section 5.3.4 is also valid for the engine scale.

Chapter conclusions

The results of the lab scale and engine scale configurations, in particular their similarities for the heat transfer part, are crucial for the present study: in spite of important pressure differences for the pressure observed between the lab scale and the engine scale configurations (amplitude, signal shape and phase difference), they enable to validate the similitude methodology. Two major conclusions can be drawn from this validation. First, the experimental results obtained with Pprime rig are applicable in the context of acoustic liners. Secondly, the adequation of numerical results to the experimental data (although with known limitations), validate the use of the numerical engine scale configuration. This will be much valuable for the next part of the study, since the simulations are cheaper with the engine scale configuration than the lab scale configuration, allowing to compute more operating points.

7

Impact of freestream turbulence injection

The reference operating point of the lab scale configuration, described and analysed in Part II, implies the presence of a turbulent grazing flow. However, it was chosen for the simulations to neglect the upstream turbulence and to inject the velocity profile at the inlet with no fluctuating velocities. In the present chapter, results from a simulation that takes into account this turbulence are presented. They are then confronted to that of the reference numerical simulation in order to quantify the impact of upstream turbulence on the wall heat transfer. This comparison is provided for the lab scale and the engine scale. Finally, the importance of the $M = \overline{W}/U_0$ parameter, when inlet turbulence is considered, is discussed.

7.1 Impact of inlet turbulence on the lab scale reference operating point

7.1.1 Turbulent inlet condition

A numerical simulation is dedicated to better understand the impact of upstream turbulence on wall heat transfer. This operating point is completely similar to the reference one, apart from the inlet velocity profile over which fluctuating axial velocities are superimposed. The u_{rms} profile is provided by the experimental data and adapted to get a null value at the wall. The experimental and numerical profiles are presented in Fig. 7.1. The maximal turbulent intensity is equal to 10.5 %. The turbulence is numerically injected with the Kraichnan/Celik method [146, 147].

7.1.2 Flow structures

A Q-criterion isosurface corresponding to the middle of the ejection mid-period ($t = 0$) is provided in Fig. 7.2 , for the lab scale configuration with and without up-

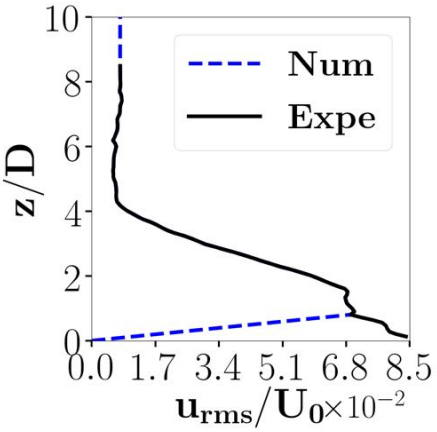

Figure 7.1: Inlet axial *rms* velocity profile.

stream turbulence. The different flow structures, which have already been described in details in the previous chapters, are well retrieved in the turbulent case. The horseshoe vortices are clearly visible on global, top and front views (Figs. 7.2b, 7.2d and 7.2f, respectively), and the hairpins can be seen in all of the provided views. In addition to that, some small structures are observed in the turbulent case only. They are due to the fluctuating velocities imposed at the inlet and their size appears smaller when compared to those generated by the synthetic jets. Although the formation and development of the hairpins is retrieved with the injection of upstream turbulence, their geometry is affected.

- To begin with, the hairpins are more asymetric and more bent compared to the reference case without turbulence. Due to the multi-perforation character of the present study, once formed, the hairpins are impacted by the important velocity gradient due to the downstream jets. This leads to an accelerated coherence loss (compared to a hypothetic single jet configuration). However, this loss of coherence happens more rapidly with upstream turbulence and hairpins dissipate faster than in the case without upstream turbulence injection.

- The top views (Figs.7.2c and 7.2d) show a spanwise expansion that seems more important in the turbulent case.

7.1.3 Boundary layer development

Time-average vertical velocity profiles are compared with and without upstream turbulence in Fig. 7.3 in the jet axis and compared to the experimental data. As in the previous chapters, the profiles correspond to the coordinates: $x/D = 0$, $x/D = 8$, $x/D = 16.4$, $x/D = 28.4$, $x/D = 33.2$ and $x/D = 40$. The axial velocity u/U_0 is very similar for both cases and corresponds to the experimental data in the jet axis. There, the axial velocity is correctly retrieved without upstream turbulence. On the contrary, the vertical velocity (Fig. 7.3b), which characterises the jets, is

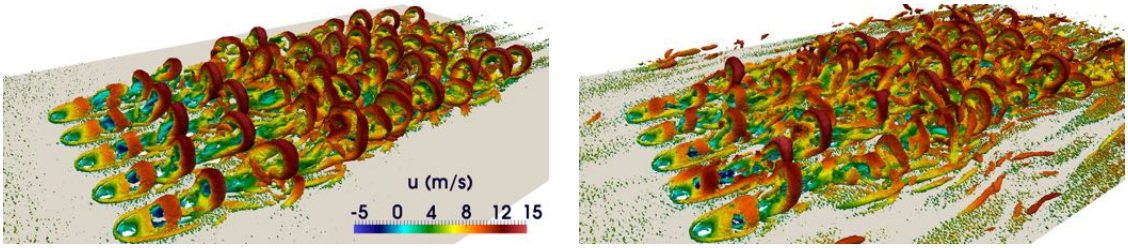

(a) Global view, without turbulence

(b) Global view, with turbulence

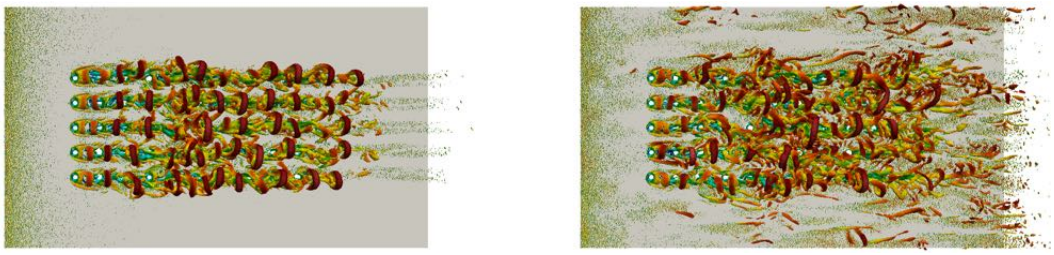

(c) Top view, without turbulence

(d) Top view, with turbulence

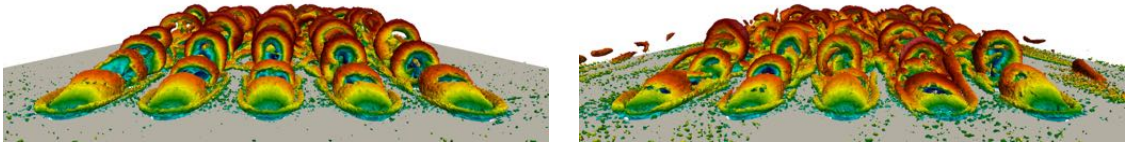

(e) Front view, without turbulence

(f) Front view, with turbulence

(g) Side view, without turbulence

(h) Side view, with turbulence

Figure 7.2: Instantaneous Q criterion isosurfaces (10^6 s^{-2}) along the plate, with and without turbulence injection at inlet. $t = 0$.

better predicted in the turbulent case: without turbulence at inlet, the jet velocities are overpredicted. Consistently with the Q criterion analysis, the synthetic jets are more folded in the presence of upstream turbulence. Some differences are observed for the fluctuating velocities (Fig. 7.3d) between the numerical results and experimental data in the upstream part of the plate. An important difference is the levels of turbulence that do not seem to be identical between the experimental data and the turbulent case in the upstream part of the plate. As a reminder, a lack of seeding particles far from the plate can explain the aspect of these profiles (from $x/D = 0$ to $x/D = 0.155$, where the profiles are noisy). The numerical profiles get closer to the experimental data and even superimposed downstream of the jets, where the simulations correctly predict the velocity profiles. Here again, taking into account the upstream turbulence contributes to increasing the simulation quality since this superposition happens faster than in the case without upstream turbulence.

Figure 7.4 provides the same time averaged velocity profiles, but between the jets. Here, no experimental data can be used as a reference since experimental velocity fields are not available in this plane. Similarly to the jet axis results, the

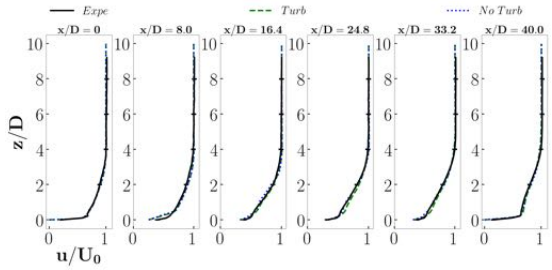

(a) Time-averaged axial velocity profiles

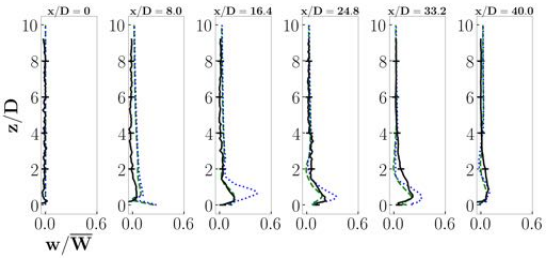

(b) Time-averaged vertical velocity profiles

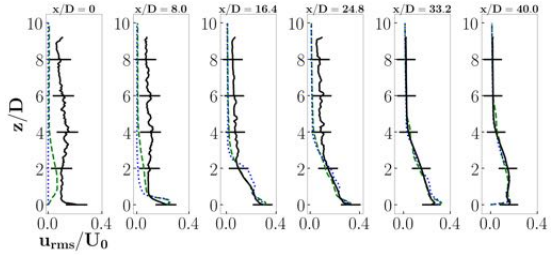

(c) *rms* of axial velocity profiles

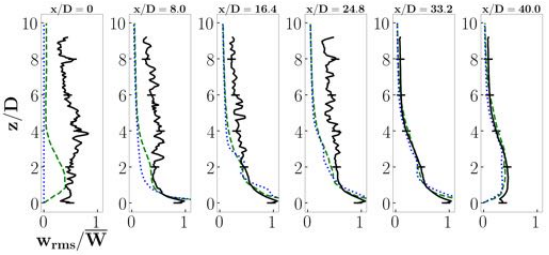

(d) *rms* of vertical velocity profiles

Figure 7.3: Comparison of velocity numerical results for lab scale numerical results with and without inlet turbulence with experimental data. Fields averaged over several periods of the pistons motion. Jet axis.

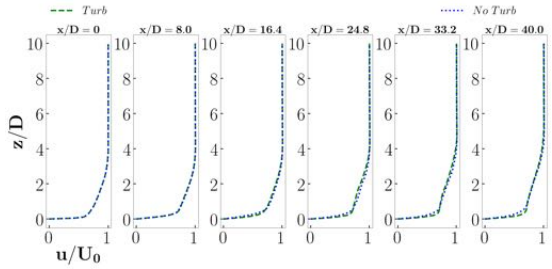

(a) Time-averaged axial velocity profiles

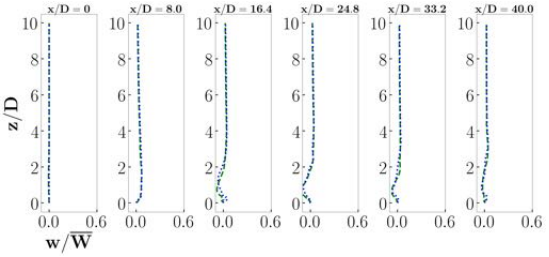

(b) Time-averaged vertical velocity profiles

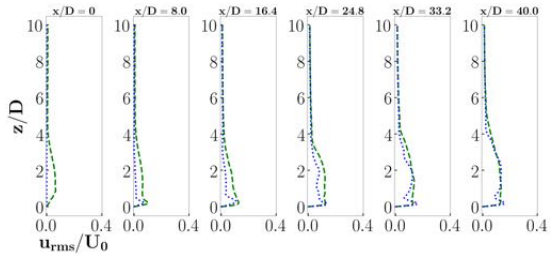

(c) *rms* of axial velocity profiles

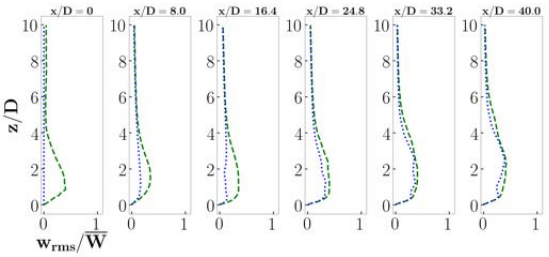

(d) *rms* of vertical velocity profiles

Figure 7.4: Comparison of velocity numerical results for lab scale numerical results with and without inlet turbulence. Fields averaged over several periods of the pistons motion. Between jets.

axial velocity u remains very close with and without upstream turbulence. No significant differences are observed either for the vertical velocity w. However, both axial and vertical *rms* velocities reach higher values for the turbulent case. The gap between profiles with and without upstream turbulence decreases along the plate

and eventually gets null downstream the tenth perforation row, where the profiles get superimposed due to the contribution of the synthetic jets.

7.1.4 Flow impact on plate and wall heat transfer

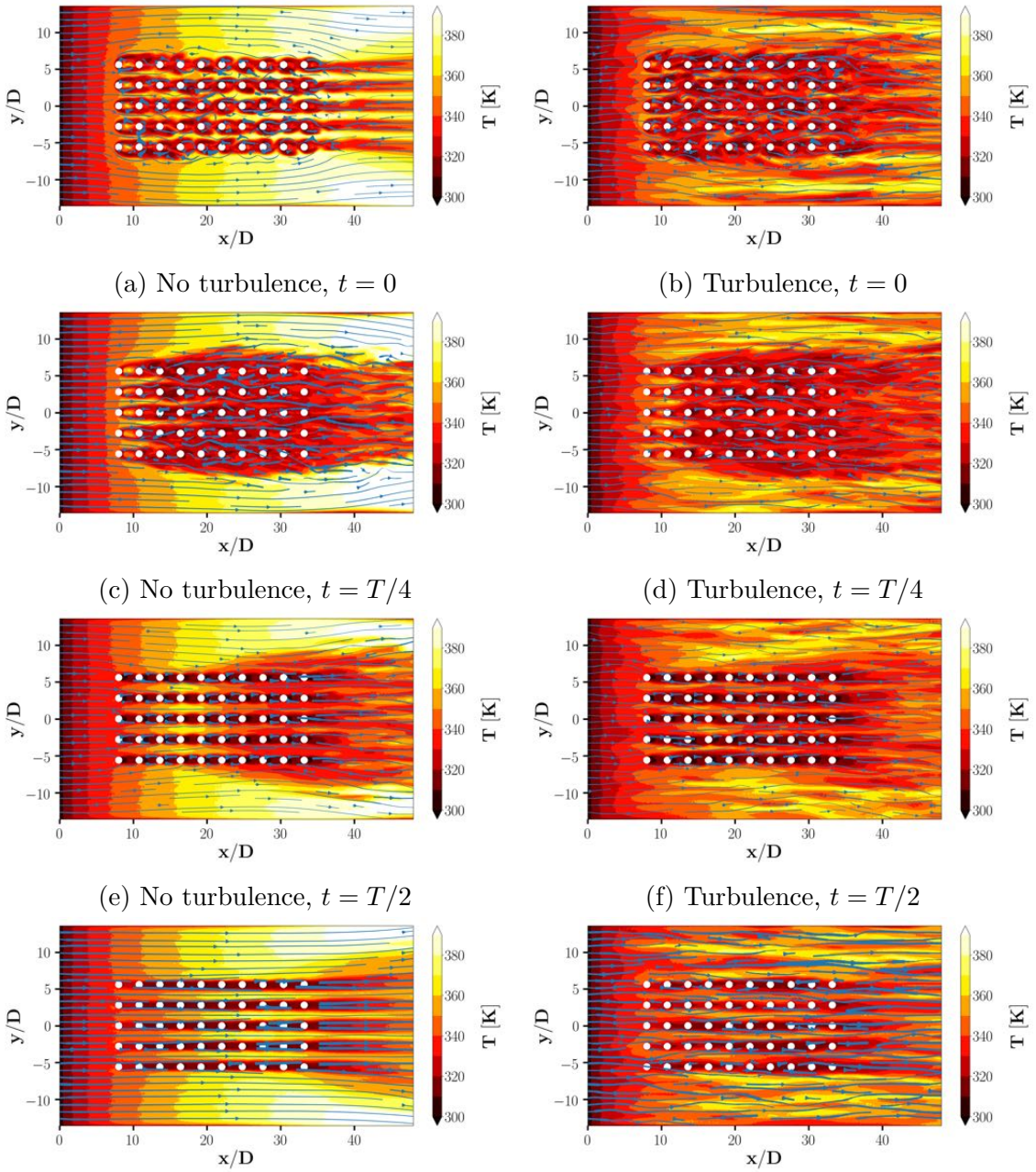

(a) No turbulence, $t = 0$

(b) Turbulence, $t = 0$

(c) No turbulence, $t = T/4$

(d) Turbulence, $t = T/4$

(e) No turbulence, $t = T/2$

(f) Turbulence, $t = T/2$

(g) No turbulence, $t = 3T/4$

(h) Turbulence, $t = 3T/4$

Figure 7.5: Instantaneous plate wall shear stress (blue streamlines) and temperature (colorfield) with and without turbulence.

Since the synthetic jets and the flow structures they generate drive the heat transfer along the plate, the modifications due to the upstream turbulence are ex-

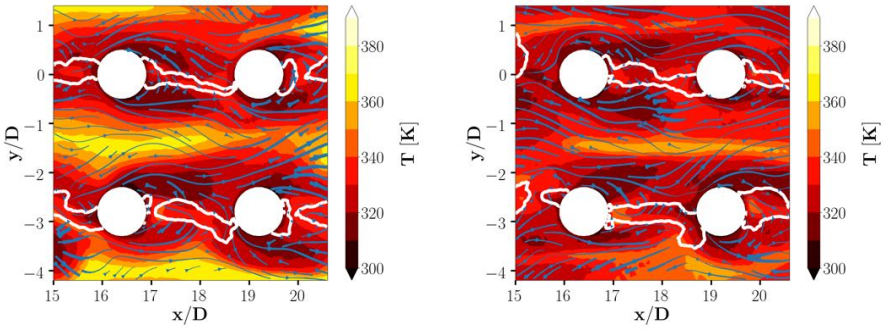

(a) No turbulence, $t = 0$ (b) Turbulence, $t = 0$

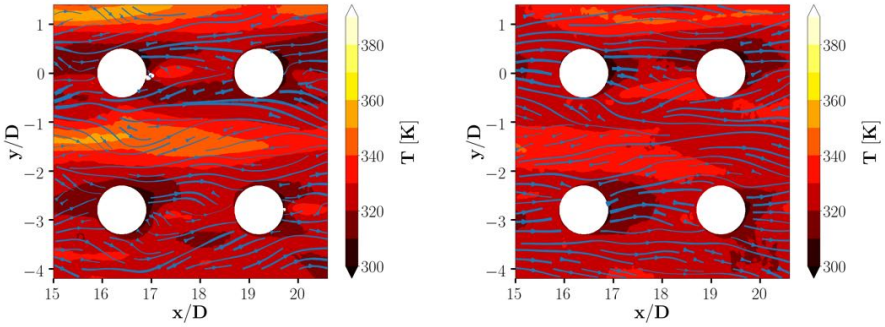

(c) No turbulence, $t = T/4$ (d) Turbulence, $t = T/4$

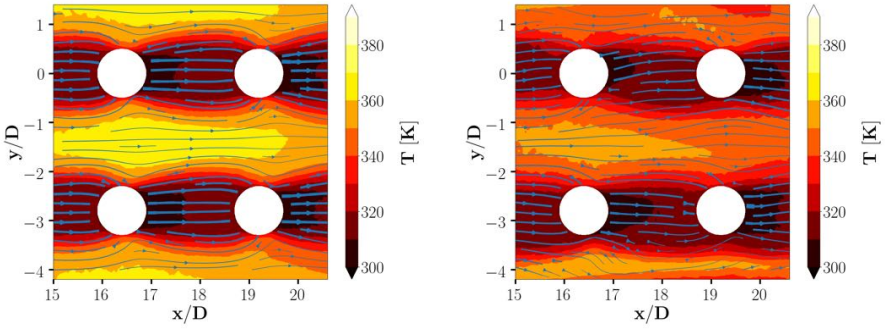

(e) No turbulence, $t = T/2$ (f) Turbulence, $t = T/2$

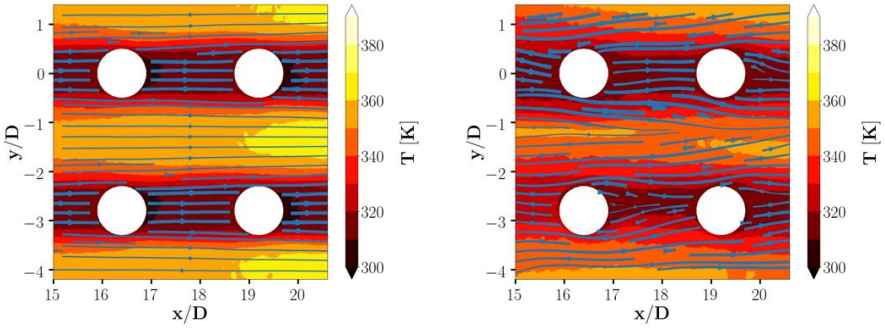

(g) No turbulence, $t = 3T/4$ (h) Turbulence, $t = 3T/4$

Figure 7.6: Instantaneous plate wall shear stress (blue streamlines) and temperature (colorfield) with and without turbulence. The white line corresponds to the isoline $u = 0$ m.s^{-1}, identifying recirculation zones. Focus around four perforations.

pected to modify the wall heat transfer. In order to visualise these modifications,

Fig. 7.5 shows the evolution of the wall temperature field along the plate through a jet period T. In addition, wall shear stress streamlines are represented. These fields are compared to the cases without upstream turbulence. Figure 7.6 provides a focus around four perforations.

First of all, far from the jets, it appears clearly that the wall reaches higher temperatures for the non turbulent case. This is coherent with the theory, which states that a turbulent boundary layer enhances heat transfer, thus leading to lower temperatures. Moreover, the temperature tends to be more homogeneous in the non turbulent case, while the impact of turbulent structures developping in the boundary layer locally modifies it on the turbulent case. Regarding the wall shear stress streamlines, they are straighter for the non turbulent case. Apart from these main differences, the same trends, already described in Section 5.3, can be observed. During the ejection mid-period, the jets widely impact the plate which temperature is homogenised along the perforated area, from the fifth or sixth perforation row. On the contrary, the temperature is heterogeneous during the aspiration mid-period: in the jet wakes, the plate is efficiently cooled down while between them, the developping boundary layer leads to higher temperatures. The wall shear stress streamlines are coherent with the jet evolution. They do not remain perfectly aligned over time. Partly due to the blockage effect, they circumvent the perforated area. On the contrary, during the aspiration phase, they converge nearer to the perforations.

The focus around four perforations in Fig. 7.6 shows that the temperatures are mainly similar with and without turbulence in the jet wakes. Similar patterns are observed, such as the temperature decrease in the jet wakes during the aspiration or the blockage effect and the horseshoe impact during the ejection. In both cases, recirculation zones are observed during the ejection. They can be seen in Figs. 7.5a and 7.5b, where the isoline of null streamwise wall shear stress is represented in white. Such recirculation zones and their impact on the wall temperature were already identified in Section 5.3.3 for the case without turbulence.

Inbetween the jets, the impact of turbulence appears more clearly, especially during the aspiration. As already identified, there and then, the jets do not impact the plate anymore and the developping boundary layer is responsible for the wall heat transfer. Thus, the heat transfer becomes characteristic of that of a flat plate and results can be compared to that of the zone far from the perforations. With a higher turbulence rate, the wall shear stress increases leading to a higher wall heat transfer. Therefore, the grazing flow cooling effect is more important with upstream turbulence, explaining the lower wall temperatures that are observed.

Figure 7.7 compares the wall shear stress evolution along a period T with and without upstream turbulence, along different plate axes. In order to detect general trends, the profiles are phase averaged over five periods to be smoothed. However an increased number of periods would be necessary to totally erase the turbulent fluctuations. As for the previous chapters, the lateral sides of the plate, near its edges, are assumed far enough from the perforations not to be too much impacted

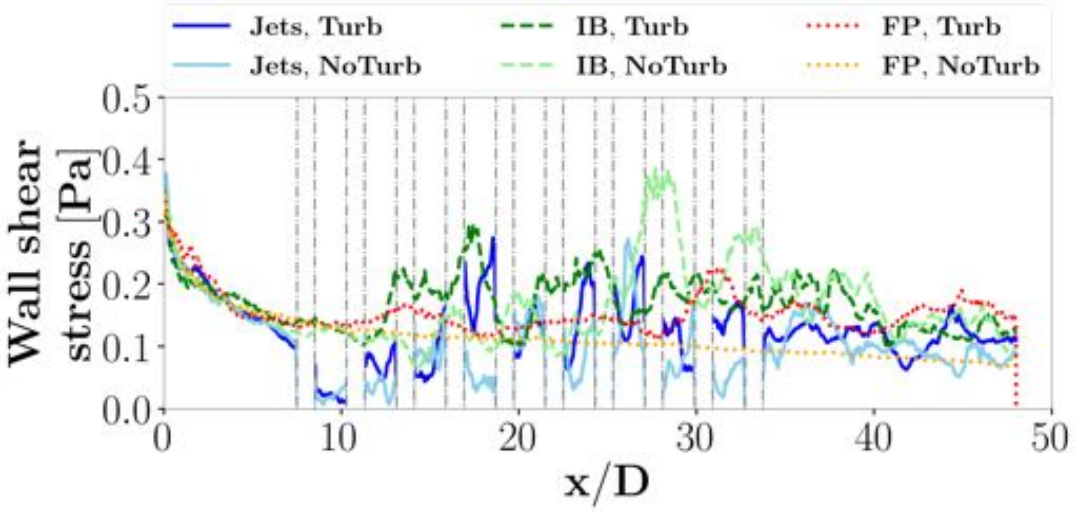

(a) $t = T/4$

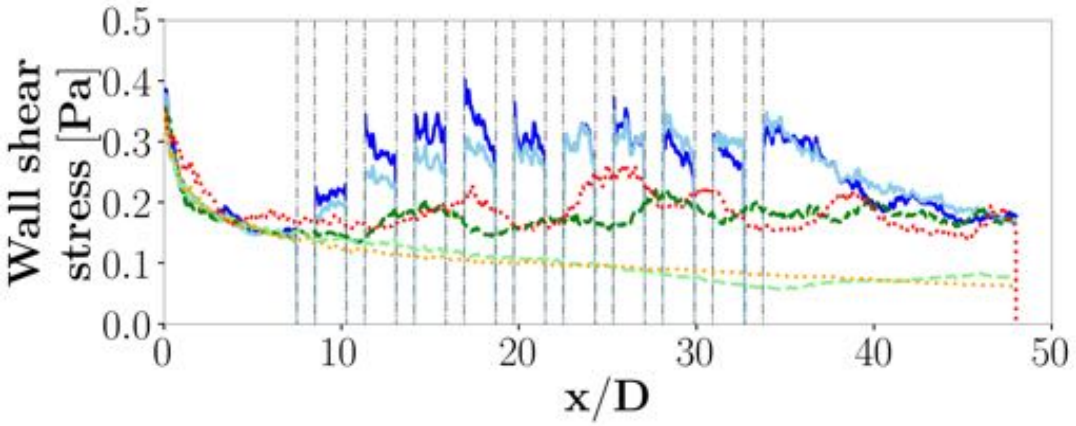

(b) $t = 3T/4$

Figure 7.7: Phase averaged wall shear stress along the perforated plate, with and without turbulence at inlet, for three axis: the symmetry line (Jets), in-between the jets (IB), and far from the jets (FP: "flat plate").

by the jets and thus representative of an equivalent flat plate, thus an axis along this edge is considered as "flat plate". It can be noticed that, for both mid-periods, the case with turbulent inlet is characterised by a higher wall shear stress than the case without upstream turbulence. Some differences are observed between the two mid-periods. During the ejection mid-period ($t = T/4$, Fig. 7.7a), apart from the first perforation rows, the wall shear stress in the jet wakes and between the jets is similar and characterised by important fluctuations. The jets impose the flow dynamics. On the contrary, during the suction mid-period ($t = 3T/4$, Fig. 7.7b), specific trends can be observed. Along the jet axis, the wall shear stress is not affected by the upstream turbulence and present a similar evolution in both simulations. Between the jets, the wall shear stress evolution, for both cases, follows that of the corresponding flat plate. This is coherent with the flow analysis obtained for the non turbulent case in Chapter 5, which showed that the suction is not important enough to affect this zone. Therefore, the flow is not driven by the synthetic jets

but rather by the upstream conditions, leading to a higher wall shear stress in the turbulent case.

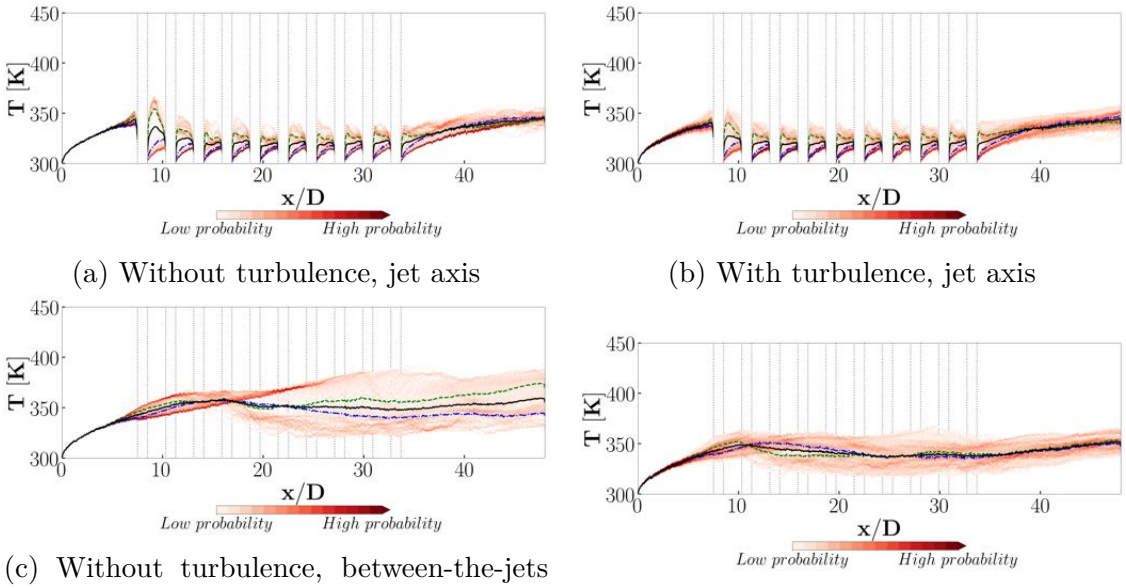

(a) Without turbulence, jet axis

(b) With turbulence, jet axis

(c) Without turbulence, between-the-jets axis

(d) With turbulence, between-the-jets axis

Figure 7.8: PDF of wall temperature with and without upstream turbulence, for the lab scale, reference operating point, in different axis.

The analysis of the temperature PDF in Fig. 7.8 provides further understanding on how the turbulence role is important for wall heat transfer. Since both reference and turbulent operating points are based on the same jet parameters, the same trends are found out in the temperature PDF. However, two main differences can be noticed. First of all, although the "paths" that were observed for the reference case can also be found in the presence of upstream turbulence, they are larger and lighter. This implies that the standard deviation is more important in the turbulent case. The second point is that higher temperatures can be reached in the reference case than in the turbulent case. This is particularly visible in the symmetry plane between the first and second perforations, where a temperature peak around 360 K is found out for the reference case while it reaches only 350 K in the turbulent case. Such a difference in temperature can also be observed between the jets. For $x/D > 25$, the maximal temperature reaches around 380 K in the reference case while it does not get higher that 360 K with upstream turbulence. This can be attributed to the development of the hairpins, which were shown to widen in the presence of turbulence, leading to lower temperatures farther from the jets. Moreover, the higher turbulence levels also lead to an increased mixing, therefore lower wall temperatures.

The previous results on wall shear stress and temperature with and without upstream turbulence show that the synthetic jets drive the flow mechanisms most of the time, however upstream turbulence can become preponderant in some specific locations and at specific times of a period. As a result, the Nusselt number Nu is

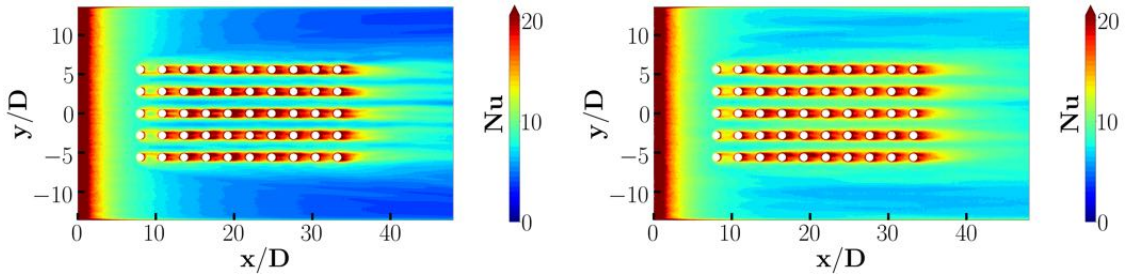

(a) Without turbulence (b) With turbulence

Figure 7.9: Time-averaged Nusselt number Nu with and without upstream turbulence.

different regarding the inlet flow conditions. Figure. 7.9 provides time-averaged Nusselt number fields with and without turbulence. The Nusselt number along the jet axis (Fig. 7.10a) and between the jets (Fig. 7.10a), for lab scale simulations with and without upstream turbulence, is compared with the experimental data in Fig. 7.10a. On the jet axis, the simulation without upstream turbulence was already close to the experimental data. This is consistent with the conclusions obtained from the wall shear stress analysis: the synthetic jets drive the flow at this location. However, there is still one difference along the first two perforation rows, where the results are even closer to the experimental data for the turbulent case. The upstream jets are directly bent by the grazing flow, and thus by the upstream turbulence, while the downstream jets are impacted by the upstream jets, which impose their dynamics to the flow. Between the jets, the upstream turbulence is much more important than for the jet axis. In particular, the Nusselt number gets higher in the turbulent case from the third perforation on and remains higher until the end of the plate. This higher value is closer to that of the experimental data downstream of the perforations, while the simulation without upstream turbulence is characterised by an underpredicted Nusselt number. Here again, this observation is consistent with the wall shear stress analysis: between the jets, the flow behaviour is less driven by the synthetic jets but rather by the upstream conditions. It is thus logical to better predict heat transfer at this location with the appropriate numerical upstream conditions.

The importance of the upstream conditions clearly appears when comparing the raw Nu values with the normalised ones. For example, the Nu profile of the case with upstream turbulence is much similar to that of the reference case in the symmetry plane. When observing the normalised Nu/Nu_{FP} profile, an important difference appears and increases with x/D. It is due to the flat plate profiles which are used for the normalisation: the upstream turbulence modifies the flow behaviour and the heat transfer for the flat plate as well as in the perforated zone. Moreover, a lower Nusselt number is observed in the turbulent case than the reference case. It was shown that one of the mechanisms through which the synthetic jets contribute to enhance wall heat transfer is an increased turbulence. In the turbulent case, there is already turbulence in the grazing flow, therefore the jets have a lower impact on the wall heat transfer and are less effective to increase the Nusselt number. On the

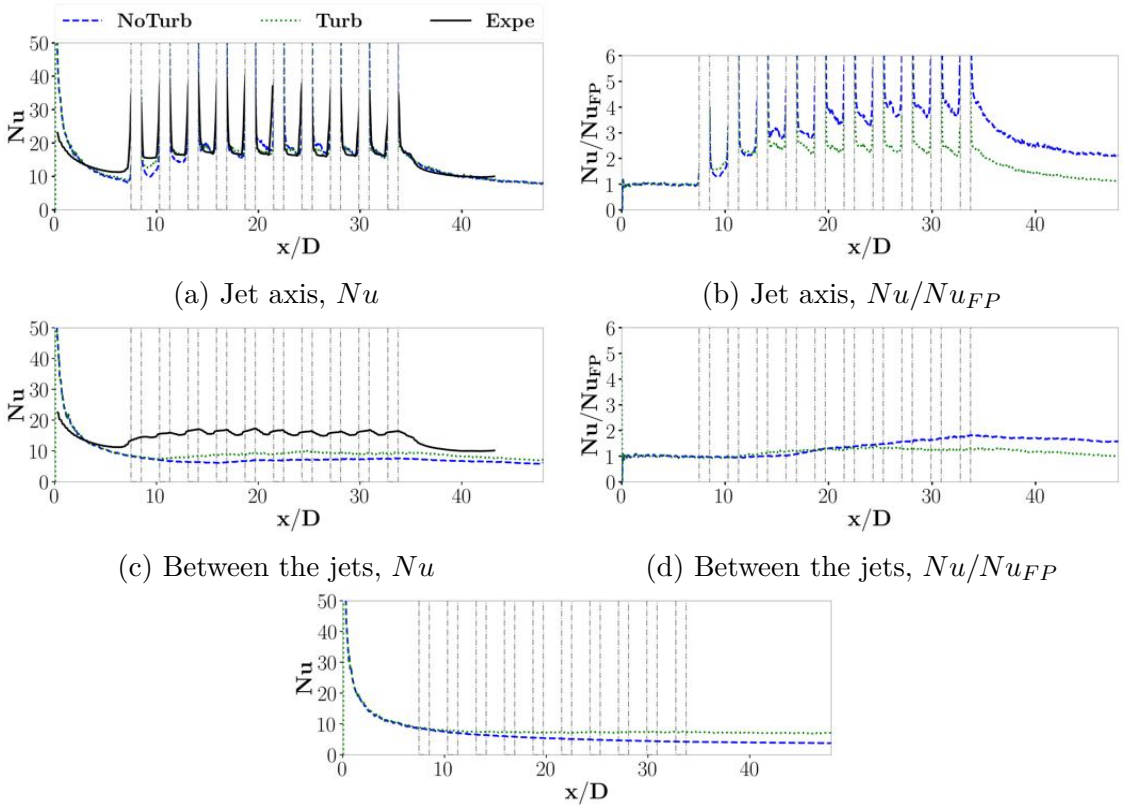

(a) Jet axis, Nu

(b) Jet axis, Nu/Nu_{FP}

(c) Between the jets, Nu

(d) Between the jets, Nu/Nu_{FP}

(e) Flat plate, Nu

Figure 7.10: Time averaged Nusselt number Nu and time averaged Nusselt number normalised by the equivalent flat plate Nusselt number Nu/Nu_{FP}, with and without upstream turbulence, at different positions along the perforated plate. Comparison with the experimental data. Lab scale configuration.

jet axis, this lower impact can be seen from the third perforation to the end of the plate. Between the jets, the turbulent case appears to lead to a lower Nu/Nu_{FP} values on the second part of the plate, from the seventh perforation row onward.

To conclude this analysis, the flow is mainly driven by two different mechanisms: the synthetic jets and the upstream conditions. In the specific operating point considered for the present study, the synthetic jets are the dominant mechanism, especially along the jet axis. Neglecting the upstream turbulence does not strongly affect the numerical results. However, between the jets the upstream turbulence does have an impact and should not be neglected. It should be kept in mind that this conclusion is valid for this specific operating point. Next section focuses on the importance of the velocity ratio M on the turbulence impact on wall heat transfer.

7.1.5 Impact of the velocity ratio M on the upstream turbulence importance on the flow development

The importance of the upstream conditions of the jets is characterised by the velocity ratio $M = \overline{W}/U_0$, which for the specific operating point considered in this chapter is equal to 0.16. Other behaviours should be expected at different M values. In order to analyse more deeply this question, more operating points than those simulated for this study framework should be considered. However, some preliminary elements of answer can be provided by the comparison of different operating points with the experimental data.

Figure 7.11 compares the Nusselt number Nu along the two axes (jet axis and between jets) for three different operating points with the experimental data. The first operating point is the reference one, used through this whole part. The second one, referenced to as "low M" on the figure, is obtained with a lower piston amplitude than for the reference case, leading to a lower velocity $\overline{W}$ and thus a lower velocity ratio M. Finally, a case without jets (the pistons remain still) is also presented, yielding $M = 0$. For these three cases, the upstream conditions are similar: the velocity profile with a velocity $U_0 = 12.8\text{m.s}^{-1}$ far from the wall, used for the reference case, is injected at the inlet. No turbulence is superimposed to that velocity profile. The figure shows that the reference case, whose velocity ratio M is the highest of the three considered operating points, is the case for which the heat transfer is best reproduced, in both axes. Along the jet axis, the low M case is better reproduced than the no jet case. Inbetween the jets, both low M and no jet cases present a similar Nusselt number evolution along the plate. This is attributed to the fact than, in the low M case, the jets are no longer strong enough to reach the axis between the jets. Therefore, the flow behaviour is similar to that of a flat plate, as for the no jet case.

It was shown in the previous sections that, for the reference operating point, the absence of inlet turbulence in the simulation leads to an underprediction of the Nusselt number. The comparison of the three cases without inlet turbulence in Fig. 7.11 shows that this underprediction rises when the velocity ratio M decreases. This might suggest that upstream turbulence has a greater effect on the jet behaviour, and thus its impacts on wall heat transfer, for low M cases. While it was shown that both jets and upstream conditions have an impact on the wall heat transfer, the importance of their respective impact relatively to each other is dependent on the velocity ratio M. It is suspected that for higher M values, the upstream conditions would actually become negligible, even between the jets, while low M values would lead to the preponderance of the upstream conditions over the synthetic jet flow dynamics.

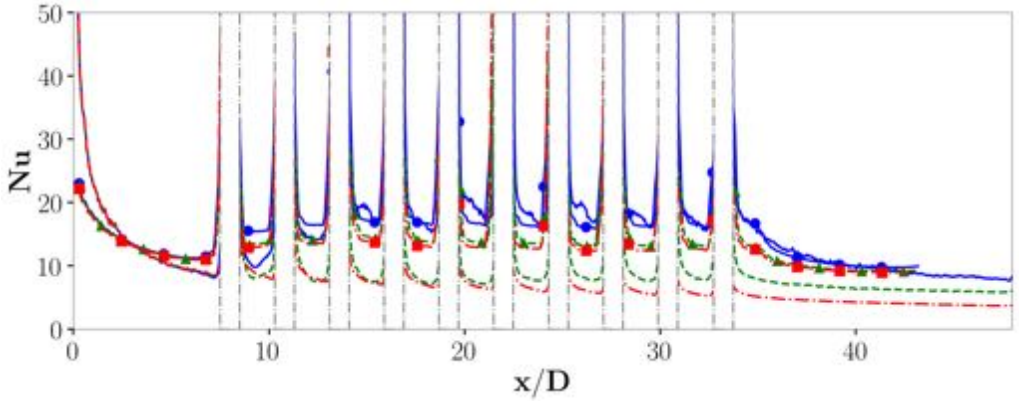

(a) Jet wakes

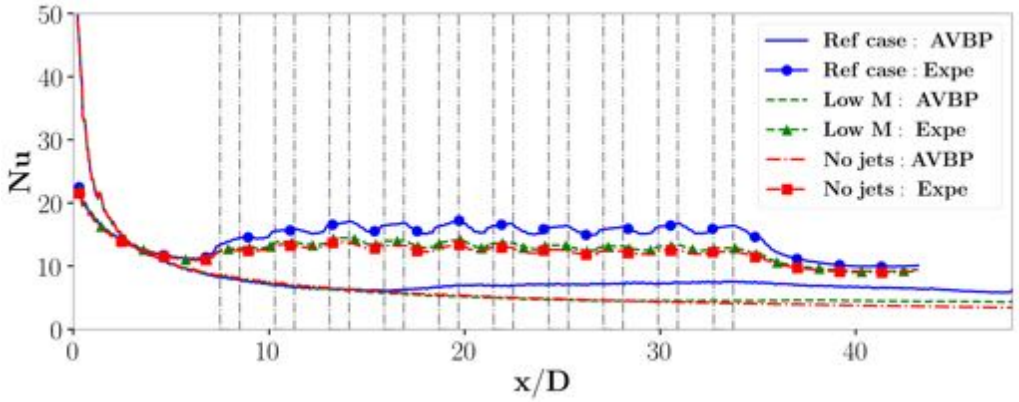

(b) Between jets

Figure 7.11: Time-average (over 5 periods) Nusselt number Nu for different operating points.

7.2 Effect of turbulence injection on the engine scale reference case

Similarly to the lab scale configuration, simulations taking into account the turbulence were run for the engine scale configuration. Velocity fluctuations were injected at the inlet using the same formalism. The identical u_{rms} profile was used, after being adapted through the similitude ratios. Since the impacts of the upstream turbulence on the flow dynamics and the wall heat transfer were already analysed and discussed for the lab scale configuration in the previous section, it was prefered here to compare both scales rather than engine scale with and without upstream turbulence. It should be noted that the low cost of the engine scale simulations allowed to average results on 42 periods, which is much longer than the 5 periods used for the lab scale averaging.

Figure 7.12 provides time-averaged velocity profiles for the lab and engine scales with upstream turbulence in the symmetry plane, compared to the experimental data. The mean and rms axial velocities are almost perfectly identical, implying a

similar boundary layer development. The vertical velocities are similar, apart from two differences that can be seen both on the mean and *rms* profiles. On the first perforation (second profile from the left, $x/D = 8$), the vertical velocities are lower for the engine scale than the lab scale. When compared to the experimental data, this leads to an underpredicted mean velocity. However, the *rms* profile seems to be better reproduced. The second main difference is present at the last perforation (second profile from the right, $x/D = 33.2$). There, the engine scale is characterised by higher vertical velocities than for the lab scale, implying an overprediction of the experimental data.

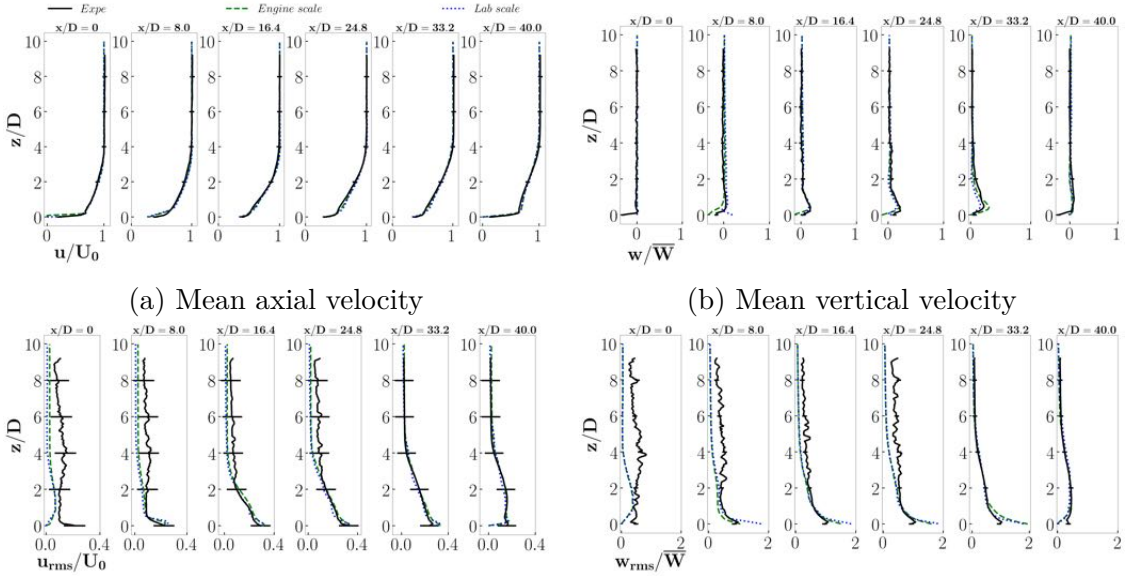

(a) Mean axial velocity

(b) Mean vertical velocity

(c) *rms* axial velocity

(d) *rms* vertical velocity

Figure 7.12: Time-averaged velocities with upstream turbulence.

Instantaneous wall temperature fields and wall shear stress streamlines are provided in Figs 7.13 for the whole plate. Here again, results for the engine scale with upstream turbulence are provided with results from the lab scale, turbulent simulations. The temperature fields appear smoother for the lab scale compared to the engine scale, which is attributed to the different Y^+ that were obtained through the mesh generation process (see Fig. 6.3 in Chapter 6). So are the "break lines" that can be seen around $x/D = 8$ and $x/D = 34$, that appear only for the engine scale and are not seen in the lab scale results: they correspond to the limits of a particularly refined zone of the mesh. Similar trends are found and the analysis developped in the previous section is still valid in this case.

The time averaged wall shear stress along the plate of the engine scale is confronted to that of the lab scale in Fig. 7.14. The first aspect that needs to be pointed out is the strange behaviour that is observed for the engine scale upstream the perforations, in particular at the beginning of the plate. There, the decreasing trend of the wall shear stress for the lab scale is consistent with what is expected for a flat plate with a grazing flow. On the contrary, the engine scale is characterised by a

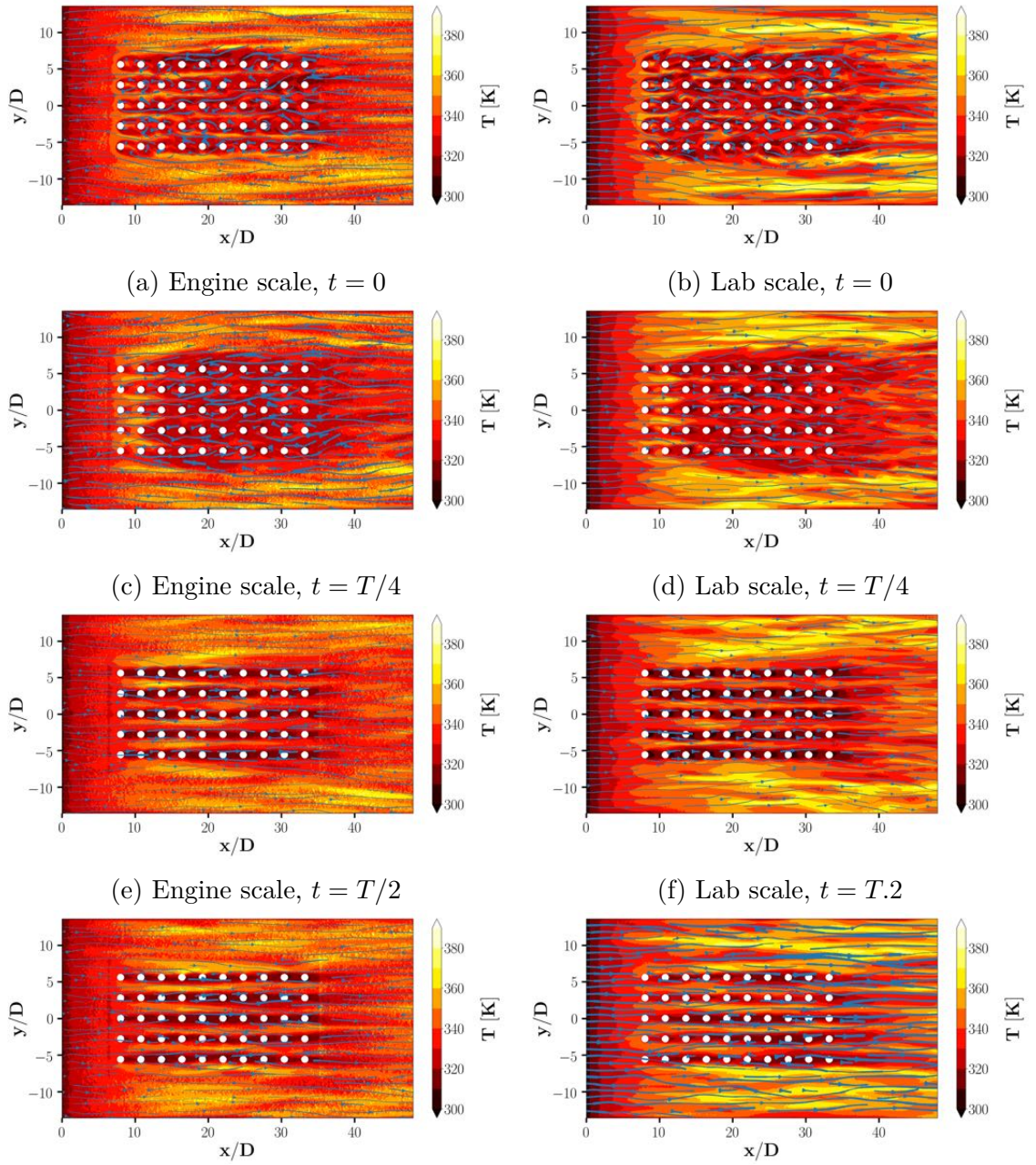

(a) Engine scale, $t = 0$

(b) Lab scale, $t = 0$

(c) Engine scale, $t = T/4$

(d) Lab scale, $t = T/4$

(e) Engine scale, $t = T/2$

(f) Lab scale, $t = T.2$

(g) Engine scale, $t = 3T/4$

(h) Lab scale, $t = 3T/4$

Figure 7.13: Instantaneous plate wall shear stress and temperature with turbulence, for the engine and lab scale configurations.

close-to-zero wall shear stress at the beginning of the plate, which rapidly increases until it reaches a plateau. This plateau corresponds to that of the lab scale wall shear stress just before the first perforation. This unexpected behaviour of the wall shear stress is partly attributed to the mesh effect that was described in Section 6.1, but not entirely understood nor explained. It would be at least required to enhance the mesh resolution to better solve this problem. Nonetheless, the results along the perforated zone and downstream the jets show acceptable comparisons. In particular, the comparison of the "flat plate" results show that, from around $x/D = 8$, the

wall shear stress is identical for both cases. Since the flow dynamics there, far from the jets, is driven essentially by the upstream conditions, this proper comparison implies that the mesh effect at the beginning of the plate does not affect much the quality of the simulation after $x/D = 8$. The second observation that can be made from this figure is that the wall shear stress for the engine scale tends to be slightly overestimated when compared to the lab scale results.

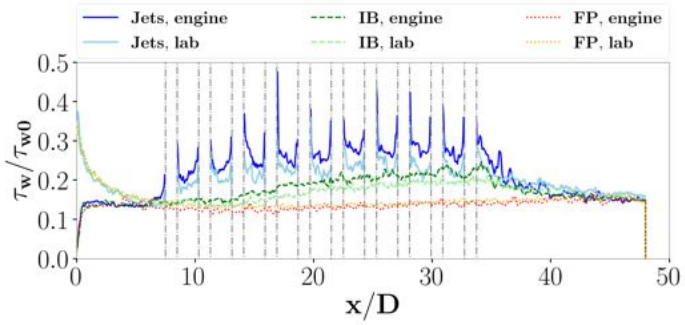

Figure 7.14: Time averaged wall shear stress along different lines of the perforated plate for the engine and lab scales, with upstream turbulence. IB: between jets, FP: flat plate. Operating point: 500 W.m^{-2} (lab scale), 6.25*500 W.m^{-2} (engine scale).

The locally higher wall shear stress leads to a higher Nusselt number, as can be seen in Fig. 7.15. This figure compares the Nusselt number Nu for the engine scale and lab scale, with upstream turbulence. Results are compared with the experimental data. In spite of the mesh effect that was observed at the beginning of the plate, which consequenctly impacts the wall shear stress, the Nusselt number seems to be better reproduced with the engine scale simulation than with the lab scale one upstream of the perforations. In the jet axis (Fig. 7.15a), results are close for both simulations. The wall heat transfer seems to be slightly better predicted around the first two perforations with the engine scale, but the trend is then opposite and the wall heat transfer is better predicted with the lab scale around the last four perforations. Downstream of the perforations, the Nusselt number is overpredicted with the engine scale, in accordance with the higher wall shear stress that was previously analysed. Inbetween the jets, similar observations can be made. The wall heat transfer is better predicted with the engine scale upstream of the perforations. Dowstream of the perforations, results are overpredicted when compared to the lab scale. However, there, the lab scale results underpredict the wall heat transfer and the higher values obtained for the engine scale match much better that of the experiment. The wavy part of the experimental data, and the large underprediction of the Nusselt number, have already been analysed in the manuscript and will not further be discussed here (see Section 5.2.2 and 7.1.4). In general, results are similar to that obtained through the previous analysis on lab and engine scale configurations and contribute to validating the similitude.

To conclude this section, lab scale and engine scale results were compared in case of upstream turbulence. It is found that the results are very close, however some care should be taken when considering the engine scale results. Indeed, the mesh

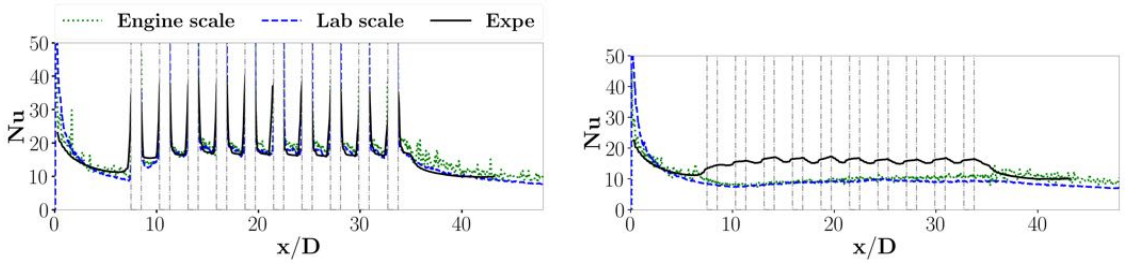

(a) Jet wakes

(b) Between jets

Figure 7.15: Time-averaged Nusselt number Nu with upstream turbulence

appears to be better resolved for the lab scale than for the engine scale and local effects can be observed (mesh effect at the beginning of the plate, higher wall Y^+). Nonetheless, results in the zone of interest appear to be satisfying.

Chapter conclusions

The impact of upstream turbulence on the synthetic jet development and resulting wall heat transfer was investigated for the lab and engine scale configurations. This analysis is motivated by two purposes: (i) contributing to the validation of the numerical set-up, by determining the importance of upstream conditions, and (ii) improving the knowledge of the turbulence role on the flow physics for such a configuration.

It is found that the upstream conditions play a non-negligible part in the jet formation and therefore in the wall heat transfer. It is particularly the case near the first perforation rows, which are directly impacted by the grazing flow while the downstream jets are more impacted by the upstream jets and the recirculation zones. The other important impact of upstream turbulence is observed between the jet axis during the aspiration. During this phase, which the jets do not impact, this part of the plate and therefore a classic flat plate boundary layer development is observed. Therefore, the upstream conditions become preponderant and should not be neglected.

The turbulence observed in the study has two origins: the upstream conditions and the synthetic jets. For this operating point, it is found that the jet turbulence plays the most important part, at least in the jet axis, where the flow is totally driven by the jets. This is not completely the case between the jets, due to the development of the boundary layer during the aspiration phase. It is suspected that the velocity ratio $M = \overline{W}/U_0$ has a major effect on which the synthetic jets and upstream conditions become preponderant in driving the flow: at high M values, the jet would be the driving effect and the upstream conditions would become negligible, while the opposite would be observed for low M values. Although more investigation is required to support this hypothesis, the comparisons of different operating points

provided in Chapter 9 seem to back it up.

Finally, since the upstream conditions appear to be important especially between the jet axes because of the aspiration phase, it would be interesting to wonder how the jets and wall heat transfer would be in a staggered perforation configuration. Indeed, the flat plate boundary layer would not be able any more to develop. This point, not considered through the present study, is more discussed in the conclusions and perspectives of this manuscript.

Part III

Database analysis

8 Jet in cross-flow

The presence of the cross flow along acoustic liners, which was already discussed in Sections 1.3.2 and 2.2.3, greatly impacts the synthetic jet development. Another classic configuration that faces such flow conditions is the continuous jet in cross flow, to which synthetic jets are often compared. In the present chapter, a new numerical simulation is presented: the lab scale configuration is used, however the pistons under the cavities are replaced by an inlet boundary condition to reproduce the behaviour of continuous jets. The results are compared to that of the lab scale reference operating point. This enables to compare the aerodynamics and resulting wall heat transfer of synthetic jets and continuous jets in a multi-perforation configuration. Note that with the continuous jets, cold air flow is added in the system which is not the case with the synthetic jets.

8.1 Continuous *versus* synthetic jets

As seen in Section 2.2.2, it is usual to compare synthetic jets, which have been introduced quite recently, to continuous jets which have been studied widely and for a longer time [67, 79, 148]. However, these comparisons are usually restricted to single jet configurations in quiescent flows. In particular, continuous jets in cross-flow are used in multi-perforation configurations to generate film cooling which is a privileged cooling system in aeronautic applications. Such configurations, which are extensively described in the literature [56, 130, 149], are close to that of the present study, where the heat transfer due to the synthetic jets along the wall they cross is studied. It is thus of interest in the present framework to compare the synthetic jets to classic continuous jets in order to compare cooling efficiencies and to find out whether some parallels can be drawn.

The new numerical simulation is based on the lab scale configuration and uses

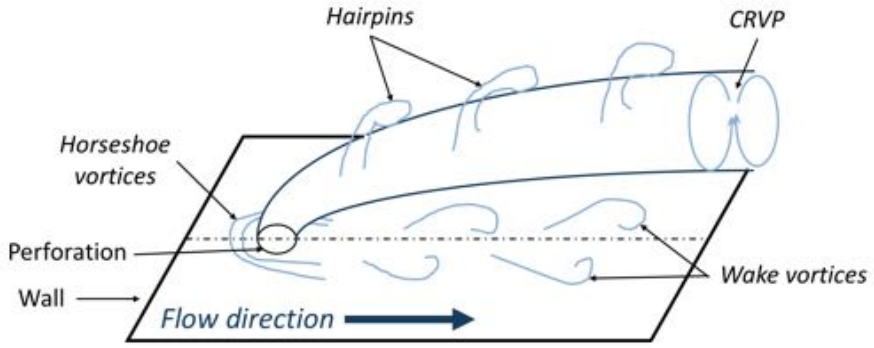

Figure 8.1: Characteristic flow structures of a continuous jet in cross-flow. Scheme adapted from those proposed by Fric *et al.* [150] and Bocquet *et al.* [145].

the same geometry and mesh. The main difference relies in the boundary conditions corresponding to the lower part of the cavities. In the synthetic jet configuration, these boundary conditions are moving walls reproducing the pistons. In this new, continuous jet configuration, the mesh is not moving any more and the piston walls are replaced by inlets with a constant vertical velocity $w = 0.5615$ m.s^{-1}. This value is chosen to obtain a jet Reynolds number in the upper part of the cavities equal to 829.2, corresponding to the synthetic jet Reynolds number of the reference operating point.

Since continuous jets are characterised by a stationary flow while synthetic jets are periodic, the comparisons are mainly performed on averaged fields. The only exception is the Q criterion which is shown for instantaneous fields. The flow structures are first compared. Finally, the wall shear stress and heat transfer are analysed.

Nota bene: for the sake of clarity, the acronyms JICF (Jet In Cross-Flow, standing for classic, continuous jets) and SJ (Synthetic Jets) are used throughout this chapter.

8.2 Comparison of aerodynamics in JICF and SJ

8.2.1 Flow structures

As mentionned, continuous jets in cross-flow are widely documented in the literature. Figure 8.1 shows the main structures that can be found when an isolated continuous jet is generated through a cross-flow. They appear to be very similar to that observed with synthetic jets. In particular, horseshoe vortices, counter-rotating vortex pairs and hairpins are clearly illustrated. In the lab scale - continuous jet configuration, these structures are correctly retrieved for the first rows of perforations as shown in Fig. 8.2a. The multi-perforated character of this configuration obviously impacts the formation of the structures which, as for the synthetic jet results presented in Chapter 5, lose their coherence around the three downstream

perforation rows.

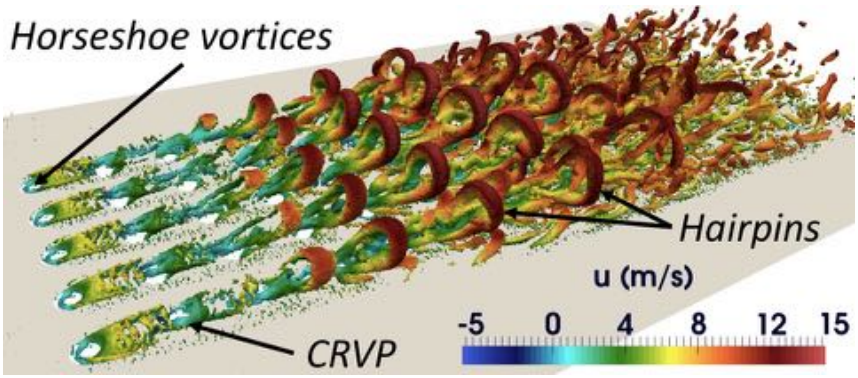

(a) Global view, continuous jets

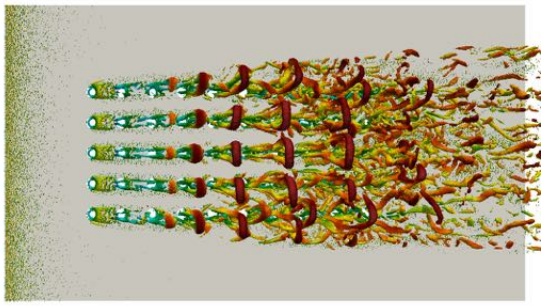

(b) Top view, continuous jets

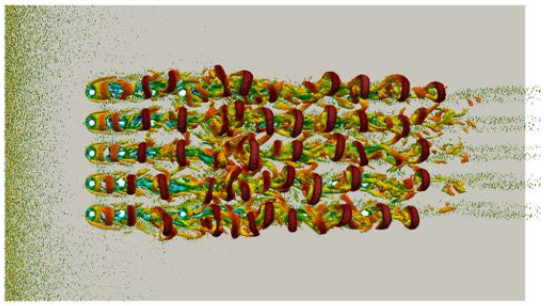

(c) Top view, synthetic jets, $t = 0$

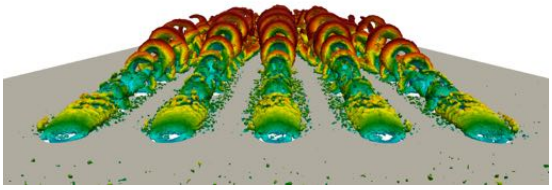

(d) Front view, continuous jets

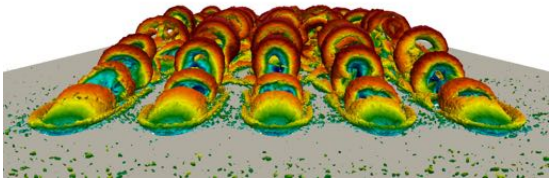

(e) Front view, synthetic jets, $t = 0$

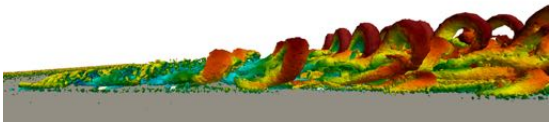

(f) Side view, continuous jets

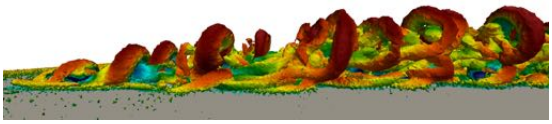

(g) Side view, synthetic jets, $t = 0$

Figure 8.2: Instantaneous Q criterion isosurfaces (10^6 s^{-2}) along the plate, comparison of synthetic and continuous jets.

Figure 8.2 compares different views of Q criterion isosurfaces for continuous and synthetic jets. The synthetic jet results are that of the lab scale reference operating point, taken at $t = 0$ corresponding to the maximum jet velocity $\overline{W}$. In general, the main flow structures are retrieved in both configurations. However their development and convection along the plate are different from one case to the other. Obviously, the fact that the SJ flow dynamics is periodic while that of the JICF is steady is responsible for these differences. It shall also be kept in mind that the results provided here correspond to instantaneous fields. Finally, the results for the SJ are

shown for the maximum jet velocity, which is higher that the mean, constant JICF velocity. The main observations that can be made for the different flow structures are as follows.

- The flow requires a longer distance to be established for the JICF if compared to the SJ: while the main flow behaviour is established as soon as at the third perforation row for the SJ, it is not the case of the JICF until the fourth or fifth perforation row. Moreover, along this establishement zone, the flow structures do not expand as much as in the synthetic jet case. This appears clearly in the top views (Figs. 8.2b and 8.2c) and even more in the front view (Figs. 8.2d and 8.2e).

- In the continuous jet case, along the first six perforation rows, the structures and more specifically the hairpin heads remain aligned with the perforation axis. This is not the case for the SJ, for which the alignement is not as good.

- The **spanwise expansion** of the structures, which can be observed in Figs. 8.2b and 8.2c, is wider for the continuous jet case than for the synthetic jet case at $t = 0$. However, as discussed in Section 5.3.2, this spanwise expansion gets wider for the synthetic jets at the end of the ejection phase, at $t = T/4$. The spanwise expansion of the continuous jet case appears to be somewhere between that of the synthetic jet at $t = 0$ and at $t = T/4$.

- **Counter-rotating vortex pairs** are found in both configurations. It is particularly complex to state more since they are hidden by hairpins most of the time. As a reminder, a more complete discussion on these structures, which might not be CRVP for the SJ case, is proposed in Section 5.3.2.

- **Horseshoe vortices** are also recovered with continuous as well as synthetic jets. However, they appear to be bigger for the synthetic jet case.

- The head of the **hairpins**, which are the structures that penetrate the highest into the cross flow, seem to reach the same height for both configurations. This is visible from the side views in Figs.8.2f and 8.2g. Hairpins appear to be similar in both configurations only from the fourth to the sixth perforation rows. While they are present all along the plate with the synthetic jets, they are not formed before the third perforation row in the continuous jet case. Upstream of the sixth perforation row, they lose coherence in the continuous case which is not yet the case with the synthetic jet case. This latest difference is due to the unsteady character of synthetic jets and the choice of using $t = 0$ results. As discussed in Section 5.3.2, these hairpins are expected to lose their coherence later on during the synthetic jet cycle. As a matter of fact, the global aspect of the hairpins observed on the continuous jet case seem to

be a mix between that observed at $t = 0$ and $t = T/4$ for the synthetic jet case.

8.2.2 Boundary layer development and resulting wall shear stress

As already analysed in Chapter 5, the synthetic jets modify the boundary layer develoment. This statement is also true for the JICF. The time averaged velocity fields along the symmetry plane, corresponding to the middle jet axis, are presented in Fig. 8.3 for both JICF and SJ. As expected from the flow structure observations, some similarities can be found in the boundary layer development however several differences are also to be indicated.

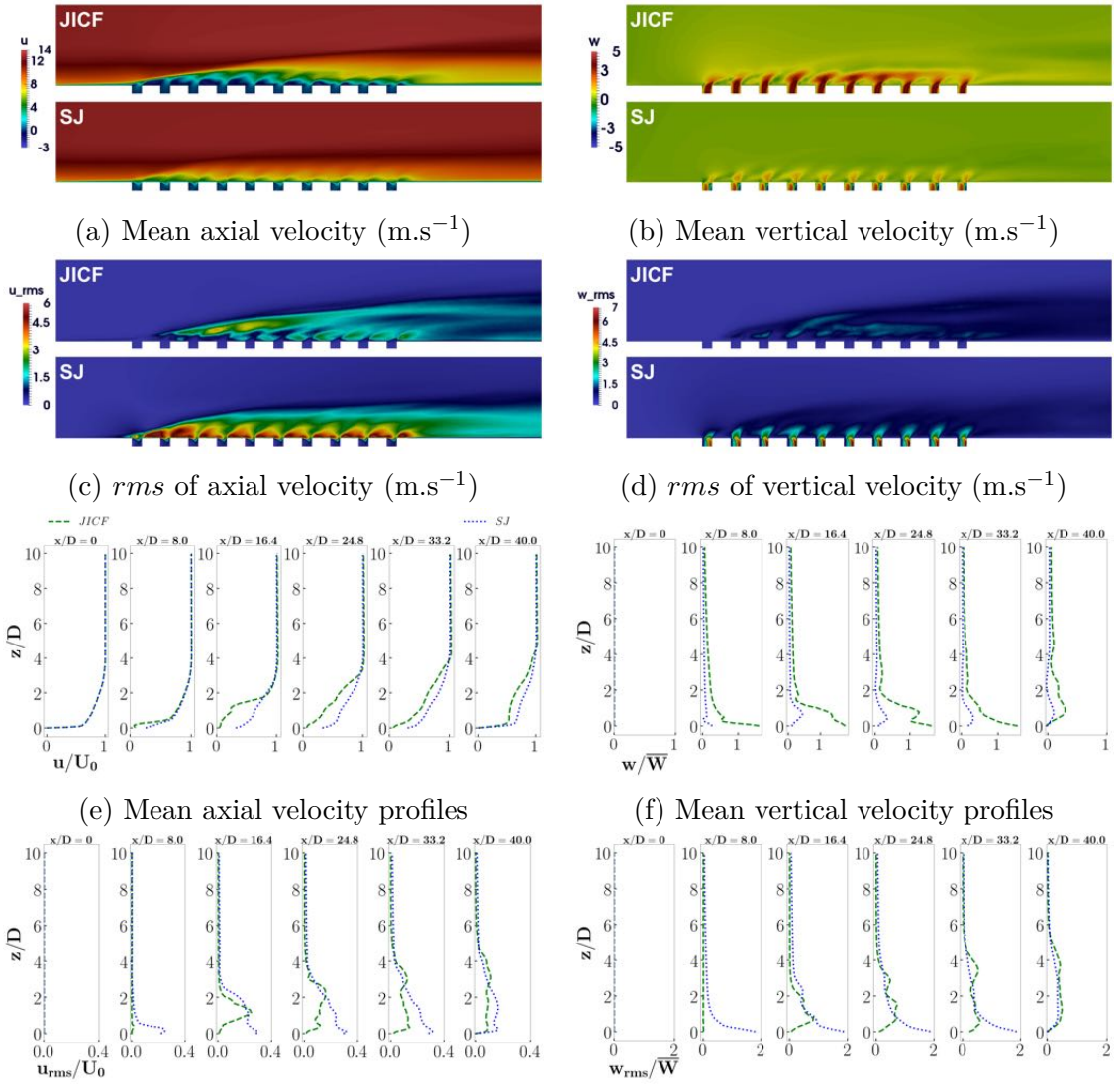

(a) Mean axial velocity (m.s^{-1})

(b) Mean vertical velocity (m.s^{-1})

(c) *rms* of axial velocity (m.s^{-1})

(d) *rms* of vertical velocity (m.s^{-1})

(e) Mean axial velocity profiles

(f) Mean vertical velocity profiles

(g) *rms* of axial velocity profiles

(h) *rms* of vertical velocity profiles

Figure 8.3: Comparison of the time averaged velocity fields along symmetry plane for continuous and synthetic jets.

To begin with, as expected from the flow structure evolution, the JICF establishement requires a longer distance along the plate than the SJ. Then, the velocity profiles (Figs. 8.3e to 8.3h) show that the boundary layer thickness is similar with SJ and JICF along the perforations. This was suspected with the observation of the flow structures: the hairpins reach the same height into the grazing flow in both configurations. However, the profiles are very different within the boundary layer and, at the end of the plate, downstream the perforations, the boundary layer thickens faster in the case of the JICF than for the SJ.

Within the boundary layer, the mean vertical velocity w is higher for the JICF than for the SJ. On the contrary, the axial velocity u is lower and important recirculation zones can be observed between each perforations, especially near the five or six first perforations. They are probably due to an important blockage effect. Similar recirculation zones were observed for the SJ during the ejection mid-period (see Section 5.3.3), but they do not appear in the time-averaged fields. This difference is explained by the unsteady character of SJ *versus* the steady character of JICF. While the time average fields of the JICF case correspond to a continuous ejection, only half of this specific period is present for the SJ, *ie*: the ejection, the other half corresponding to the aspiration. The aspiration mid-period contributes to stabilising the boundary layer and reducing the thickening due to the ejection mid-period. Therefore, on average fields, the jets penetrate lower within the boundary layer. On the contrary, the *rms* velocities u_{rms} and w_{rms} are higher for the SJ than for the JICF, especially near the plate ($z/D < 2$ for u_{rms} and $z/D < 1$ for w_{rms}). This is also attributed to the steady *versus* unsteady characters of the flows.

Time-averaged wall shear stress fields and profiles comparisons are provided for the JICF and SJ in Fig. 8.4. Since similar upstream conditions are used, the wall shear stress evolution far from the perforations ("flat plate") is similar for both cases. On the contrary, large differences are observed around the perforated zone. First of all, in the JICF case, the time-averaged wall shear stress is larger inbetween the jets than in their wakes. In addition, the wall shear stress in the jet axis is even lower than that of the equivalent flat plate. This is due to the strong blockage effect that was identified in the time-averaged velocity fields. The aspiration mid-period, which brings the highest wall shear stress contribution in the SJ case, cannot be retrieved in this continuous jet configuration. The blockage effect appears to be stronger for the first perforation rows, particularly the three first ones. With the first perforation row, the blockage effect is so important that its effect can be seen on the wall shear stress between the jets (see the IB, JICF profile in Fig. 8.4c, with a lower value than that of the flat plate just upstream the first perforation). Inbetween the jets, the JICF wall shear stress profile has several similarities with that of the SJ: at first it remains close to that of the flat plate, then it increases until a plateau value higher than that of the flat plate. However, there are still differences. First of all, as mentionned above, there is a lower peak value just upstream the first perforation row, due to the strong blockage effect, that was not observed for the SJ. Then, between $x/D = 8$ and $x/D = 20$, although the wall shear stress remains near that of the flat plate, it is much more chaotic, with high and low peaks. Finally, after $x/D = 20$,

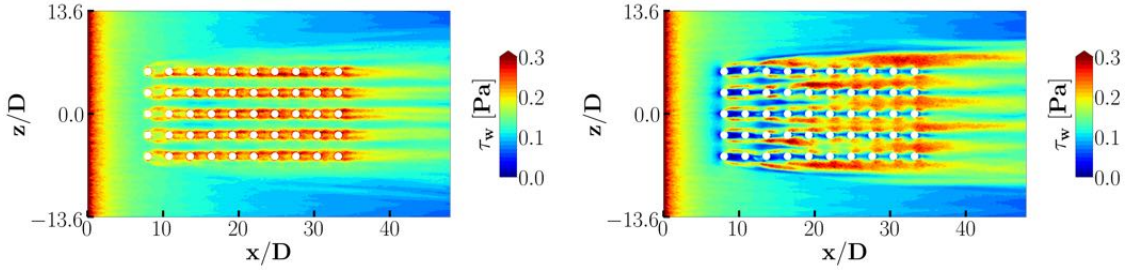

(a) Synthetic jet

(b) Jet in cross-flow

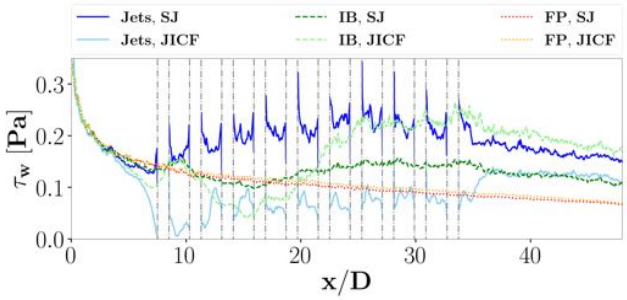

(c) Comparison of SJ and JICF wall shear stress profiles along three axis: the jet axis, the axis between the jet (IB) and far from the perforations (equivalent flat plate, FP)

Figure 8.4: Wall shear stress comparison on SJ and JICF cases.

the wall shear stress increase leads to much higher values than those observed in the SJ case. Donwstream the perforations, the wall shear stress is even higher than that observed in the jet axis for the SJ case. This higher plateau can be explained by the impact of the flow structures in a permanent regime. As already analysed, for the SJ case, although the ejection mid-period leads to a higher wall shear stress, the flow behaviour during the aspiration phase is that of a boundary layer thickening along a flat plate, leading to a much lower wall shear stress.

8.3 Heat transfer

8.3.1 Temperature and wall heat transfer

The heat transfer results are coherent with the aerodynamics ones: similarities between JICF and SJ can be observed but important differences should be pointed out. To support this assertion, the time averaged temperature fields are shown on the symmetry plane in Fig. 8.5, alongside the T_{rms} fields, and on the plate in Fig. 8.6. Then, the Nusselt number of both configurations are compared in Fig. 8.7. The wall temperature fields are obtained with the simulations using a $\Phi = 1500$ W.m^{-2} wall heat flux for the perforated plate. In order to compare more quantitatively the results, the Nusselt number along the jet axis and between the jets is compared for JICF and SJ in Fig. 8.8.

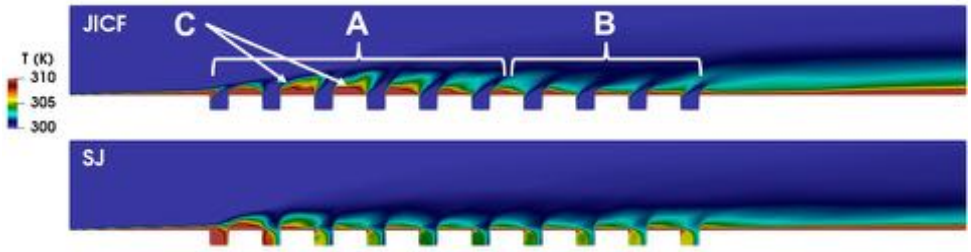

(a) Time-averaged temperature

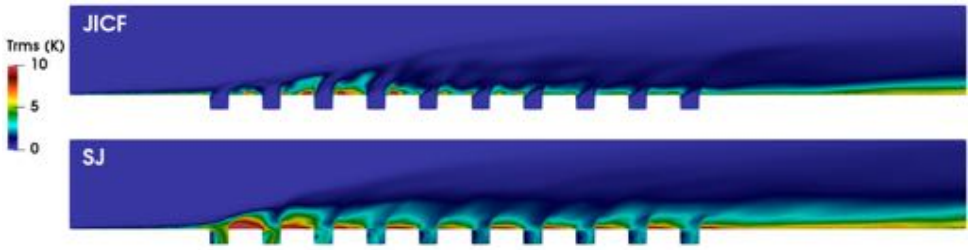

(b) *rms* temperature

Figure 8.5: Time-averaged and *rms* temperature near the perforations along the symmetry plane, for the JICF and SJ configurations.

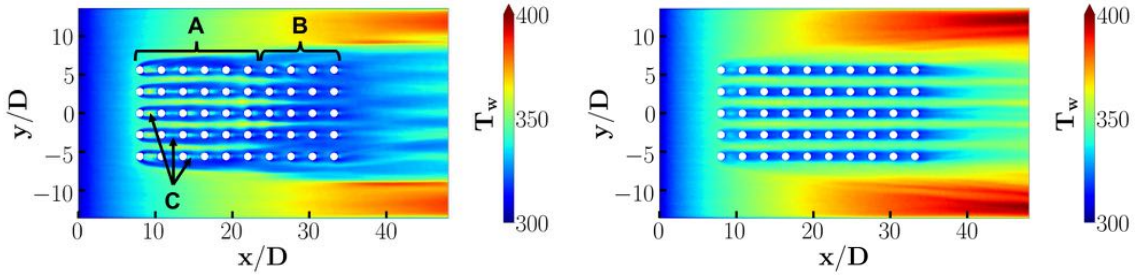

(a) Continuous jets

(b) Synthetic jets

Figure 8.6: Time averaged wall temperature.

First of all, the JICF perforated zone can be divided into two main zones, characterised by totally different behaviours: the upstream part, where the temperature is very heterogeneous (A in Figs. 8.5a and 8.6a), and the downstream part, where it is much more homogeneous (B in Figs. 8.5a and 8.6a). This latter part corresponds to the established flow, and the jets are significantly efficient at cooling down the plate. Two main effects can explain the heterogeneities observed on the upstream part of the perforated area. First, the spanwise expansion of the jets is quite long and it requires a significant distance along the plate for the jets to impact the zone inbetween the perforation lines. Then, the strong blockage effects that were identified on the previous section lead to low velocity zones between two inline perforations, leading to a rising temperature (C in Figs. 8.5a and 8.6a).

The impact of the horseshoe vortices on the plate is much more visible for the

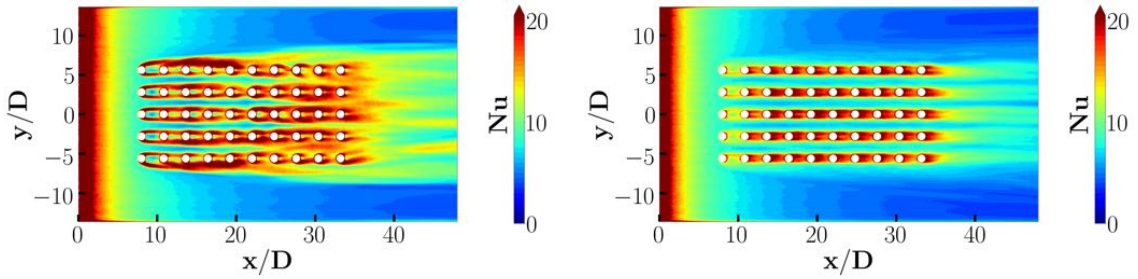

(a) Jets in cross-flow (b) Synthetic jets

Figure 8.7: Time averaged Nusselt number Nu along the perforated plate.

JICF than for the SJ. Moreover, the footprint of these vortices on the plate is clearly visible around several perforation rows for the JICF while for the SJ case, it is observed around the first perforation row only. The absence of these footprints beyond the first row could be due to the aspiration phase, during which no flow structures are ejected and the flow is stabilised. On average, the contribution of the structures would be lowered. The important impact of the horseshoe vortices on the plate heat transfer for the JICF configuration, around the four first perforation rows, could be due to the absence of hairpins. Then, another point needs to be raised: the spanwise expansion of the vortices, which has been shown to be different for each configurations, leads to different impacts on the wall heat transfer. Here again, for the SJ, the temperature and Nusselt number fields result from a combination of the ejection and aspiration mid-period effects. Therefore, the spanwise expansion of the flow structures is observed but it appears to be negligible compared to the significant impact of the aspiration mid-period flow stabilisation. On the contrary, the JICF is chararacterised by a constant ejection so the spanwise expansion is more important: the impact of the flow structures on both sides of the jet wake, downstream the perforations, is more important than that observed for the SJ, where it remains essentially in the perforation wakes due to the aspiration mid-period. This is even more important after the sixth perforation row, where the temperature field becomes homogeneous (identified as zone B in Figs. 8.5a and 8.6a).

Finally, the wall heat transfer can be compared between the two configurations more locally, along the jet axis and between the perforations. In the jet axis, as seen in Fig. 8.8a, the wall heat transfer is higher for the SJ than for the JICF. This is logical since the aspiration mid-period, which exists only for the SJ case, is particularly efficient at decreasing the wall temperatures in the perforation wakes. As a reminder, during the aspiration and downstream the perforations, the flow is stabilised and a new boundary layer is starting. Therefore, the wall shear stress increases and the heat transfer is consequently more important. The Nusselt number comparison provides different results for the axis between the jets, as shown in Fig. 8.8b. There, the Nusselt number is identical for both configurations from the inlet ($x/D = 0$) to the seventh perforation row (around $x/D = 27$). The spanwise expansion of the jets is not important enough to entirely cover the zone between the perforations. Therefore, the heat transfer is much more driven by the upstream flow conditions than by the jets, either continuous or synthetic, which explains the

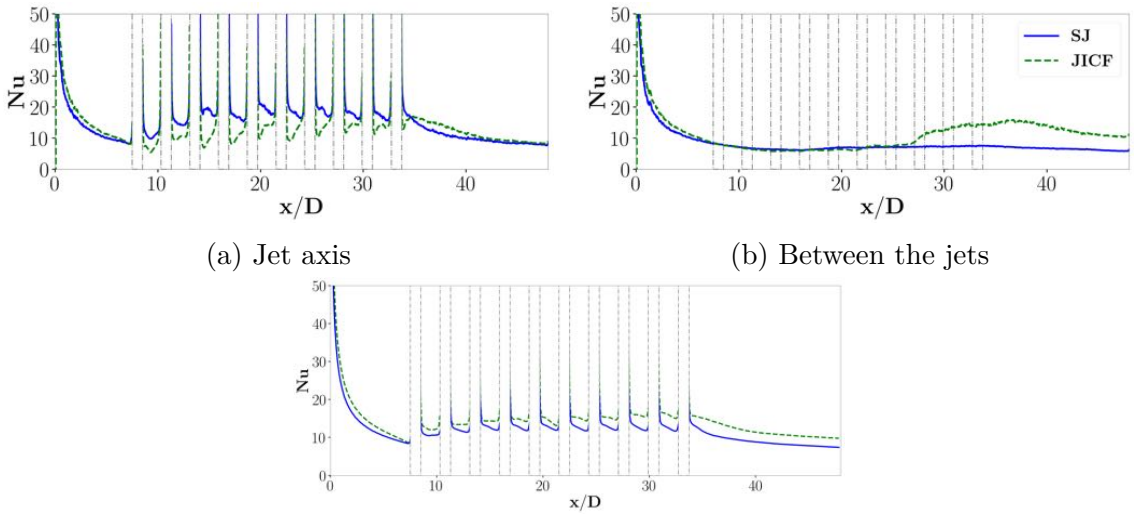

(a) Jet axis

(b) Between the jets

(c) Transverse value

Figure 8.8: Time averaged Nusselt number Nu along the perforated plate.

identical results. After the seventh perforation row, the Nusselt number remains at the same level for the SJ while it rises up to a new plateau value for the JICF. This rise is due to the spanwise expansion of the flow structures, which importantly increases in this zone with the hairpin formation. Finally, the transverse Nusselt number is provided in Fig. 8.8c. The wall heat transfer appears to be globally higher for the JICF than for the SJ case. Although the wall heat transfer seems to rise along the perforations, until the tenth row, no plateau similar to the one observed inbetween the jets can be observed.

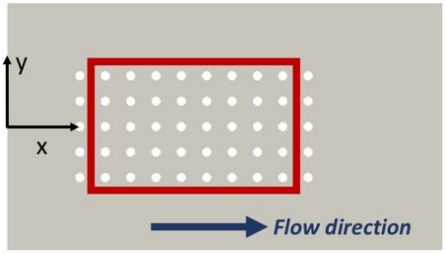

Figure 8.9: Red rectangle: area over which the Nusselt number Nu was integrated.

To complete the comparison, the averaged Nusselt number is calculated for the perforated zone. To do so, the Nu fields are integrated along a specific area of the plate. Indeed, in order to avoid the "flat plate" effects observed far from the perforations, and potential edge effects (such as the strong horseshoe vortices which are seen only on the first perforation row with SJ), not all the plate is considered. The area over which the Nusselt number is averaged is presented in Fig. 8.9. The results are presented in Tab. 8.1. The Nusselt number appears to be around 27 % higher for the JICF than for the SJ. This higher value is coherent with the observation made with the transverse Nusselt number. However, considering the previous analysis of the flow structures and the wall heat transfer as well as the literature, it seems relevant to raise some points that question this result and are discussed in Section 8.3.2.

Case	JICF	SJ
$\overline{h}$ [W.m^{-2}.K^{-1}]	15.6	12.2

Table 8.1: Nusselt number averaged over the perforated zone of the plate.

8.3.2 Discussion

As mentionned before, JICF have been widely studied and are extensively described in the literature. Their geometry has been optimised targeting film cooling applications [56], for example by determining the best spanwise and streamwise distances between the holes, porosity or injection angle. Moreover, it is well known that staggered configurations provide a higher wall heat transfer than aligned jets. From a heat transfer point of view, the JICF configuration used in the present study is under-optimised and a higher heat transfer could be expected with the appropriate geometric parameters. Regarding synthetic jets, it could be imagined to enhance heat transfer through an optimised geometry based on the JICF literature. The following paragraphs discuss the relevance of modifying the jet angle and using a staggered configuration rather than aligned perforations. Finally, the length of the plate and the number of perforations are questionned.

Jet angle. It has been shown that JICF with inclined injections provide a more efficient film cooling than normal ones [132] as used in the present configuration. However, it might be counterproductive to apply such a conclusion to SJ. Indeed, acoustic liner are firstly designed in accordance with acoustic performance objectives, not heat transfer ones. Moreover, SJ flow dynamics implies that the flow goes alternatively in both directions (within and without the resonating cavity, through the neck). Thus, modifying the neck angle based on the optimised geometry of a JICF configuration does not seem such a good idea when talking about acoustic liners. This ejection mid-period might be more efficient in cooling the plate, however the aspiration would be impeded, which would have at least two major drawbacks. (i) The heat transfer would not be that much enhanced and could even decrease since it was seen that the heat transfer is maximised in the jet axis by the aspiration. (ii) Even more importantly, the acoustic damping is ensured by the proper formation of the synthetic jets, thus entraving it would lead to a decreased acoustic performance.

Staggered perforations. Contrarily to the jet angle, staggered configurations should be considered, the main reason being that staggered perforations can already be found in classical acoustic liners. It is thus all the more interesting to ponder whether heat transfer would be increased or decreased in such a configuration, as it is the case for JICF when compared to aligned configurations [132]. The results for the Nusselt number in the jet wakes (Fig. 8.8a) and between the jets (Fig. 8.8b) show that the heat transfer is more important in the jet axis. It was shown that this is essentially due to the aspiration phase, during which the flow is stabilised and a new boundary layer starts over after each perforation. Using a staggered configuration would enable to extend this effect to a larger part of the plate and "break" the developing boundary layer which lowers heat transfer between the jets. All that

being said, the heat transfer is expected to be more important with staggered perforations. It was observed here that the heat transfer was higher for the JICF than for the SJ however the heat transfer is locally higher for the SJ in the jet axis: a staggered configuration could lead to global heat transfer higher for the SJ than for the JICF. However more investigation would be required to support this assumption.

Plate length. Finally, the plate length and number of perforation rows should be discussed. Indeed, it is here limited to 10. However, in real configurations, this number is much more important. Between the jets, the JICF results show a local increase of the Nusselt number after the seventh perforation row, up to a plateau value. Although this plateau is not present in the transverse results and is not retrieved in the SJ results, it could be of interest to determine what would happen with a greater number of perforations. This idea is supported by the results of Duchaine [52] who showed a similar plateau formation on acoustic liner heat transfer.

Chapter conclusions

The synthetic jets of the lab scale, reference operating point were compared to an equivalent, jet in cross-flow configuration. Although the flow structures of the SJ observed during the ejection mid-period show some similarities with those of the JICF, the absence of an aspiration phase on the JICF configuration leads to completely different aerodynamic time-averaged fields, and therefore different wall heat transfer mechanisms. In particular, the cooling due to the aspiration in the jet axis cannot be observed with the JICF. Even more, with this configuration, some recirculation zones, leading to smaller velocities and therefore lower wall shear stress and resulting heat transfer, are observed between two perforations on the same line. On the contrary, the absence of the aspiration phase inbetween the jet axis avoids the flat plate boundary layer that is observed with the SJ, and contributes to decreasing the wall shear stress. It also requires a longer distance for the flow to reach the establishment along the plate. Finally, the comparison with JICF, for which the impact of the perforation geometric parameters on the wall shear stress has been much more studied than for the SJ, raises the question of the interest of a staggered configuration to increase the wall shear stress for the SJ configuration.

9

Investigation of the impact of synthetic jet characteristic parameters on wall heat transfer

The configuration has been detailed and the numerical set-ups as well as the similitude methodology have been validated, before emphasising the important role of turbulence in the jet development and boundary layer evolution. A comparison with continuous jets has also been discussed. The different operating points are now used and compared to each other. The whole database is composed of the experimental data, the simulations on the lab scale configuration, and the simulations on the engine scale configuration. The aim is to understand the importance of the different synthetic jet characterising parameters on the flow mechanics that impact the wall heat transfer within acoustic liners. The results of Pprime are a first start in this work, and the present numerical study enables to extend the data range to more flight realistic conditions.

9.1 Main outcomes of the experimental database

The Pprime experiment [126] considered a large range of operating conditions, as detailed in Tab. 4.2. This enabled the production of a large database, whose analysis evidenced the influence of different parameters on wall heat transfer. This section briefly summarises their main conclusions before reminding the operating points that were considered for the numerical study.

One of the main results of Giachetti *et al.* [126] is the important heat transfer enhancement that can be obtained with synthetic jets when compared to a classical flat plate with a grazing flow. Figure 9.1 provides the comparison of the Nusselt

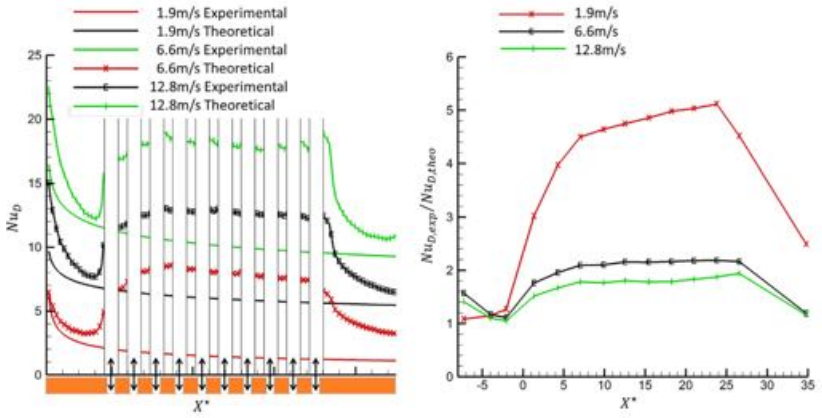

Figure 9.1: Nusselt number evolution when varying incoming flow velocity U_0 along the plate for different operating conditions, compared to the equivalent theoretical flat plate [126]; $f = 12.8$ Hz, $K = 11$ mm.

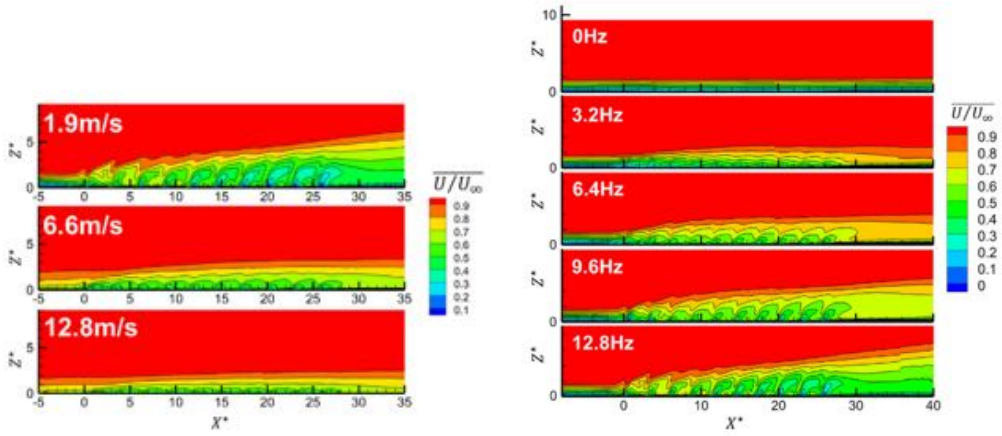

(a) U_0 impact ($f = 12.8$ Hz, $K = 11$ mm, $\overline{W} = 2.07$ m.s^{-1})

(b) $\overline{W}$ impact ($U_0 = 1.9$ m.s^{-1}, $K = 11$ mm)

Figure 9.2: Time-averaged axial velocity u fields for varying incoming flow velocity U_0 (a) and varying piston frequency f (b) [126].

number of different operating points (change in grazing flow velocity U_0) with the equivalent theoretical flat plate (left, Nu_D), along with the same experimental Nusselt number normalised by the equivalent theoretical flat plate Nusselt value (right, $Nu_{D,exp}/Nu_{D,theo}$). All of the cases are characterised by an increase of the Nusselt number with regard to the equivalent flate plate. In their study, a maximal increase of 175% was reached for the lower U_0 case.

The second important conclusion of their study is the key role of the velocity ratio $M = \overline{W}/U_0$ in the heat transfer gain, which can already be noticed in Fig. 9.1. Indeed, the higher this ratio, the higher the impact of the jets on the plate and the higher the Nusselt number. This can be seen in Figs. 9.2 and 9.3. Figure 9.2 shows the mean axial velocity fields for different operating points. in Fig. 9.2a, the jet velocity $\overline{W}$ is fixed and the upstream velocity U_0 is the considered variable pa-

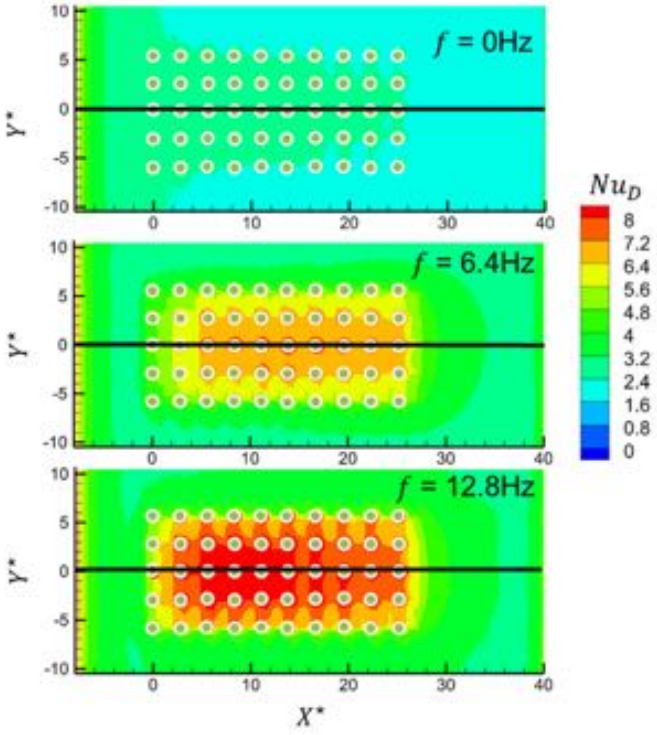

Figure 9.3: Time-averaged Nusselt number fields for varying piston frequency f with $U_0 = 1.9$ m.s^{-1}. $f = 0$ Hz: $\overline{W} = 0$ m.s^{-1}, $M = 0$; $f = 6.4$ Hz: $\overline{W} = 1.04$ m.s^{-1}, $M = 0.55$; $f = 12.8$ Hz: $\overline{W} = 2.07$ m.s^{-1}, $M = 1.09$ [126].

rameter. On the contrary, in Fig. 9.2b, U_0 is fixed and different values of $\overline{W}$ are compared (through the frequency of the pistons f). Both comparisons lead to the same conclusion: an increase of the velocity ratio M leads to the formation of synthetic jets that penetrate higher into the boundary layer and have a greater impact on its development. This leads to an increased impact on wall heat transfer, as shown in Fig. 9.3 with the Nusselt number fields for different M values.

Finally, a third point was evidenced by the analysis of Giachetti *et al.* The jet velocity $\overline{W}$ depends on the frequency f as well as the amplitude K of the pistons. Giachetti *et al.* observed that modifying $\overline{W}$ through either f of K, at fixed U_0 values, had the same consequences, as can be seen in Fig. 9.4. This evidences that the leading parameter is $\overline{W}$ and, since these observation were made at iso-U_0, the velocity ratio M.

The present numerical study is complementary to the experiment and brings more knowledge about the synthetic jet impact on the wall heat transfer. Several experimental operating points were simulated and their results compared to the experimental data. However, the point was not to just reproduce the experimental results but to go further. This being said, and taking into account the cost of the simulations, not all of the experimental operating points were numerically reproduced. In the end, three types of operating points were simulated: (i) the direct reproduction of some selected experimental operating points, for the sake of vali-

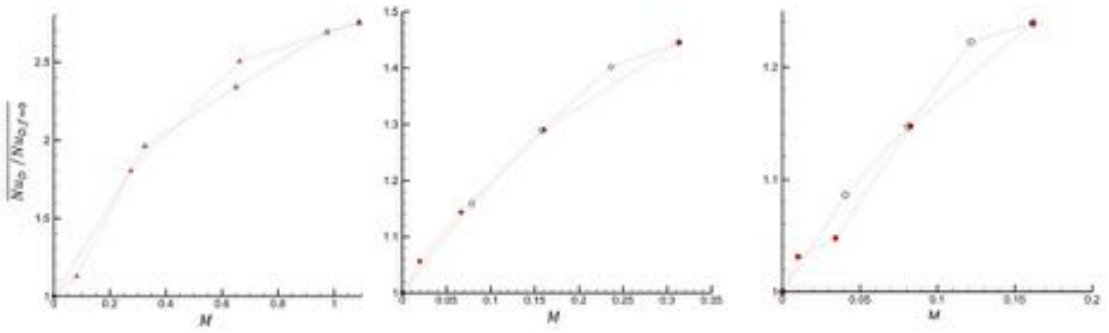

(a) $U_0 = 1.9$ m.s^{-1} (b) $U_0 = 6.6$ m.s^{-1} (c) $U_0 = 12.8$ m.s^{-1}

Figure 9.4: Time-averaged Nusselt number ratio evolution according to the velocity ratio M, for three axial velocity U_0 [126]. Solid symbols correspond to the modification of the amplitude and empty symbols to the modification of the frequency.

dation; (ii) the same operating points applied to the engine scale configuration, in order to validate the representativity of the lab-scale rig; (iii) some more operating points with the engine scale configuration in order to extend the range of the considered operating conditions. The complete set of numerical operating conditions is reminded in Tab. 9.1. Operating conditions on the engine-scale set-up were chosen so as to cover a large range of velocity ratio $M = \overline{W}/U_0$, since Giachetti *et al.* showed the importance of this parameter. Different values of dimensionless stroke length L_0/D and jet Reynolds number Re were also considered. Since Giachetti *et al.* showed that changing either the frequency or the amplitude of the pistons led to similar impacts on the jet velocity, and for the sake of lowering the simulation costs, it was also chosen for the lab scale simulations to use only the highest experimental frequency ($f = 12.8$ Hz). When required, the jet velocity was changed only through the piston amplitude. The operating point presented and analysed in Chapter 5 is used as reference, with both lab and engine scale configurations, and other cases are compared to it. Five of those operating points are more specifically analysed in the present chapter. Two lab scale operating points are developped. The first one, refered to as "low M", other things being equal, is characterised by a lower amplitude K of the pistons than the reference case, leading to a lower velocity ratio M and dimensionless stroke length L_0/D. Then, the "high M" case is characterised by a lower axial velocity U_0 and a laminar profile (adapted from the experimental data). This low axial velocity leads to higher velocity ratio M and dimensionless stroke length. This point led to the generation of a mesh dedicated to this case, as discussed in Section 4.2.2.2, in order to ensure that the synthetic jet behaviour would be correctly simulated. Along with the turbulent case (see Chapter 7), this operating point enables the investigation of the importance of the upstream conditions on the synthetic jet development and resulting wall heat transfer. It should be kept in mind that these different velocity ratios are not obtained by modifying the same jet parameter for both cases, which impacts the flow in different ways and enables the analysis of the importance of different flow parameters. Finally, in addition to the reference case for which the Mach number is equal to 0.24 at engine scale, three operating points are considered with the engine scale to cover a large range of

upstream Mach number and velocity ratio values: a case with a Mach number equal to 0.12, and, in order to extend the analysis to more flight-representative conditions, two cases with a Mach number equal to 0.60. These two latter operating points differ by the SPL of the acoustic signal imposed at inlet: 150 dB for the first one (which is similar to the other cases) and 139 dB for the second one. In this case, the velocity ratio is even lower than in the lab scale "low M" case. The ojective is to observe the wall heat transfer within a liner in a linear acoustic regime (*cf.* Chapter 1). Indeed, in the piston configuration, the jet velocity and stroke length are directly defined by the amplitude and frequency of the pistons. In a real liner, the synthetic jet parameters depend on the impacting acoustic signal characteristics and are formed only at a high enough Sound Pressure Level, in a regime called "non-linear". At lower SPL, the acoustic response of the liner is reduced and much smaller vortices are formed. For these three new cases (Mach 0.12 and Mach 0.6), the upstream conditions were not experimentally considered. In the absence of experimental data, the velocity profile of such a case is not known. Therefore, the velocity profile that was injected is that of the reference case, which also corresponds to turbulent regime, scaled to get the adequate velocity U_0 far from the wall.

The analysis of the results for both lab and engine scale configurations, are detailed in Section 9.2. Finally, a synthesis of the results, with comparisons of the different operating points in regard to the jet characterising parameters, is developed in Section 9.3.

Lab scale configuration							
Case name	U_0 (m.s^{-1})	f (Hz)	K (mm)	$\overline{W}$ (m.s^{-1})	Re	L_0/D	M ($\times 10^{-2}$)
Reference	12.8	12.8	11	2.07	829.2	12.94	16.17
Low M	12.8	12.8	2.35	0.44	176.4	2.75	3.44
High M	1.9	12.8	11	2.07	829.3	12.94	108.95
Engine scale configuration: experimental operating conditions							
Case name	U_0 (m.s^{-1})	f (Hz)	SPL (dB)	$\overline{W}$ (m.s^{-1})	Re	L_0/D	M ($\times 10^{-2}$)
Reference, Mach 0.24	80 (12.8)	500 (12.8)	150	14.2 (2.27)	910.3	14.2	17.75
Engine scale configuration: extended operating conditions							
Case name	U_0 (m.s^{-1})	f (Hz)	SPL (dB)	$\overline{W}$ (m.s^{-1})	Re	L_0/D	M ($\times 10^{-2}$)
Mach 0.12	41.25 (6.6)	500 (12.8)	150	19.6 (3.1)	1256.4	19.6	47.51
Mach 0.60, high SPL	208.31 (33.3)	500 (12.8)	150	7.6 (1.2)	487.2	7.6	3.65
Mach 0.60, low SPL	208.31 (33.3)	500 (12.8)	139	2.39 (0.4)	153.2	2.39	1.15

Table 9.1: Overview table of the numerical operating points. Main flow parameters (left) and corresponding dimensionless parameters (right). For the engine scale cases, the similitude-equivalent parameters of the lab scale configuration are provided in brackets.

Discussion on the jet velocity $\overline{W}$. The analysis of the jet velocity in the engine scale configuration raised an additional limitation to the use of pistons to reproduce the liner behaviour. With the lab scale configuration, the jet velocity $\overline{W}$ is entirely defined by the amplitude and frequency of the pistons. Therefore, the jet Reynolds number Re and stroke length L_0 depend only on these piston parameters and the upstream conditions, including the axial velocity U_0, only impact the velocity

ratio M. If this statement were still valid for the engine scale configuration, the jet velocity would only depend on the acoustic signal frequency and amplitude. As already mentionned in Chapter 6, for the engine scale configuration, the jet velocity does not depend only on the acoustic conditions but also on the grazing flow velocity. With three operating points that only differ by the axial velocity U_0, the jet velocity $\overline{W}$ is equal to 19.6 m.s^{-1} at Mach 0.12, 14.2 m.s^{-1} at Mach 0.24 and 7.6 m.s^{-1} at Mach 0.60 and 150 dB (*ie* all other things being equal with the other two operating points).

9.2 Effect of jet velocity ratio on fluid dynamics and wall heat transfer

As for the previous chapters, the numerical results are presented in the following order: the flow behaviour is first observed (Section 9.2.1), then its impact on the wall heat transfer is analysed (Section 9.2.2). The objective is now to compare the different operating points and the impact of several synthetic jet parameters on the wall heat transfer enhancement.

9.2.1 Flow field

The velocity fields in the symmetry plane, that is to say the jet axis, are presented in Figs. 9.5 (for the mean and *rms* axial velocities) and 9.6 (for the mean and *rms* vertical velocities), for the lab scale cases only. The velocity profiles extracted from these planes are presented in Figs. 9.7a, 9.7b, 9.8a and 9.8b.

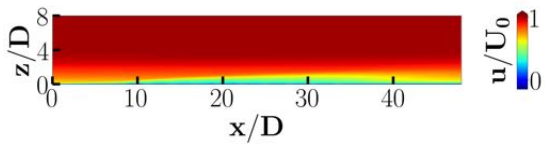

(a) Low M (Low K), time-averaged

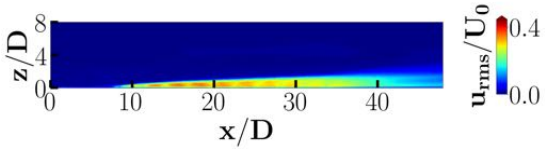

(b) Low M (Low K), *rms*

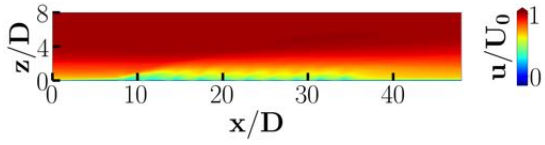

(c) Reference, time-averaged

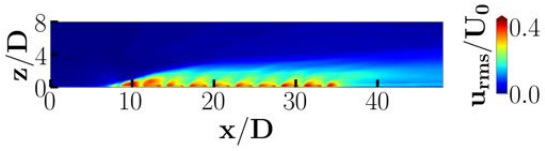

(d) Reference, *rms*

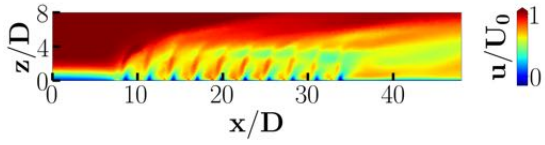

(e) High M (low U_0), time-averaged

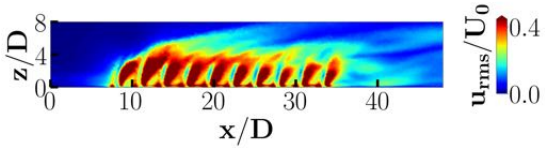

(f) High M (low U_0), *rms*

Figure 9.5: Axial velocity fields. Lab scale.

Similarly to the experimental results, the velocity fields, presented in Figs. 9.5 and 9.6, show that a higher velocity ratio M leads to a higher penetration of the jets into the grazing flow boundary layer. The low M vertical velocity fields show that the resulting jets penetrate lower into the grazing flow and tend to be more folded than that of the reference case. The boundary layer thickening is thus lower, as seen with the comparison of the axial velocities. For the high M case, the jets are not really folded and are even strong enough to remain almost vertical. Moreover, they penetrate into the grazing flow much higher than in the other cases and outreach the grazing flow boundary layer.

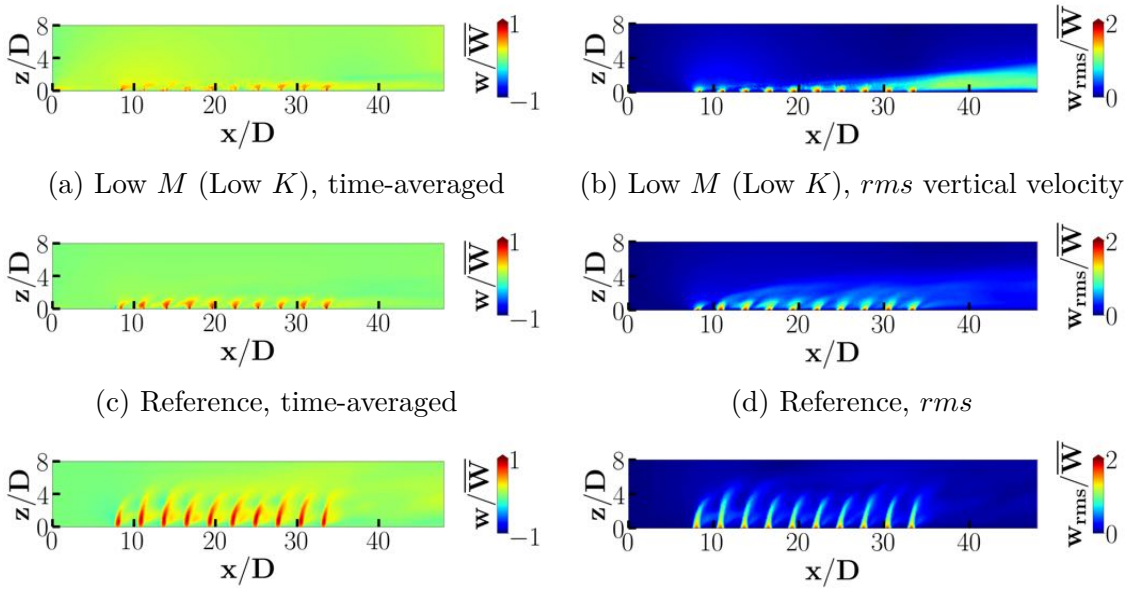

(a) Low M (Low K), time-averaged

(b) Low M (Low K), rms vertical velocity

(c) Reference, time-averaged

(d) Reference, rms

(e) High M (low U_0), time-averaged

(f) High M (low U_0), rms

Figure 9.6: Vertical velocity fields. Lab scale.

The velocity profiles bring similar information than the fields but enable to quantify more accurately the differences. More specifically, the boundary layer thickening due to the jets can be estimated. This thickening appears to be almost similar for the reference and low M cases. For these cases, the jets penetrate into the boundary layer and modify its inner behaviour in different ways but lead to a similar boundary layer thickening. The boundary layer thickness can be evaluated around $z/D = 3$ along the plate (axial velocities, Fig. 9.7a) while the jets can reach $z/D = 2$ (vertical velocities, Fig. 9.8a). On the contrary, as noticed with the velocity field, the high M case is characterised by jets wich are strong enough to outreach the boundary layer and penetrate higher into the grazing flow, and can reach heights as high as $z/D = 8$.

Velocity profiles for the engine scale configuration are provided in Figs. 9.9 and 9.10. As discussed before, the normalised operating points are almost identical to the lab scale ones, but only the main trends are targetted on this study. The observations are globally similar to that made with the lab scale cases. In particular, the higher the velocity ratio (*ie*: the lower the Mach number), the higher the

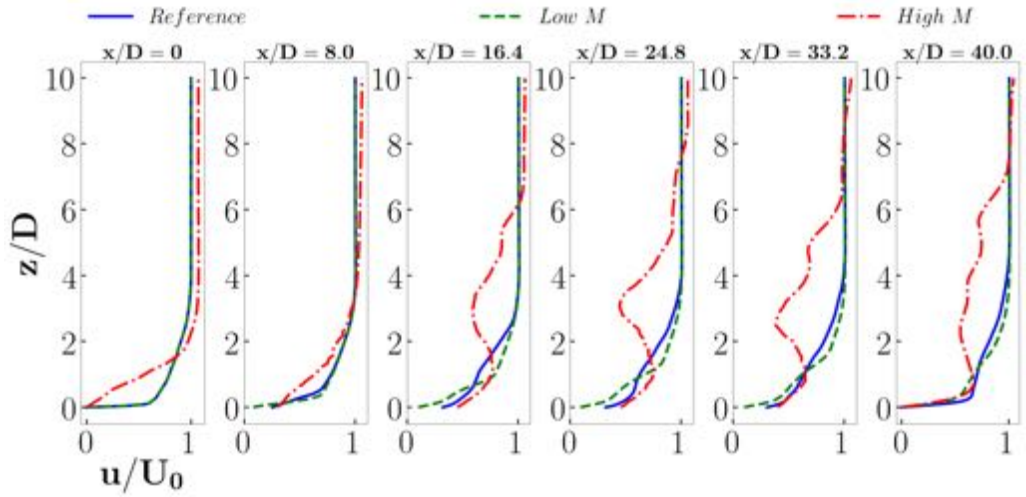

(a) Mean axial velocity

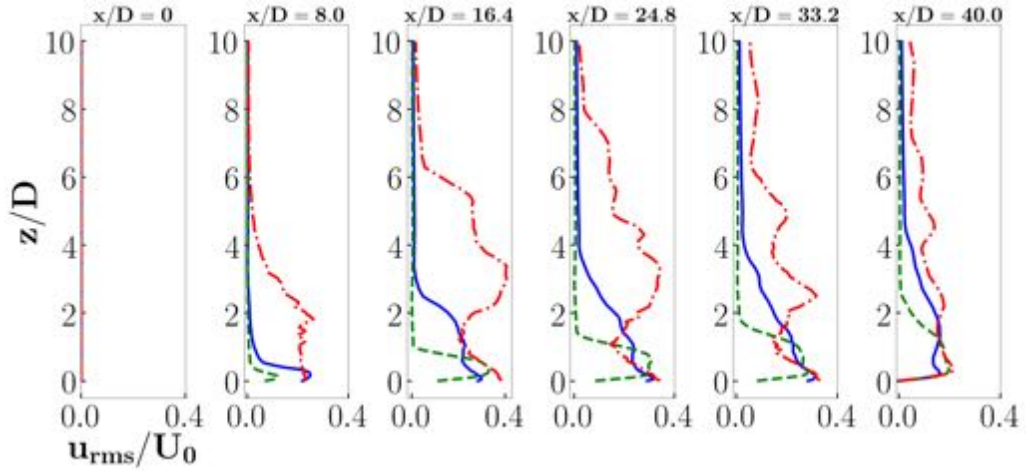

(b) *rms* axial velocity profiles

Figure 9.7: Axial velocity profiles for different operating points. Lab scale.

penetration of the jets into the boundary layer. The jet velocity profiles (Fig. 9.10) show that the jets can reach $z/D = 2$ for the *Mach* 0.12 and *Mach* 0.24 cases, while the jets in the *Mach* 0.60 cases do not get higher than $z/D = 1$. The axial velocity profiles (Fig. 9.9), which enable to observe the boundary layer evolution, show that in the highest velocity ratio case (*Mach* 0.12), the boundary layer thickens until $z/D = 5$ while for the lowest velocity ratio value (*Mach* 0.60) it is lower than $z/D = 4$.

9.2.2 Wall heat transfer

9.2.2.1 Temperature evolution through a whole period

As already described in the previous chapters, the flow dynamics is driven by the jets that impose a periodic behaviour, with important differences between the ejection

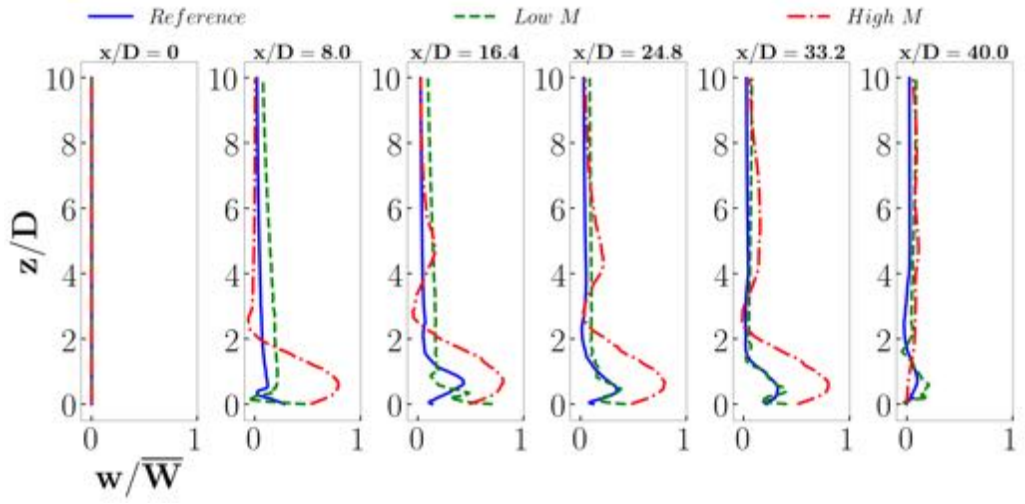

(a) Mean vertical velocity

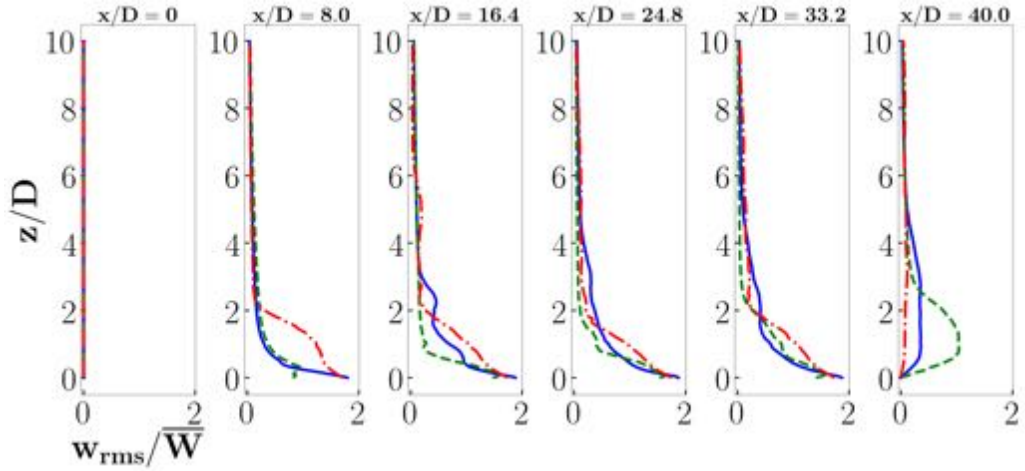

(b) *rms* vertical velocity

Figure 9.8: Vertical velocity profiles for different operating points. Lab scale.

and suction mid-periods. This behaviour is also different from one place to another along the perforated plate: different flow characteristics were shown for the jet axis, between the jets and far from the jets (also refered to as "flat plate"). Therefore, the temperature evolution through time is different for these three axes. Temperature PDF were described in Section 5.3.4 for the lab scale, reference operating point. The objective is now to compare similar results for different operating points. These results are shown in Fig. 9.11 for the jet axis and in Fig. 9.13 for the between-the-jets axis. Same results, but normalised by the equivalent flat plate mean temperature, are shown in Figs. 9.12 and 9.14. Three of these operating points correspond to the lab scale. Results for the reference operating point are provided, along with those of the low M case (low K), and the high M case (low U_0). For the engine scale, results for the reference (Mach 0.24) and the Mach 0.60, 150 dB cases only are also provided. The engine-scale reference case enables to compare results between the two scales, and the Mach 0.60 case provides results for a high grazing flow velocity which is not reached with the lab scale configuration.

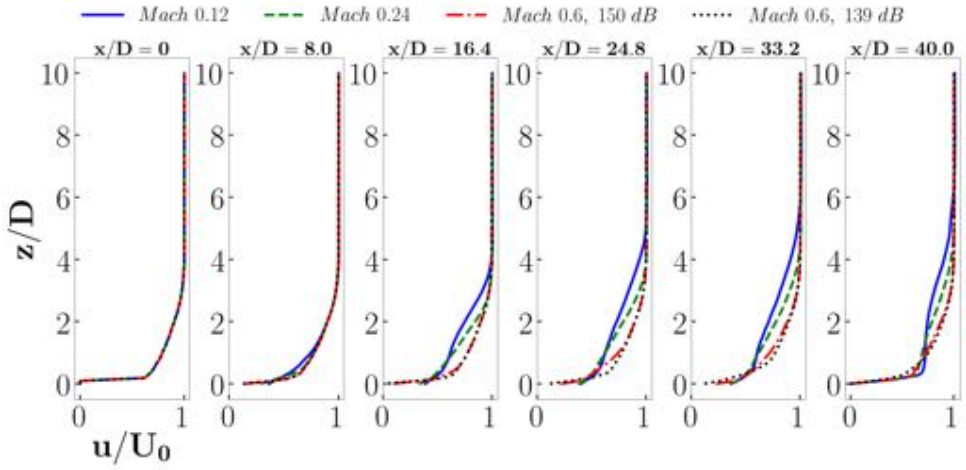

Figure 9.9: Mean axial velocity profiles. Engine scale.

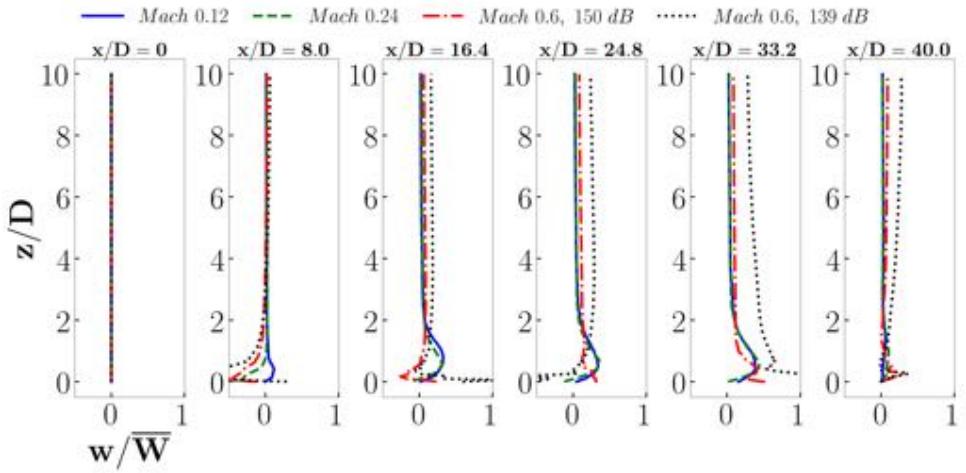

Figure 9.10: Mean vertical velocity profiles. Engine scale.

- **Low M (low K):** This operating point is characterised by a lower velocity ratio $M = \overline{W}/U_0$, while the upstream flow conditions remain similar to that of the reference operating point. This leads to the formation of synthetic jets that are less efficient to decrease the wall temperature than for the reference case. Several aspects support this statement. First of all, the range of possible temperature is wider and reaches much higher values than those obtained with the reference case, both in the jet axis and between the jets. Secondly, either maximal, minimal and mean values are higher for the present case than the reference one. In the symmetry plane, the peak effect that was observed only between the first and second perforation can here be seen between the first and second perforation, but also be seen between the following perforations. The temperature decrease just upstream of the first perforation, due to the blockage effet, is also smaller. Finally, between the jets, the enveloppe is much narrower. This result is thus closer to that of the flat plate, at least

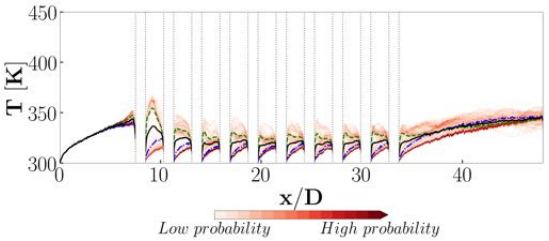

(a) Lab scale, reference case

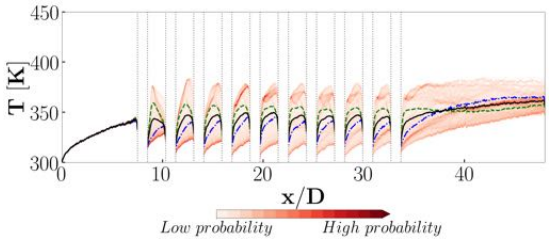

(b) Lab scale, low M

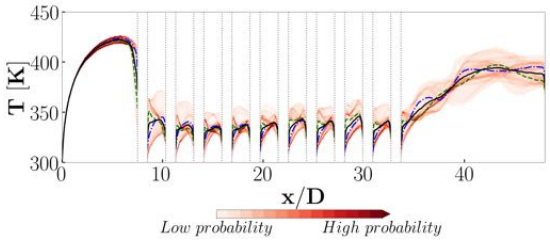

(c) Lab scale, high M

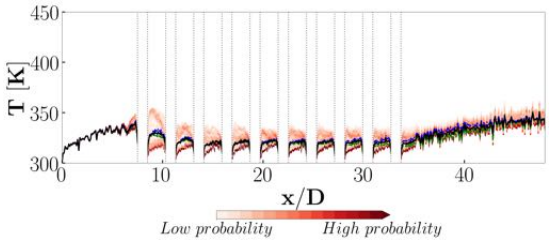

(d) Engine scale, reference case

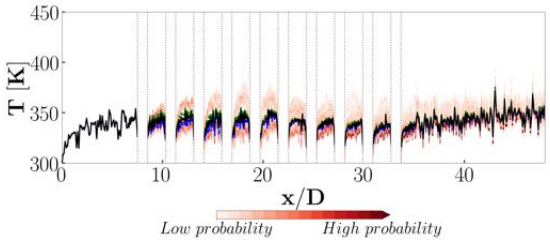

(e) Engine scale, Mach 0.6

Figure 9.11: PDF of wall temperature for different operating points in the jet axis.

until $x/D = 28$, showing that the jets and the flow structure they generate do not expand spanwise as much as in the reference case. Even downstream $x/D = 28$, the PDF coloration shows that the temperature is more likely to follow the flat plate temperature evolution. Similar conclusions can be made from the normalised figures.

- **High M (low U_0):** The jets expand more widely in the spanwise direction: it is the only case for which the blockage effet, and the resulting temperature decrease just upstream of the first perforation, can be observed on the inbetween-jet axis. Also, with these different upstream conditions, the flat plate results that were obtained for the reference case can no longer be considered as equivalent to this configuration. This is clearly visible upstream and downstream of the perforations, where the temperature reaches much higher values than for the reference case (greater than 400 K), implying a cooling less efficient than for the reference case. On the contrary, the normalised values show that the jets are much more efficient in this high M case than in the reference case, including inbetween the jets. The comparison of this two cases is useful to observe the two competing phenomena that contribute to the wall heat transfer: the jets, but also the upstream conditions which can play a significant part. (i) For a classical flat plate, the higher the flow velocity is, the higher the wall heat transfer is. Thus, for a higher U_0, it is expected to

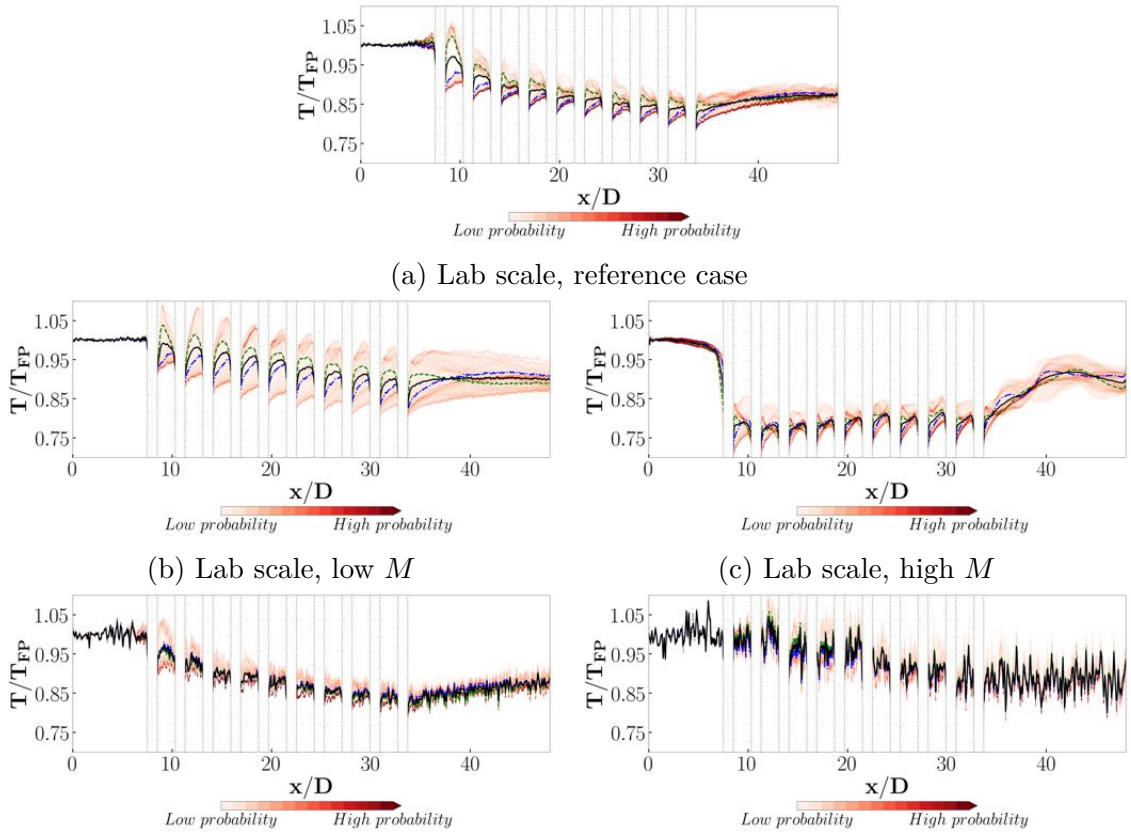

(a) Lab scale, reference case

(b) Lab scale, low M

(c) Lab scale, high M

(d) Engine scale, reference case

(e) Engine scale, Mach 0.6

Figure 9.12: PDF of wall temperature for different operating points in the jet axis, normalised by the equivalent flat plate time-averaged wall temperature.

observe lower temperatures, more specifically between the jets where the flow evolution corresponds to that of a flat plate case during the aspiration mid-period. (ii) Other things being equal, increasing the flow velocity leads to a smaller jet velocity ratio $M = \overline{W}/U_0$. Therefore, the contribution of the jets to the wall heat transfer is lowered. The high Mach number case, based on the engine scale, is used to determine how these competing phenomena impact the wall heat transfer for high velocity grazing flows.

- **Engine scale, reference case:** The engine scale, reference case wall temperature PDF is presented here to briefly compare engine and lab scales. The main trends are present in both cases, although some local differences can be observed. For example, the peak effect between the first and the second perforations is not as important in the engine scale case as in the lab scale case. As for previous results, it can also be noticed that the results for the engine scale case, especially the mean values, are noisier than for the lab scale. This is due to the higher wall Y^+ that was obtained with the engine scale mesh.

- **Engine scale, Mach 0.60, 150 dB:** This point corresponds to a very low velocity ratio M. Due to the high velocity grazing flow, and since the mesh was not adapted to this specific point, the Y^+ values are higher than for the

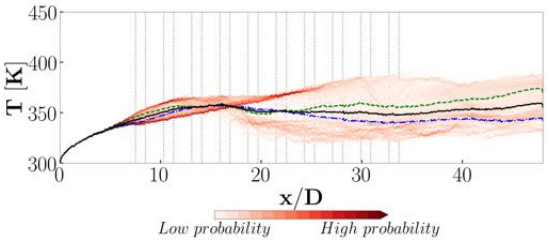

(a) Lab scale, reference case

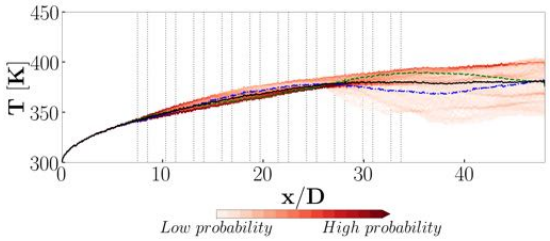

(b) Lab scale, low M

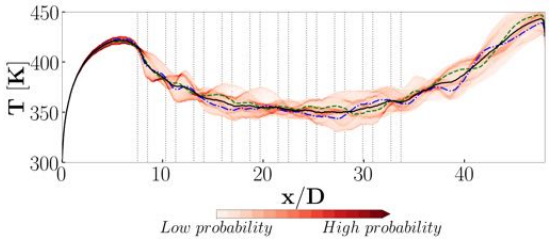

(c) Lab scale, high M

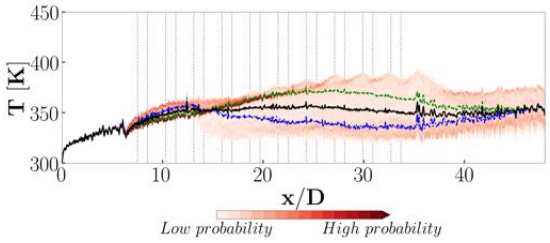

(d) Engine scale, reference case

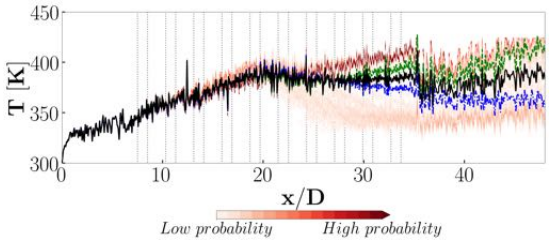

(e) Engine scale, Mach 0.6

Figure 9.13: PDF of wall temperature for different operating points between the jets.

reference case which explains the important fluctuations that can be observed. A first point that should be noted is that it takes a longer distance to get a plateau of temperature in the jet axis: around $x/D = 25$ (seventh perforation), to be compared with the reference case: around $x/D = 12$ (third perforation). It is even more visible between the jets, where the enveloppe remains very narrow and close to the equivalent flat plate until $x/D = 20$. This behaviour, similar to that of the lab scale, low M case, indicates that the synthetic jets do not expand widely enough in the spanwise direction to impact the plate temperature on this axis. As discussed for the lab scale high M case, two competing phenomena are observed: the high velocity grazing flow contributes to increase the wall heat transfer, but also to decrease the contribution of the synthetic jets in the wall heat transfer enhancement. However, although the jets are not as efficient as in the reference case, they still play a part in enhancing heat transfer: temperatures are still lower than for the equivalent flat plate as can be seen with the normalised values. It seems that, between the jets, the temperature can locally get higher than that of the flat plate. This is not expected since with the low M value and raw temperature PDF suggest that this operating point low jets hardly reach the zone near the jets, and the flow dynamics and wall heat transfer should be led almost only by the upstream conditions. Therefore, values close to 1 should be observed for the

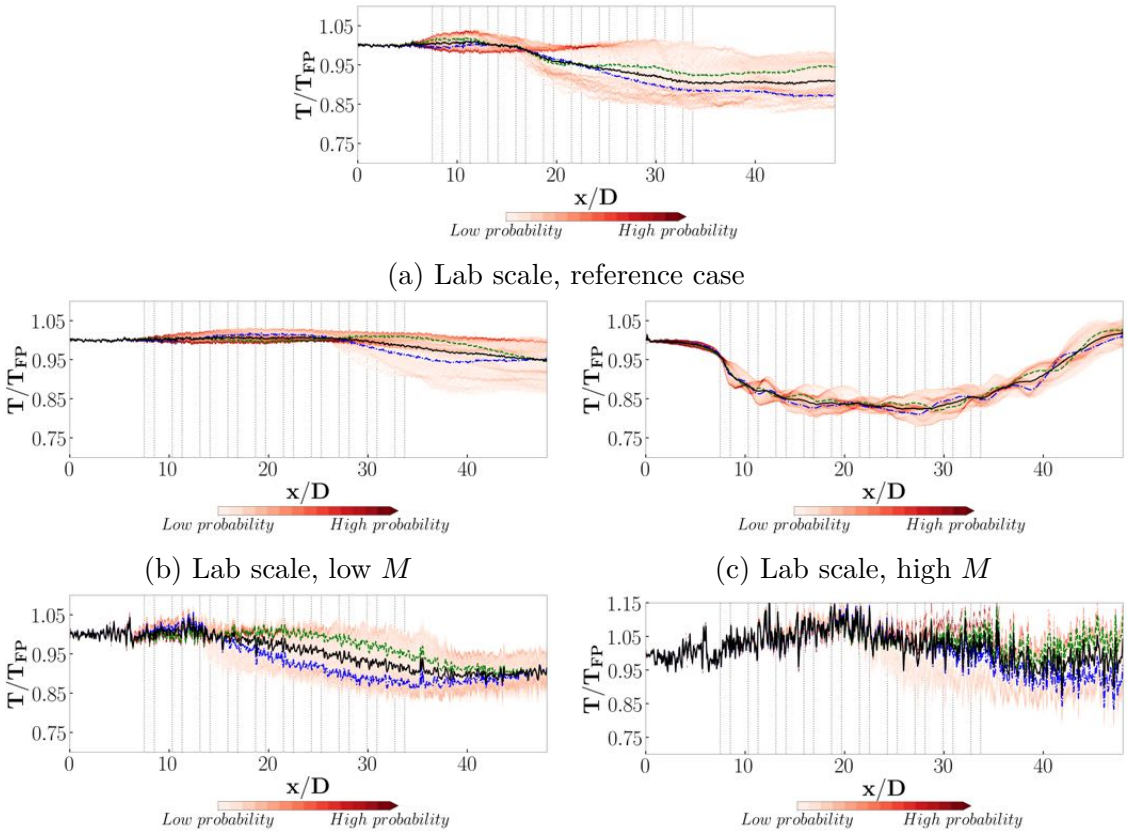

(a) Lab scale, reference case

(b) Lab scale, low M

(c) Lab scale, high M

(d) Engine scale, reference case

(e) Engine scale, Mach 0.6

Figure 9.14: PDF of wall temperature for different operating points between the jets, normalised by the equivalent flat plate time-averaged wall temperature.

normalised data, such as for the lab scale, low M case. It is thus wondered whether the mesh quality plays a part there.

Another way to investigate the temperature evolution is presented in Figs. 9.15 and 9.16 for four operating points. The temporal evolution of the temperature (y axis) over three acoustic periods is shown alongside different line cuts along the perforated plate (x axis) for the jet axis (Fig. 9.15) and between the jets (Fig. 9.16). Note that the colorbars have been adjusted to the proper range for each operating condition. The operating points are presented from the lowest to the highest grazing flow Mach numbers, *i. e.* from the highest to the lowest velocity ratio M (except for the latest case, for which the synthetic jets are triggered by a different acoustic signal).

Similar patterns are found for the different cases. In particular, the alternation of ejection and aspiration mid-period are visible through the alternation of higher and lower temperatures, in the jet axis. Between the jets, this is opposite: the coldest temperatures correspond to the ejection while the highest ones correspond to the aspiration. The peak phenomenon, more important in the reference case, is well retrieved as well as the blockage effect upstream the first perforation. This visualisation also enables to observe the convection of the flow structures donwstream the

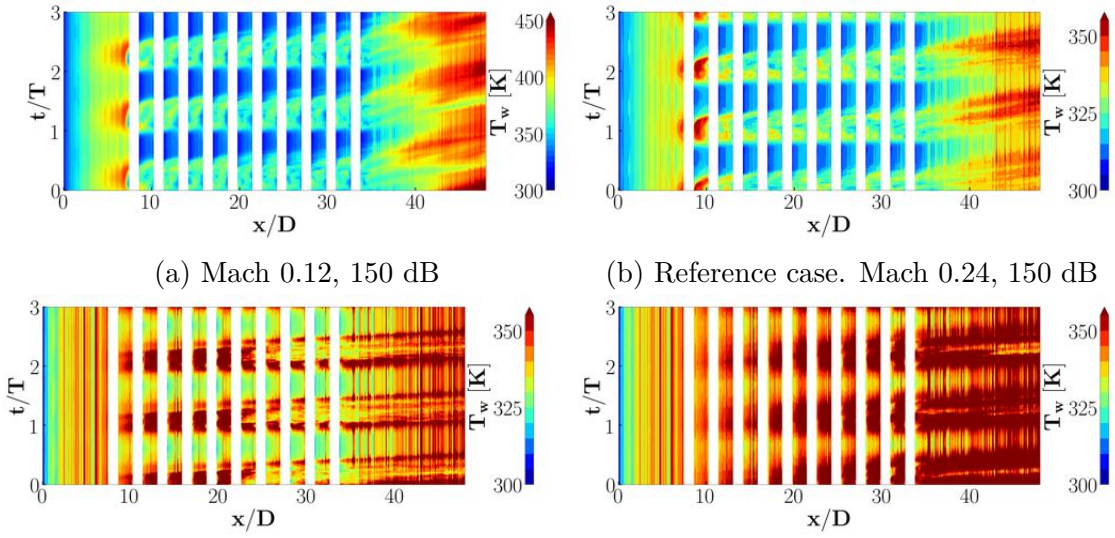

(a) Mach 0.12, 150 dB

(b) Reference case. Mach 0.24, 150 dB

(c) Mach 0.6, 150 dB

(d) Mach 0.6, 139 dB

Figure 9.15: Temperature time evolution through three periods. Engine scale, , $\Phi = 1500 * 6.25$ W.m^{-2}. Jet axis.

perforations. The angle α of the different color stripes with the horizontal is directly correlated to the flow velocity. Indeed, the mean velocity V of a structure convected on a distance d during the time t is found to be equal to: $V = D/t = 1/\tan\alpha$. Since the convection velocity increases with a higher grazing flow Mach number, the higher the Mach number, the lower the angle. Another information, which was not visible with the PDF figures, is the fact that, for all of the cases, the ejection can be roughly characterised by the alternation of three coloured stripes: the first and the last one correspond to higher temperatures, while the middle stripe shows a short temperature decrease. This fact is more visible in the jet axis. A reverse phenomenon can be seen between the jets, with two colder stripes surroundind a higher temperature stripe. This succession of two temperature peaks might be linked to the evolution of the temperature observed within the perforations in Section 6.2.1.

The high Mach number cases are characterised by higher temperatures than the reference case, as already shown with the PDF figures. Although the higher velocity grazing flow contributes to enhance heat transfer, the jet velocity ratio is lowered and so is their cooling contribution. During the ejection, the low temperature stripes are not completely established until x/D around 25. This is even truer between the jets, where the impact of the flow structures are not visible upstream of the second perforation, for the 150 dB case, and even $x/D = 20$ for the 139 dB case. For this latter case, the velocity ratio is even lower than for the Mach 0.6, 150 dB case.

9.2.2.2 Nusselt number

The time averaged Nusselt number Nu is presented for different operating points, on the lab scale configuration, in Fig. 9.17. In order to better compare the oper-

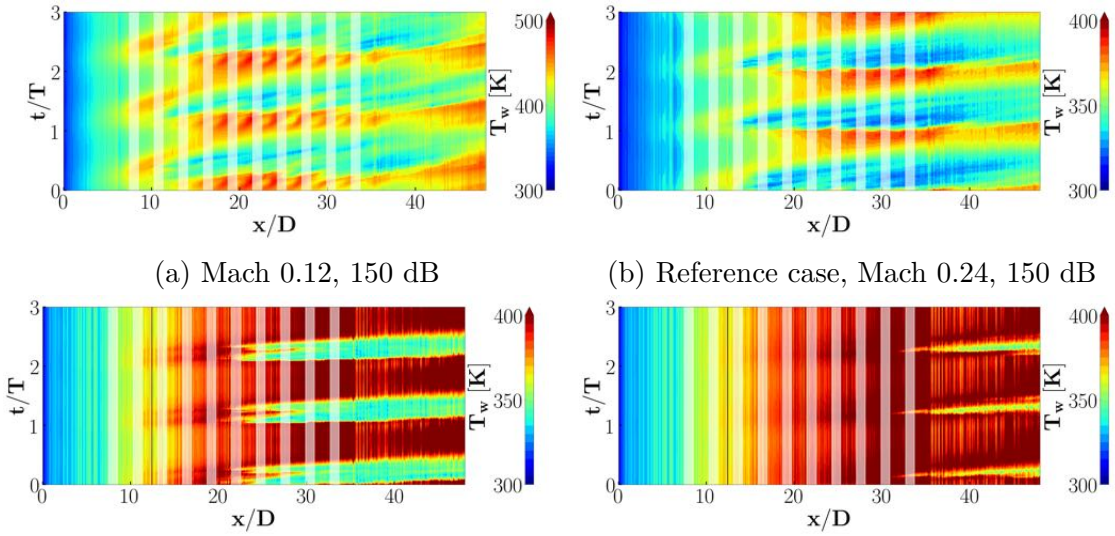

(a) Mach 0.12, 150 dB

(b) Reference case, Mach 0.24, 150 dB

(c) Mach 0.6, 150 dB

(d) Mach 0.6, 139 dB

Figure 9.16: Temperature time evolution through three periods. Engine scale, , $\Phi = 1500 * 6.25$ W.m^{-2}. Between the jets.

ating points between each other, Nu profiles are shown in Fig. 9.18. There, the Nusselt number is shown in the jet axis (Fig. 9.18a), between the jets (Fig. 9.18c) and far from the perforations, that is to say the equivalent flat plate (Fig. 9.18e). It is also shown in the same locations but normalised by the Nusselt number of the equivalent flat plate (Figs. 9.18b in the jet axis and 9.18d between the jets). Similar conclusions that for the previous sections can be drawn. First, the temperature peak that was observed for the temperatures between the first and the second perforation rows can be compared to the low heat transfer level in the same zone, relatively to the remaining perforations. Secondly, the higher the velocity ratio, the wider the spanwise expansion of the jet impacts on the plate. The impact of the blockage effect can also be seen, in particular for the high M case for which it is the more important. It is more visible in the Nu profiles and normalised profiles. In general, the main physical trends can be found for the different operating points with the contributions of both ejection and aspiration mid-periods, leading to a drastically higher Nusselt number in the jet axis than between the jets. All other things being equal, the higher the piston amplitude is, the higher the Nusselt number is, especially in the jet axis. This appears when comparing the reference case (Fig 9.17a) and the low M case (Fig. 9.17b). It should be noted that modifying the amplitude of the pistons impacts the jet velocity and thus all three of the jet characterising parameters (Reynolds number, stroke length and velocity ratio). On the contrary, modifying the grazing flow velocity impacts only one of these parameters: the velocity ratio. However, as discussed in the previous sections, the upstream flow conditions play a non negligible part in the wall heat transfer. This can be seen on the high M case, for which the grazing flow velocity is much lower than for the reference case. A globally lower Nusselt number is observed for this case. This is mainly due to the low Reynolds number grazing flow, and comparing the jet axis to the "flat plate" zone shows that the jets are efficient in enhancing heat transfer. This

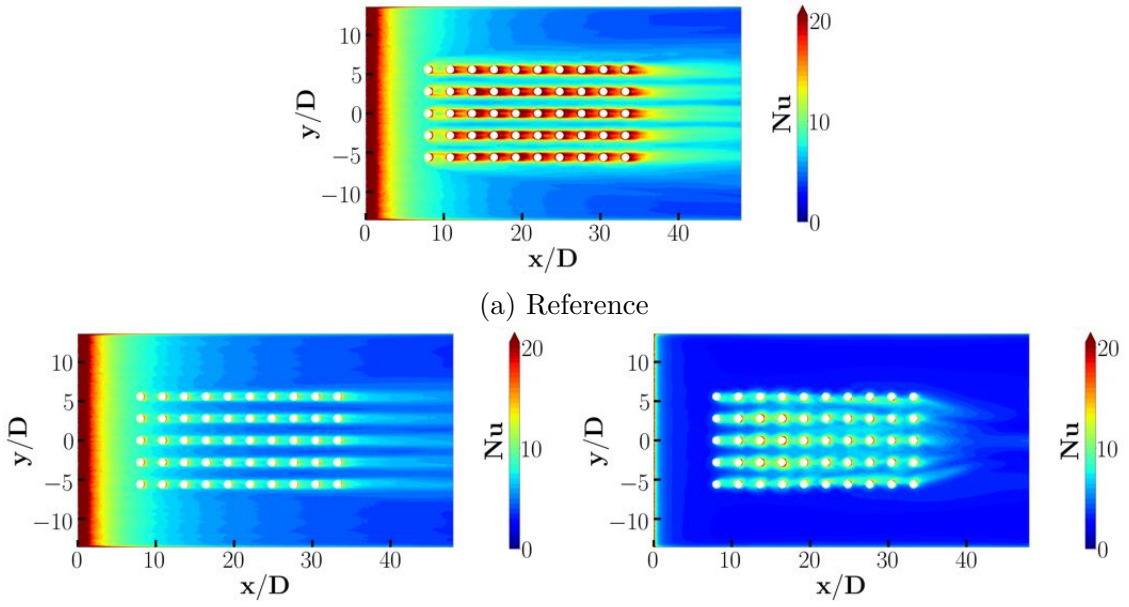

(a) Reference

(b) Low M

(c) High M

Figure 9.17: Time averaged Nusselt fields for different operating points. Lab scale configuration.

comparison is made more specifically in the jet axis and between the jets in Fig. 9.18.

As discussed in Section 6.2.4, the wall heat transfer coefficient and its normalisation the Nusselt number fields can be obtained by approximating $T_{ref} = 300\ K$. With this hypothesis, only a single wall heat flux operating point is required which reduces by half the simulation cost. Several engine scale operating points were therefore treated based on this hypothesis. The Nusselt number fields of these operating points are presented in Fig. 9.17. The raw and normalised profiles are shown in Fig. 9.20. Again, the observations that can be made are similar to that of Section 9.2.2.1. The main conclusions are detailed hereafter.

- Coherently with the experimental results from Giachetti *et al.* [126] as well as previous results of the present study, the velocity ratio $M = \overline{W}/U_0$ is a key factor when studying heat transfer issues. A higher velocity ratio leads to a higher wall heat transfer enhancement, when normalised with the equivalent flat plate results. It also implies a wider spanwise expansion of the synthetic jets, meaning that the heat transfer is also more enhanced between the jets, and not only in their wakes.

- The grazing flow velocity is also a key factor that should not be neglected. Although a rising axial velocity U_0 contributes to lower the velocity ratio of the jets, and thus to decrease their contribution in heat transfer, the grazing flow does contribute to enhance heat transfer as well. Here, the highest Nusselt number values are found for the highest Mach number tested in the different operating points. On the contrary, the normalised profiles (Fig. 9.20) show

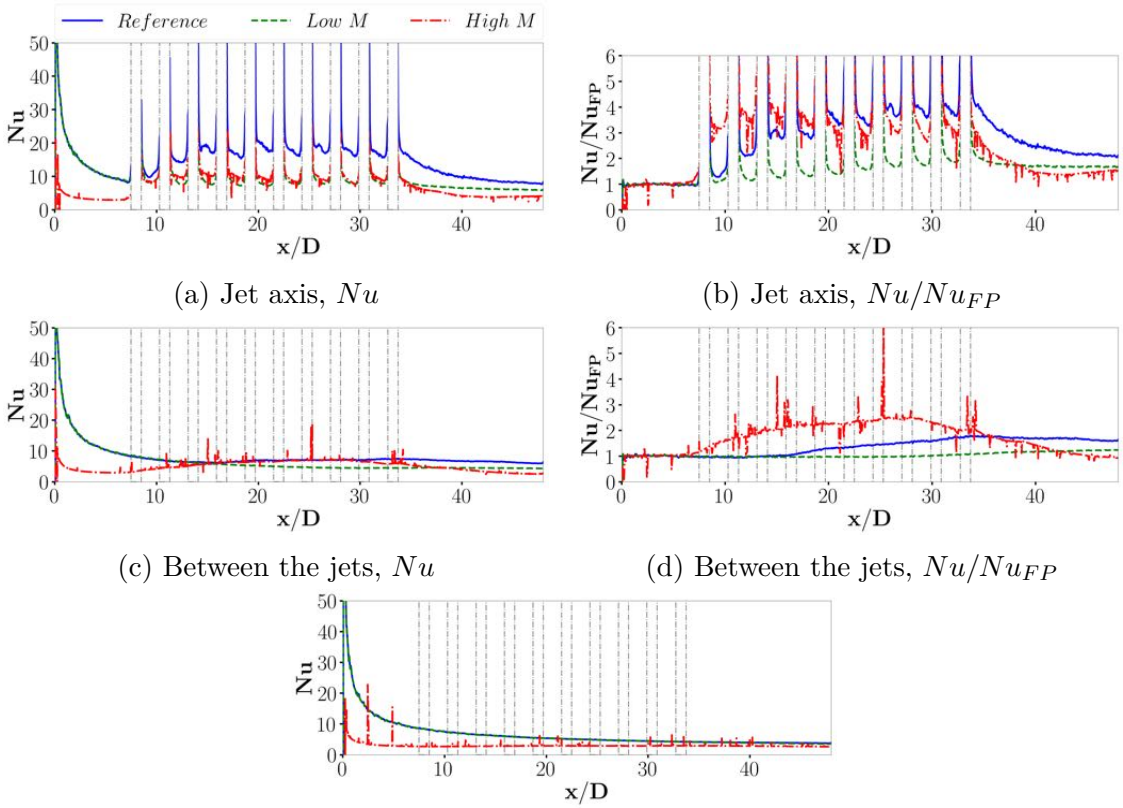

(a) Jet axis, Nu

(b) Jet axis, Nu/Nu_{FP}

(c) Between the jets, Nu

(d) Between the jets, Nu/Nu_{FP}

(e) Flat plate, Nu

Figure 9.18: Time averaged Nusselt Nu and time averaged Nusselt normalised by the equivalent flat plate Nusselt N/Nu_{FP} for different operating points and different positions along the perforated plate. Lab scale configuration.

that the operating points which are the most efficient in enhancing the wall heat transfer, when compared to their equivalent flat plates, are those with the highest velocity ratio.

- In the engine scale configuration, for which the synthetic jets are triggered by the acoustic signal, modifying the acoustic amplitude is equivalent to modifying the amplitude of the pistons in the lab scale configuration. The only difference between cases c and d in Fig. 9.19 is the acoustic amplitude. With the lowest amplitude (Fig 9.19d), the velocity of the jets is reduced and so are the jet Reynolds number, stroke length and velocity ratio. When comparing the Nu field with that of the high amplitude case (Fig. 9.19c), it appears that the Nusselt number is globally following the same trends but with lower values. In the jet axis, the heat transfer is more important right after the perforations but decreases rapidly while with the highest amplitude it remains high until the following perforations.The jets also expand less widely in the spanwise direction, consistently with the analysis that showed the impact of the velocity ratio on the spanwise expansion. This leads to a lower heat transfer between the jets. This comparison shows that the observations that were made for the lab scale configuration (Figs. 9.17a and 9.17b), in case of a low grazing flow

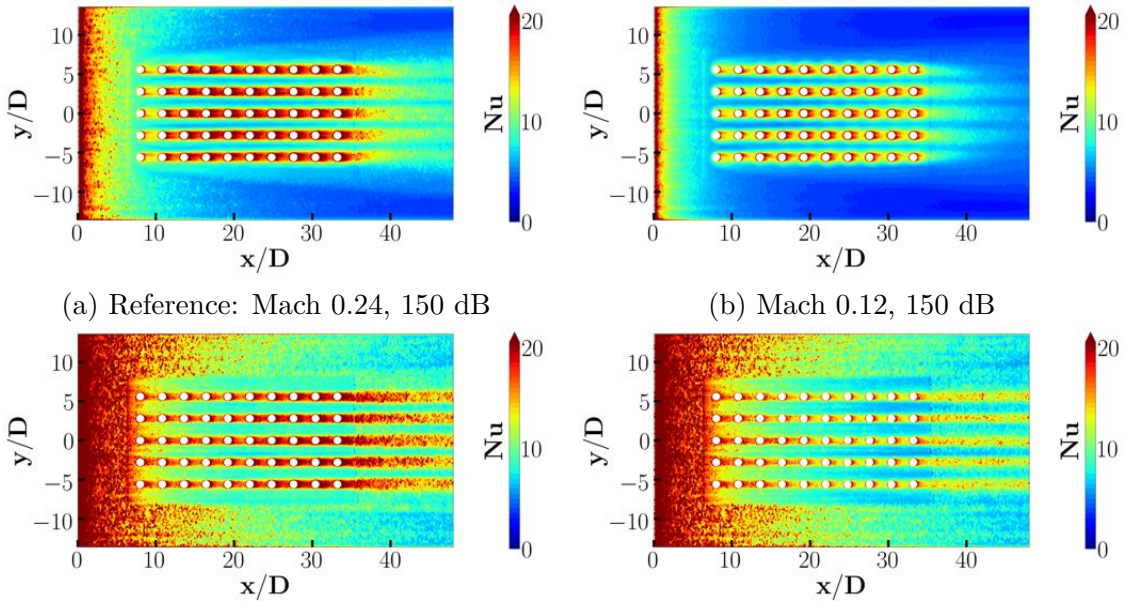

(a) Reference: Mach 0.24, 150 dB

(b) Mach 0.12, 150 dB

(c) Mach 0.6, 150 dB

(d) Mach 0.6, 139 dB

Figure 9.19: Time averaged Nusselt fieds for different operating points. Engine scale configuration. Nu estimated by assumming $T_{ref} = 300$ K.

Mach number, are still valid for high velocity grazing flows.

9.3 Synthesis: wall heat transfer for different synthetic jet parameters

In order to quantify and compare the wall heat transfer for the different operating points, a surface-averaging of the Nusselt number is calculated from the time-averaged fields. Since for some of the operating points, only one wall heat flux simulation was performed, and for the sake of comparison, this calculation is based on a single wall heat flux operating point for all of the cases. The considered surface is the same as that used for the comparison in Chapter 8 for the comparison of synthetic jets with jets in cross-flow, and is remindered here in Fig. 9.21a. As already discussed, several jet and upstream flow parameters were modified to obtain the different operating points. Therefore, a comparison of the time- and surface-averaged Nusselt number is proposed for each of this parameters: the jet Reynolds number, the dimensionless stroke length, the upstream flow Mach number and the velocity ratio. Moreover, in these figures, the values are normalised by the time- and surface-averaged Nusselt number of the equivalent flat plate which enables to quantify the importance of the synthetic jets in the wall heat transfer. For a better visualisation, the lab scale values are provided in blue while the engine scale ones are in red. The seven operating points analysed through this chapter are considered. In addition to those, a case on the lab scale configuration without jets (still pistons) is proposed. The upstream conditions, in particular the velocity profiles, correspond to that of the lab scale, reference operating point that are also that of the low M

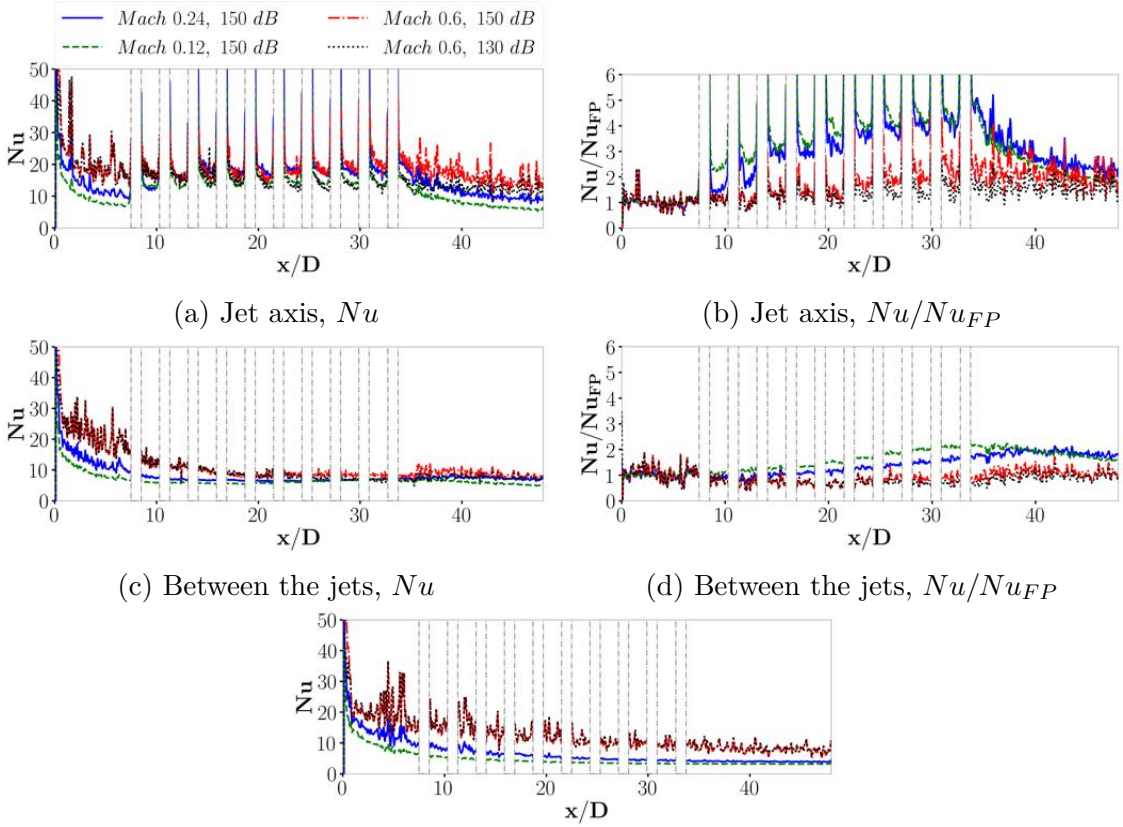

(a) Jet axis, Nu

(b) Jet axis, Nu/Nu_{FP}

(c) Between the jets, Nu

(d) Between the jets, Nu/Nu_{FP}

(e) Flat plate, Nu

Figure 9.20: Time averaged Nusselt Nu and time averaged Nusselt normalised by the equivalent flat plate Nusselt Nu/Nu_{FP} for different operating points and different positions along the perforated plate. Engine scale configuration.

case. The main trends observed with Figs. 9.21c to 9.21f confirm the experimental observations of Giachetti *et al.* and provide a proper synthesis of the present work: the impact of the different jet parameters is retrieved, and the importance of the upstream conditions and velocity ratio is underlined.

As discussed through this manuscript, there are some limitations to the numerical simulations that should be kept in mind. Two of them are reminded here to properly interpret Fig. 9.21. The first one is that the high grazing flow Mach number cases were simulated with a mesh that was designed for lower grazing flow velocity conditions. Therefore, the simulation is not wall-resolved for these cases and the numerical errors and resulting uncertainties are increased. Therefore, the value of Nu/Nu_{FP} lower than 1 observed for the Mach 0.60, SPL=139 dB case might not be accurate enough to conclude that this case is indeed less efficient than a flat plate to cool down the plate. The second point is about the lab scale, high M case, for which the spanwise expansion of the jets is much more important than for the other cases. Therefore, the zone that is considered to compute the "equivalent flat plate" values is more strongly impacted by the jets than for the other cases. This leads to some uncertainty about the flat plate Nusselt value. In spite of these uncertainties,

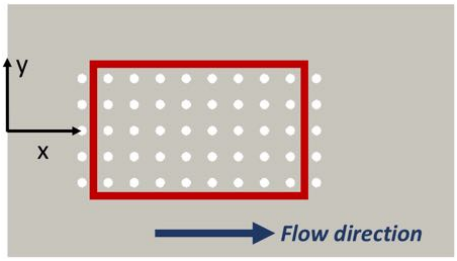

(a) Red rectangle: area over which the Nusselt number was integrated.

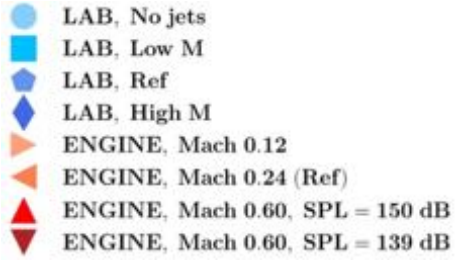

(b) Key for Figs. 9.21c to 9.21f.

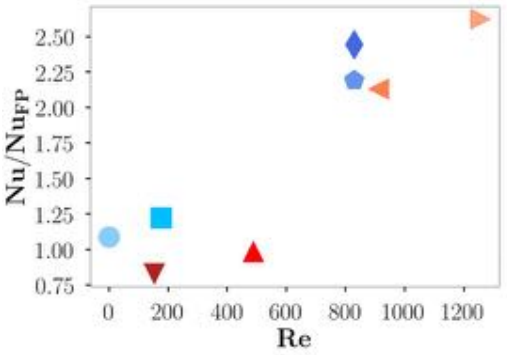

(c) Reynolds number Re.

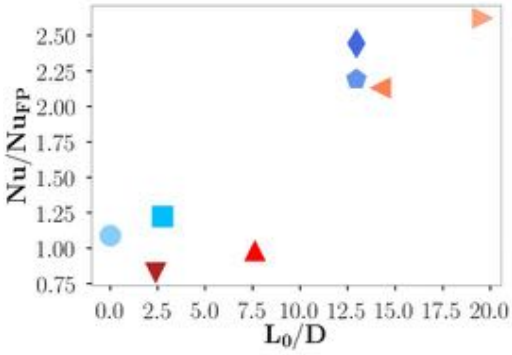

(d) Dimensionless stroke length L_0/D.

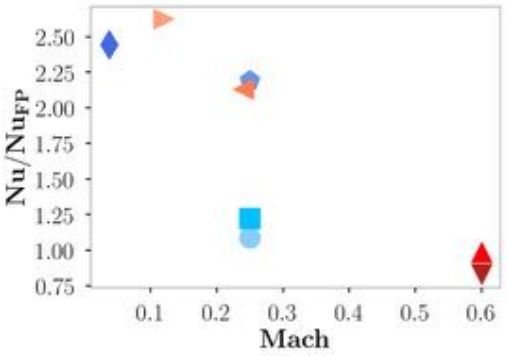

(e) Grazing flow Mach number.

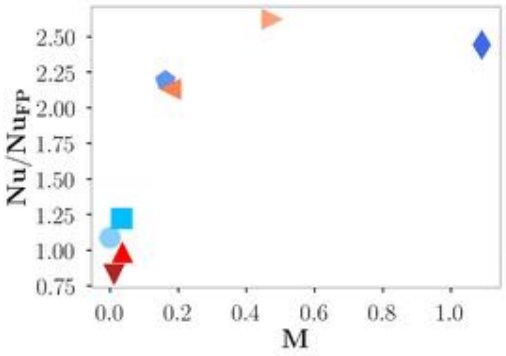

(f) Velocity ratio M.

Figure 9.21: Time- and surface-averaged Nusselt number Nu in regards to different jet and upstream flow parameters.

the results are considered interesting enough to provide orders of magnitude and trends in the Nusselt number evolution.

The comparison of cases with respect to the Reynolds number and dimensionless stroke length are provided in Fig. 9.21c and Fig. 9.21d, respectively. The dimensionless stroke length depends on the jet velocity and frequency ($L_0/D = \overline{W}/(2fD)$) while the Reynolds number depends on the jet velocity ($Re = \overline{W}D/\nu$). Since the frequency is unchanged for the different operating conditions considered through this study, the evolution of the Nusselt number in regard to the dimensionless stroke length follows the same evolution as that observed in regards to the Reynolds number. For both cases, the main trend is that the higher the Reynolds number (or the dimensionless stroke length), the higher the normalised Nusselt number.

As already discussed all along this manuscript, the upstream conditions play a non-negligible part in the jet behaviour and the resulting wall heat transfer. Figures 9.21e and 9.21f show the evolution of the normalised Nusselt number for the different operating points, in regard to the upstream flow Mach number and the jet velocity ratio $\overline{W}/U_0$, respectively. The normalised Nusselt number decreases when the Mach number rises, showing the reduction of the impact of the synthetic jets on the wall heat transfer enhancement (therefore: the Nusselt number rise) in comparison with an equivalent flat plate. The normalised Nusselt number evolution in regard to the velocity ratio is characterised by a rising value followed by a plateau. As already discussed, two competing phenomena contribute to enhance the wall heat transfer: the synthetic jets, but also the grazing flow and boundary layer evolution. With a higher grazing flow velocity, the Nusselt number of a flat plate rises. However, as this velocity rises, the jets are more bent and folded, and lose in efficiency to cool down the plate. This competition explains both the trends observed in Figs. 9.21e and 9.21e. With an increased grazing flow Mach number, the part that the jets play in wall heat transfer is reduced, hence the normalised Nusselt number tends to 1, meaning that the case is almost equivalent to a flat plate and the role of the jets become negligible. The plateau observed when confronting the Nusselt number evolution to the velocity ratio is also explained by this competition, coherently with the analysis provided through this chapter.

Chapter conclusions

The aim of this chapter was to compare different operating points in order to determine the influence of different jet and upstream parameters on the wall heat transfer enhancement induced by synthetic jets. Such a comparison was already performed by Giachetti*et al.* for low grazing flow Mach numbers. The interest of the present work it to (i) provide more information about the operating points that are in common with their experimental study and (ii) to extend some of the flow parameters range to values that were not considered in the experimental study. In particular, the high Mach number cases considered for the engine scale case enable to reach operating points closer to the operating conditions of a classic acoustic liner.

The main conclusions of this analysis are as follows. First, as observed by Giachetti *et al.*, for the same upstream conditions, the higher the jet velocity, the higher the Nusselt number. Then, the upstream conditions play a significant role in the wall heat transfer for two reasons: they impact the jet development, in particular the upstream rows, and they are predominant over the jets inbetween the jet axis, at least during the aspiration phase. Therefore, when the axial velocity increases, a plateau effect can be observed: the higher velocity contributes to increase the Nusselt number, but competes with the jets for which the velocity ratio M decreases, reducing their efficiency in all heat transfer enhancement. This observation obtained thanks to the engine scale configuration is cru-

cial since the high Mach number cases are the most flight-representative cases.

Conclusions and perspectives

Aircraft engine architectures have evolved through years, and are expected to keep evolving in the coming years, in order to meet public health and environmental impact requirements. They are already high temperature systems and complex heat transfer issues have to be considered. This will be even more the case for future architectures for which the temperatures are expected to keep rising, while material melting temperatures remain lower and the use of temperature sensitive electronic devices keeps increasing. Therefore, different cooling systems and heat transfer enhancement strategies have to be implemented. This thesis focuses on the wall heat transfer that occur along turbofan nacelle walls, around the fan and in the bypass ducts. These walls are lined up with acoustic treatments that modify the boundary layer behaviour, and thus the wall heat transfer. It was suspected that the presence of these liners would increase the wall heat transfer, in comparison with a classical flat plate, and could therefore be exploited in future engine architectures to enhance wall heat transfer. Indeed, acoustic liners trigger a phenomenon called synthetic jet which, in other contexts, have already been used to enhance heat transfer. However, acoustic liners have been studied more for their acoustic performance and impact on hydrodynamics than for their influence on wall heat transfer, and synthetic jets are usually used in heat transfer enhancement context in single perforation, impacting jet configurations. Thus, little knowledge is available about the impact of synthetic jets on wall heat transfer in multi-perforated, cross-flow configurations, as it is the case for acoustic liners. The present work, as part of the OPTIMA project, is a preliminary study that aims at better understanding heat transfer within acoustic liners.

This work is based on a test rig developped and exploited at Institut Pprime, Poitiers, France. For this experiment, the synthetic jets that are naturally present with an acoustic liner were generated thanks to pistons placed underneath the perforated plate. The present numerical study is complementary to Giachetti *et al*'s work, which provided data about wall heat transfer in a multiperforated synthetic jet configuration for a wide range of operating points. Experimental data was used in the present work to successfully validate the numerical set-up, which was then used to validate the test rig principle of using pistons instead of acoustic resonance to reproduce the behaviour of the liners. To do so, the lab scale numerical configuration, directly reproducing the Pprime rig, was compared to an engine scale configuration, more representative of a classical liner since the synthetic jets were

triggered by the acoustic resonance of the cavity placed under the cavity. These validation steps implied two crucial conclusions: first, the results obtained by Giachetti *et al.* are applicable to acoustic liners; then the numerical simulations can be used to extend their analysis, both by providing more data on quantities that were not experimentally reachable and by extending the operating points to more flight-representative conditions. To the author's knowledge, the Pprime study (lab scale configuration) is the first to consider wall heat transfer in such a complete system, with taking into account both the grazing flow and the multiperforation aspect. The present study, with the engine scale configuration, is also the first one that directly considers wall heat transfer in an acoustic liner.

The numerical results where thus used to provide knowledge about the flow dynamics that were not experimentally observable. In particular, a focus on a specific operating point was made in order to deeply analyse the flow dynamics, boundary layer evolution and resulting wall heat transfer. As a reminder, the synthetic jets that are generated by an acoustic liner are characterised by the periodic succession of an ejection and aspiration phases. The numerical results showed that both these phases contribute to enhancing wall heat transfer, when compared to an equivalent flat plate: however these contributions are completely different. During the ejection phase, the vortices shed by the jets modify the boundary layer development, increase the wall shear stress and bring cold flow nearer to the wall. Once they are spread enough spanwise the perforations, this leads to an increased wall heat transfer all along the perforated zone and homogeneous temperatures. On the contrary, during the aspiration phase, the flow behaviour becomes much more heterogeneous, due to the alignment of the perforations. In the jet axis, the suction of the flow within the cavities leads to a drastic decrease of the boundary layer, which starts again after each of the boundary layer. In the jet wakes, the wall shear stress is then maximum and so is the wall heat transfer. Between the jet lines, the flow behaviour is completely different since the aspiration is not strong enough to affect this zone. There, the boundary layer evolves similarly to that of a flow along a classic flat plate and no more wall heat transfer enhancement is observed. The importance of upstream conditions, in particular related to turbulence, on the flow behaviour, was evidenced with a dedicated simulation. Indeed, the upstream turbulence contributes to modifying the jet development and therefore the resulting wall heat transfer enhancement. Moreover, it was shown that the velocity ratio M plays a significant role in the jet impact on wall heat transfer, in particular for the importance of upstream conditions. Indeed, for high enough values of M, the jets are predominant in driving the flow while at low M values the upstream conditions play a more significant part in the flow evolution. At high grazing flow Mach number, that is to say rather low velocity ratio M, this seems to lead to a plateau for the wall heat transfer enhancement that can be obtained thanks to the jets. Indeed, two competing phenomena are observed: a higher grazing flow Mach number leads to a higher wall heat transfer, however it also leads to the reduction of the heat transfer enhancement that can be obtained with the synthetic jets due to the lowering of the M.

Finally, both lab and engine scale configurations were used to simulate several

operating points. First, a comparison between synthetic jets and jets in cross-flow was provided, which showed that the same orders of magnitude can be obtained for the wall heat transfer. The main advantage for synthetic jets when compared to jets in cross-flow is that there is no need for complex plumbing to bring cold flow since the jets are generated directly from the ambient flow. The JICF was shown to be the best wall heat transfer enhancement on a specific operating point, however it would be interesting to consider staggered configurations. Then, although some limitations can be pointed out (as discussed hereafter), the simulations of different operating points, some of which designed to extend the parameter range proposed by Pprime to higher cross-flow velocities, provided a database that was used to better observe the impact of different synthetic jet parameters on wall heat transfer. The jet Reynolds number Re and dimensionless stroke length L_0/D were discussed. All other things being equal, the higher the jet Reynolds number, the higher the impact of the jets on the perforated plate. Similar conclusions were obtained for the stroke length which was expected since all of the operating points were designed for the same jet frequency. Therefore, the stroke length is directly proportional to the Reynolds number. The velocity ratio M, already discussed here, was shown to be crucial since the importance of the upstream conditions on the jet development and resulting wall heat transfer depend on it.

Even though many different configurations have been computed by LES providing an extensive numerical database, several questions remain open linked to the geometry and the flow conditions studied here. They are the following:

- **Damped acoustic wave:** With the lab scale configuration, all of the jets are triggered by pistons following the exact same movement. In the engine scale configuration, only one resonant cavity is considered. With a real acoustic liner, it has to be kept in mind that (i) several resonant cavities are present and (ii) the reason acoustic liners are used is the necessity to damp acoustic noise. Therefore, as the acoustic wave propagates along the liner, its intensity decreases. As a result, and contrarily to what is observed on the cases studied throughout this work, the jet velocity is not the same from one perforation to another. Since the present work, and that of Pprime, showed that a lower jet velocity leads to a lower wall heat transfer enhancement, it could be expected to observe a wall heat transfer enhancement that decreases along the plate, correlated to the progressive acoustic damping. A study on a configuration with several resonant cavities would be enlightening.

- **Number of perforations:** Another limitation of the study is the small number of perforations that was considered. Although 50 perforations is quite a high number for such LES work (the literature review showed that it is usual to consider only a single perforation on numerical studies), it remains low in comparaison to real liners. It was observed through this work that, regarding the considered operating point, some phenomena require at least five or six perforation rows to reach establishment. This corresponds to at least half of the considered perforated area and has therefore a great weight in some aver-

aging that were done. Considering several resonant cavities as in the previous point would tell whether a saturated steady state has been reached, or whether the expected decreasing jet velocity would lead to an evolution. However, the cost of such a numerical simulation still remains very high.

- **Aligned versus staggered perforations:** In the test rig, and thus in the numerical configurations, the perforations are aligned in the upstream flow axis. However, it is usual with acoustic liners to have staggered perforations. The impact of this difference is currently not known and only hypothetical answers can be provided to that question. The flow analysis however suggested that for a staggered configuration, the wall heat transfer averaged over all of the perforated area would be greater than that obtained with an aligned configuration. However, for the synthetic jets, this remains hypothetical and one shall keep in mind that a staggered configuration could lead to unsuspected phenomena modifying wall heat transfer. It would thus be of great interest to perform simulations of staggered configurations and, similarly to what was done for the jets in cross-flow, to quantify the importance of different geometrical parameters such as the distance between the perforations.

- **Impact of turbulence:** A whole chapter of this manuscript was dedicated to the analysis of the role of upstream turbulence, which was shown to play a non negligible part on the synthetic jet evolution, and the resulting wall heat transfer under some conditions. As discussed in the manuscript, only one operating point was simulated with the presence of upstream turbulence. Therefore, results should be considered with caution, especially for low velocity ratios. However, it is found out that the importance of upstream turbulence, compared to that of the synthetic jets, depends on the velocity ratio M. More simulations, for different upstream turbulence levels, would be required to deeper study this importance. It would moreover be required, to obtain better results, to target wall-modelled simulations for the high Mach cases on the engine scale configurations, which was not obtained here. Finally, it would be interesting to perform a similar analysis of the upstream turbulence impact on wall heat transfer with a staggered configuration. It is suspected that with a staggered configuration upstream conditions would be less important. The flow dynamics would be even more importantly driven by the synthetic jets. Therefore, upstream turbulence could have a less significant impact on wall heat transfer. This remains hypothetical and further work is required to investigate this question.

List of Figures

List of Tables

Bibliography

[1] Tamer Elnady. *Modelling and Characterization of Perforates in Lined Ducts and Mufflers*. PhD thesis, The Royal Institute of Technology (KTH) - Stockholm, 2004. (Cited p. xiv and 179.)

[2] Pierre Aillaud. *Simulations aux grandes échelles pour le refroidissement d'aubages de turbine haute-pression*. PhD thesis, Université de Toulouse, 2017. (Cited p. xiv, 51, 52 and 180.)

[3] Meherwan P. Boyce. Theoretical and Actual Cycle Analyses. In *Gas Turbine Engineering Handbook*, pages 89–137. 2012. (Cited p. xiv)

[4] Romain Bizzari, Dorian Lahbib, Antoine Dauptain, Florent Duchaine, Stephane Richard, and Franck Nicoud. Low order modeling method for assessing the temperature of multi-perforated plates. *International Journal of Heat and Mass Transfer*, 127:727–742, 2018. (Cited p. xiv and 68.)

[5] Joe Walsh. Progress in Engine Noise Reduction and Future Challenges Rolls. In *Greener by Design Conference*, London, United Kingdom, 2016. Royal Aeronautical Society. (Cited p. xv)

[6] J A Rosero, J A Ortega, E Aldabas, and L Romeral. Moving Towards a More Electric Aircraft. *IEEE Aerospace and Electronic Systems Magazine*, 22(3):3–9, 2007. (Cited p. xv)

[7] M Arik and R S Bunker. Electronics Packaging Cooling: Technologies From Gas Turbine Engine Cooling. *Journal of Electronic Packaging*, 128(3):215–225, 2006. (Cited p. xv)

[8] D. Casalino, F. Diozzi, R. Sannino, and A. Paonessa. Aircraft noise reduction technologies: A bibliographic review. *Aerospace Science and Technology*, 12(1):1–17, jan 2008. (Cited p. 3)

[9] L Leylekian, M Lebrun, and P Lempereur. An Overview of Aircraft Noise Reduction Technologies. *AerospaceLab*, 1(7):1–15, 2014. (Cited p. 3)

[10] Dale Van Zante, Aircraft Noise Reduction Sub-project, United States, Douglas Nark, Hamilton Fernandez, Aircraft Noise Reduction Sub-project, and United States. Propulsion Noise Reduction Research in the NASA Advanced Air

Transport Technology Project. *Proceedings of the 23rd ISABE Conference*, 2017. (Cited p. 3)

[11] John Paul Clarke. The role of advanced air traffic management in reducing the impact of aircraft noise and enabling aviation growth. *Journal of Air Transport Management*, 9(3):161–165, 2003. (Cited p. 4 and 179.)

[12] Edmane Envia. Fan Noise Reduction: An Overview. *International Journal of Aeroacoustics*, 1(1):43–64, 2002. (Cited p. 4)

[13] Thierry Poinsot and Denis Veynante. *Theoretical and numerical combustion - Third Edition*. the authors, 2011. (Cited p. 5)

[14] Lawrence E. Kinsler, Austin R. Frey, Alan B. Coppens, and James V. Sanders. *Fundamentals of Acoustics, third edition*. John Wiley and Sons, 1982. (Cited p. 5 and 15.)

[15] P. M. Morse and K. U. Ingard. *Theoretical Acoustics*. McGraw-Hill, Princeton, New Jersey, 1968. (Cited p. 5)

[16] Allen D. Pierce. *Acoustics: An Introduction to Its Physical Principles and Applications*. the Acoustical Society of America, New York, 1994. (Cited p. 5)

[17] Herman Ludwig F. von Helmholtz and Alexander J. Ellis. *On the sensations of tone as a physiological basis for the theory of music*. Longmans, Green and Company, London, 1875. (Cited p. 6, 7 and 179.)

[18] U. Ingård and S Labate. Acoustic Circulation Effects and the Nonlinear Impedance of Orifices. *The Journal of the Acoustical Society of America*, 22(2):211–218, 1950. (Cited p. 9, 10, 18, 19, 32, 37 and 179.)

[19] Christopher K. W. Tam and Konstantin A. Kurbatskii. Microfluid dynamics and acoustics of resonant liners. *AIAA Journal*, 38(8):1331–1339, 2000. (Cited p. 9, 10, 19 and 34.)

[20] John William Strutt Rayleigh. On the theory of resonance. In *Scientifc papers*, volume 1, chapter 5, pages 33–75. University Press, Cambridge, MA, USA, 1899. (Cited p. 9)

[21] Jean-Michel Roche. *Simulation numérique de l'absorption acoustique de matériaux résonants en présence d'écoulement*. PhD thesis, Université du Maine, Le Mans, France, 2011. (Cited p. 10, 11, 13, 14, 20, 21, 22 and 179.)

[22] Christopher K. Tam, Nikolai Pastouchenko, Michael G. Jones, and Willie R. Watson. Experimental Validation of Numerical Simulation for An Acoustic Liner in Grazing Flow. *19th AIAA/CEAS Aeroacoustics Conference*, 2013. (Cited p. 11 and 14.)

[23] L. D. Gomes, W. J. Crowther, and N. J. Wood. Towards a practical piezoceramic diaphragm based synthetic jet actuator for high subsonic applications - Effect of chamber and orifice depth on actuator peak velocity. *Collection of*

Technical Papers - 3rd AIAA Flow Control Conference, 1(August):267–283, 2006. (Cited p. 11)

[24] Tyler Van Buren, Edward Whalen, and Michael Amitay. Synthetic Jet Actuator Cavity Acoustics: Helmholtz Versus Quarter-Wave Resonance. *Journal of Vibration and Acoustics*, 137(5), 2015. (Cited p. 11 and 33.)

[25] R.E. Motsinger and Kraft R.E. Design and Performance of Duct Acoustic Treatment. In *Aeroacoustics of Fight Vehicles: Theory and Practice. Volume 2: Noise Control*. NASA, Langley Research Center, 1991. (Cited p. 12)

[26] Michael Jones, Maureen Tracy, Willie Watson, and Tony Parrott. Effects of Liner Geometry on Acoustic Impedance. In AIAA, editor, *8th AIAA/CEAS Aeroacoustics Conference & Exhibit*, pages 1–10, Breckenridge, Colorado, USA, 2002. (Cited p. 13)

[27] T. H. Melling. The acoustic impendance of perforates at medium and high sound pressure levels. *Journal of Sound and Vibration*, 29(1):1–65, 1973. (Cited p. 14, 17 and 19.)

[28] C. K.W. Tam, H. Ju, M. G. Jones, W. R. Watson, and T. L. Parrott. A computational and experimental study of slit resonators. *Journal of Sound and Vibration*, 284(3-5):947–984, 2005. (Cited p. 14, 19, 20 and 179.)

[29] Xiaodong Jing, Xiaofeng Sun, Jingshu Wu, and Kun Meng. Effect of grazing flow on the acoustic impedance of an orifice. *AIAA Journal*, 39(8):1478–1484, 2001. (Cited p. 14 and 21.)

[30] Stéphane Moreau. Turbomachinery Noise Predictions : Present and Future. *Acoustics*, 1:92–116, 2019. (Cited p. 14)

[31] Jeffrey W. Moe, John J. Wunsch, and Michael S. Sperling. Method and apparatus for noise abattement and ice protection of an aircraft engine nacelle inlet lip, 2009. (Cited p. 14)

[32] Jacky Mardjono, Riou Georges, Boiteux Jean-Michel, and Frederic Boubila. EPSL static tests demonstration of liners noise reduction concepts. In *19th AIAA/CEAS Aeroacoustics Conference*, pages 1–13, Berlin, Germany, 2013. (Cited p. 14)

[33] Michael G Jones. NASA Langley Activities on Broadband Fan Noise Reduction via Novel Liner Technologies, 2015. (Cited p. 15)

[34] Benjamin S. Beck, Noah H. Schiller, and Michael G. Jones. Impedance assessment of a dual-resonance acoustic liner. *Applied Acoustics*, 93:15–22, 2015. (Cited p. 15)

[35] L. Danielle Koch. Investigation of a Bio-Inspired Liner Concept. *Acoustics Technical Working Group Meeting*, pages 1–28, 2017. (Cited p. 15)

[36] A Kundt. III . Acoustic experiments. *The London, Edinburgh, and Dublin Philosophical Magazine and Journal of Science. Philosophical Magazine Series 4*, 35(234):41–48, 1868. (Cited p. 16)

[37] P. D. Dean. An in situ method of wall acoustic impedance measurement in flow ducts. *Journal of Sound and Vibration*, 34(1):97–130, 1974. (Cited p. 16 and 17.)

[38] Cécile Malmary. *Etude théorique et expérimentale de l'impédance acoustique de matériaux en présence d'un écoulement d'air tangentiel*. PhD thesis, Université du Maine, 2000. (Cited p. 16, 17, 21 and 22.)

[39] Q. Zhang and D. J. Bodony. Numerical Simulation of Two-Dimensional Acoustic Liners with High-Speed Grazing Flow. *AIAA Journal*, 49(2):365–382, 2011. (Cited p. 17, 22 and 50.)

[40] Jean-Michel Roche, Laurent Leylekian, Grégory Delattre, and François Vuillot. Aircraft Fan Noise Absorption: DNS of the Acoustic Dissipation of Resonant Liners. In *15th AIAA/CEAS Aeroacoustics Conference (30th AIAA Aeroacoustics Conference)*, pages 11–13. American Institute of Aeronautics and Astronautics (AIAA), 2009. (Cited p. 20)

[41] Jean-Michel Roche, François Vuillot, Laurent Leylekian, Grégory Delattre, Estelle Piot, and Frank Simon. Numerical and Experimental Study of Resonant Liners Aeroacoustic Absorption Under Grazing Flow. In *16th AIAA/CEAS Aeroacoustics Conference*, pages 1–18. American Institute of Aeronautics and Astronautics (AIAA), 2010. (Cited p. 20, 21 and 22.)

[42] Sjoerd W. Rienstra. A classification of duct modes based on surface waves. *Wave Motion*, 37(2):119–135, 2003. (Cited p. 20)

[43] M. Brandes and Dirk Ronneberger. Sound amplification in flow ducts lined with a periodic sequence of resonators. In *First Joint CEAS/AIAA Aeroacoustics Conference (16th AIAA Aeroacoustics Conference)*, pages 893–901, 1995. (Cited p. 20)

[44] Y. Aurégan and M. Leroux. Experimental evidence of an instability over an impedance wall in a duct with flow. *Journal of Sound and Vibration*, 317(3-5):432–439, 2008. (Cited p. 20 and 49.)

[45] E. J. Brambley. Review Of Acoustic Liner Models With Flow. In *Acoustics*, pages 3429–3434, Nantes, 2012. (Cited p. 21 and 49.)

[46] Maud Lavieille, Estelle Piot, and F. Micheli. Numerical simulations of perforate liners: Part II – Local velocity fields validation. In *19th AIAA/CEAS Aeroacoustics Conference*, 2013. (Cited p. 21)

[47] Fabien Mery, Estelle Piot, Delphine Sebbane, Philippe Reulet, Frank Simon, and A. Carazo Méndez. Experimental assessment of the effect of temperature gradient across an aeroacoustic liner. *Journal of Aircraft, AIAA*, pages 1–13, 2019. (Cited p. 21, 24, 25 and 46.)

[48] Michael G. Jones, Willie R. Watson, and Douglas M. Nark. Effects of Flow Profile on Educed Acoustic Liner Impedance. In *16th AIAA/CEAS Aeroacoustics Conference*, 2010. (Cited p. 21 and 25.)

[49] Christopher K.W. Tam, Hongbin Ju, and Bruce E. Walker. Numerical simulation of a slit resonator in a grazing flow under acoustic excitation. *Journal of Sound and Vibration*, 313(3-5):449–471, 2008. (Cited p. 21 and 22.)

[50] W. J. Worraker and N. A. Halliwell. Jet engine liner impedance: An experimental investigation of cavity neck flow/acoustics in the presence of a Mach 0·5 tangential shear flow. *Journal of Sound and Vibration*, 103(4):573–592, 1985. (Cited p. 22)

[51] R. Kirby and A. Cummings. The impedance of perforated plates subjected to grazing gas flow and backed by porous media. *Journal of Sound and Vibration*, 217(4):619–636, 1998. (Cited p. 22)

[52] F. Duchaine. Sensitivity analysis of heat transfer in a honeycomb acoustic liner to inlet conditions with large eddy simulation. In *Proceedings of the ASME Turbo Expo 2017: Turbomachinery Technical Conference and Exposition. Volume 5B: Heat Transfer*, Charlotte, NC, U.S.A, 2017. (Cited p. 22, 23, 25, 46 and 150.)

[53] J. Kompenhans and D. Ronneberger. The acoustic impedance of orifices in the wall of a flow duct with a laminar or turbulent flow boundary layer. In *AIAA 6th Aeroacoustics Conference*, Hartford, Connecticut, USA, 1980. (Cited p. 23)

[54] Qi Zhang and Daniel J. Bodony. Numerical investigation of a honeycomb liner grazed by laminar and turbulent boundary layers. *Journal of Fluid Mechanics*, 792:936–980, 2016. (Cited p. 23 and 50.)

[55] Pontus Nordin, Sohan Sarin, and Edward Rademaker. Development of New Liner Technology for Application in Hot Stream Areas of Aero-engines. In *10th AIAA/CEAS Aeroacoustics Conference*, pages 1–13, 2004. (Cited p. 24)

[56] Romain Bizzari. *Modélisation aérodynamique et thermique des plaques multi-perforées en LES*. PhD thesis, Université de Toulouse, 2018. (Cited p. 24, 139 and 149.)

[57] L. Rayleigh. The explanation of certain acoustical phenomena. *Nature*, 18:319–321, 1878. (Cited p. 24)

[58] Bernhard Ćosić, Thoralf G. Reichel, and Christian Oliver Paschereit. Acoustic Response of a Helmholtz Resonator Exposed to Hot-Gas Penetration and High Amplitude Oscillations. *Journal of Engineering for Gas Turbines and Power*, 134(10):101503, 2012. (Cited p. 24)

[59] B. Ćosić, D. Wassmer, S. Terhaar, and C. O. Paschereit. Acoustic response of Helmholtz dampers in the presence of hot grazing flow. *Journal of Sound and Vibration*, 335:1–18, 2015. (Cited p. 24)

[60] Trevor Howard Wood, Todd Garrett Wetzel, Jonathan Glenn Luedke, and Thomas Michael Tucker. Combined acoustic absorber and heat exchanging outlet guide vanes, 2012. (Cited p. 24)

[61] R. D. James, J. W. Jacobs, and A. Glezer. A round turbulent jet produced by an oscillating diaphragm. *Physics of Fluids*, 8(9):2484–2495, 1996. (Cited p. 27)

[62] Barton L. Smith and Ari Glezer. The formation and evolution of synthetic jets. *Physics of Fluids*, 10(9):2281–2297, 1998. (Cited p. 27 and 40.)

[63] Ryan Holman, Yogen Utturkar, Rajat Mittal, Barton L. Smith, and Louis Cattafesta. Formation Criterion for Synthetic Jets. *AIAA Journal*, 43(10):2110–2116, 2005. (Cited p. 27, 29, 30, 31 and 179.)

[64] Uno Ingard. On the theory and design of acoustic resonators. *Energy*, 1953. (Cited p. 30)

[65] B L Smith, M A Trautman, and A Glezer. Controlled interactions of adjacent synthetic jets. In *37th AIAA Aerospace Sciences Meeting and Exhibitc*, 1999. (Cited p. 30 and 32.)

[66] Jennifer M. Shuster and Douglas R. Smith. A study of the Formation and Scaling of a Synthetic Jet. In *42nd AIAA Aerospace Sciences Meeting and Exhibit*, Reno, Nevada, U.S.A., 2004. (Cited p. 30 and 34.)

[67] Barton L Smith and Gregory W Swift. Synthetic Jets at Large Reynolds Number and Comparison to Continuous Jets. In *15th AIAA Computational Fluid Dynamics Conference*, Anaheim, CA, USA, 2001. (Cited p. 30 and 139.)

[68] Prakit Rampunggoon. *Interaction of a synthetic jet with a flat plate boundary layer*. PhD thesis, University of Florida, 2001. (Cited p. 30 and 48.)

[69] Yogen Utturkar, Ryan Holman, Rajat Mittal, Bruce Carroll, Mark Sheplak, and Lou Cattafesta. A Jet Formation Criterion for Synthetic Jet Actuators. In *41st Aerospace Sciences Meeting and Exhibit*, 2003. (Cited p. 30 and 31.)

[70] Girish K. Jankee and Bharathram Ganapathisubramani. Influence of internal orifice geometry on synthetic jet performance. *Experiments in Fluids*, 2019. (Cited p. 32, 34, 35 and 179.)

[71] Donald P Rizzetta, Miguel R Visbal, Michael J Stanek, U S Air Force, Wright Patterson, and Air Force. Numerical Investigation of Synthetic-Jet Flow elds Introduction. *AIAA Journal*, 37(8):919–927, 1999. (Cited p. 33, 35 and 50.)

[72] Y. Utturkar, R. Mittal, P. Rampunggoon, and L. Cattafesta. Sensitivity of synthetic jets to the design of the jet cavity. In *40th Aerospace Sciences Meeting and Exhibit*, 2002. (Cited p. 33 and 35.)

[73] Manu Jain, Bhalchandra Puranik, and Amit Agrawal. A numerical investigation of effects of cavity and orifice parameters on the characteristics of a synthetic jet flow. *Sensors and Actuators, A: Physical*, 165(2):351–366, 2011. (Cited p. 33, 34, 35 and 50.)

[74] Mark A. Feero, Philippe Lavoie, and Pierre E. Sullivan. Influence of cavity shape on synthetic jet performance. *Sensors and Actuators, A: Physical*, 223:1–10, 2015. (Cited p. 33)

[75] R. Mittal, P. Rampunggoon, and H. Udaykumar. Interaction of a synthetic jet with a flat plate boundary layer. In *15th AIAA Computational Fluid Dynamics Conference*, 2001. (Cited p. 34, 35 and 50.)

[76] M A Leschziner and Sylvain Lardeau. Simulation of slot and round synthetic jets in the context of boundary-layer separation control. *Philosophical Transactions of the Royal Society*, pages 1495–1512, 2011. (Cited p. 34 and 52.)

[77] David J. Nani and Barton L. Smith. Effect of orifice inner lip radius on synthetic jet efficiency. *Physics of Fluids*, 24(11), 2012. (Cited p. 35)

[78] Morteza Gharib, Edmond Rambod, and Karim Shariff. A universal time scale for vortex ring formation. *Journal of Fluid Mechanics*, 360:121–140, 1998. (Cited p. 37, 41 and 44.)

[79] Ivana M. Milanovic and K. B.M.Q. Zaman. Synthetic jets in crossflow. *AIAA Journal*, 43(5):929–940, 2005. (Cited p. 37, 39 and 139.)

[80] M. Jabbal, J. Wu, and S. Zhong. The performance of round synthetic jets in quiescent flow. *Aeronautical Journal*, 110(1108):385–393, 2006. (Cited p. 37 and 44.)

[81] M. Jabbal and S. Zhong. The near wall effect of synthetic jets in a boundary layer. *International Journal of Heat and Fluid Flow*, 29(1):119–130, 2008. (Cited p. 37, 41, 42, 43, 45, 46, 79, 84, 97 and 179.)

[82] Z. Trávníček, Z. Broučková, J. Kordík, and T. Vít. Visualization of synthetic jet formation in air. *Journal of Visualization*, 18(4):595–609, 2015. (Cited p. 37, 38 and 179.)

[83] J C Bera, M Michard, N Grosjean, and G.Comte-Bellot. Flow analysis of two-dimensional pulsed jets by particle image velocimetry. *Experiments in Fluids*, 31:519–532, 2001. (Cited p. 38, 39 and 179.)

[84] B. L. Smith and G. W. Swift. A comparison between synthetic jets and continuous jets. *Experiments in Fluids*, 34(4):467–472, 2003. (Cited p. 39)

[85] Michael Amitay, Andrew Honohan, Mark Trautman, and Ari Glezer. Modification of the aerodynamic characteristics of bluff bodies using fluidic actuators. *28th Fluid Dynamics Conference*, 1997. (Cited p. 40)

[86] Michael Amitay, Barton L. Smith, and Ari Glezer. Aerodynamic flow control using synthetic jet technology. *36th AIAA Aerospace Sciences Meeting and Exhibit*, 1998. (Cited p. 40)

[87] Catalin Nae. Synthetic jets influence on NACA 0012 airfoil at high angles of attack. In *23rd Atmospheric Flight Mechanics Conference*, pages 854–859, Boston, MA, U.S.A., 1998. (Cited p. 40)

[88] Catalin Nae. Unsteady flow control using synthetic jet actuators. In *Fluids 2000 Conference and Exhibit, Fluid Dynamics and Co-located Conferences*, 2000. (Cited p. 40)

[89] D. McCormick. Boundary layer separation control with directed synthetic jets. *38th Aerospace Sciences Meeting and Exhibit*, 2000. (Cited p. 40, 47 and 48.)

[90] Ari Glezer. Some aspects of aerodynamic flow control using synthetic-jet actuation. *Philosophical Transactions of the Royal Society A: Mathematical, Physical and Engineering Sciences*, 369(1940):1476–1494, 2011. (Cited p. 41)

[91] A. Crook and N. J. Wood. Measurements and visualisations of synthetic jets. *39th Aerospace Sciences Meeting and Exhibit*, 2001. (Cited p. 41)

[92] S. Zhong, F. Millet, and N. J. Wood. The behaviour of circular synthetic jets in a laminar boundary layer. *Aeronautical Journal*, 109(1100):461–470, 2005. (Cited p. 41, 44, 45 and 84.)

[93] Mark Jabbal and Shan Zhong. Measurements of synthetic jets in a boundary layer. In *37th AIAA Fluid Dynamics Conference and Exhibit*, Miami, FL, U.S.A., 2007. (Cited p. 41)

[94] Jue Zhou and Shan Zhong. Numerical simulation of the interaction of a circular synthetic jet with a boundary layer. *Computers and Fluids*, 38(2):393–405, 2009. (Cited p. 42 and 46.)

[95] Jue Zhou and Shan Zhong. Coherent structures produced by the interaction between synthetic jets and a laminar boundary layer and their surface shear stress patterns. *Computers and Fluids*, 39(8):1296–1313, 2010. (Cited p. 43, 44, 46, 80 and 180.)

[96] Rajes Sau and Krishnan Mahesh. Dynamics and mixing of vortex rings in crossflow. *Journal of Fluid Mechanics*, 604:389–409, 2008. (Cited p. 43, 44, 80 and 84.)

[97] Xin Wen and Hui Tang. On hairpin vortices induced by circular synthetic jets in laminar and turbulent boundary layers. *Computer and Fluids*, 95, 2014. (Cited p. 45 and 84.)

[98] Zdeněk Trávníček and Václav Tesař. Annular synthetic jet used for impinging flow mass-transfer. *International Journal of Heat and Mass Transfer*, 46(17):3291–3297, 2003. (Cited p. 45)

[99] Dan S. Kercher, Jeong Bong Lee, Oliver Brand, Mark G. Allen, and Ari Glezer. Microjet cooling devices for thermal management of electronics. *IEEE Transactions on Components and Packaging Technologies*, 26(2):359–366, 2003. (Cited p. 45 and 46.)

[100] Alan McGuinn, Tim Persoons, Pierre Valiorgue, Tadhg S. O'Donovan, and Darina B Murray. Heat transfer measurements of an impinging synthetic air jet with constant stroke length. In *5th European Thermal-Sciences Conference (Eurotherm)*, Eindhoven, the Netherlands, 2008. (Cited p. 45)

[101] Gopal Krishan, Kean C Aw, and Rajnish N Sharma. Synthetic jet impingement heat transfer enhancement – A review. *Applied Thermal Engineering*, 149:1305–1323, 2019. (Cited p. 45 and 46.)

[102] Paul Manning, Tim Persoons, and Darina Murray. Heat transfer and flow structure evaluation of a synthetic jet emanating from a planar heat sink. In *Journal of Physics: Conference Series*, volume 525, 2014. (Cited p. 46)

[103] Quentin Gallas, Jose Mathew, Anurag Kasyap, Ryan Holman, Toshikazu Nishida, Bruce Carroll, Mark Sheplak, and Louis Cattafesta. Lumped Element Modeling of Piezoelectric-Driven Synthetic Jet Actuators. *AIAA Journal*, 41(February):240–247, 2003. (Cited p. 47)

[104] Quentin Gallas, R. Holman, Reni Raju, Rajat Mittal, Mark Sheplak, and Louis Cattafesta. Low Dimensional Modeling for Zero-Net Mass-Flux Actuators. *2nd AIAA Flow Control Conference*, 2004. (Cited p. 47)

[105] Barton L. Smith and Ari Glezer. Vectoring of Adjacent Synthetic Jets. *AIAA Journal*, 43(10):2117–2124, 2005. (Cited p. 47)

[106] Ruben Rathnasingham and Kenneth S. Breuer. Characteristics of resonant actuators for flow control. *AIAA Journal*, 35(5):832–837, 1997. (Cited p. 47)

[107] Tim Persoons. General Reduced-Order Model to Design and Operate Synthetic Jet Actuators. *AIAA Journal*, 50:916–927, 2012. (Cited p. 47, 48 and 92.)

[108] Tim Persoons, Rick Cressall, and Sajad Alimohammadi. Validating a Reduced-Order Model for Synthetic Jet Actuators Using CFD and Experimental Data. *Actuators*, 7(4):67, 2018. (Cited p. 47, 92, 93 and 181.)

[109] Tim Persoons and Tadhg S. O'Donovan. A pressure-based estimate of synthetic jet velocity. *Physics of Fluids*, 19(12), 2007. (Cited p. 47 and 92.)

[110] Matteo Chiatto, Francesco Capuano, Gennaro Coppola, and Luigi De Luca. LEM characterization of synthetic jet actuators driven by piezoelectric element: A review. *Sensors (Switzerland)*, 17(6), 2017. (Cited p. 48)

[111] Reni Raju, Ehsan Aram, Rajat Mittal, and Louis Cattafesta. Reduced-Order Models of Zero-Net Mass-Flux Jets for Large-Scale Flow Control Simulations.

In *26th AIAA Applied Aerodynamics Conference*, pages 1–14, 2008. (Cited p. 48, 49 and 180.)

[112] Linda D. Kral, John F. Donovan, Alan B. Cain, and Andrew W. Cary. Numerical simulation of synthetic jet actuators. *4th Shear Flow Control Conference*, 1997. (Cited p. 48)

[113] Edward James Brambley. Fundamental problems with the model of uniform flow over acoustic linings. *Journal of Sound and Vibration*, 322(4-5):1026–1037, 2009. (Cited p. 49)

[114] E. J. Brambley. Viscous boundary layer effects on the Myers impedance boundary condition. *15th AIAA/CEAS Aeroacoustics Conference*, 2009. (Cited p. 50)

[115] Sjoerd W Rienstra. Impedance models in time domain. In *12th AIAA/CEAS Aeroacoustics Conference*, Cambridge, MA, USA, 2006. (Cited p. 50)

[116] Qi Zhang and Daniel J. Bodony. Numerical investigation and modelling of acoustically excited flow through a circular orifice backed by a hexagonal cavity. *Journal of Fluid Mechanics*, 693:367–401, 2012. (Cited p. 50)

[117] Stephen B Pope. *Turbulent Flows*. Cambridge University Press, Cambridge, IK, 2000. (Cited p. 51)

[118] Lewis Fry Richardson. *Weather Prediction by Numerical Process*. 1922. (Cited p. 51)

[119] A. N. Kolmogorov. The Local Structure of Turbulence in Incompressible Viscous Fluid for Very Large Reynolds Numbers. *Proceedings of the Royal Society A: Mathematical, Physical and Engineering Sciences*, page Dokl. Akad. Nauk SSSR, 1941. (Cited p. 51)

[120] Nicolas Odier, Florent Duchaine, Laurent Gicquel, Guillaume Dufour, and Nicolas Garcia Rosa. COMPARISON OF LES AND RANS PREDICTIONS WITH EXPERIMENTAL RESULTS OF THE FAN OF A TURBOFAN. In *Proceedings of 12th European Conference on Turbomachinery Fluid dynamics & Thermodynamics*, pages 1–14, Stockholm, Sweden, 2017. (Cited p. 52)

[121] Nicolas Odier, Florent Duchaine, Laurent Gicquel, Gabriel Staffelbach, Adrien Thacker, Nicolas Garcia Rosa, Guillaume Dufour, and Jens-Dominik Muller. Evaluation of Integral Turbulence Scale Through the Fan Stage of. In *ASME Turbo Expo 2018 Turbomachinery Technical Conference and Exposition GT2018*, 2018. (Cited p. 52 and 73.)

[122] Maël Harnieh. *Prédiction de la génération des pertes des écoulements compressibles anisothermes appliquée aux distributeurs hautes pressions avec les simulations aux grandes échelles*. PhD thesis, Université de Toulouse, 2020. (Cited p. 52)

[123] C. L. Rumsey, T. B. Gatski, W. L. Sellers, V. N. Vatsa, and S. A. Viken. Summary of the 2004 CFD validation workshop on Synthetic Jets And Turbulent Separation Control. In *2nd AIAA Flow Control Conference*, Portland, Oregon, USA, 2004. (Cited p. 52)

[124] Julien Dandois, Eric Garnier, and Pierre Sagaut. Unsteady Simulation of Synthetic Jet in a Crossflow. *AIAA Journal*, 44(2):225–238, 2006. (Cited p. 52)

[125] B Giachetti, M Fénot, D Couton, and F Plourde. Influence of Reynolds number synthetic jet dynamic in crossflow configuration on heat transfer enhancement. *International Journal of Heat and Mass Transfer*, 118:1–13, 2018. (Cited p. 56, 61, 64 and 66.)

[126] B Giachetti, M Fénot, D Couton, and F Plourde. Influence of multi-perforation synthetic jet configuration on heat transfer enhancement. *International Journal of Heat and Mass Transfer*, 125:262–273, 2018. (Cited p. 56, 61, 64, 65, 66, 72, 75, 77, 78, 86, 115, 151, 152, 153, 154, 167, 180, 183 and 185.)

[127] Patrick Chassaing. *Mécanique des fluides, Eléments d'un premier parcours, 3ème édition revue et augmentée*. Editions Cépaduès, Toulouse, 2010. (Cited p. 62)

[128] M. Fénot, E. Dorignac, and G. Lalizel. Heat transfer and flow structure of a multichannel impinging jet. *International Journal of Thermal Sciences*, 90:323–338, 2015. (Cited p. 66 and 67.)

[129] Xin Wen, Hui Tang, and Fei Duan. Vortex dynamics of in-line twin synthetic jets in a laminar boundary layer. *Physics of Fluids*, 083601(27), 2015. (Cited p. 67, 93, 94, 95 and 181.)

[130] Ronald S. Bunker. A review of shaped hole turbine film-cooling technology. *Journal of Heat Transfer*, 127(4):441–453, 2005. (Cited p. 68 and 139.)

[131] D. E. Metzger, D. I. Takeuchi, and P. A. Kuenstler. Effectiveness and heat transfer with full-coverage film cooling. *Journal of Engineering for Gas Turbines and Power*, 95(3):180–184, 1973. (Cited p. 68)

[132] P. V. Le Brocq, B. E. Launder, and C. H. Priddin. Discrete Hole Injection As a Means of Transpiration Cooling; an Experimental Study. *Inst Mech Eng (Lond) Proc*, 187(17):149–157, 1973. (Cited p. 68 and 149.)

[133] Soizic Esnault, Florent Duchaine, and Laurent Gicquel. Large-Eddy Simulations of heat transfer within a multi-perforation synthetic jets configuration. In *Proceedings of ASME Turbo Expo 2019: Turbomachinery Technical Conference and Exposition*, Phoenix, Arizona, USA, 2019. (Cited p. 69, 71, 72, 77, 78, 85, 87, 89, 180 and 181.)

[134] Nicolas Lamarque. *Schémas numériques et conditions limites pour la simulation aux grandes échelles de la combustion diphasique dans les foyers d'hélicoptère*. PhD thesis, Université de Toulouse, 2007. (Cited p. 69)

[135] Peter Lax and Burton Wendroff. Systems of conservation laws. *Communications on Pure and Applied Mathematics*, 13(2):217–237, 1960. (Cited p. 69)

[136] Olivier Colin and Michael Rudgyard. Development of High-Order Taylor – Galerkin Schemes for LES. *Journal of Computational Physics*, (2):338–371, 2000. (Cited p. 69)

[137] J. Smagorinsky. General Circulation Experiments With the Primitive Equations. *Monthly Weather Review*, 91(3):99–164, 1963. (Cited p. 70)

[138] Franck Nicoud, Hubert Baya Toda, Olivier Cabrit, Sanjeeb Bose, and Jungil Lee. Using singular values to build a subgrid-scale model for large eddy simulations. *Physics of Fluids*, 23(8), 2011. (Cited p. 70)

[139] Thierry J. Poinsot and Sanjiva K. Lele. Boundary conditions for direct simulations of compressible viscous flows. *Journal of Computational Physics*, 1992. (Cited p. 72)

[140] Victor Granet, Olivier Vermorel, Thomas Léonard, Laurent Gicquel, and Thierry Poinsot. Comparison of Nonreflecting Outlet Boundary Conditions for Compressible Solvers on Unstructured Grids. *AIAA Journal*, 48(10):2348–2364, 2010. (Cited p. 72)

[141] Guillaume Daviller, Maxence Brebion, Pradip Xavier, Gabriel Staffelbach, Jens-Dominik Müller, and Thierry Poinsot. A mesh adaptation strategy to predict pressure losses in LES of swirled flows. *Flow, Turbulence and Combustion*, 99(1):93–118, 2017. (Cited p. 73 and 74.)

[142] C. W. Hirt, A. A. Amsden, and J. L. Cook. An arbitrary Lagrangian-Eulerian computing method for all flow speeds. *Journal of Computational Physics*, 14(3):227–253, 1974. (Cited p. 77)

[143] Vincent Moureau, G. Lartigue, Y. Sommerer, C. Angelberger, O. Colin, and T. Poinsot. Numerical methods for unsteady compressible multi-component reacting flows on fixed and moving grids. *Journal of Computational Physics*, 202(2):710–736, 2005. (Cited p. 77)

[144] A M Ruiz, G Lacaze, and J C Oefelein. Flow topologies and turbulence scales in a jet-in-cross-flow. *Physics of Fluids*, pages 1–36, 2015. (Cited p. 84)

[145] S Bocquet, J Jouhaud, H Deniau, J Boussuge, and M J Estève. Computers & Fluids Wall-Modelled Large-Eddy Simulation of a hot Jet-In-Cross-Flow with turbulent inflow generation. *Computer and Fluids*, 101:136–154, 2014. (Cited p. 84, 140 and 183.)

[146] Robert H Kraichnan. Diffusion by a Random Velocity Field. *Physics of Fluids*, 22, 1970. (Cited p. 119)

[147] A Smirnov, S Shi, and I Celik. Random Flow Generation Technique for Large Eddy Simulations and Particle-Dynamics Modeling. *Journal of Fluids Engineering*, 123, 2001. (Cited p. 119)

[148] Xiao Ming Tan, Jing Zhou Zhang, Shan Yong, and Gong Nan Xie. An experimental investigation on comparison of synthetic and continuous jets impingement heat transfer. *International Journal of Heat and Mass Transfer*, 90:227–238, 2015. (Cited p. 139)

[149] S. Mendez and J. D. Eldredge. Acoustic modeling of perforated plates with bias flow for Large-Eddy Simulations. *Journal of Computational Physics*, 228(13):4757–4772, 2009. (Cited p. 139)

[150] T. F. Fric and A Roshko. Vortical structure in the wake of a transverse jet. *Journal of Fluid Mechanics*, 279:1–47, 1994. (Cited p. 140 and 183.)